

1. Table of contents

2. Jia Grace Lu Preface	537
3. J. R. Schrieffer Pairing, Magnetic Spin Fluctuations, and Superconductivity Near a Quantum Critical Point	539
8. P. L. Richards Bolometric Detectors for Measurements of the Cosmic Microwave Background	545
14. W. A. Little and M. J. Holcomb Oscillator-Strength Sum Rule in the Cuprates	551
22. D. van der Marel Optical Spectroscopy of Plasmons and Excitons in Cuprate Superconductors	559
39. Anatoli Polkovnikov, Ehud Altman, Eugene Demler, Bertrand I. Halperin, and Mikhail D. Lukin Decay of Supercurrents in Condensates in Optical Lattices	577
47. Antonio Barone The Strong Impact of the Weak Superconductivity	585
55. T. M. Klapwijk Proximity Effect From an Andreev Perspective	593
74. John R. Clem Pancake Vortices	613
91. P. Fulde and G. Zwicknagl Superconductivity Through Intra-Atomic Excitations	631
100. C. J. Lobb When are Superconductors Really Superconducting?	641
111. N. Gauss, A. G. M. Jansen, and P. Wyder Effect of Nuclear Field on Magnetotransport Quantum Oscillations in InSb	653
121. M. R. Beasley Materials Physics and Quantum Coherence in Superconducting Qubits	663
126. Vladimir Z. Kresin, Stuart A. Wolf, and Yuri N. Ovchinnikov “Pseudogap” State of Novel Superconductors: Energy Scales and Structural and Diamagnetic Transitions	669
130. Donald M. Ginsberg Michael Tinkham: The Early Years	673
132. Chris Lobb My 14 years in the Tinkham Group	675
133. Selected Publications M. Tinkham and Group	677

Preface

To Professor Tinkham on his 75th Birthday



This festschrift of *Journal of Superconductivity* is dedicated to Professor Michael Tinkham on the occasion of his 75th birthday. As a true scientist, an excellent mentor, and a kind-hearted person, his colleagues, students, and friends are honored to present this collection of memoirs and papers.

Mike Tinkham has been a defining figure in the field of superconductivity for half a century. He had done pioneering experiments and applied theoretical physics to experimental data to obtain a deep understanding of superconductivity. Professor Tinkham's work has spanned many areas: infrared spectroscopy, vortex physics, Josephson effect, and mesoscopic systems. Of seminal importance, he was the first to show spectroscopic evidence of superconducting energy gap preceding the BCS theory; he made important contributions to the understanding of nonequilibrium effects in superconductors; and he established the famous Blonder–Tinkham–Klapwijk (BTK) model describing Andreev reflection and related tunneling phenomena. Many of the papers in this issue reflect his influence on these fields. The papers have been arranged together with biographical reminiscences.

It is a pleasure to thank all the authors for their contributions to this special issue. Thanks are also due to Dr. Vladimir Kresin for his encouragement and patient assistance to make this issue come true.

Let's all join together in sending our warmest wishes to Mike, his wife Mary, and their family.

Jia Grace Lu
Guest Editor

Pairing, Magnetic Spin Fluctuations, and Superconductivity Near a Quantum Critical Point

J. R. Schrieffer¹

Received August 15, 2004; accepted September 4, 2004

The properties of a wide variety of intermetallic compounds exhibiting magnetic localized spin and superconducting fluctuations near a quantum critical point (QCP) are reviewed. They show highly anomalous critical indices (anomalously small). Laws of corresponding are observed in these materials and a theory is presented which gives a fully quantitative explanation of these laws. The theory employs a gauge transformation which rotates the electron spin quantization axis \hat{z} into the direction of the instantaneous staggered localized spin direction $\vec{M}(\vec{r}, t) = \vec{M}_0(\vec{r}, t) \cos \vec{Q} \cdot \vec{r}$, where \vec{Q} is the localized spin array wave vector. Many properties of these materials are worked out on the basis of this theory. The technological promise of these substances is truly immense, including energy generation, storage and transmission, MRI magnets, industrial and scientific magnets, maglev, cellular communications, μ -wave electronics, etc.

KEY WORDS: Magnetic spin fluctuations; quantum critical point; high T_c .

1. INTRODUCTION

The critical indices corresponding to the spin susceptibility $\chi(\vec{Q}, \omega, T)$, in a large number of ferromagnetic and antiferromagnetic intermetallic compounds and the specific heat $C_V(T)$, as well as many other quantities, exhibit critical indices which are highly anomalous (i.e., exceedingly small). For example, it is found that near the Quantum critical point QCP [1],

$$\chi(\vec{Q}, \omega_n = 0, T) \propto 1/T^\gamma, \quad \gamma \simeq 0.14. \quad (1)$$

Also, the specific heat $C_V(T)$ is found to obey

$$C_V(T) \propto \ln(T/T_0), \quad (2)$$

over a wide range of T/T_0 about the QCP. Thus a law of corresponding states exists. Here we present a theory which explains this anomalous behavior [2]. It is known that

$$\chi_0(\vec{Q}, \omega_n = 0, T) \propto 1/(T - T_N) \quad (3)$$

and

$$C_{0V}(T) \propto T \quad (4)$$

in a mean field approach.

Hertz [3], in his pioneering studies of the QCP in ferromagnetic materials, used a fermion functional integral action S_H worked out to fourth order in the spin fluctuation field (i.e., the one fermion loop level) and found highly anomalous critical indices near the QCP, although he did not investigate χ and C_V . In later studies, Millis [4] confirmed Hertz's results results in a calculation at a higher loop level. Further studies [5–11] excluding the present work, have shed little additional light on these remarkable phenomena.

For clarity we study the spin fermion model

$$H(t)_{SF} = - \sum_{ijs} t_{ij} \psi_{is}^\dagger \psi_{is} + J \sum_{iss'} \psi_{is}^\dagger \psi_{is'} \vec{\sigma}_{ss'} \cdot \vec{S}_i(t), \quad (5)$$

where ψ^\dagger , ψ , and \vec{S} satisfy

$$\{\psi_{is}^\dagger, \psi_{js'}\} = \delta_{ij} \delta_{ss'} \quad (6)$$

and

$$[S_{i\alpha}, S_{j\beta}] = i\hbar S_\gamma \delta_{ij}, \quad (7)$$

with α , β , and γ being related cyclically.

¹Department of Physics and NHMFL, Florida State University, Tallahassee, Florida 32310.

We have explored these anomalous phenomena in the Hubbard model and find nearly identical results to those presented here, although the analysis is far more complex.

To carry through the analysis, we exploit the slow spatial and temporal variation of the critical degrees of freedom near the QCP. By making a WKB-like adiabatic unitary transformation $U(t)$, which rotates the electron-spin quantization axis \hat{z} to that of the direction of the local instantaneous staggered magnetization,

$$\vec{M}_i(t) \equiv \cos \vec{Q} \cdot \vec{r}_i \vec{S}_i(t), \quad (8)$$

we obtain rapid convergence of all observable quantities, near the QCP, such as $\chi(T)$, $C_V(T)$, etc. We find excellent agreement of all observable quantities with experiment. A preliminary discussion of this theory was published [12] in the *Journal of Low Temperature Physics* in 1998. A more recent account was published in *Physical Review Letters* [2]. Here we review this theory and apply it to many experimental observables.

2. SPIN-ROTATION TRANSFORMATION

We define the unitary electron-spin rotation operator $U(t)$ as

$$U(t) = T e^{\frac{i}{2} \sum_{iss'} \psi_{is}^\dagger(t) \vec{\sigma}_{ss'} \cdot \vec{\Omega}_i(t) \psi_{is'}(t)} \quad (9)$$

Here $\vec{\Omega}_i(t)$ is the vector electron spin rotation angle, defined by

$$\vec{\Omega}_i(t) = \sin^{-1} |\hat{z} \times \vec{M}_i(t)| \cdot \frac{\hat{z} \times \vec{M}_i(t)}{|\hat{z} \times \vec{M}_i(t)|} \quad (10)$$

Making the transformation,

$$\bar{H}(t) = U^\dagger(t) H U(t), \quad (11)$$

we find

$$\bar{H}(t) = H_0(t) + H_{\text{sdp}}(t) + H_{\text{dia}}(t) + \bar{H}_J(t), \quad (12)$$

where $H_0(t)$ is given by the electron hopping in the rotated basis \bar{s} , by

$$H_0(t) = - \sum_{ij\bar{s}} t_{ij} \psi_{i\bar{s}}^\dagger \psi_{j\bar{s}}. \quad (13)$$

We find H_{sdp} is given by

$$H_{\text{sdp}}(t) = - \sum_{iss'} t_{ij} \psi_{is}^\dagger(t) \vec{\sigma}_{ss'} \cdot \vec{\nabla}_i \psi_{is'}(t) \cdot \times [\vec{\nabla}_{r_i} \vec{\Omega}(\vec{r}_i, t) + \vec{\Omega}(\vec{r}_i, t) \vec{\nabla}_{r_i}], \quad (14)$$

H_{sdp} is the spin deformation potential, analogous to the electron-phonon deformation potential $H_{\text{el-ph}}$ in solids [13],

$$H_{\text{el-ph}}(t) = \sum_{is\lambda} g_\lambda \psi_{is}^\dagger(t) \psi_{js}(t) (\vec{r}_i - \vec{r}_j) \cdot \vec{\nabla} \vec{u}_i(t) \cdot \hat{\epsilon}_{\lambda i} \quad (15)$$

where $(\vec{r}_i - \vec{r}_j) \cdot \vec{\nabla} \vec{u}_i(t) \cdot \hat{\epsilon}_{\lambda i}$ is the local lattice dilation and g_λ is the electron-phonon deformation potential constant (units of energy/length where λ) which is typically of order $1 - 4eV/\text{\AA}$ in solids.

In addition, there is a diamagnetic-like coupling

$$H_{\text{dia}}(t) = \sum_{is} t_{ij} \psi_{is}^\dagger(t) \psi_{is}(t) |\nabla_i \vec{\Omega}_i(t)|^2, \quad (16)$$

similar to the A^2 term of QCD. For a free electron band, H can be written as

$$\begin{aligned} \bar{H}(t) = & -\frac{\hbar^2}{2m} \sum_s \int d\vec{r} \psi_s^\dagger(\vec{r}, t) \nabla^2 \psi_s(\vec{r}, t) \\ & - \frac{\hbar^2}{2m} \sum_{ss'} \int d\vec{r} \psi_s^\dagger(\vec{r}, t) \vec{\sigma}_{ss'} \cdot \vec{\nabla} \psi_{s'}(\vec{r}, t) \cdot \\ & \times [\vec{\nabla} \vec{\Omega}(\vec{r}, t) + \vec{\Omega}(\vec{r}, t) \vec{\nabla}] \\ & + \sum_s \int d\vec{r} \psi_{is}^\dagger(\vec{r}, t) \psi_j(\vec{r}, t) |\nabla \Omega(t)|^2 \\ & + J \sum_{\bar{s}\bar{s}'} \int d\vec{r} \psi_{\bar{s}}^\dagger(\vec{r}, t) \vec{\sigma}_{\bar{s}\bar{s}'} \cdot \vec{S}(\vec{r}, t) \psi_{\bar{s}'}(\vec{r}, t), \quad (17) \end{aligned}$$

where \bar{s} is quantized along the instantaneous staggered magnetization $\vec{M}(\vec{r}, t)$. More compactly, \bar{H} can be written as

$$\begin{aligned} \bar{H}(t) = & -\frac{\hbar^2}{2m} \sum_{ss'} \int d\vec{r} \psi_s^\dagger(\vec{r}, t) (\vec{\nabla} \delta_{ss'} + i \vec{A}_{ss'}(\vec{r}, t)) \\ & \times (\nabla \delta_{ss'} t_i \vec{A}_{ss'}(\vec{r}, t)) \psi_s(\vec{r}, t) \\ & + J \sum_{\bar{s}'} \int d\vec{r} \psi_{\bar{s}}^\dagger \sigma_{\bar{s}\bar{s}'} \psi_{\bar{s}'} S_{\bar{s}}(\vec{r}, t), \quad (18) \end{aligned}$$

$\vec{A}_{ss'}(\vec{r}, t)$ is defined by

$$\vec{A}_{ss'}(\vec{r}, t) \equiv \vec{\sigma}_{ss'} \cdot (\vec{\nabla} \vec{\Omega}(\vec{r}, t) + \vec{\Omega}(\vec{r}, t) \vec{\nabla}) \quad (19)$$

It is H_{sdp} and H_{dia} that lead to the anomalous critical indices near the QCP [1].

While the discussion to this point is exact it is useful to make the pairing correlations explicit by introducing the Gor'kov two component spinor $\psi_s^\dagger(r, t)$ [14] defined by

$$\psi_s^\dagger(\vec{r}, t) = [\psi_s^\dagger(\vec{r}, t), \psi_{-s}(\vec{r}, t)]. \quad (20)$$

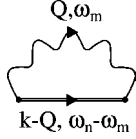


Fig. 1. Gor'kov self-energy $\Sigma(k, \omega_n, T)$ in the one-loop approximation.

We introduce the Pauli pseudo spin matrices,

$$\tau_{i=0,1,2,3} \quad (21)$$

where τ_0 is the unit pseudo-spin matrix.

It is straightforward to see that the electrons couple to the charge and spin through the vertices τ_3 for charge and τ_0 for spin [14]. All of our calculations are manifestly gauge invariant, as opposed to the original BCS calculations.

3. T_c AND THE GAP EQUATION

As in BCS, T_c is determined by the linearized gap equation. The first remarkable fact is that H_{sdp} leads to p -wave ($l = 1, s = 1$) pairing for ferromagnetic spin fluctuations, at a remarkably high temperature of order $T_c \simeq 30,000^\circ$ K. H_{dia} and \bar{H}_J lead to d -wave ($l = 2, s = 0$) and s -wave ($l = 0, s = 0$) pairing, as in the work of Scalapino [15] and of Pines [16], where \bar{H}_J plays the role of the weak electron-phonon coupling. As we will see below, T_c is highest for p -wave ($l = 1, s = 1$) pairing and it should be readily observed in electron tunneling, ARPES, $C_V(T)$, $\chi(Q, \omega, T)$ neutron scattering measurements, Raman, IR, $\lambda(T)$, $K_T(T)$, etc. These and many other measurements should show highly anomalous properties near the QCP [2].

The Gor'kov (see Fig. 1) one-electron self-energy [17] is given at the one loop level by

$$\begin{aligned} \Sigma(\vec{k}, \omega_n, T_c) = & - \sum_{Q, \omega_m} [V(\vec{Q}, \omega_m, T) \\ & \times \mathbb{G}(\vec{k} + \vec{Q}, \omega_n - \omega_m, T)], \quad (22) \end{aligned}$$

where V is the pairing interaction arising from H_{sdp} , H_{dia} , and \bar{H}_J , with $\omega_n = 2n\pi k_B T$ and $\omega_m = (2m + 1)\pi k_B T$. The gap equation [14] (see Fig. 1) is given for the complex pairing order parameter $\Delta(\vec{k}, \omega_n, T)$ by

$$\begin{aligned} \Delta(\vec{k}, \omega_n, T) = & - \sum_{Q, \omega_m} \frac{1}{Z(\vec{k}, \omega_n, T)} [V(\vec{Q}, \omega_m) \\ & \mathbb{G}(\vec{Q} + \vec{k}, \omega_n - \omega_m, T)]_{12} \quad (23) \end{aligned}$$

The normal state renormalization function $Z(\vec{k}, \omega_n, T)$ is given by [14]

$$\begin{aligned} i\omega_n Z(k, \omega_n, T) = & -\frac{1}{2} \sum_{\vec{Q}, \omega_m} [V(\vec{Q}, \omega_m, T) \\ & \times \mathbb{G}(\vec{k} + \vec{Q}, \omega_n - \omega_m, T)]_{11+22} \quad (24) \end{aligned}$$

and the renormalized kinetic energy $\bar{\epsilon}$ is defined by

$$\bar{\epsilon}(k, \omega_n, T) \equiv \epsilon_k + \bar{\chi}(k, \omega_n, T), \quad (25)$$

where $\bar{\chi}$ is given by

$$\begin{aligned} \bar{\chi}(k, \omega_n, T) = & -\frac{1}{2} \sum_{Q, \omega_m} [V(Q, \omega_m, T) \\ & \times \mathbb{G}(k + Q, \omega_n + \omega_m, T)]_{11-22}. \quad (26) \end{aligned}$$

4. SUPER-HIGH T_c (SHTC)

For the p -wave ($l = 1, s = 1$) phase T_c is given for a square potential model [14] as

$$k_B T_c = 1.14 \omega_s e^{-\frac{1+\lambda_Z}{\lambda_V}}, \quad (27)$$

where

$$\hbar \omega_s = \frac{J^2}{W}, \quad (28)$$

is the spin fluctuation frequency. The renormalization constant λ_Z for $l = 1$ is zero due to the p -wave character of the potential in (24).

$$\lambda_V = \left(\frac{W}{J} \right)^2. \quad (29)$$

Maximizing T_c for fixed W , we find

$$(k_B T_c)_{\text{max}} = 1.14 \frac{J^2}{W} e^{-\frac{1}{\lambda_{V, \text{max}}}}, \quad (30)$$

with

$$\lambda_{V, \text{max}} = \frac{W^2}{J^2} = 1. \quad (31)$$

for $W = 10$ eV, $T_{c, \text{max}}$ is given by,

$$T_c = 1.14 W e^{-1} \simeq 30,000 \text{ K} \quad (32)$$

Plotting $\ln T_c/W$ vs. J/W (see Fig(2)) we find T_c remains relatively stable for $0.5 \leq J/W \leq 5$. This gives the advantage that T_c is highly insensitive to impurity concentration, fluctuations, etc., a fact of great importance in technological as well as scientific applications of SHTC. For $J/W > 5$, one enters the Kondo spin compensated regime.

5. THERMODYNAMICS

The grand potential $\Lambda(T)$ is given by

$$\Lambda(T) = -k_B T \ln \text{Tr} T e^{-\beta(\bar{H} - \mu N_{el})} \quad (33)$$

where μ is the electrochemical potential. $C_V(T)$ is given by

$$C_V(T) = -\frac{d}{dT} \Lambda(T) \quad (34)$$

Within the random phase approximation, $\Lambda(T)$ is given by

$$\begin{aligned} \Lambda_{\text{RPA}}(T) = & -\frac{1}{2} \sum_{\vec{Q}, \omega_n, s} \text{Tr} V(\vec{Q}, \omega_n, T) \Phi_0(\vec{Q}, \omega_n, T) \\ & \times \left[1 - \frac{1}{2} \text{Tr} V(\vec{Q}, \omega_n, T) \Phi_0(\vec{Q}, \omega_n, T) \right]^{-1} \end{aligned} \quad (35)$$

(see Fig. 3). The zeroth-order irreducible polarizability is defined by

$$\Phi_0 \equiv -2 \sum_{k, \omega_m} G_0(\vec{k} + \vec{Q}, \omega_n + \omega_m, T) G_0(\vec{k}, \omega_n, T) \quad (36)$$

where the factor of 2 arises from the spin sum in the fermion loop.

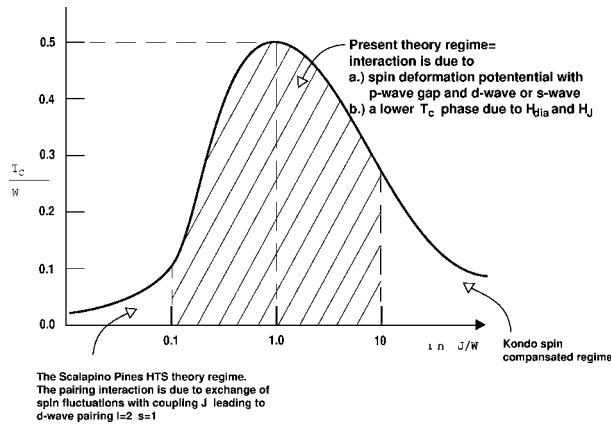


Fig. 2. The phase diagram of the $t - J$ model, showing the conventional nearly antiferromagnetic fermi liquid of Scalapins and Pines valid for $J \leq 0.01 W$, where J is the electron localized spin exchange coupling and W is the electronic band width. For $0.01 W \leq J \leq 10 W$ a novel p -wave, ($l = 1, s = 1$) phase is predicted with an extremely high T_C of immense technological importance (see the text). In this phase the existence of Leggett-like collective modes is predicted, corresponding to an oscillation at frequency ω_L of the angle between \vec{L} and \vec{s} of a pair. However, here the novel strong spin deformation raises ω_L to a high value near IR range vs. the low frequency of superfluid ^3He , where the spin orbit coupling H_{so} is extremely weak.

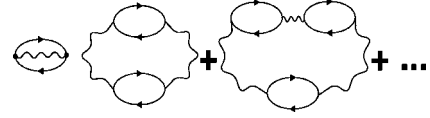


Fig. 3. RPA Grand canonical potential $\Lambda_{\text{RPA}}(T)$.

6. ELECTRON TUNNELING, ARPES MEASUREMENTS, AND COLLECTIVE (LEGGETT) MODES

As Bardeen showed, the Giaever differential tunnelling conductance is given by

$$\frac{dI}{dV} \propto \text{Im} \mathbb{G}(\vec{k}, eV, T)_{11+22}. \quad (37)$$

This should show p -wave ($l = 1, s = 1$) pseudogap behavior in the SHTC phase.

The ARPES differential cross section is given by

$$\frac{d\sigma}{d\vec{k} d\omega} \propto \text{Im} \mathbb{G}(k, \omega, T)_{11+22}, \quad (38)$$

and should demonstrate p -wave ($l = 1, s = 1$) pseudogap behavior, as will the London penetration depth $\lambda(T)$.

7. MAGNETIC SPIN SUSCEPTIBILITY AND NEUTRON SCATTERING

The dynamic electronic spin susceptibility is given by

$$\begin{aligned} \chi(\vec{Q}, \omega_m, T)_{\alpha\beta} = & \mu_B \sum_{kss'\omega_n} \psi_s^\dagger(\vec{k} + \vec{Q}, \omega_n + \omega_m) \vec{\sigma}_{\alpha ss'} \psi_s \\ & \times (\vec{k}, \omega_n, T) \psi_{\vec{s}}^\dagger(k - \vec{Q}, \omega_n - \omega_m) \\ & \times \vec{\sigma}_{\beta \vec{s} \vec{s}'} \psi_{\vec{s}'}(k, \omega_n) \end{aligned} \quad (39)$$

The results of the present theory agree very well with the observed neutron scattering spectra [1].

8. ACOUSTIC ATTENUATION

The acoustic attenuation rate is given by

$$\begin{aligned} \alpha_\lambda(\vec{Q}, \omega_m) = & -g_\lambda^2 \sum_{k, \omega_n, s, s', \vec{s}, \vec{s}'} \text{Im} \text{Tr} [\tau_{3ss'} \mathbb{G}_{ss'}(\vec{k} + \vec{Q}, \omega_n \\ & + \omega_m, T) \tau_{3\vec{s}\vec{s}'} \mathbb{G}_{\vec{s}\vec{s}'}(\vec{k}, \omega_n, T)]. \end{aligned} \quad (40)$$

α should show power law T behavior at low T corresponding to the pseudogap behavior of the p -wave ($l = 1, s = 1$) phase.

9. NMR

The $1/T$ NMR relaxation rate of p -wave $l = 1$, $s = 1$ pairing is given by

$$\frac{1}{T_1} \propto \lim_{\omega \rightarrow 0} \text{Im} \frac{\chi(Q, \omega, T)}{\omega} \coth^{-1}(\omega/k_B T). \quad (41)$$

$1/T_1$ should also show p -wave $l = 1$, $s = 1$ pairing analogous to the power law behavior observed for the d -wave, $l = 2$, $s = 0$ pairing of conventional high-temperature superconductors.

10. IR AND OPTICAL ABSORPTION PLUS THE ELECTRONIC RAMAN SCATTERING

The complex dynamic electromagnetic conductivity is given by

$$\begin{aligned} \sigma_{\alpha\beta}(\vec{Q}, \omega_n, T) = & -e^2 \left(\frac{\hbar^2}{2m} \right)^2 \int dt dt' \sum_{ss'\bar{s}\bar{s}'k} \\ & \times \langle T[\psi_s^\dagger(\vec{k} + \vec{Q}t) \tau_3 ss' \psi_{s'}(\vec{k}, t) \psi_{\bar{s}}^\dagger \\ & \times (\vec{k} - \vec{Q}t') \psi_{\bar{s}'}(\vec{k}, t')] \rangle e^{i\omega_n(t-t')}. \quad (42) \end{aligned}$$

The function should also show power law pseudogap behavior, characteristic of p -wave ($l = 1$, $s = 1$) pairing.

11. CONCLUSIONS

We have given an account of the observable properties of novel SHTC materials [2]. These materials are predicted to exhibit highly anomalous behavior, in that (1) the critical indices are highly anomalous (being small) near the QCP, and (2) the properties should show power law T dependence at low T , reflecting p -wave, ($l = 1$, $s = 1$) pairing with a tremendously high $T_c \geq 30,000^\circ$ K.

The potential for applications of SHTS to electric power generation, storage and transmission,

MRI, maglev, industrial and scientific magnets, and μ -wave electronics should be tremendous. Since these materials involve coupled pairing and magnetic spin fluctuations, highly nonlinear electrodynamic properties should be observed, with applications in communication, computers, etc.

ACKNOWLEDGMENTS

The author is grateful to the organizers of the Spectroscopies in Novel Superconductors for their kind hospitality. The author also thanks several colleagues for helpful discussions: Profs Megan Aronson, Nicholas Bonesteel, Lev P. Gor'kov, and Kun Yang. The author also thanks the NSF for Grant No. 0084173 and the Department of Energy for Grant No. DE-FG03-03NA00066. The author expresses his sincere thanks to Layla Hormozi for help with the manuscript.

REFERENCES

1. Megan Aronson, . ()
2. J. R. Schrieffer, Preprint (2004).
3. J. A. Hertz, *Phys. Rev. B* **14**, 1165–1184 (1976).
4. A. J. Millis, *Phys. Rev. B* **48**, 7183 (1993).
5. A. V. Chubukov and D. L. Maslov, *Phys. Rev. B* **68**, 155113 (2003).
6. P. Schlottmann, *Phys. Rev. B* **68**, 125105 (2003).
7. Q. Si, S. Rabello, K. Ingersent, and J. L. Smith, *Phys. Rev. B* **68**, 115103 (2003).
8. S. Sachdev and T. Morinari, *Phys. Rev. B* **66**, 235117 (2002).
9. Z. Wang, W. Mao, and K. Bedell, *Phys. Rev. Lett.* **87**, 257001 (2001).
10. V. P. Mineev and M. Sigrist, *Phys. Rev. B* **63**, 172504 (2001).
11. M. J. Lercher and J. M. Wheatly, *Phys. Rev. B* **63**, 12403 (2001).
12. J. R. Schrieffer, *J. Low Temp. Phys.* **99**, 397 (1995).
13. J. M. Ziman, *Electrons and Phonons* (Oxford Press, Oxford, 1954).
14. J. R. Schrieffer, *Superconductivity* (Academic Press, New York, 1962).
15. D. J. Scalapino, . ()
16. D. Pines, . ()
17. Gorkov-Eliashberg, . ()
18. A. J. Leggett, . ()

Bolometric Detectors for Measurements of the Cosmic Microwave Background

P. L. Richards¹

Received August 15, 2004; accepted September 4, 2004

Measurements of the Cosmic Microwave Background radiation provide the strongest support for the standard model of Inflationary Big Bang Cosmology. This paper sketches the impact of past and future CMB measurements on this rapidly developing field. Cryogenic millimeter wave bolometric detectors contribute strongly to this important experimental effort. The first such detectors were developed in the laboratory of Professor Michael Tinkham in the Berkeley Physics Department in the late 1950s. This development was first driven by the study of the superconducting energy gap, and other spectroscopy of other condensed matter systems. Later, it was driven very strongly, by the requirements for measurements of the CMB. This interaction between bolometer developments and the requirements of specific measurements is described. Until the past few years, the most useful bolometers had semiconductor thermistors and JFET readout amplifiers. The new superconducting voltage biased Transition Edge Sensor (TES) bolometers with SQUID readouts are beginning to have an impact and are expected to be the technology of choice in the future.

KEY WORDS: cosmic microwave background; bolometric detectors; superconducting devices.

1. INTRODUCTION

The Cosmic Microwave Background radiation (CMB) is the oldest electromagnetic radiation that reaches the earth. Observations of the CMB give a detailed picture of the universe 380,000 years after the Big Bang, and strongly support standard Big Bang Cosmology. The smoothness of this radiation supports the idea of an inflationary expansion of the Universe at an early epoch. The black body spectrum shows that the early Universe was very close to thermal equilibrium. It constrains energy release in the Universe back to about 2 months after the Big Bang. Small anisotropies in the temperature of the CMB provide a record of the interaction between matter and radiation. On scales of tens of degrees, this anisotropy tell us about the primordial fluctuations created by quantum fluctuations during the époque of Inflation. The anisotropy on degree scales confirms the 35-year-old theory that acoustic waves mod-

ify the primordial fluctuations and play a dominant role in the formation of structure in the Universe. The angular power spectrum of this anisotropy shows that structures observed on the far side of the observable Universe are neither magnified nor demagnified. This means that space is not curved, but flat over the largest observable distances. Therefore, the average density of mass-energy in the Universe is at the critical value. It also provides much information about the contents of the Universe, giving strong support to the picture that ordinary Baryonic Matter makes up only 4% of the Universe, that Dark Matter is 23% and that Dark Energy is 72%. This astonishing result is also strongly supported by measurements of the brightness and redshift of the most distant supernovas and by counts of the numbers of clusters of galaxies as a function of redshift. The existence of Dark Matter has been recognized for many years from its gravitational effects. It is thought to be exotic particles left over from the Big Bang, that have not yet been detected directly. Dark Energy interacts by gravity and by a pressure that is causing the expansion of the universe to accelerate. Understanding

¹Department of Physics, University of California, Berkeley, California 94720-7300.

the nature of Dark Energy has been called the most important current problem in fundamental Physics. This standard cosmological model has been discussed in many hundreds of publications [1,2].

There is much current interest in measurements of the temperature anisotropy of the CMB on angular scales less than 10 arcmin. Scattering of CMB photons passing through the plasma of hot electrons trapped by gravity in clusters of galaxies shifts the photons to higher energies. This decreases the brightness below the peak in the black body curve and increases the brightness above the peak. Detailed studies of this Sunyaev-Zeldovich effect can provide a wealth of information including a value of the Hubble constant and large scale flows from peculiar velocities. Because the temperature of the CMB increases with redshift, the surface brightness of the SZ features does not decrease with the distance to the cluster. For this reason, the SZ effect is an excellent way to locate clusters of galaxies back to the epoch of cluster formation. In the future, large area SZ surveys, coupled with redshifts from optical follow-up, will test theories of structure development, and constrain the equation of state of the Dark Energy.

Observations of the anisotropy of the polarization of the CMB have the potential to provide information about the Universe near the instant of its birth. Some mechanisms for polarization, such as scattering from density fluctuations, produce so-called E-mode Polarization, which has no curl-like component. Measurements of this E-Mode Polarization are already providing additional confirmation of the standard cosmological model and contributing to our knowledge of important cosmological constants. Gravitational waves created during Inflation are thought to have imprinted a different and distinctive Curl-like pattern on the CMB radiation called the B-Mode Polarization. The detection of this extremely small B-Mode Polarization would be a great triumph for inflationary cosmology, providing us a picture of physical processes in the Universe at the time of Inflation, which is thought to have occurred about 10^{-34} seconds after the Big Bang. It would provide information about particle physics on energy scales that cannot be reached with any conceivable man made particle accelerator.

2. DETECTORS FOR CMB MEASUREMENTS

One approach to CMB measurements at millimeter wavelengths is to use low noise transistor

amplifiers based on high electron mobility (HEMT) Transistors. A typical receiver includes a conical antenna, a HEMT amplifier, a band pass filter, and a diode detector. The HEMT amplifiers can be cooled to ~ 20 K to minimize their noise. Microwave integrated circuit (MIMIC) techniques and new materials are improving manufacturability and high frequency performance and reducing the noise in these amplifiers. Because linear phase-conserving amplification is involved, HEMT receivers are subject to quantum noise, which corresponds to a fluctuation of ± 1 in the number of photons in the amplifier on the time scale set by the inverse of the bandwidth. Reasonable projections of the development of HEMT receivers suggests that in the next few years they will have noise equal to ~ 3 times the quantum limit in bandwidths of 20–30% for frequencies up ~ 100 GHz. HEMT amplifiers have been used in many CMB temperature anisotropy and polarization anisotropy experiments. The largest instruments use arrays of 10–15 receivers. In principle, much larger arrays of HEMT amplifiers could be used. Aperture synthesis interferometers, which use HEMT amplifiers, are useful for CMB anisotropy experiments. After amplification, the same signals are combined with different baselines to simultaneously measure many different spatial frequencies on the sky.

Bolometers are thermal detectors, which consist of an absorbing element, a resistive thermometer to measure the temperature, and a weak thermal connection to a heat sink at some low temperature. As there is no phase conserving amplification involved in the detection process, bolometers do not produce quantum noise. Bolometric receivers use cooled baffles and filters to minimize the photons from sources other than the in-band signal from the CMB. Modern low background bolometric receivers can be photon noise limited on the signal from the CMB itself in bandwidths of 20–30%. They have optical efficiencies $> 50\%$, values of the noise equivalent power (NEP) as low as 10^{-18} $\text{WHz}^{-1/2}$ and use heat sink temperatures as low as 100 MK.

A comparison between the sensitivities of HEMT and bolometer receivers depends on both the rate of arrival of the detected photons and their correlations. If the photon occupation number is unity, as is the case when observing a black body in the Rayleigh-Jeans limit, then the correlated photon noise is exactly the same as the quantum noise. In practice, the sensitivities of optimized single polarization bolometers and HEMTs are essentially

the same for CMB measurement at frequencies up to ~ 60 GHz. At frequencies approaching the peak of the black body curve, however, the photon occupation number falls below unity, the photon correlations disappear, and the performance of photon noise limited bolometric receivers becomes rapidly better than that of quantum noise limited HEMT receivers.

Due to the efforts of many dedicated workers, the NEP available from bolometers optimized for low backgrounds had improved from $\sim 3 \times 10^{-11}$ in the late 1950's to $\sim 3 \times 10^{-19}$ $\text{Whz}^{-1/2}$ by the late 1990's. This corresponds to an increase in the speed of measurement by a factor 10^{16} for a single pixel. Since focal planes of ~ 100 pixels were coming into use, the speed of the most capable systems had increased by a factor 10^{18} in 40 years. The corresponding doubling of the speed every 12 months is more dramatic than the 18-month doubling time for the speed of digital computation. Measurements of the CMB that are routine today were inconceivable only a few years ago. However, since the sensitivities of HEMT receivers below 100 GHz and of bolometric receivers are approaching the photon noise limit, future improvements in CMB measurements will come from the use of larger arrays.

3. HISTORY OF CRYOGENIC MILLIMETER WAVE BOLOMETERS

In the late 1950s, I was a Graduate Student in the laboratory of Professor Michael Tinkham in the Physics Department of the University of California at Berkeley. My assignment, in the early days of the BCS theory, was to show that superconducting Pb has an energy gap. The technique that Mike suggested was to measure the reflectivity of Pb as a function of frequency at millimeter and submillimeter wavelengths. Fellow graduate student Don Ginsberg was measuring the transmittance of superconducting films in the same wavelength range. We used a Mercury arc source, a diffraction grating spectrometer, and a Golay pneumatic detector. In my experiment, Light pipes were used to convey the radiation from the spectrometer to a cold Pb cavity and out to the room temperature detector. At a critical stage in these experiments, a paper arrived from Boyle and Rogers [3] at Bell Laboratories reporting the development of a cryogenic infrared bolometer made from a flake of material taken from a carbon radio resistor. I quickly reproduced this device, increasing its

area and thickness to absorb Millimeter wavelengths. My experiment was well adapted to bolometric detection. The input light pipe limited the short wavelength background radiation on the bolometer, which was located in the cavity. It was no longer necessary to convey the radiation out of the cryostat to a room temperature detector. This experiment gave the first unambiguous evidence for a clean superconducting energy gap and gave gap widths close to the BCS prediction in several superconductors [4].

In the early 1960s at Bell Laboratories, I developed far-infrared and millimeter-wave Fourier transform spectroscopy with bolometric detectors to measure low lying excitations in many condensed matter systems. Following a suggestion by Ted Geballe, I experimented with bolometers made from doped Ge. As expected, they had much lower noise than the resistor material, but they did not absorb millimeter waves well. The bolometers had to be very thick and the resulting heat capacity caused very slow response. I even tried a composite structure with a carbon resistor absorber and a doped Ge thermistor. The heat capacity was still high, but even this clumsy device was useful at the time. At this time a paper arrived from Frank Low [5] at Texas Instruments describing his doped Ge far infrared bolometer. He was doing astronomy in the $100 \mu\text{m}$ wavelength range where absorption in the doped Ge was not a problem, so his bolometer worked very well.

I did not find a solution to the absorption problem until after I returned to Berkeley and set out to measure the spectrum of the CMB. The answer was a thin metal film absorber on the thinnest possible dielectric substrate. We used Bi film absorbers with sheet resistances of 200 ohms per square deposited on $30\text{-}\mu\text{m}$ thick sapphire substrates to absorb free space radiation efficiently. Current designs use 377 ohms per square absorbers on $1\text{-}\mu\text{m}$ thick membranes of silicon or silicon nitride. A reflecting backshort produces nearly perfect absorption in useful bandwidths. Using this approach, bolometers with the large areas necessary for millimeter-wave experiments can be made with adequate speed of response. This idea was first announced in connection with a superconducting bolometer development done in collaboration with John Clarke [6]. At the time it was believed that superconducting thermistors had less low-frequency noise than doped Ge. The observed noise was low, but the reason was the careful temperature regulation implemented to keep the bolometer operating on the superconducting transition. It was immediately clear that composite bolometers made

with metal film absorbers attached to small doped germanium thermistors were useful and convenient. It took some time to realize that ideal performance could be obtained, limited only by thermodynamic energy fluctuations and/or photon noise.

In the early 1970s David Woody and I (with early contributions from John Mather) measured the spectrum of the CMB from a stratospheric balloon, using a Winston horn antenna, a Martin-Puplett polarizing interferometer, and a composite bolometer [7]. For more than a decade, this balloon experiment provided the best evidence that the CMB has a black body spectrum. This was the first use of a ^3He -cooled bolometer in astronomy. Tinkham student Al Sievers at Cornell had previously pioneered the use of such cold bolometers for the spectroscopy of solids. Many of the technologies developed for this experiment were used in the very accurate FIRAS measurement of the CMB spectrum on the COBE spacecraft [8].

The desire to search for the very small degree-scale anisotropies of the CMB drove a new generation of bolometer development. I encouraged Eugene Haller to produce small thermistors of neutron transmutation doped (NTD) Ge with ion implanted contacts, which are now used worldwide. Our Balloon CMB anisotropy experiment MAX (with Andrew Lange, Phil Lubin, and George Smoot) developed measurement techniques and demonstrated the power of the balloon approach. It made the first observations of the degree scale anisotropies [9] at the time when the COBE spacecraft measured the primordial fluctuations at larger angular scales [10]. For the later MAX flights, we used composite bolometers cooled to 100 mK by an adiabatic demagnetization refrigerator. I reviewed the status of bolometric detectors at that time [11].

The next big step in bolometer development was carried out by Andrew Lange and Ernst Kreysa, who did part of their work at Berkeley. Their bolometers use metal film absorbers on silicon nitride membranes with a reflecting backshort. The metallized membranes developed by Lange and Jamie Bok are patterned into a mesh or "spider web" to minimize heat capacity and cosmic ray cross section. The metal absorber has an average sheet resistance of 377 ohms per square. The NTD-Ge thermistors are current-biased, and read out through JFET amplifiers which operate at ~ 100 K to minimize their noise. An AC bias is used when very good low frequency stability is required. These devices have been perfected by the Caltech/JPL group and are used in a large number of important CMB anisotropy experiments.

My group (including Shaul Hanany, Adrian Lee, Andrew Lange, and many others) built the MAXIMA balloon CMB anisotropy experiment using an array of 16 JPL bolometers at 100 mK. This provided the first test of the 100-mK spider web technology that is incorporated in the forthcoming Plank Surveyor spacecraft. We produced an accurate millimeter wave map of 100 square degree of the sky. The analysis of the Maxima data [12] presented in the spring of 2000, agreed well with the results of the Boomerang experiment, which were released a week earlier [13]. The agreement between these two independent experiments showed that systematic errors had been adequately controlled. Together, the results convinced an excited community that the acoustic mode model of structure formation in the Universe was correct and that the Universe is flat. In 2003, the results from the WMAP spacecraft confirmed the MAXIMA results exactly and made large improvements in our knowledge of important cosmological constants [2].

Polarization-sensitive bolometers are made by replacing the mesh absorber with a one dimensional grid supported on a mesh of silicon nitride. Dual polarization bolometers have two closely separated orthogonal grids. Each grid is attached to a separate thermistor and each is sensitive to a different linear polarization. Dual polarization bolometers from Caltech/JPL will be used on the next generation of CMB polarization anisotropy experiments.

The current generation of bolometers gives excellent performance in many applications, but there are practical limits to the number of pixels that can be used. The JFET amplifiers limit the ability to produce arrays of more than a few hundred pixels. In addition to thermal and microphonics issues, the relatively poor amplifier noise margin causes system problems. Fortunately, very promising new approaches are under active development. The voltage-biased superconducting bolometer with a voltage-biased superconducting transition edge sensor (TES) and SQUID readout amplifier is a negative-feedback thermal detector which can be made entirely by thin film deposition and optical lithography. The feedback reduces the response time, improves the linearity, and isolates the bolometer responsivity from changes in infrared loading or heat sink temperature. There is also some suppression of Johnson noise. The SQUID amplifiers operate at bolometer temperatures, dissipate very little power, and have significant noise margin. Adrian Lee in our group at Berkeley pioneered the

development of these bolometers [14,15], which are now being produced in several laboratories.

In addition, there is work on bolometers for CMB polarization measurements that are coupled to the optics by planar lithographed antennas and superconducting microstrip transmission lines. The antennas are inherently polarization sensitive and the transmission lines can incorporate high performance microstrip bandpass filters. In essence, the low loss in superconductors is being used to extend MIMIC technology to higher frequencies. There is a strong interest in wideband antennas so that the radiation reaching one pixel can be divided into several photometric bands. The transmission lines can branch to form diplexers so that one antenna can feed bolometers which measure adjacent millimeter wave bands. Our group in Berkeley is making crossed double-slot dipole antennas coupled to two bolometers through microstrip filters. The sum and difference of the outputs of the bolometers gives the intensity and degree of polarization of the signal illuminating the pixel.

Simultaneously with the development of millimeter-wave bolometers, my coworkers and I invented and developed several other detectors and mixers for far-infrared and millimeter wavelengths. Some of these, like the Josephson Effect mixer, underwent extensive development, but proved not to be useful. Others have been very useful for ground, and/or space astronomy. The stressed Ge photoconductor (developed with Eugene Haller) is a direct detector for the 100–200- μm band [16]. It has been used for a number of aircraft, balloon, and rocket observations, as well as on the ISO and Spitzer space observatories. The Superconductor Insulator Superconductor (SIS) Quasiparticle Heterodyne Mixer was developed with Tek-Ming Shen and many others, including Tinkham graduates Andy Smith and Dan Prober [17]. It is used in astronomical heterodyne receivers for molecular line observations from 100 to 600 GHz in many radio astronomy observatories. Nearly 1000 SIS mixers will be used in the ALMA interferometer, which is beginning construction.

4. CURRENT BERKELEY PROJECTS

The group that I started at Berkeley in 1966 is now being led by Adrian Lee. The focus has shifted to the development of technology to make large format arrays of voltage-biased superconducting TES

bolometers and to carry out several major new CMB projects. The group has grown to include Senior Scientists: John Clarke, Bill Holzapfel, Adrian Lee, Paul Richards, and Helmuth Spieler, as well as Post-docs: Sherry Cho, Matt Dobbs, Niels Halverson, and Huan Tran.

Large format arrays of TES bolometers require output multiplexing to avoid very large numbers of leads leaving the cryostat. Lines of 30–50 detectors can be multiplexed before amplification using superconducting thin film technology. The NIST group has developed a time-domain multiplexer which uses a SQUID for each bolometer to switch the outputs sequentially through a single SQUID ammeter. Our group in Berkeley has pioneered a frequency-domain multiplexer. Each bolometer in a row is biased at a different frequency. The signals are then combined, amplified by a single SQUID ammeter, and separated with ambient temperature lock-in amplifiers.

Bolometric array technology has advanced to the point that it is attractive to build instruments to survey hundreds of square degrees of sky at ~ 150 GHz to locate clusters of galaxies with the SZ effect. A European consortium, including the MPIFR at Bonn have purchased a 12-m on-axis ALMA prototype telescope. This Atacama Pathfinder Experiment (APEX) telescope is now installed at 5000-m elevation in the Chilean high desert. Our group is preparing to carry out a 150 GHz SZ sky survey on this telescope in collaboration with Bonn. A ~ 300 pixel receiver is being built in Berkeley using horn-coupled TES spider web bolometers with a heat sink temperature of 250 mK. The baseline design calls for one SQUID amplifier per pixel, but multiplexing will be used if it is ready. In three seasons of observation it should be possible to survey 250 square degrees to a noise level of $100 \mu\text{K}_{\text{CMB}}$ per 0.8-arcmin pixel at 150 GHz. Simulations show that all galaxy clusters in the field that are larger than 4×10^{14} solar masses will be detected, regardless of redshift. This survey should increase the number of known clusters of galaxies by an order of magnitude. The NSF has funded the 9-meter South Pole Telescope project under the direction of John Carlstrom. The Berkeley group is designing a 1000-pixel TES bolometer array with multiplexed readout for this telescope to do a more ambitious search for clusters of galaxies using the SZ effect.

The POLAR BEAR experiment is being developed by the Berkeley group to measure the anisotropy of the polarization of the CMB from a

small ground-based telescope at White Mountain in California. Polar Bear-I uses an array of 300 dual-polarization, antenna-coupled TES bolometers operated at 250 mK and configured for measurements at 90, 150, and 270 GHz. With 3 years of observations, the effective integration time for CMB polarization is essentially the same as for the Planck space mission. Current TES technology developments will be used to expand the 300 bolometer focal plane to 2000 multiplexed pixels. In terms of sensitivity and angular scale, this POLAR BEAR-II is the most capable CMB polarization experiment yet proposed. Even so, the estimated sensitivity is just adequate to measure the contribution to B-mode polarization predicted from inflation at the energy scale of Grand Unification particle theories. The biggest challenge of this project is to control systematic errors, so that the sensitivity will produce accurate results.

ACKNOWLEDGMENTS

This paper is dedicated to Professor Michael Tinkham in honor of his long and productive career. I learned to build cryogenic millimeter wave bolometers in Mike's laboratory. These devices subsequently proved to be of great value in answering some of the most important questions of Cosmology. More important, Mike has been a friend and a mentor throughout my career. He has set the highest standards for quality, intellectual honesty, and the courage to innovate. I learned from him that experimental Physics is both a worthy endeavor and a lot of fun.

The work described in this paper would not have been possible without the dedicated work of many professional colleagues including more than 55 graduate students and Postdocs with whom I have had the privilege to work. I regret that it has not been possible to acknowledge the contributions of everyone.

REFERENCES

1. D. Scott and G. Smoot, *Phys. Lett. B* **592**, 1 (2004).
2. C. L. Bennett, M. Halpern, G. Hinshaw, N. Jarosik, A. Kogut, M. Lemon, S. S. Meyer, L. Page, D. N. Spergel, G. S. Tucker, E. Wollak, E. I. Wright, C. Barnes, M. R. Greason, R. S. Hill, E. Komatsu, M. R. Nolte, N. Odegard, V. H. Peiris, L. Verde, and J. L. Weiland, *Astrophys. J.* **148** (Suppl.), 1 (2003).
3. W. S. Boyle and K. F. Rogers, Jr., *J. Opt. Soc. Am.* **49**, 66 (1959).
4. P. L. Richards and M. Tinkham, *Phys. Rev.* **119**, 575 (1960).
5. F. J. Low, *J. Opt. Soc. Am.* **51**, 1300 (1961).
6. J. Clarke, P. L. Richards, and N.-H. Yeh, *Appl. Phys. Lett.* **30**, 664 (1977).
7. D. P. Woody and P. L. Richards, *Phys. Rev. Lett.* **42**, 925 (1979).
8. J. C. Mather, E. S. Cheng, R. E. Eplee, Jr., R. B. Isaacman, S. S. Meyer, R. A. Shafer, R. Weiss, E. L. Wright, C. L. Bennett, N. W. Boggess, E. Dwek, A. S. Gulkis, M. G. Hauser, M. Janssen, T. Kelsall, P. M. Lubin, S. H. Moseley, Jr., T. L. Murdock, R. F. Silverberg, G. F. Smoot, and D. T. Wilkinson, *Astrophys. J.* **357**, L37 (1990).
9. P. Meinhold, A. Clapp, D. Cottingham, M. Devlin, M. Fischer, J. Gundersen, W. Holmes, A. Lange, P. Lubin, P. Richards, and G. Smoot, *Astrophys. J. Lett.* **409**, L1 (1993).
10. G. F. Smoot, C. L. Bennett, A. Kogut, E. L. Wright, J. Aymon, N. W. Boggess, E. S. Cheng, G. De Amici, S. Gulkis, M. G. Hauser, G. Hinshaw, P. D. Jackson, M. Janssen, E. Kaita, T. Kelsall, P. Keegstra, C. D. Lineweaver, T. Murdock, L. Rokke, R. F. Silverberg, L. Tenorio, R. Weiss, and D. T. Wilkinson, *Astrophys. J.* **396**, L1 1992.
11. P. L. Richards, *J. Appl. Phys.* **76**, 1 (1994).
12. S. Hanany, P. Ade, A. Balbi, J. Bock, J. Borrill, A. Boscaleri, P. de Bernardis, P. G. Ferreira, V. V. Hristov, A. H. Jaffe, A. E. Lange, A. T. Lee, P. D. Mauskopf, C. B. Netterfield, S. Oh, E. Pascale, B. Rabbii, P. L. Richards, G. F. Smoot, R. Stompor, C. D. Winant, J. H. P. Wu, *Astrophys. J. Lett.* **545**, L5 (2000).
13. P. de Bernardis, P. A. R. Ade, J. J. Bock, J. R. Bond, J. Borrill, A. Boscaleri, K. Coble, B. P. Crill, G. De Gasperis, P. C. Farese, P. G. Ferreira, K. Ganga, M. Giacometti, E. Hivon, V. V. Hristov, A. Iacoangeli, A. H. Jaffe, A. E. Lange, L. Martinis, S. Masi, P. Mason, P. D. Mauskopf, A. Melchiorri, L. Miglio, T. Montroy, C. B. Netterfield, E. Pascale, F. Piacentini, D. Pogosyan, S. Prunet, S. Rao, G. Romeo, J. E. Ruhl, F. Scaramuzzi, D. Sforna, and N. Vittorio, *Nature (Lond)* **404**, 955 (2000).
14. A. T. Lee, P. L. Richards, S.-W. Nam, B. Cabrera, and K. D. Irwin, *Appl. Phys. Lett.* **69**, 1801 (1996).
15. J. M. Gildemeister, A. T. Lee, and P. L. Richards, *Appl. Phys. Lett.* **74**, 868 (1999).
16. E. E. Haller, M. R. Hueschen, and P. L. Richards, *Appl. Phys. Lett.* **34**, 495 (1979).
17. P. L. Richards, T.-M. Shen, R. Harris, and F. L. Lloyd, *Appl. Phys. Lett.* **34**, 345 (1979).

Oscillator-Strength Sum Rule in the Cuprates

W. A. Little¹ and M. J. Holcomb²

Received August 15, 2004; accepted September 4, 2004

The oscillator-strength sum rule played an important role in the first work on the energy gap of superconductors by Tinkham. Recently, a small but measurable depletion in the sum rule integral has been observed at optical frequencies in the cuprates. It has been suggested that this behavior contradicts what is expected of traditional models of superconductivity. We disagree with this conclusion. We show that this depletion is consistent with earlier Thermal Difference Reflectance (TDR) measurements and their interpretation within the strong coupling extension of the BCS theory, as evidence of an electronic contribution to the pairing interaction at energies between 1.0 and 2.0 eV for these materials. We show quantitative agreement with the magnitude of the depletion and agreement with recent work with ARPES on the dispersion and lifetime of quasiparticles from the same model. We have located the two transitions responsible for the electronic contribution from TDR measurements of the thermal derivative of the dielectric function.

KEY WORDS: pairing interaction; superconductivity; cuprates; phonon mechanism.

1. INTRODUCTION

It is appropriate to note on this occasion that it was Glover and Tinkham [1], who were the first to observe directly an energy gap of order kT_c in superconductors. The superconducting gap Δ was revealed by measuring the change of the transmission of far infrared radiation through films of Pb and Sn on entering the superconducting state. They found a dramatic *reduction* in the conductivity of the superconductor at energies below approximately $5kT_c$. This reduction depleted the value of the integral of the real part of the complex, frequency-dependent conductivity $\sigma_{s1}(\omega)$ when taken over all frequencies. It presented a problem at the time as the total value of this integral, which represents the total number of electrons contributing to the optical processes at all frequencies, has to be preserved. This relationship is known as the oscillator-strength sum rule and can be

cast in the form:

$$\int_0^\infty \sigma_1(\omega) d\omega = \frac{\pi n e^2}{2m} \quad (1)$$

where $\sigma_1(\omega)$ is the real part of the optical conductivity, n is the electron density, and e and m are the charge and mass of the electron, respectively. Tinkham and Ferrell [2] were able to explain the discrepancy and showed that the missing area was transferred to a delta function at the origin ($\omega = 0$), which represented the response of the supercurrent to a *dc* electric field, thus tying the BCS gap function to the London response of the superconductor. With the addition of the delta function at zero frequency, the measured $\sigma_{s1}(\omega)$ data then satisfied the oscillator-strength sum rule.

Recent studies by Molegraaf *et al.* [3] on the high T_c , cuprate superconductor, $\text{Bi}_2\text{Sr}_2\text{CaCu}_2\text{O}_{8+\delta}$ using spectroscopic ellipsometry shows a small but measurable depletion in the area of the oscillator-strength sum rule in the region between 10,000 and 20,000 cm^{-1} (1.24 to 2.49 eV) on entering the superconducting state. This energy lies well above that of Δ , which is approximately 25 meV at temperatures

¹Physics Department, Stanford University, Stanford, California 94305.

²Nove Technologies, 3380 South Lapeer Road, Metamora, Michigan 48455.

well below T_c . Others have obtained similar results with various interpretations^[4]. Molegraaf *et al.* suggest that such behavior contradicts what would be expected from traditional models of superconductivity and argue that this depletion represents a strong indication that superconductivity in the cuprates is unconventional. Their experimental observations agree with our earlier published work [5] on other cuprate superconductors, but in contrast to their conclusion we argue that this behavior is well described qualitatively and quantitatively by the proper application of the Eliashberg theory [6, 7] with an electronic interaction added to the phonon pairing interaction. At the time the possibility of such an electronic interaction was first suggested [8] the idea was considered unconventional, but today we believe it is more nearly main stream.

Previous work [9–11] by our group had shown that for all the optimally doped high T_c cuprate superconductors studied ($\text{Tl}_2\text{Ba}_2\text{Ca}_2\text{Cu}_3\text{O}_{10}$, $\text{Tl}_2\text{Ba}_2\text{CaCu}_2\text{O}_8$, $(\text{BiPb})_2\text{Sr}_2\text{Ca}_2\text{Cu}_3\text{O}_{10}$, $\text{YBa}_2\text{Cu}_3\text{O}_{7-x}$, $\text{Bi}_2\text{Sr}_2\text{CaCu}_2\text{O}_{8+\delta}$, and $\text{HgBa}_2\text{CaCu}_2\text{O}_6$) there exists in addition to a phonon mediated pairing interaction, a high-energy, presumably electronic contribution to the pairing interaction. Our analysis was based on the optical properties of strongly coupled superconductors developed by Nam [12] and further refined by Shaw and Swihart [13] to understand the optical properties of superconducting Pb films. We found it was necessary to include an electronic-component to the pairing interaction, in addition to the electron-phonon interaction, to account for both the changes in the optical properties of the material at photon energies between 1.0 and 3.0 eV on entering the superconducting state, and the high T_c . The changes in the optical properties of these materials at T_c are small, but can be determined with good signal-to-noise ratio with the appropriate technique.

Ellipsometric, and direct reflectance measurements allow changes of the optical properties to be determined, at best, to an accuracy of a few parts in a thousand ($\sim 0.3\%$) at a given energy. On the other hand at photon frequency ω , the fractional change of the reflectance on entering the superconducting state can be expected, on general grounds, to be of order Δ^2/ω^2 , which for the cuprates at 1.5 eV and $0.5 T_c$ is about 0.02%. For this reason we have used a Thermal Difference Reflectance (TDR) technique [14] that can measure *changes* in the reflectance of a material with temperature at a level of 0.005%. This technique has enabled us to resolve structure present in the optical properties of the material on entering

the superconducting state that would be lost in the noise of conventional reflectance measurements.

2. REFLECTANCE MEASUREMENTS

Our early work used a modified Drude model [9–11] to describe the optical properties of the normal state. With this we could account qualitatively for *changes* in the optical properties of these cuprates on entering the superconducting state. However, significant deviations between the data and the calculated changes of reflectance were found for some of the cuprates, in particular, for $\text{Tl}_2\text{Ba}_2\text{CaCu}_2\text{O}_8$. We believed that these differences were due to the poor representation of the optical properties of the normal state by the modified Drude model not to the inadequacy of the theory. In order to test this hypothesis we have made a direct determination of the near-normal reflectance at room temperature of $\text{Tl}_2\text{Ba}_2\text{CaCu}_2\text{O}_8$ over energies from 0.1 to 6.0 eV and used a Kramers–Kronig analysis [15] to determine the real and imaginary parts of the frequency-dependent dielectric function $\epsilon(\omega)$, from which the optical conductivity $\sigma(\omega)$ can be determined in a model-independent manner. We then used the TDR technique to determine the *changes* in the reflectance of the material with temperature. Using the room temperature reflectance spectrum, and a series of TDR spectra collected at successively lower temperatures, we obtain the reflectance of the material at any given temperature.

The $\text{Tl}_2\text{Ba}_2\text{CaCu}_2\text{O}_8$ sample was a shiny, high quality, thin film grown epitaxially on a Mg-O substrate, 7 mm \times 7 mm in size, with a T_c of 105 K, manufactured by Dupont Superconductivity, Central Research and Development, Wilmington, DE.

The reflectance spectrum was measured at 300 K using a single beam, near-normal incidence reflectance spectrometer [16] that had a background noise of 0.3% of the reflectance of a Spectralon [17] control sample between 0.5 and 6.0 eV, and 0.6% of the reflectance of a silver control sample between 0.1 and 0.5 eV. In the region from 0.5 to 6.0 eV four detectors were used. Changes in the observed reflectance data on switching between detectors was found to be less than 0.2% of the reflectance of a test sample. TDR spectra were measured at near-normal incidence from 300 to 90 K in 10 K increments, with the sample mounted in a UHV optical chamber. The baseline noise of the TDR spectrometer was found to be approximately 0.005% from 0.1 to 5 eV. With the

measured reflectance spectrum, and TDR spectra obtained on the same sample, but at successively lower temperatures, we determined the optical reflectance ratio $R_s(\omega)/R_n(\omega)$, where the subscripts s and n refer to the superconducting and normal state, respectively. Using this ratio, and the measured $R_n(\omega)$, we obtain $R_s(\omega)$. We then use a Kramers–Kronig analysis as described previously to determine $\sigma_{s1}(\omega)/\sigma_n(\omega)$ over this energy range independent of any model of the optical properties of the material in the normal state. These data, shown in Fig. 1(a), display structure in the phonon region and in the region between 1 and 2 eV.

3. DATA ANALYSIS

Shortly after Tinkham's work on the energy gap, Mattis and Bardeen [18] calculated $\sigma_{s1}(\omega)/\sigma_n(\omega)$ within the framework of the BCS theory [19] where the gap is a fixed energy-independent quantity. Nam [12] extended this to the strong coupling case taking into account the retarded nature of the electron–phonon interaction. The gap function $\Delta(\omega)$ now becomes energy dependent and complex. As shown by

Shaw and Swihart [13] this takes the form:

$$\frac{\sigma_{s1}(\omega)}{\sigma_n} = \frac{2}{\omega} \int_{\Delta_0}^{\omega/2} d\omega_1 \left[\text{Re} \left\{ \frac{\omega_1}{[\omega_1^2 - \Delta(\omega_1)^2]^{1/2}} \right\} \right. \\ \times \text{Re} \left\{ \frac{\omega - \omega_1}{[(\omega - \omega_1)^2 - \Delta(\omega - \omega_1)^2]^{1/2}} \right\} \\ \left. - \text{Re} \left\{ \frac{\Delta(\omega_1)}{[\omega_1^2 - \Delta(\omega_1)^2]^{1/2}} \right\} \right. \\ \left. \times \text{Re} \left\{ \frac{\Delta(\omega - \omega_1)}{[(\omega - \omega_1)^2 - \Delta(\omega - \omega_1)^2]^{1/2}} \right\} \right] \quad (2)$$

The first term is the convolution of the density of states above and below the Fermi energy, while the second results from the corresponding case II coherence factors [20]. Here $\sigma_n(\omega)$ is the optical conductivity in the normal state and Δ_0 the magnitude of the $\text{Re} \Delta(\omega)$ for $\omega = 0$ (i.e. the gap edge). This expression is valid in both the extreme anomalous and London limits. The London limit is appropriate for the cuprates, where the mean free path, l and the coherence length, ξ are each much less than the penetration length.

It is known from many studies of phonon-mediated superconductors that $\Delta(\omega)$ peaks at phonon frequencies where the coupling function $\alpha^2 F(\omega)$ is large. Furthermore, Shaw and Swihart showed that at high energies, where $\omega \gg \Delta_0$ the expression (2) reduces to:

$$\sigma_{s1}(\omega)/\sigma_n(\omega) \sim 1 - \frac{2\Delta_0 \text{Re}\{\Delta(\omega - \Delta_0)\}}{\omega^2} \ln \frac{2\omega}{\Delta_0} \dots \quad (3)$$

At energies where $\text{Re}(\Delta(\omega))$ is large and positive (i.e. energies where $\alpha^2 F(\omega)$ is large), a characteristic dip occurs in the ratio $\sigma_{s1}(\omega)/\sigma_n(\omega)$. We use this to help fit the data.

Note that the only energy dependent part of Eq. (2) of significance at high energies is the part that comes from the coherence terms. Our analysis of the optical properties of the cuprates is critically dependent on the presence of these terms. Although the existence of such terms is implicit in the understanding of many experiments including tunneling, ultrasonic attenuation, and nuclear-spin relaxation their explicit energy dependence in the cuprates had not been determined until recently. In an elegant paper in 2003, Matsui *et al.* [21], verified by angle-resolved photoemission spectroscopy (ARPES) measurements on $\text{Bi}_2\text{Sr}_2\text{Ca}_2\text{Cu}_3\text{O}_{10}$ the existence of these coherence terms and their

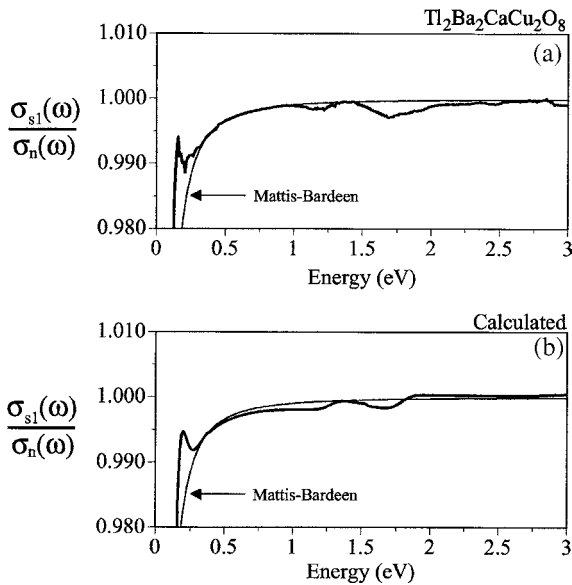


Fig. 1. (a) Measured value of the ratio $\text{Re}(\sigma_s/\sigma_n)$ for Tl-2212 at 90 K, as a function of photon energy (heavy line), compared to the Mattis–Bardeen result (light line) for an energy independent gap of 9 meV; (b) Calculated ratio of $\text{Re}(\sigma_s/\sigma_n)$ as a function of photon energy assuming a gap function derived from the Eliashberg Equations using the coupling function $G(\omega)$ shown in Fig. 2(a).

BCS [18] energy dependence. These measurements validate the use of the Nam, and Shaw and Swihart analysis in the calculation of $\sigma_{s1}(\omega)/\sigma_n(\omega)$ and their application in what follows.

To fit the $\sigma_{s1}(\omega)/\sigma_n(\omega)$ spectrum obtained from the measured $R_n(\omega)$ and $R_s(\omega)$, we replace the conventional electron–phonon coupling function $\alpha^2F(\omega)$ in the Eliashberg Equations [6] by a generalized trial function $G(\omega)$ that includes a phonon term and electronic terms near 1.5 eV. We then solve the Eliashberg Equations on the real-energy axis at 90 K to obtain the mass renormalization function $Z(\omega)$, and the complex superconducting gap function $\Delta(\omega)$ [22]. Using this energy-dependent gap $\Delta(\omega)$ in Eq. (2) we then calculate $\sigma_{s1}(\omega)/\sigma_n(\omega)$, and adjust $G(\omega)$ to get the best fit. The fit is constrained by the known T_c and the detailed optical data. The model T_c is determined by solving for $\Delta(\omega)$ using the trial $G(\omega)$ and trial μ^* for a series of temperatures, and finding the temperature at which $\Delta(\omega)$ collapses to zero. As anticipated from Eq. (2), the resultant complex, energy-dependent gap function $\Delta(\omega)$ modulates the ratio $\sigma_{s1}(\omega)/\sigma_n(\omega)$ near the energies where the peaks in $G(\omega)$ occur, even in the visible region of the spectrum. Good agreement is obtained between the calculated ratio, Fig. 1b, and the observed one, Fig. 1a, with a minimum set of fitting parameters—just the width and strength of three terms—one phonon and two electronic. This is illustrated in Fig. 1 using the data taken on $\text{Tl}_2\text{Ba}_2\text{CaCu}_2\text{O}_8$. For comparison, the Mattis–Bardeen calculation for a BCS gap of 9 meV at 90 K is included. Deviations from the Mattis–Bardeen curve occur in the phonon region and at the two energies, 1.2 and 1.7 eV—a generalization of the deviations seen in conventional superconductors [7,12,13] such as Pb, which occur at the phonon frequencies.

The phonon and electronic terms can be described by an effective coupling constant λ , defined in the usual way for each of the three regions:

$$\lambda = 2 \int_0^\infty d\omega \frac{G(\omega)}{\omega} \quad (4)$$

From the fit we obtain the following: $\lambda_{\text{phonon}} = 0.91$, $\lambda_{1.2\text{eV}} = 0.114$, and $\lambda_{1.7\text{eV}} = 0.294$, giving $\lambda_{\text{total}} = 1.318$ for $\text{Tl}_2\text{Ba}_2\text{CaCu}_2\text{O}_8$. A key feature in explaining the high transition temperature is the strong phonon contribution *plus* the high energy electronic contribution. Neither one alone, yields a high transition temperature nor is able to account for the optical properties [22].

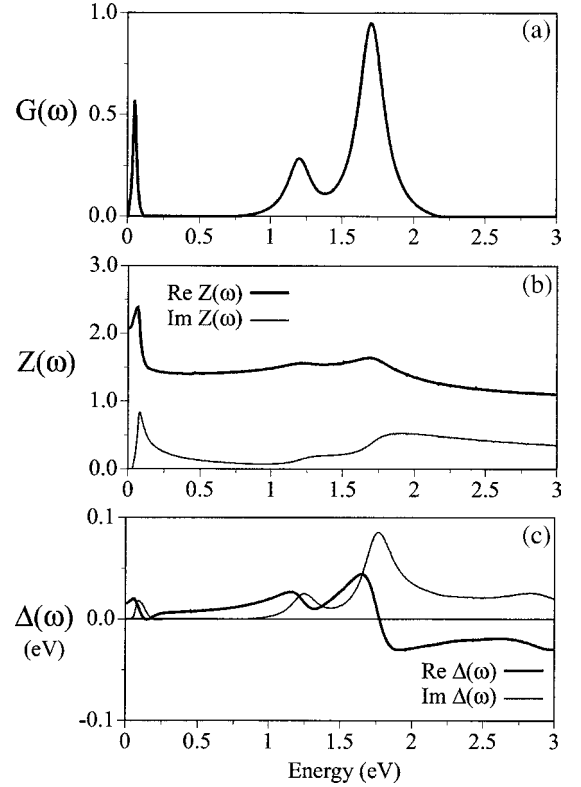


Fig. 2. (a) Coupling function $G(\omega)$ that gave the best fit to the experimental data shown in 1(a); (b) Renormalization function $Z(\omega)$, calculated from the Eliashberg equations using $G(\omega)$ of 2(a): Re $Z(\omega)$ (heavy line) and Im $Z(\omega)$ imaginary (light line); (c) Gap function $\Delta(\omega)$ calculated from the Eliashberg equations using $G(\omega)$ of 2(a): Re $\Delta(\omega)$ (heavy line) and Im $\Delta(\omega)$ imaginary (light line).

In Fig. 2a we plot $G(\omega)$ that gave the best fit to the experimental data. With a $\mu^* = 0.15$, the resultant real and imaginary parts of $Z(\omega)$ calculated for this $G(\omega)$ are shown in Fig. 2b, and the real and imaginary parts of $\Delta(\omega)$ in Fig. 2c. The real part of $Z(\omega)$ is large below the phonon peak and falls rapidly above this energy. However, unlike a simple strongly coupled superconductor [7] such as Pb, the real part of $Z(\omega)$ does not fall to unity monotonically above this energy. Rather, the real part of $Z(\omega)$ plateaus at a value of approximately 1.45 due to the effect of the electronic coupling terms at higher energies and peaks again at 1.25 and 1.7 eV before ultimately approaching 1.0 at much higher energies.

The phonon, and the high-energy components in $G(\omega)$ manifest themselves in the energy dependence of the superconducting gap function. Below the characteristic energy of the phonon, the real part of $\Delta(\omega)$ remains close to Δ_0 . Above the phonon energy, the real part of $\Delta(\omega)$ drops abruptly to near zero, *but*

then remains positive up to the energy of the electronic terms. In contrast, the real part of $\Delta(\omega)$ in conventional strongly coupled superconductors changes sign immediately above the phonon energies and remains negative at high energies due to the Coulomb pseudopotential μ^* . The absence of this reversal of sign in the real part of $\Delta(\omega)$ gives a characteristic signature in the superconducting to normal reflectance ratio that indicates the presence of high energy terms that contribute to the pairing [10,11].

In our model calculation, the real part of $\Delta(\omega)$ rises to about three times Δ_0 at the peak of the electronic terms then reverses sign above this. Although the gap in this region is large, its effect on the energy of the quasi-particles is small ($\sim 0.05\%$) because it occurs at such a high energy. The large peak in the imaginary part of $Z(\omega)$ indicates heavy damping near 2.0 eV and to a lesser extent for energies up to 3.5 eV.

Having established the fit, the model fixes the renormalization of the particle velocity through $Z(\omega)$ and the particle lifetime through the imaginary part of this function. In Fig. 3a we show our calculation of the quasi-particle dispersion for $\text{Tl}_2\text{Ba}_2\text{CaCu}_2\text{O}_8$. We compare these in Fig. 3b with dispersion curves of Lanzara *et al.* [23] on similar materials, in this case $\text{Bi}_2\text{Sr}_2\text{CaCu}_2\text{O}_8$, determined using ARPES and plotted in the same fashion. A similar change of slope of the curves above and below the phonon peak is seen. We find 1.85 ± 0.20 for the ratio of these slopes for $\text{Tl}_2\text{Ba}_2\text{CaCu}_2\text{O}_8$, and Lanzara's data for optimally doped $\text{Bi}_2\text{Sr}_2\text{CaCu}_2\text{O}_{8+\delta}$ ($\delta = 0.16$) gives about the same value $\sim 1.91 \pm 0.10$. Our figure also agrees with data from eight other cuprates reported by Lanzara *et al.* in the same paper. The ratio of these slopes is given approximately by $1 + \lambda_{\text{phonon}}$ for a pure phonon superconductor but due to the effects of the electronic terms discussed above this is only a rough approximation.

Our plot exhibits an upward turn and then a steep drop immediately after the peak in the phonon energies due to our choice of a single sharp Lorentzian electron-phonon contribution centered at 50 meV, whereas Lanzara's data has a smoother change of slope. A more realistic, broader distribution of phonons in our model calculation would produce a smoother change of slope in the resulting quasiparticle dispersion curves. However, Lanzara *et al.*, noted a sharpening of the kink for dispersions off the $(0, 0) - (\pi, \pi)$ direction in an insert to their Fig. 1b that shows a steepening of the plot, remarkably similar in shape to ours.

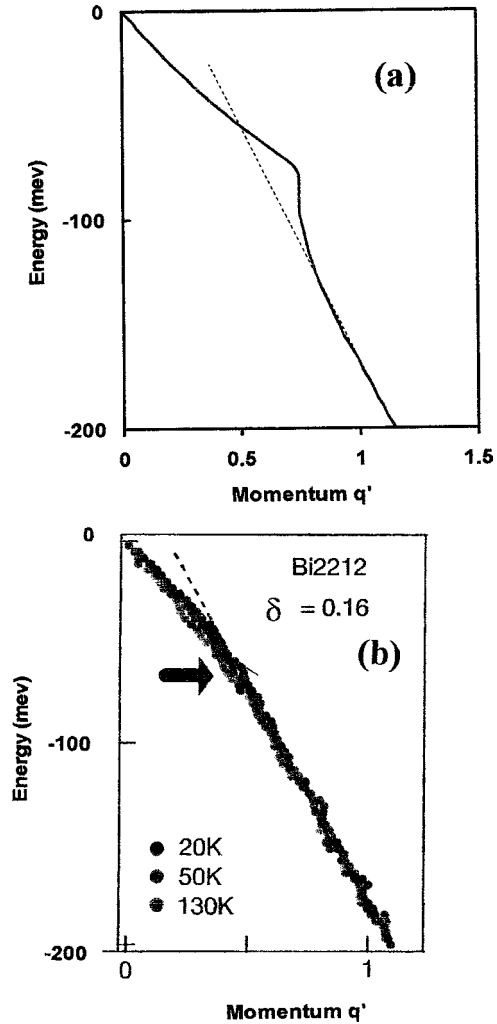


Fig. 3. (a) Calculated energy dispersion of quasi-particles in $\text{Tl}_2\text{Ba}_2\text{CaCu}_2\text{O}_8$, based on the renormalization function, $Z(\omega)$ derived from the Eliashberg equations using $G(\omega)$ of Fig. 2(a). Momenta have been normalized relative to the Fermi momentum in the same way as done by Lanzara *et al.* [23]. Note the change of slope of the curve from below to above the energy of the phonon peak of $G(\omega)$. (The upward curl and sharp drop in energy close to the phonon energies arise from the use of a single narrow phonon peak in $G(\omega)$. A broader distribution of phonon energies would yield a smoother transition at the Debye energy); (b) Reproduction of Lanzara's dispersion curves for $\text{Bi}_2\text{Sr}_2\text{CaCu}_2\text{O}_8$ ($\delta = 0.16$). Note the similar change in slope from below to above ~ 50 meV quasiparticle energy to that shown in (a) for the calculated dispersion.

In Fig. 4a we plot the quasiparticle widths determined by ARPES on $(\text{BiPb})_2\text{Sr}_2\text{Ca}_2\text{Cu}_3\text{O}_{10}$, and underdoped, optimally and overdoped $\text{Bi}_2\text{Sr}_2\text{CaCu}_2\text{O}_8$ by Lanzara *et al.* [23]. Similar results were obtained by Bogdanov *et al.* [24]. In Fig. 4b we plot our width as determined from $Z(\omega)$ from our best fit $G(\omega)$. Our width is about half of theirs and hence our

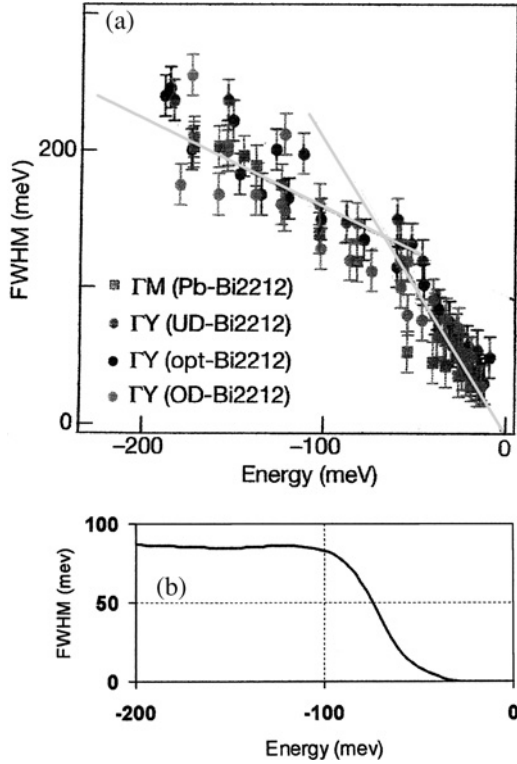


Fig. 4. (a) Quasi-particle width along the ΓY direction for Bi2212 and Pb-Bi2212, and along the ΓM direction for Pb-Bi2212 determined by Lanzara *et al.* [23] by ARPES measurements. (width of quasi-particle *momentum* state); (b) quasi-particle width calculated for Tl2212 from the renormalization function, $Z(\omega)$ derived from the fitting of the coupling function, $G(\omega)$ to the optical properties shown in Fig. 1(a). (width of quasi-particle *energy* state). Thus, the life of a pure momentum state prepared in ARPES is shorter than the life of the quasi-particle itself. This is consistent with the fact that the single particle part of a quasiparticle state of a given energy, is a linear combination of momentum states mixed by elastic scattering [25].

lifetime about twice as long. Our result is determined by the life of the *energy state* of the quasiparticle, while theirs is determined by the life of a *momentum state*. The single-particle portion of the quasi-particle state of a given energy is not an eigenstate of momentum but a combination of states of different momenta mixed by elastic scattering. This has been shown by Hoffman *et al.* [25], who observed interference effects in $\text{Bi}_2\text{Sr}_2\text{CaCu}_2\text{O}_8$ using scanning tunneling spectroscopy that arise from this mixture of momentum states. Similar behavior is to be expected in all the superconducting cuprates. The difference between the lifetimes measured in our work and those of Lanzara and Bogdanov *et al.* can be explained as follows. A quasi-particle prepared in a particular momentum state at $t = 0$, as in an ARPES

experiment, can evolve into its other momentum components before it de-excites. Consequently, the life of these individual momentum states will be less than that of the quasi-particle excited state, itself. Our TDR experiments determine the life of the excited state via $Z(\omega)$; and thus our width is smaller than theirs. The difference depends on a number of factors including the energy of the particle, the degree of disorder, and details of the elastic scattering cross-section. Further work would be needed to investigate these factors.

Our measurement of $R_s(\omega)/R_n(\omega)$ by TDR, along with the determination of $R_n(\omega)$, allows us to determine $\sigma_{s1}(\omega)$ and thus any depletion of the sum rule integral in the superconducting state for $\text{Tl}_2\text{Ba}_2\text{CaCu}_2\text{O}_8$. In addition it allows us to determine the region in energy where this depletion occurs. We define the depletion, D in the following way:

$$D \equiv 1.0 - \frac{\int_a^b \sigma_{s1}(\omega) d\omega}{\int_a^b \sigma_{n1}(\omega) d\omega}, \quad (5)$$

where we take the lower limit, ‘ a ’ below the first electronic peak, at 1 eV for $\text{Tl}_2\text{Ba}_2\text{CaCu}_2\text{O}_8$, and the upper limit, ‘ b ’ at the point where the calculated ratio $\sigma_{s1}(\omega)/\sigma_n(\omega)$ crosses unity, 1.85 eV. In this way we capture the depletion caused by all the electronic terms. At 90 K, which is a reduced temperature of 0.86 for our sample, we find a value for D of 0.0015 ± 0.0002 from our measured data, and 0.0013 ± 0.0002 for our fitted data. We find from Molegraaf’s published data on $\text{Bi}_2\text{Sr}_2\text{CaCu}_2\text{O}_8$ [26], a depletion of 0.0029 between T_c and $0.86 T_c$. Of this, 0.0015 comes from an extrapolation from above T_c of the temperature-dependent normal state depletion, and the remainder, 0.0014 to the growth of the superconducting gap. We thus find the same order of magnitude depletion for $\text{Tl}_2\text{Ba}_2\text{CaCu}_2\text{O}_8$ between 1.0 and 1.85 eV, as do Molegraaf *et al.* for $\text{Bi}_2\text{Sr}_2\text{CaCu}_2\text{O}_8$ between 1.24 and 2.49 eV at the same reduced temperature. Above these energies the real part of $\Delta(\omega)$ becomes negative, $\sigma_{s1}(\omega)/\sigma_n(\omega)$ becomes greater than unity, and the integral approaches its sum rule value.

4. DISCUSSION

The dips we observe in $\sigma_{s1}(\omega)/\sigma_n(\omega)$ in the region between 1 and 2 eV, and the depletion of the oscillator-strength integral at similar energies observed by Molegraaf *et al.* provide persuasive evidence of the existence of a superconducting energy gap at these energies. Starting with the strong

coupling extension of the BCS theory and a trial function, $G(\omega)$, we have calculated the superconducting gap function $\Delta(\omega)$ and renormalization function $Z(\omega)$. Using an iterative procedure, we then vary the trial $G(\omega)$ an μ^* and repeat the calculations until a satisfactory fit is obtained between the calculated and the observed $\sigma_{s1}(\omega)/\sigma_n(\omega)$ from the infrared to the ultraviolet, all the while requiring the calculated T_c to match the measured T_c . A good match is eventually achieved. However, the electronic terms that are added to the phonon terms to explain these properties, present a problem. The strong coupling, or Eliashberg theory is based on the validity of Migdal's theorem [27] that states that corrections to the lowest order electron-phonon vertex are of order (m_e/M_{ion}) , and thus can be neglected. For an electronic interaction the mass of the ion must be replaced by that of the electron and the corrections then could be expected to be *of the order of unity*. However, Allen and Mitrovic [28] have shown that these corrections can be much smaller. They show that the first correction is of the order of the product of the electronic coupling parameter $\lambda_{\text{electronic}}$ and a phase space factor (<1.0) that depends on the energy of the excitation and the structure of the Fermi surface. We have found that for $Tl_2Ba_2CaCu_2O_8$, the electronic coupling term $\lambda_{\text{electronic}}$ is small ~ 0.36 , and have estimated [29] the phase space factor to be about 0.28, giving a 10% correction to the lowest order Migdal term. The inclusion of these terms would give a vertex with a small additional energy and momentum dependence. However, we do not know, *a priori*, the bare interaction, so whatever the corrections are to this, they are contained in the effective interaction which we approximate by $G(\omega)$. In the end, the measured $\sigma_{s1}(\omega)/\sigma_n(\omega)$ spectrum is fit using the causal $\Delta(\omega)$ obtained from the solutions of the Eliashberg equations and Eq. (2). The calculated $\sigma_{s1}(\omega)/\sigma_n(\omega)$ spectrum obtained in this manner then automatically satisfies the oscillator-strength sum rule when taken over a sufficiently large energy.

No evidence is seen of these electronic excitations in the direct optical reflectance of $Tl_2Ba_2CaCu_2O_8$ [16]. However, using $R_n(\omega)$ and TDR data collected at 300 K, we have determined the temperature derivative of the complex dielectric function $\Delta\epsilon/\Delta T$ for $Tl_2Ba_2CaCu_2O_8$ [16]. Structure in $\Delta\epsilon/\Delta T$ reveals optically-weak temperature-dependent changes in the dielectric function of the material. In a Drude-Lorentz model, for example, structure in $\Delta\epsilon/\Delta T$ occurs at the energy of the

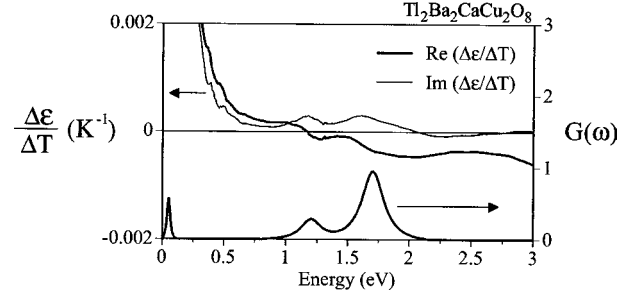


Fig. 5. Left axis: plot of real and imaginary parts of the derivative dielectric function versus energy for T12212 obtained from TDR measurements. Right axis, lower panel: plot of the pairing interaction, $G(\omega)$ that gives the best fit to $\text{Re}(\sigma_S/\sigma_N)$ of Figure 1(a); The two peaks in $\text{Im}(\Delta\epsilon/\Delta T)$, and the corresponding dispersive curves in $\text{Re}(\sigma_S/\sigma_N)$, clearly match the peaks at 1.25 eV and 1.7 eV in $\text{Re}(\sigma_S/\sigma_N)$ and $G(\omega)$. These excitations, plus the phonon contribution, are responsible for the high transition temperature of this cuprate. Identification of these transitions should provide an understanding of the superconductivity of these materials.

oscillators, i.e. zero frequency for the Drude term and at the transition energy for the Lorentz terms. The presence of the two electronic components of the generalized coupling function $G(\omega)$ obtained from the fit of the $\sigma_{s1}(\omega)/\sigma_n(\omega)$, are revealed as weak optical transitions in the $\Delta\epsilon/\Delta T$ spectra shown in Fig. 5. We have thus located the electronic transitions that are responsible for the large superconducting gap at optical frequencies, which, with the help of the phonons, explain the high transition temperature.

The nature of these excitations has not yet been determined. Their weakness in the visible suggests that they are not dipole allowed but are probably quadrupolar in nature. We have suggested [5] that they arise from symmetry forbidden $d-d$ transitions in the Cu-O plane of the material. An understanding of their true nature might be obtained from Medium Energy, Electron Energy Loss studies in reflectance mode, where the higher momenta available with electrons could probe these symmetry forbidden transitions. In studies of high temperature superconductivity, the experimental identification of these excitations should be given the highest priority for they appear to hold the secret to the understanding of the superconductivity of the cuprates.

5. A TRIBUTE

It is great pleasure to present this article as a tribute to Mike Tinkham on the occasion of his 75th birthday. I (WAL) am indebted to him for

teaching me some of the elements of far-infrared spectroscopy, and for the correct explanation of experiments done with Ron Parks on fluxoid quantization, many years ago. I have long admired Mike's work and willingness to tackle and solve theoretically and experimentally problems that often appeared to be wholly intractable, such as the decrease of resistance of a "one-dimensional" wire through the superconducting transition [30]. We both have benefited from the teachings of the 'BTK' paper [31] and his book has been within arm's reach, for at least one of us, for a quarter of a century. His wry wit and low key presentations have been a goldmine of inspiration. Thank you Mike, and many happy returns!

ACKNOWLEDGMENTS

We are indebted to J. P. Collman, C. L. Perry, and K. Collins for many valuable discussions and comments. We acknowledge Dr Todd Eberspacher for assistance with the TDR data collection, and acknowledge financial support for this work from the Department of Energy (Grant DEFG03-86ER45245) and Office of Naval Research contract N00014-96-1-0939.

REFERENCES

1. R. E. Glover and M. Tinkham, *Phys. Rev.* **104**, 844 (1956).
2. M. Tinkham and R. A. Ferrel, *Phys. Rev. Lett.* **2**, 331 (1959).
3. H. J. A. Molegraaf, C. Presura, D. van der Marel, P. H. Kes, and M. Li, *Science* **295**, 2239 (2002).
4. M. Rübhausen, A. Gozar, M. V. Klein, P. Guptasarma, and D. G. Hinks, *Phys. Rev. B* **63**, 224514 (2001); A. F. Santander-Syro, R. P. S. M. Lobo, N. Bontemps, Z. Konstantinovic, Z. Z. Li, and H. Raffy, *Europhysics Letters*, **62**(4), 568 (2003); and A. F. Santander-Syro, R. P. S. M. Lobo, and N. Bontemps, *cond-mat/0404290* **1**, 13 Apr 2004.
5. W. A. Little and M. J. Holcomb, *J. Superconduct.* **13**, 695 (2000).
6. G. M. Eliashberg, *Sov. Phys. JETP* **11**, 696 (1960).
7. D. J. Scalapino, in *Superconductivity*, R. D. Parks eds. (Dekker, New York, 1969) **1**, p. 449.
8. W. A. Little, *Phys. Rev.* **134**, A1416 (1964).
9. M. J. Holcomb, J. P. Collman, and W. A. Little, *Phys. Rev. Lett.* **73**, 2360 (1994).
10. M. J. Holcomb, C. L. Perry, J. P. Collman, and W. A. Little, *SPIE* **2696**, 606 (1996).
11. M. J. Holcomb, C. L. Perry, J. P. Collman, and W. A. Little, *Phys. Rev. B* **53**, 6734 (1996).
12. S. B. Nam, *Phys. Rev.* **156**, 470 (1967).
13. W. Shaw and J. C. Swihart, *Phys. Rev. Lett.* **20**, 1000 (1968).
14. M. J. Holcomb, J. P. Collman, and W. A. Little, *Rev. Sci. Instrum.* **64**, 1867 (1993).
15. J. S. Toll, *Phys. Rev.* **104**, 1760 (1956).
16. K. Collins, Ph.D. Thesis, Stanford University Physics Department, Copyright 1997, Stanford University.
17. Spectralon integration sphere (Labsphere, Shaker Street, North Sutton, NH, 03260).
18. D. C. Mattis and J. Bardeen, *Phys. Rev.* **111**, 412 (1958).
19. J. Bardeen, L. Cooper, and J. R. Schrieffer, *Phys. Rev.* **108**, 1175 (1957).
20. M. Tinkham, *Introduction to Superconductivity* (McGraw-Hill, New York, 1975), p. 57.
21. H. Matsui, T. Saito, T. Takahashi, S.-C. Wang, H.-B. Yang, H. Ding, T. Fujii, T. Watanabe, and A. Matsuda, *Phys. Rev. Letters* **90**, 217002 (2003).
22. M. J. Holcomb, *Phys. Rev. B* **54**, 6648 (1996).
23. A. Lanzara, P. V. Bogdanov, X. J. Zhou, S. A. Kellar, D. L. Feng, E. D. Lu, T. Yoshida, H. Eisaki, A. Fujimori, D. Kishio, J.-I. Shimoyama, T. Noda, S. Uchida, Z. Hussain and Z.-X. Shen, *Nature* **412**, 510 (2001).
24. P. V. Bogdanov, A. Lanzara, S. A. Kellar, X. J. Zhou, E. D. Lu, W. J. Zheng, G. Gu, J.-I. Shimoyama, K. Kishio, H. Ikeda, R. Yoshizaki, Z. Hussain and Z.-X. Shen, *Phys. Rev. Lett.* **85**, 2581 (2000).
25. J. E. Hoffman, K. McElroy, D.-H. Lee, K. M. Lang, H. Eisaki, S. Uchida, and J. C. Davis, *Science* **297**, 1148 (2002).
26. See [3], Figure 3 (left).
27. A. B. Migdal, *Sov. Phys. JETP* **7**, 996 (1958).
28. P. B. Allen and B. Mitrovic, in *Solid State Physics*, H. Ehrenreich, F. Seitz, and D. Turnbull, eds. **37** (Academic Press, New York, 1963) p. 1.
29. W. A. Little, K. Collins, and M. J. Holcomb, *J. Superconduct.* **12**, 89 (1999).
30. M. Tinkham, *Introduction to Superconductivity* (McGraw-Hill, New York, 1975), p. 231.
31. G. E. Blonder, M. Tinkham, and T. M. Klapwijk, *Phys. Rev. B* **25**, 4515 (1982).

Optical Spectroscopy of Plasmons and Excitons in Cuprate Superconductors

D. van der Marel¹

Received August 15, 2004; accepted September 4, 2004

An introduction is given to collective modes in layered, Josephson coupled high T_c superconductors. An experimental demonstration is treated of the mechanism proposed by Anderson whereby photons travelling inside the superconductor become massive, when the U(1) gauge symmetry is broken in the superconductor to which the photons are coupled. Using the Ferrell-Tinkham sumrule the photon mass is shown to have a simple relation to the spectral weight of the condensate. Various forms of Josephson plasmons can exist in single-layer and bilayer cuprates. In the bilayer cuprates a transverse optical plasma mode can be observed as a peak in the c -axis optical conductivity. This mode appears as a consequence of the existence of two different intrinsic Josephson couplings between the CuO_2 layers. It is strongly related to a collective oscillation corresponding to small fluctuations of the relative phases of the two condensates, which has been predicted in 1966 by A. J. Leggett for superconductors with two bands of charge carriers. A description is given of optical data of the high T_c cuprates demonstrating the presence of these and similar collective modes.

KEY WORDS: superconductivity; collective mode; Higgs mechanism; Tinkham-Ferrell sumrule; exciton.

1. INTRODUCTION

Electrons form, together with the atomic nuclei, the basic fabric of materials. In order to expose the organizing principles of matter, experimental physicists take apart the complicated fabric of matter, aimed with a vast array of different spectroscopic methods experimental physicists. Spectroscopic tools typically expose the sample to an external field or a beam of particles, and one measures the response of the sample to this external stimulus. Most of the spectroscopic tools, such as optical absorption or inelastic scattering, do not reveal the nuclei or the electrons directly. Instead one observes a spectrum of excited states which typically involve the excitation of several or many electrons and/or nuclei simultaneously.

The reason is, of course, that the elementary particles forming a solid behave in a correlated way,

and this is already the case for the ground state of the material. As a result one can not excite a single electron without influencing the state of the other particles in its vicinity. Usually, if the amplitudes are not too large, the excitations can be treated in the harmonic approximation. Regardless of the details of the material and of the type of interactions between the particles one can, in principle and at least for small amplitudes, identify a set of fundamental modes in the harmonic approximation. These so-called collective modes form an orthogonal set of eigenstates of the material. To treat the electrical transport properties of metals it is usually much simpler to refer to the language of electrons and holes. Nevertheless, even for simple metals like aluminum or sodium, the metallic luster is caused by the plasma oscillations, which are one out of several possible collective modes in a conducting material.

One of the relevant features of collective excitations is, that they provide the dynamical fluctuations transforming between different states of matter. They can be populated either by varying the

¹Département de Physique de la Matière Condensée, Université de Genève, CH-1211 Genève 4, Switzerland.

Table I. Some Analogies Between the Theory of Superconductivity and the Electroweak Theory

Superconductivity	Electroweak symmetry breaking
Spontaneous symmetry breaking of the pairing order parameter, Ψ .	Spontaneous symmetry breaking of the Higgs field, Φ .
$ \Psi $ is proportional to the gap in the electron-hole excitation spectrum.	$ \Phi $ is proportional to the mass of the Higgs-boson.
The coupling between Ψ and the EM-field, $(\partial_\mu + iqA_\mu)\Psi$, generates a mass-gap for plasmons and photons interior to the superconductor.	The coupling between the Higgs- and $W^{+/-}$, Z-fields, $(\partial_\mu + ig\tau \cdot W_\mu + ig'B_\mu Y)\Phi$, causes the W^+ , W^- , and Z bosons to be massive.

temperature or by applying an external field, for example an electrical field, pressure, or magnetism. Broken symmetries are typically accompanied by collective modes. We will now discuss a few examples.

(1) The phase of the order parameter in a superconductor is an example of a spontaneously broken $U(1)$ symmetry. This implies that the ground state is not unique but has a continuous degeneracy. In neutral superfluid the fluctuations of this phase then possess linear dispersion [1–3].

(2) Earlier Anderson had shown from the gauge-invariant treatment required for the Meissner effect, and taking into account the long-range nature of the Coulomb interactions, that in a superconductor the longitudinal modes are massive [4–6], and that the transverse electromagnetic waves traveling in a superconductor acquire a mass due to their coupling to the superconducting condensate. An experimental example of this effect is shown in Fig. 4. A detailed discussion of these data follows in section VI.

(3) Anderson's mechanism was later used in the context of elementary particle physics to predict, among other things, the occurrence of a novel massive elementary particle due to spontaneous symmetry breaking, the Higgs boson, and to show that the W and Z bosons acquire a finite mass due to the coupling to the symmetry broken Higgs-field [4,5,7–9]. The analogy between the theory of superconductivity and the electroweak theory is summarized in Table I. The collective modes spectrum of the amplitude of the order parameter of a superconductor has a gap, which has been observed experimentally in NbSe_2 with Raman spectroscopy, and which plays a role equivalent to the Higgs particle in the electroweak theory [115–117].

(4) Motivated by the observation of a precursor infrared absorption in Pb and Hg by Ginsberg *et al.* [10], Bardasis and Schrieffer have predicted excitons in the superconducting gap, corresponding to pairing

symmetries different from those of the ground state [11,12]. Figure 1 shows an example of such a mode in a model where the pairing-interaction has both an s-wave and a d-wave channel. In the absence of a local repulsive potential, the calculation predicts a soft excitonic mode near $k = (0, 0)$, which corresponds to a transition from s-wave to d-wave order parameter. Increasing the on-site interaction results in an increase of the energy of this exciton, implying the d-wave order parameter becomes more stable compared to s-wave symmetry.

(5) A different type of exciton has been predicted by Leggett for the case where a superconducting gap occurs in two or more overlapping bands [14] provided that a weak Josephson-coupling between those bands is present. A similar type of exciton is expected for the case where the crystal structure contains pairs of weakly coupled two-dimensional layers

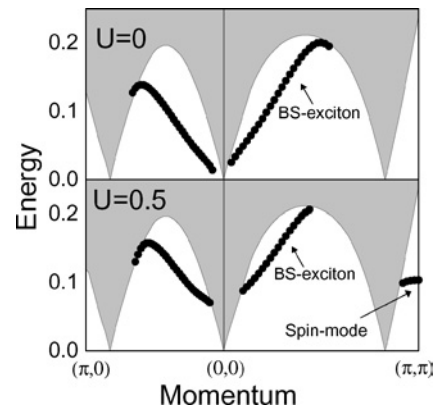


Fig. 1. RPA calculation of the collective modes of a layered d-wave superconductor using a tight-binding calculation, reproduced from Ref. [13]. Below the particle-hole continuum two types of modes occur: A fluctuation between d-wave and s-wave pairing symmetry of the variety predicted by Bardasis and Schrieffer [11] and a spin-fluctuation near the (π, π) point. The plasma-mode along the planes is at a much higher energy, not visible in this diagram.

[15,16]. For the latter case the Coulomb interaction between the layers plays a dominant role. An experimental example is shown in Fig. 11. A detailed discussion of these data follows in section XIV.

(6) Various additional collective modes have been identified, which are associated with a rotation between different order parameters permitted by models containing additional symmetries. Examples are the SO(4) symmetry of the negative U Hubbard model [17], the SO(5) symmetry [18], and the SU(2) symmetry groups [19], where the latter two have been proposed in the context of the $t - J$ model. The complex order parameter permitted by these models corresponds to a rich and complicated spectrum of collective modes. The SO(5) model generates a bosonic excitation with spin quantum number $S = 1$ and momentum (π, π) . This mode has been proposed for the resonance with the same quantum numbers in the cuprates, which has been observed with inelastic neutron scattering [20].

(7) A paramagnetic Fermi-liquid is composed of two degenerate liquids of opposite spin. The plasma-oscillations discussed above correspond to an in-phase modulation of the two spin-densities. The out-of-phase modulation is called a paramagnon. Because the two spin-liquids oscillate out of phase, there is no net charge-displacement, and consequently no restoring electric force as for the ordinary plasmon. These modes are therefore inside the particle-hole continuum and they are normally overdamped. However, if the particle-hole continuum is gapped, as happens in the superconducting state, a paramagnon branch can occur below the particle-hole continuum, with a correspondingly weak damping. In order to exist on an energy scale below the superconducting gap, the paramagnon must be very soft, implying that the system has been tuned close to a spin-density wave instability. In Fig. 1 an example of this fine-tuning is given, which was calculated using the generalized random phase approximation scheme by Anderson [4] and Bogoliubov *et al.* [1]. Increasing a local repulsive interaction vertex U from 0 to 0.5, results in the emergence of a soft spin-density mode near the (π, π) point. Similar behavior has been observed with inelastic neutron scattering in the cuprate superconductors [106,107], where indeed a transition takes place to a spin ordered state when the Mott-insulating state is approached by tuning the carrier concentration.

The superfluid phases of He^3 provide particularly beautiful examples where several of the collective modes mentioned above (and several oth-

ers which are not in this list) have been observed experimentally [21]. In this article we concentrate mostly on collective modes which can be observed with optical spectroscopy, i.e., items 1–5 of the previous list involving flow of charge and current. Because the cuprates are strongly correlated materials, and many of their properties can not be explained within the context of the random-phase approximation, a large part of the subsequent discussion will be based on classical field theory. The penalty one pays for this, is that the set of properties which one can address with such a formalism is limited to a particular set of collective modes. The advantage is, that the results calculated with such a model do not heavily rely on details on the microscopic level.

2. SOUND AND PLASMONS

We begin by discussing the collective mode spectrum of a classical compressible fluid of interacting particles of charge e^* in a charge-compensating background. The compressibility of the fluid is $\kappa = n^{-2} \partial n / \partial \mu$, which is a scalar. The mass of the particles, m , is in some cases an anisotropic tensor. The fluctuations of the particle density around its equilibrium value are described by the field $n(r, t) = n^{tot}(r, t) - n_0$. We furthermore allow the coupling of the fluid to an electromagnetic field, $\vec{E}(r, t) = -\vec{\nabla}\phi(r, t) - c^{-1} e^* d\vec{A}(r, t)/dt$, $\vec{B}(r, t) = \vec{\nabla} \times \vec{A}(r, t)$. The dynamical behavior of such a fluid can be described with the Hamiltonian [22]

$$H = \int \vec{\pi}(r) \cdot \frac{n_0}{2\bar{m}} \cdot \vec{\pi}(r) d^3r + \int \frac{|n(r)|^2}{2\kappa n_0^2} d^3r + \int \int \frac{e^{*2} n(r)n(r')}{2|r-r'|} d^3r d^3r' + \int e^* \phi(r) n(r) d^3r \quad (1)$$

where

$$\vec{\pi}(r) \equiv \vec{\nabla}v(r) + \vec{\nabla} \times \vec{\mu}(r) - \frac{e^* \vec{A}(r)}{c}$$

The first set of Hamiltonian equations of motion for the longitudinal currents are $dn/dt = \delta\mathcal{H}/\delta v = \partial\mathcal{H}/\partial v - \vec{\nabla} \cdot \partial\mathcal{H}/\partial(\vec{\nabla}v)$, and $-dv/dt = \delta\mathcal{H}/\delta n$. The second set for the transverse currents is $d\vec{\eta}/dt = \delta\mathcal{H}/\delta\vec{\mu} = \partial\mathcal{H}/\partial\vec{\mu} + \vec{\nabla} \times \partial\mathcal{H}/\partial(\vec{\nabla} \times \vec{\mu})$, and $-d\vec{\mu}/dt = \delta\mathcal{H}/\delta\vec{\eta}$. The potential energy does not depend on $\vec{\eta}$, because a liquid has zero shear-modulus. This provides four coupled relations between the currents

and the density fluctuations

$$\begin{aligned}
-\frac{d}{dt}v(r) &= \frac{n(r)}{\kappa n_0^2} + e^{*2} \int d^3r' \frac{n(r')}{|r-r'|} + e^*\phi(r) + \frac{v(r)}{\tau} \\
-\frac{d}{dt}\vec{\mu}(r) &= 0 \\
\frac{d}{dt}n(r) &= -\vec{\nabla} \cdot \frac{n_0}{\vec{m}} \cdot \left(\vec{\nabla}v(r) + \vec{\nabla} \times \vec{\mu}(r) - \frac{e^*\vec{A}(r)}{c} \right) \\
\frac{d}{dt}\vec{\eta}(r) &= \vec{\nabla} \times \frac{n_0}{\vec{m}} \cdot \left(\vec{\nabla}v(r) + \vec{\nabla} \times \vec{\mu}(r) - \frac{e^*\vec{A}(r)}{c} \right)
\end{aligned} \tag{2}$$

where the last term of the first line was introduced to represent the effect of dissipation on the current. Combining these expressions we obtain the wave-equation

$$\begin{aligned}
n_0 e^* \vec{\nabla} \cdot \frac{1}{\vec{m}} \cdot \vec{E}(r) + \left\{ \frac{d^2}{dt^2} + \frac{1}{\tau} \frac{d}{dt} \right\} n(r) \\
= \vec{\nabla} \cdot \frac{1}{\vec{m}} \cdot \vec{\nabla} \left\{ \frac{n(r)}{\kappa n_0} + e^{*2} n_0 \int d^3r' \frac{n(r')}{|r-r'|} \right\}
\end{aligned} \tag{3}$$

for the propagation of density fluctuations, or plasmons, of a charged fluid.² For plane waves $\vec{E}(r, t) = \vec{E}_k e^{ikr - i\omega t}$, $n(r, t) = n_k e^{ikr - i\omega t}$, this amounts to

$$\left(\omega^2 + \frac{i\omega}{\tau} - \vec{k} \cdot \left[\frac{w_p^2}{|\vec{k}|^2} + v_s^2 \right] \cdot \vec{k} \right) n_k = i\vec{k} \cdot \frac{e^* n_0}{\vec{m}} \cdot \vec{E}_k \tag{4}$$

where $\omega_p = (4\pi n_0 e^{*2}/m)^{1/2}$ is the plasma frequency and $v_s = (\kappa n_0 m)^{-1/2}$ is the sound-velocity. We should keep in mind that m , ω_p^2 , and v_s^2 are tensors; when the mass-tensor is anisotropic, the plasma-frequency and it's dispersion depend on the direction of propagation in the medium.

3. ISOTROPIC PLASMON-DISPERSION

Let us first consider the case of an isotropic charged fluid. In this case the plane wave solutions obey the dispersion relation

$$\omega(k)^2 = \omega_p^2 + v_s^2 k^2 \tag{5}$$

²The wave-equation for the transverse modes are $\frac{d^2}{dt^2}\vec{\eta}(r) = \vec{\nabla} \times \frac{n_0}{\vec{m}} \cdot (e^*\vec{E}(r) - \vec{\nabla} \int d^3r' \frac{e^{*2}n(r')}{|r-r'|} - \frac{\vec{\nabla}n(r)}{\kappa n_0^2} - \frac{\vec{\nabla}v(r)}{\tau})$. For waves traveling along one of the principle axis of the mass tensor: $\frac{d^2}{dt^2}\vec{\eta}(r) = -\frac{e^*n_0}{\vec{m}} \frac{d}{dt}\vec{B}(r, t)$. Solving this together with the Maxwell equations yields the polariton dispersion relation $k^2 c^2 = \omega^2 \epsilon(\omega)$.

In a 3D Fermi gas the compressibility arises purely from the density of states at the Fermi energy: $\kappa = n^{-2} dn/d\mu = 3/(mv_F^2 n)$, and consequently the zero-sound velocity is³⁴ $v_s = 3^{-1/2} v_F$. If we apply Eq. (5) to this case, we obtain $\omega_k = \omega_p + \frac{v_s^2}{6\omega_p} k^2 + O(k^4)$ for the dispersion formula. Although this resembles the result obtained with the random-phase approximation (RPA) of the electron gas model [23] $\omega^{\text{RPA}} = \omega_p + \frac{3v_s^2}{10\omega_p} k^2 + O(k^4)$ the dispersive term in the RPA is a factor 9/5 larger, which shrinks to a value closer to 1 when higher order electron-correlation diagrams are included in the calculation [23,24]. In the alkali metals a systematic reduction has been observed with high energy electron energy loss spectroscopy as the relative importance of the Coulomb interaction increases [25]. It is important to point out here, that at a qualitative level the dispersion of the plasma modes does not rely on the fact that microscopically the particles in the fluid are fermions. Indeed, Eq. (5) expresses a rather generic feature of a liquid, namely that it has a finite compressibility. For this reason Eq. (5) has a broad applicability, which goes beyond the special case of a Fermi-gas. This becomes particularly important in cases where on a microscopic level the properties are not fully understood, like in the cuprate materials: In spite of the lack of a fully established microscopic framework it is still possible to predict a certain number of properties at least at a qualitative level, in particular the collective plasma modes.

Superconductors are characterized by a macroscopic coherent state $\psi(r, t)$. Usually it is assumed that the variations of the amplitude are negligibly small, hence $\psi(r, t) = n_0^{1/2} \exp[i\varphi(r, t)]$. In this case the macroscopic current and the density of such a state are

$$n(r, t) = |\psi(r, t)|^2 = n_0 \tag{6a}$$

$$\vec{j}(r, t) = -\frac{n_0}{m} \hbar \vec{\nabla} \varphi(r, t) \tag{6b}$$

The equations of motion and the dispersion relation of the plasma-modes in the superconducting state are also given by Eqs. (3) and (5), with the dissipation $1/\tau$ set to zero, but v_s and ω_p may differ from those in normal state.

4. STRONG ANISOTROPY

Let us consider now the case of quasi-two dimensional materials, characterized by a large mass along perpendicular to the planes and a light mass

along it. For this case we obtain from Eq. (4) the dispersion relation

$$\omega(\vec{k})^2 = \frac{\omega_{p,p}^2 k_p^2 + \omega_{p,s}^2 k_s^2}{k_p^2 + k_z^2} + v_{s,p}^2 k_p^2 + v_{s,p}^2 k_z^2 \quad (7)$$

Inspection of this expression reveals, that $k = 0$ corresponds to a singular point: If we approach it along the planes, we obtain $\omega(k_p \rightarrow 0, k_z = 0) = \omega_{p,p}$, while along the z -direction $\omega(k_p = 0, k_z \rightarrow 0) = \omega_{p,z}$. In the extreme case, where the material is insulating along the z -direction, one obtains

$$\omega(\vec{k})^2 = \omega_{p,p}^2 \frac{k_p^2}{k_p^2 + k_z^2} + v_{s,p}^2 k_p^2 \quad (8)$$

which corresponds to the small k_z limit of the layered electron gas model [26–28]. In this case $\omega(k_p = 0, k_z \neq 0) = 0$. Moreover, if we consider the dispersion along the plane, while keeping k_z fixed at a finite value, it becomes sound-like: $\omega = v_{\text{eff}} k_x$, with a sound velocity $v_{\text{eff}}^2 = \omega_{p,p}^2 / k_z^2 + v_{s,p}^2$. This behavior can be measured with k -dependent electron energy loss spectroscopy [29].

5. DIELECTRIC FUNCTION

It is straightforward to solve Eq. (3) in the presence of a longitudinal external field $\vec{E}^e(r, t) = -\vec{\nabla}\phi(r, t)$: The total electric field is the sum of the externally applied field and the field arising from the charge distribution of the matter-field, $\vec{\nabla} \cdot \vec{E}(r, t) = \vec{\nabla} \cdot \vec{E}^e(r, t) + 4\pi e^* n(r, t)$. The longitudinal inverse dielectric function, describing the response to an external charge, is defined as the external field divided by the total field: $\epsilon = \vec{\nabla} \cdot \vec{E}^e / \vec{\nabla} \cdot \vec{E}$. With the help of Eq. (3) the inverse dielectric function is now easily obtained

$$\begin{aligned} \frac{1}{\epsilon(\omega, k)} &= 1 + \frac{4\pi e^* n(r, t)}{\vec{\nabla} \cdot \vec{E}^e(r, t)} \\ &= 1 - \frac{\omega_p^2}{\omega_p^2 + v_s^2 k^2 - \omega(\omega + i/\tau)} \end{aligned} \quad (9)$$

The plasma-modes correspond to the condition that an arbitrarily weak density fluctuation with wave-vector k and frequency ω can generate a finite electromagnetic response \vec{E} . Because $1/\epsilon(\omega, k)$ describes the response to the density fluctuation, in an isotropic fluid these modes have the electrical polarization parallel to the propagation direction. The charge-density modes therefore correspond to the

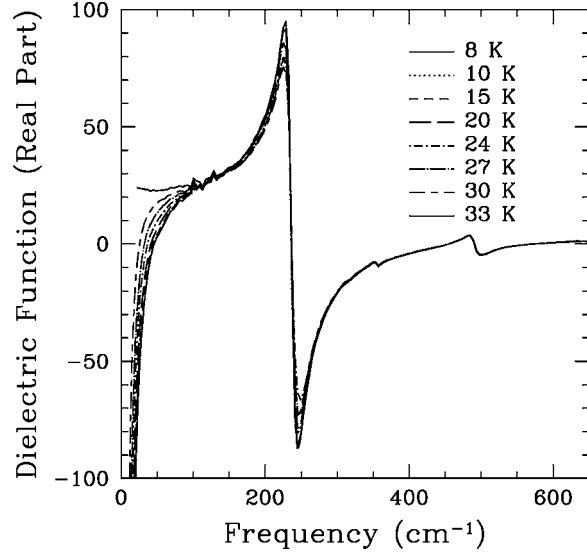


Fig. 2. Dielectric function with polarization along the c -direction of $\text{La}_{1.86}\text{Sr}_{0.14}\text{CuO}_{4+\delta}$ for different temperatures. T_c of this sample is 33 K. The data are from Ref. [108]. Copyright (1995) with permission from Elsevier.

poles of Eq. (9)

$$\omega = \frac{1}{2i\tau} \pm \sqrt{\omega_p^2 + v_s^2 k^2 - \frac{1}{4\tau^2}} \quad (10)$$

The relevant limit for optical spectroscopy is $k \rightarrow 0$ for which the mode frequencies become purely imaginary if $1/\tau > 2\omega_p$. This corresponds to the limit of overdamping. This situation is characterized by the fact that $\text{Re}\epsilon(\omega, k) > 3/4$ for all (real) frequencies. On the other hand, the condensate of a superconductor is characterized by the absence of dissipation, at least for frequencies much smaller than the superconducting gap, implying that $\epsilon(\omega, k) = 0$ *must* occur at some finite frequency. Hence in materials where the dissipation in the normal state is large enough to cause an overdamped charge response, the charge-density collective mode *must* emerge at some finite frequency within the frequency window of dissipation-less flow when the material becomes superconducting at low temperatures.

This kind of behavior is indeed observed for the c -axis optical response of the cuprate superconductors [30–36]. An example of this is shown in Fig. 2. T_c of this crystal was 33 K. At this temperature $\epsilon'(\omega)$ never crosses zero except for the phonons between 200 and 400 cm^{-1} . Below T_c a dissipation-less low-frequency electronic mode appears, characterized by a zero-crossing of $\epsilon'(\omega)$ reaching about 50 cm^{-1} for $T \ll T_c$. Note, that although superconductivity

implies the presence of a plasma-mode, the reverse is not true: In fact in most superconductors known to date, the plasmon is *not* overdamped in the normal state, and the transition into the superconducting state affects the plasma-frequency only marginally.

A second type of collective mode has the electric field perpendicular to the direction of propagation. Those modes correspond to absorption peaks of the optical conductivity function, $\sigma(\omega) = j/E$, which in the long wavelength limit is proportional to the dielectric function $\sigma_1(\omega) = \omega \text{Im}\epsilon(\omega)/(4\pi)$. In the limit that $k \rightarrow 0$ this condition requires, that an arbitrarily weak electric field results in a finite current. Hence at the transverse collective mode frequency $\sigma(\omega) \rightarrow \infty$. For a single component plasma this happens at $\omega = -i/\tau$. In a superconductor $\tau = 0$, and the condensate causes indeed a diverging conductivity at zero frequency. In a normal metal τ is finite, and the optical conductivity is characterized by a narrow Drude peak. In the cuprates, if the electric field is polarized along the c -direction, a narrow Drude peak is however *not* observed in the frequency dependence of a $\sigma(\omega, T)$. Also the temperature dependence of the c -axis conductivity is reminiscent of a semiconductor, at least in samples which are not strongly overdoped. Hence the cuprates have a strong anisotropy between ab -plane and c -axis conductivity in several respects: (i) The DC-resistivity, (ii) the superfluid spectral weight of the superconducting state, (iii) the temperature dependence of the conductivity, (iv) and the frequency dependence of the conductivity. Although (i) and (ii) can be easily explained from a large effect mass anisotropy, (iii) and (iv) imply that the transport mechanism itself is anisotropic. These observations, which belong to the oldest and most firmly established features of the cuprate superconductors, have been—and still are—the subject of many speculations, none of which have been completely satisfactory in every respect. Figure 3 demonstrates an example of this. The strong optical phonons obscure part of the electronic response along the c -axis, but it is clear from this graph that the electronic response has only a weak frequency dependence, and does not appear to agree with the Drude line-shape.

6. THE ANDERSON-HIGGS MECHANISM

For long wavelengths the energy momentum dispersion relation of transverse polarized electro-

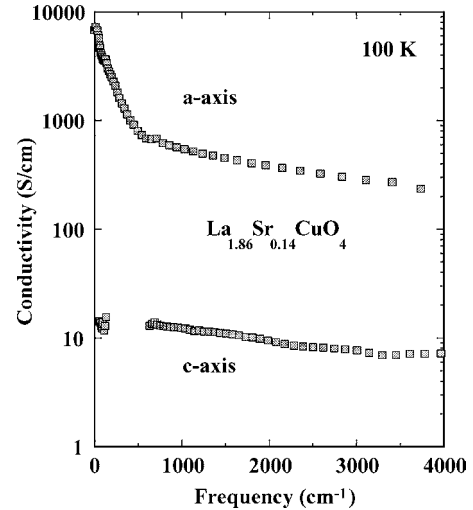


Fig. 3. Optical conductivity with polarization along the planes and along the c -direction of $\text{La}_{1.85}\text{Sr}_{0.15}\text{CuO}_{4+\delta}$ for $T = 100$ K. To obtain a high accuracy for the optical conductivity along the c -direction, the transmission coefficient was measured of a $20\text{-}\mu\text{m}$ thick slab, which had been cut along ac -plane. Because of a strong absorption by the optical phonons between 200 and 600 cm^{-1} , no transmission could be detected in this range. Therefore the c -axis optical conductivity is not shown in this range. The data are from Ref. [37]. Copyright (2000) with permission from Elsevier.

magnetic waves propagating inside the superconductor can be calculated from the relation³ $k^2 c^2 = \epsilon(\omega)\omega^2$ between the wave-vector, the frequency and the dielectric function. In Fig. 4, the data of Fig. 2 have been displayed in this way. This is an example of the Anderson-mechanism discussed in the introduction, which generates a finite mass of the photons by coupling them to a spontaneous symmetry-breaking field. Compared to the Higgs-boson in elementary particle physics this is merely a feather: the mass is about 6 meV , or $\cdot 10^{13}$ times lighter than the Higgs-boson according to recent estimates [38]. Using a cavity resonance technique, the mass-gap has been observed both for $k \parallel E \parallel c$ and for $k \perp E \parallel c$ in Bi2212 [39,40].

7. THE TINKHAM-FERRELL SUMRULE

A useful and important property of the c -axis optical conductivity concerns the spectral weight sum-rule, or f -sum rule: (i) The spectral weight represented by the zero-frequency δ -function in the

³See Footnote 2.

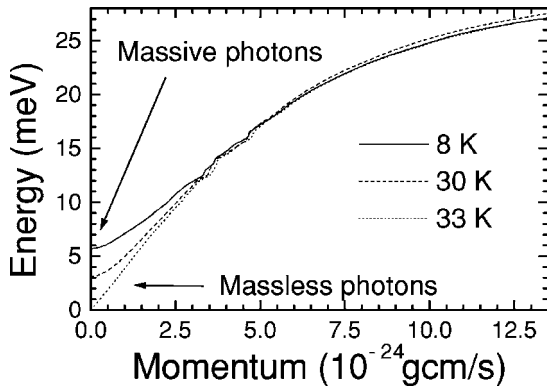


Fig. 4. Energy-momentum dispersion of photons polarized along the *c*-direction in $\text{La}_{1.85}\text{Sr}_{0.15}\text{CuO}_{4+\delta}$ for different temperatures. T_c of this sample is 33 K. The photons travelling inside the superconductor become massive, when the U(1) gauge symmetry is broken in the superconductor to which the photons are coupled.

superconducting state is represented as the square of the plasma-frequency of the condensate, $\omega_{p,s}^2$.
 (ii) A consequence of BCS theory is, that the spectral weight at finite frequencies is reduced due to the opening of a gap in the optical conductivity,
 (iii) The Tinkham–Ferrell sumrule [41–44] illustrated in Fig. 5, asserts that the spectral weight

of the condensate balances exactly the decrease of optical spectral weight integrated over all frequencies larger than zero, compared to the normal state:

$$\rho_s = \int_{0^+}^{\infty} \text{Re}(\sigma_n(\omega, \vec{q}) - \sigma_s(\omega, \vec{q})) d\omega \quad (11)$$

where the wave-vector \vec{q} is introduced in a general framework for the analysis, where all space and time-dependent quantities inside the material are Fourier-analyzed. The above stated sumrule has a general validity, irrespective of the microscopic details, due to the fact that it follows from a strict conservation law (i.e. particle number conservation). In recent years the sumrule has been an important instrument to address ideas that superconductivity may be stabilized by interlayer tunneling, or, more generally, to study the direction of change of kinetic energy when the material becomes superconducting both along the *c*-direction [45–60], and along the planar direction [61–65].

In a BCS superconductor one expects that by and large most of the spectral weight should be recovered on an energy range of four times the

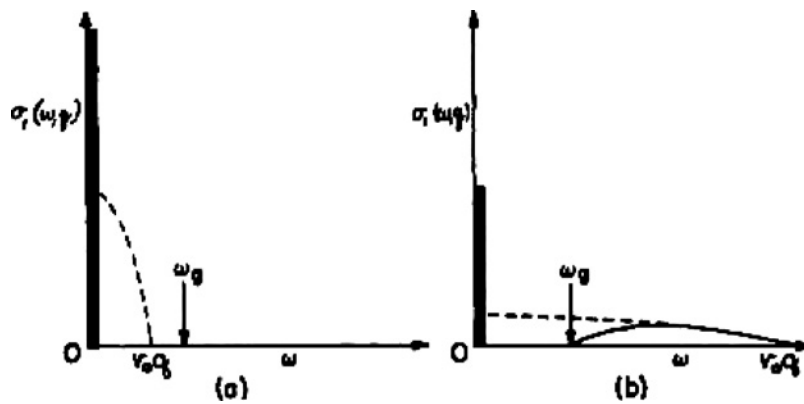


Fig. 5. Figure copied from by Tinkham and Ferrell [41]. Original caption: “Effect of the superconducting transition on the frequency-dependent conductivity for (a) long- and (b) short-wavelength transverse electromagnetic waves. The normal-state conductivity is indicated by dashed curves and extends to the maximum frequency of v_0q where v_0 is the Fermi velocity and q is the wave number. In (a) the wavelength is sufficiently long that the maximum absorption frequency in the normal state falls short of the energy gap threshold $\hbar\omega_g$. Consequently essentially all of the oscillator strength is absorbed by the delta function at zero frequency, leading to a full London current. In (b) the shorter wavelength causes the absorptions in the normal state to be spread over a frequency interval much larger than the energy gap. The strength of the delta function is therefore less and the London current is weakened. This dependence of the London current on wavelength is equivalent to the nonlocal current-field relation of Pippard.” Copyright (1959) by the American Physical Society.

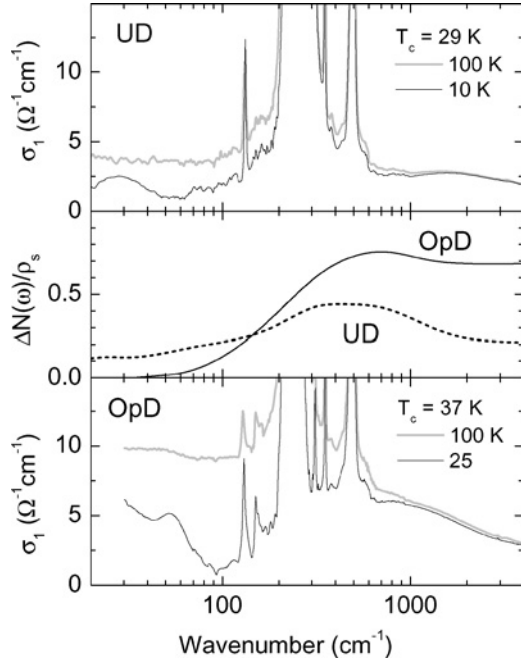


Fig. 6. Optical conductivity of underdoped (top panel) and optimally doped LSCO (bottom panel). In the middle panel the sum-rule check is displayed. The quantity displayed here corresponds to $(N^m(\omega, T) - N^{sc}(\omega, T))/\rho_s(T)$, where the temperature-dependent optical conductivity of the normal state has been extrapolated to obtain $(N^m(\omega, T)$ and $(N^{sc}(\omega, T)$ both at the same temperature below T_c . The details of this analysis are given in Ref. [67].

gap [66].⁴ Experiments with light polarized along the c -axis of the cuprates have revealed that in the underdoped samples a large fraction of the spectral weight remains unrecovered up to 20 times the gap energy [55,57,67]. At optimal doping the absolute value of nonrecovered c -axis spectral weight is even larger (see Fig. 6), but the ratio $\Delta N(\omega_m)/\rho_s \equiv \rho_s^{-1} \int_{0^+}^{\omega_m} \text{Re}(\sigma_n(\omega) - \sigma_s(\omega)) d\omega$ decreases due to the fact that ρ_s increases sharply as the doping is increased. Interestingly, in addition to the opening of the superconducting gap, we observed an *increase* of conductivity above the gap up to 270 meV with a maximal effect at about 120 meV [67]. This may indicate a new collective mode at a surprisingly large energy scale [19]. For the ab -direction of underdoped and optimally doped Bi2212 about 0.25% of the ab -

⁴However, a not widely realized consequence of BCS theory is, that in fact a small amount of superconductivity induced spectral weight transfer should occur between the Drude peak and the interband transitions, provided that the electrons have a non-parabolic $\epsilon(k)$ dispersion.

plane spectral weight remains unrecovered up to about 20 times the gap energy [63]. However, in absolute numbers the unrecovered spectral weight is orders of magnitude larger along the planes than along the c -direction.

7.1. Relation Between Photon-Mass and Spectral-Weight

The presence of the superconducting condensate contributes a term $-8\rho_s/\omega^2$ to the dielectric function. Because this term diverges for $\omega \rightarrow 0$, and $\epsilon(\omega)$ should become positive for $\omega \rightarrow \infty$, this means that in the superconducting state the dielectric function *must* cross through zero for some finite frequency. This is the plasma-frequency of the superconducting condensate. If the remaining contributions to the dielectric function, ϵ_b (for example those coming from optical photons) have a weak frequency dependence in the region where this zero crossing occurs, the plasma frequency of the condensate will be $\omega_{p,s} = (8\rho_s/\epsilon_b)^{1/2}$. In section VI we have seen that, due to Anderson's mechanism for mass generation, inside a superconductor the photons acquire a gap $\hbar\omega_{p,s}$. For the conditions described above the photon dispersion relation is $\omega^2 = (k^2c^2 + 8\rho_s)/\epsilon_b$. Because the dynamical mass of the photons is $m_A = \hbar/(d^2\omega/dk^2)$, we conclude that the following relation exists between the spectral weight removed from the optical conductivity implied by the Tinkham-Ferrell rule, and the photon-mass inside the superconductor discussed in the previous section:

$$\rho_s = \frac{m_A^2 c^4}{8\hbar^2 \epsilon_b} \quad (12)$$

In the example given in Fig. 4 we have $\rho_s \simeq 2.5 \cdot 10^{26} \text{ s}^{-1}$, and $\epsilon_b \simeq 22.7$. Using the expressions above, the dynamical mass of c -polarized photons in this compound is then $2.5 \cdot 10^{-34} \text{ g}$, which is about four-million times less than the mass of an electron.

8. MULTICOMPONENT PLASMA

The problem of a coupled two-component superconducting plasma has been studied by Leggett. In this model one considers a homogeneous mixture of two liquids, representing two different bands of charge carriers (e.g. an s -band and a d -band). Electrons can flow from one band to the other, which introduces a current between the two bands, which introduces a current between the two bands, $\frac{d}{dt}(n_s - n_d)$. Even though the two reservoirs overlap

in space, their wave-functions differ on an atomic scale, and therefore the flow of charge from one band to the other involves a real motion of electrons. This contributes a portion to the kinetic energy proportional to $(\frac{d}{dt}(n_s - n_d))^2$. The corresponding Hamiltonian is

$$\mathcal{H} = \frac{\kappa n_0^2 \Gamma^2}{4} (v_s(r, t) - v_d(r, t))^2 + \frac{1}{2\kappa n_0^2} (n_s(r, t)^2 + n_d(r, t)^2) \quad (13)$$

where Γ is a parameter which characterizes the coupling. With these definitions the Hamiltonian equations of motion are

$$\frac{d}{dt}(n_s - n_d) = \kappa n_0^2 \Gamma^2 (v_s - v_d) \quad (14a)$$

$$\frac{d}{dt}(v_s - v_d) = -\frac{1}{\kappa n_0^2} (n_s - n_d) \quad (14b)$$

The solution has of the form $\delta n(t) = \delta n(0)e^{i\Gamma t}$: This is a collective mode with a frequency Γ , where charge oscillates between the two reservoirs.

Already in a normal metal with two partly occupied bands, excitations exist which correspond to the oscillation of charge between the two bands: From the single electron band structure the lowest optical energy electron-hole transition occurs at an energy corresponding to the smallest vertical distance between the two bands, for k -values where there is one band above and one below the Fermi energy. This splitting is usually of the order of the bandwidth, i.e. of the order of 1 eV, although in principle it can be zero provided that the two bands accidentally cross at E_F (this happens in some of the bucky-tubes).

A special case occurs if the two bands are degenerate for all k -values: The presence of an interband-coupling, t scatters electrons between two different bands, while conserving their momentum, k . The eigenstates become symmetric and antisymmetric combinations of the two original bands at every k -point, split by an energy difference $2t$ (see Figs. 7

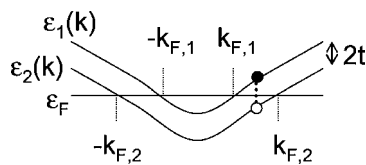


Fig. 7. A doubly degenerate band is split due to an interband coupling term t . Electromagnetic radiation at a frequency $2t/\hbar$ can excite the electrons across the split band.

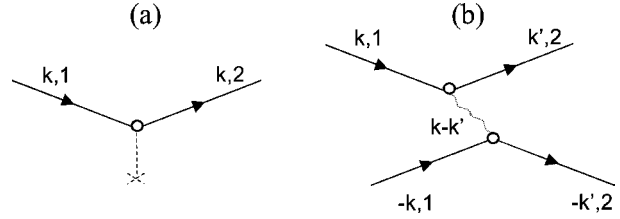


Fig. 8. (a) Interband coupling whereby a single electron is transferred from band 1 to band 2, while conserving momentum, (b) Interband coupling process whereby a pair of electrons is transferred from band 1 to 2.

and 8a). In the optical spectra this splitting causes an absorption band, corresponding to the “vertical” ($\delta k = 0$) excitations from the occupied “symmetric” to the unoccupied antisymmetric band, as indicated in Fig. 7. This absorption is peaked at a frequency $2t/\hbar$, which indicates that in this case Γ represents the single-particle interband coupling: $\hbar\Gamma = 2t$.

However, the energy of interband-excitations is usually large compared to the superconducting gap. The collective modes discussed by Leggett [14] are of a fundamentally different nature: If the two liquids are superfluids, an additional type of tunneling becomes important, i.e. the simultaneous tunneling of a *pair* of electrons. The tunneling-rate of a pair is usually much smaller than that of a single electron, and the collective modes which correspond to the dynamical oscillations of pairs between the two bands have a correspondingly low energy. If the energy is below the gap for pair-excitations, the dissipation is suppressed, hence these modes can exist by virtue of their low energy. The coupling between the reservoirs, indicated in Fig. 8b, in this case involves the scattering of a *pair* of electrons in band 1 with momentum $(k, -k)$ to a pair in band 2 with momentum $(k', -k')$ due to the interaction between the electrons. In Fig. 8 this interaction is represented by the exchange of a single boson, but more complicated processes may be involved. For coupled superconducting bands $\hbar^{-1}(v_s - v_d) = \varphi_s - \varphi_d$ is just the phase difference between the two reservoirs [14]. In this case the pre-factor of the kinetic energy in Eq. (12), $\kappa n_0 \hbar^2 \Gamma^2$, is nothing but the Josephson coupling between the two reservoirs. If the material is *not* a superconductor, *a priori* there is no reason for the exciton to be absent. However, the gap in the superconducting state removes the dissipation for frequencies below the gap, making multiband superconductors the best candidates to observe this type of collective mode. At present this type of relative-phase excitons have

been reported in two type of superconductors: (i) the high T_c cuprates [68,69], and (ii) MgB₂ [70–72]. In the following section we discuss the former case in detail.

9. LAYERED MATERIALS

The cuprates present a rather special case where the interband Coulomb interactions, which were left out of consideration in the formalism sketched in the previous section, are actually more important than the compressibility term. Following the Lawrence–Doniach model [73], we consider each plane as an individual charge reservoir, or band. Because we will be mainly interested in collective modes involving currents perpendicular to the planes, we will only deal with the discrete nature of the lattice in the c -direction. As a result it is convenient to define the Hamiltonian and the equations of motion in terms of discrete momentum- v_j and density-fields n_j (where j is a layer-index) introduced in the previous section, instead of the continuous fields $v(r, t)$ and $n(r, t)$, used in Section 2. The Hamiltonian therefore becomes similar to Eq. (12), but we also want to include a Coulomb interaction between the layer-charges. We already encountered the Coulomb interaction in Section 2. Because we want to discuss only propagation perpendicular to the planes, we work in the limit of zero charge fluctuations parallel to the planes. Integrating over the planes the Coulomb term of Eq. (1) becomes equivalent to the interaction between parallel plates of charge. The Coulomb energy of two positively charged parallel plates decreases linearly as a function of distance. The Hamiltonian density relevant to the case of c -axis plasmons in layered superconductors is then [15]

$$\mathcal{H} = \frac{\kappa n_0^2}{4} \sum_j \Gamma_{j,j+1} (v_j - v_{j+1})^2 + \frac{1}{2\kappa n_0^2} \sum_j n_j^2 - \frac{2\pi e^*2}{\epsilon_\infty} \sum_{j>1} d_{j,l} n_j n_l \quad (14)$$

where $d_{j,l}$ is the distance between the layers with indices j and l . The other parameters have already been discussed in the previous sections. In Ref. [15,16] the discussion has been limited to the Josephson coupling. In a superconductor $\hbar^{-1}(v_j - v_{j+1})$ corresponds to the phase difference $\varphi_j - \varphi_{j+1}$ between neighboring layers. However, superconductivity and long-range phase coherence are not a pre-

requisite for the validity of Eq. (14): Under special conditions the first term of the Hamiltonian corresponds to a Josephson coupling, but more generally it represents the kinetic energy related to the charge flow. It has a finite value due to the fact that the inertial mass of the charge carriers is finite.

10. PLASMA DISPERSION IN A SINGLE LAYER MATERIAL

We will first discuss the case of a stack of 2D superconducting planes, with lattice constant d along the c -direction, an compressibility κ , and an inter-layer coupling Γ . For later use we define here also the Josephson plasma frequency, and a dimensionless constant proportional to the compressibility

$$\gamma \equiv \frac{\epsilon_\infty}{4\kappa n_0^2 d e^*2} \quad (15)$$

$$\omega_j^2 \equiv \frac{2\kappa n_0^2 d e^*2 \Gamma^2}{\epsilon_\infty} = \frac{1}{2\gamma} \Gamma^2 \quad (16)$$

The Hamiltonian equations of motion, $\frac{dn_j(t)}{dt} = \frac{\partial \mathcal{H}}{\partial v_j}$, $\frac{dv_j(t)}{dt} = -\frac{\partial \mathcal{H}}{\partial n_j}$, give

$$\begin{aligned} \frac{d^2}{dt^2} n_j &= \frac{\kappa n_0^2 \Gamma^2}{2} \frac{d}{dt} ((v_j - v_{j+1}) + (v_j - v_{j-1})) \\ &= \Gamma^2 \frac{n_{j+1} + n_{j-1} - 2n_j}{2} \\ &\quad + \omega_j^2 \sum_m \frac{2d_{j,m} - d_{j+1,m} - d_{j-1,m}}{2} n_m \end{aligned} \quad (17)$$

The distances between the l th and the j th plane is $d_{j,m} = d|j - m|$. Because $2|j - m| - |j + 1 - m| - |j - 1 - m| = -2\delta_{j,m}$ the only remaining term in the summation over m corresponds to $m = j$. Substituting the plane wave expression, $n_k = \sum_j e^{ikdj} n_j$, in Eq. (17) we obtain the frequency momentum dispersion relation for Josephson-plasmons traveling perpendicular to the planes

$$\omega(k) = (\omega_j^2 + 2\gamma(1 - \cos(kd))^{1/2}) \quad (18)$$

For $k=0$ we obtain the usual value for the Josephson plasma frequency. In addition there is an upward dispersion, which is determined now by the compressibility parameter γ , similar to the dispersion in the continuum model, Eq. (5).

11. FIELD EFFECT DOPING OF A SINGLE-LAYER MATERIAL

Some special consideration deserves the doping of insulating parent compounds by the field effect. Field effect devices of high T_c materials are a technological challenge. Although this kind of technology has not yet completely matured, several groups are working into this direction, and a small tuning of the superconducting transition temperature in a cuprate based field effect device has for example already been realized [74].

The doping profile in this layered electron liquid model has a simpler form, than the doping profile in a 3D semiconductor [75], and the equations are simpler: All we need to do in order to calculate the doping profile below the insulating barrier (see Fig. 9), is to evaluate Eq. (17) in the static limit. In other words, we have to equate the lefthand side of the expression to zero. Multiplying both sides of the expression with Γ^{-2} we obtain

$$n_{j+1} + n_{j-1} - \left(2 + \frac{1}{\gamma}\right) n_j = 0 \quad (19)$$

which has the following very simple solution

$$\begin{aligned} n_j &= n_0(1-f)f^j \\ f &= 1 + \frac{1}{2\gamma} - \frac{1}{2\gamma}\sqrt{1+4\gamma} \end{aligned} \quad (20)$$

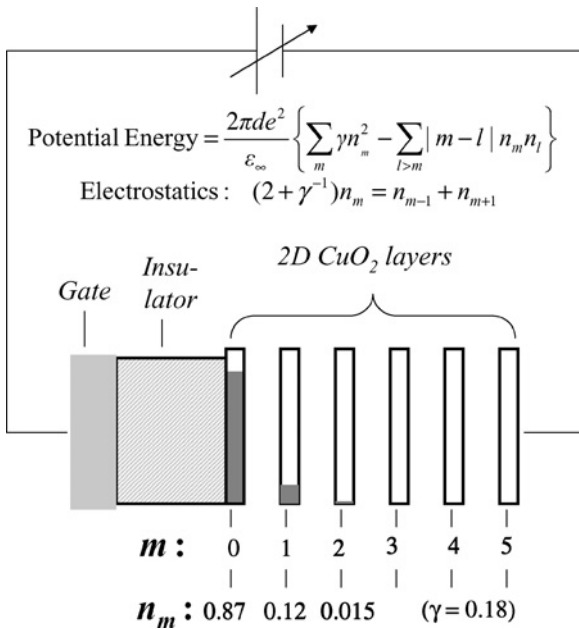


Fig. 9. Doping profile of a field-induced layered electron gas.

where $j = 0, 1, 2, \dots$. In Section 14 we will see an example of a cuprate for which γ has been measured experimentally, with the result $\gamma = 0.18$. This implies that $f = 0.13$. In other words, in a field effect device for the cuprates (in this example with a lattice spacing of 0.6 nm) the first layer is expected to receive a fraction $1 - f = 0.87$ of the total charge induced by the gate of the field effect device.⁵

12. SINGLE BILAYER

Let us now consider a single bi-layer, with a bilayer-distance d_K and a coupling frequency $\Gamma_{1,2} \equiv \Gamma_K$ between layers 1 and 2:

$$\begin{aligned} \frac{d^2}{dt^2}(n_1 - n_2) &= \kappa n_0^2 \Gamma_K^2 \frac{d}{dt}(v_1 - v_2) \\ &= -\kappa n_0^2 \Gamma_K^2 \left(\frac{1}{\kappa n_0^2} + \frac{\pi e^{*2} d_K}{\epsilon_\infty} \right) (v_1 - v_2) \end{aligned} \quad (21)$$

The first term on the righthand side, Γ_K^2 corresponds to the restoring effect on the nonequilibrium charge density due to the compressibility term (the second term in Eq. (14)), whereas the second term, $\omega_K^2 = 2\pi e^{*2} d_K \epsilon_\infty^{-1} \kappa n_0^2 \Gamma_K^2$ is due to the restoring effect of the electric field (the third term in Eq. (14)). We see, that the resonance frequency of this mode is

$$\Omega_K = \sqrt{\Gamma_K^2 + \omega_K^2} = \Gamma_K \sqrt{1 + \frac{2\pi e^{*2} d_K \kappa n_0^2}{\epsilon_\infty}} \quad (22)$$

The charge and the density appear in the combination $(e^* n_0)^2$, the value of which is independent of whether one defines n_0 and e^* as the density and charge of single electrons, or pairs. In a cuprate superconductor typically $d \sim 6 \cdot 10^{-8}$ cm, $\kappa n_0 \sim 1 \text{eV}^{-1} = 6 \times 10^{11} \text{erg}^{-1}$, the electronic density is $n_0 \sim 6 \times 10^{14} \text{cm}^{-2}$ and the background dielectric constant $\epsilon_\infty \sim 10$. Without the Coulomb interactions, i.e. assuming that $e^* = 0$ in Eq. (22), the frequency of

⁵The field-induced charge is the gate voltage divided by the capacitance of the device, both of which can be measured. Let's suppose for example that the superconducting T_c would be suppressed at a doping level of 1/8 hole per a^2 , i.e. per 2D unit cell. The top layer receives the fraction $1 - f$ of the field induced charge, and consequently the suppression of T_c will be delayed to $0.125/(1 - f)$ field induced holes per a^2 . Hence the quantitative analysis of this delay can be used to obtain an independent measurement of the electronic compressibility in the CuO₂ planes.

the collective mode is Γ_K . However, the elementary charge is $e = 4.8 \times 10^{-10} \text{ erg}^{1/2} \text{ cm}^{1/2}$, and after multiplying all factors we obtain ~ 3 for the second term under the square root. This demonstrates that the ‘‘correction’’ due to the Coulomb interaction is the dominant contribution to the internal Josephson resonance frequency of the cuprates. In fact in the first publications on this subject only the Coulomb term had been taken into account [16], whereas the second term of Eq. (21) (the term considered by Leggett) was neglected. However, for a correct quantitative description of the optical spectra it is important to take into account all three terms of the Hamiltonian Eq. (14).

Let us now consider a crystal composed of a stack of bi-layers of the type described above, where the bi-layers occupy a volume fraction f . For example $f = 1/6$ in Bi2212. Let us for the moment ignore the inter-bilayer hopping. With the model above we obtain for the dielectric function [15]

$$\epsilon(\omega) = \epsilon_\infty \frac{\omega^2 - \Omega_K^2}{\omega(\omega + i0^+) - (\Omega_K^2 - f\omega_K^2)} \quad (23)$$

This expression predicts an optical absorption at a frequency $(\Omega_K^2 - f\omega_{p,K}^2)^{1/2}$, which is lower than the collective mode of a single bi-layer, Ω_K . This reduction of the transverse polarized collective mode is a consequence of the Coulomb coupling between the bi-layers in the crystal. The longitudinal mode, i.e. the frequency for which $\epsilon(\omega) = 0$, is at Ω_K .

13. STACK OF ALTERNATING STRONG AND WEAK JUNCTIONS

Because it was assumed that there is no coupling between the bi-layers, the screening at low frequencies is not contained in Eq. (23). In order to describe this effect, Eq. (14) needs to be solved with an inter-bilayer coupling taken into account. The result obtained in Refs. [15,109–113] is the following

$$\epsilon(\omega) = \frac{\epsilon_\infty (\omega^2 - \tilde{\omega}_+^2)(\omega^2 - \tilde{\omega}_-^2)}{\omega^2 (\omega(\omega + i0^+) - \tilde{\omega}_T^2)} \quad (24)$$

where the frequencies $\tilde{\omega}_\pm$ and $\tilde{\omega}_T$ can be expressed in $\Gamma_{K,I}$ (defined in Eq. (14)) and $\Omega_{K,I}$ (defined in Eq. (22)). We use the indices K and I to indicate the bilayer and the inter-bilayer couplings

$$\tilde{\omega}_\pm^2 = \frac{1}{2} (\Omega_K^2 + \Omega_I^2) \pm \frac{1}{2} \sqrt{(\Omega_K^2 - \Omega_I^2)^2 + 4\Gamma_K^2 \Gamma_I^2}$$

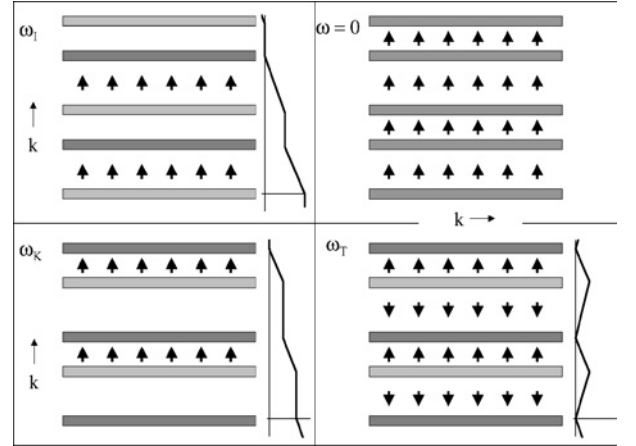


Fig. 10. Snapshot of the currents (arrows) and planar charge fluctuation amplitudes (indicated by gray-scales) of the two sets of transverse and longitudinal modes with polarization along the c -direction. On the righthand side of each plot the voltage distribution is indicated. Copyright (2001) by the American Physical Society.

$$\tilde{\omega}_T^2 = (1 - f) (\Omega_K^2 + \Gamma_I^2) + f (\Omega_I^2 + \Gamma_K^2) \quad (25)$$

The notation is slightly different from Ref. [15], providing more transparent expressions. From this expression we see, that now there are two longitudinal modes (corresponding to $\epsilon(\omega) = 0$) and one transverse mode (a divergence of $\epsilon(\omega)$) at finite frequency. The two extra modes are due to the out-of-phase oscillation of the interplane currents in alternating junctions. This situation has been sketched in Fig. 10. In the following sections we will discuss some examples, based on materials where this behavior has been observed.

14. TRANSVERSE OPTICAL PLASMON IN COMPOUNDS WITH WEAK INTER-LAYER TUNNELING

The existence of *two* longitudinal modes and *one* associated transverse plasmon mode at finite frequencies has been confirmed experimentally for the $\text{SmLa}_{0.8}\text{Sr}_{0.2}\text{CuO}_{4-\delta}$ in a series of papers [68,76–82] (see Figs. 11 and 12). Measurements of the magnetic field and temperature dependencies of the longitudinal and transverse plasmons in $\text{SmLa}_{0.8}\text{Sr}_{0.2}\text{CuO}_{4-\delta}$ could be successfully described by the multilayer model explained above, as shown in Fig. 13. It is reassuring, that fits to the data using this model provide for a wide range of temperature and magnetic field the same value for the electronic compressibility term, $\gamma = \epsilon_\infty / (4\pi d e^{*2} \kappa n_0^2) = 0.18$, where $d = 1.3 \text{ nm}$

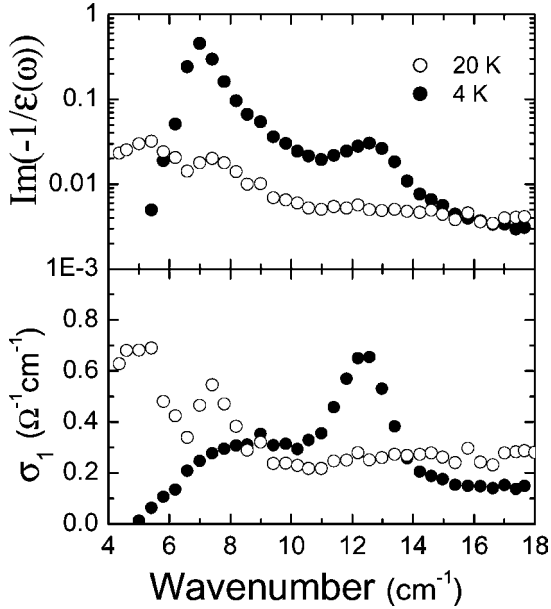


Fig. 11. The c -axis optical conductivity and loss-function, of $\text{SmLa}_{0.8}\text{Sr}_{0.2}\text{CuO}_{4-\delta}$ for 4 K (closed symbols), and 20 K (open symbols). T_c of this sample is 16 K. When the sample enters the superconducting state, two longitudinal collective modes appear (7 and 12.8 cm^{-1}) and one with transverse polarization (12.1 cm^{-1}). The two modes near 12 cm^{-1} correspond to relative phase fluctuations of the two copper-oxygen layers within the unit cell [68].

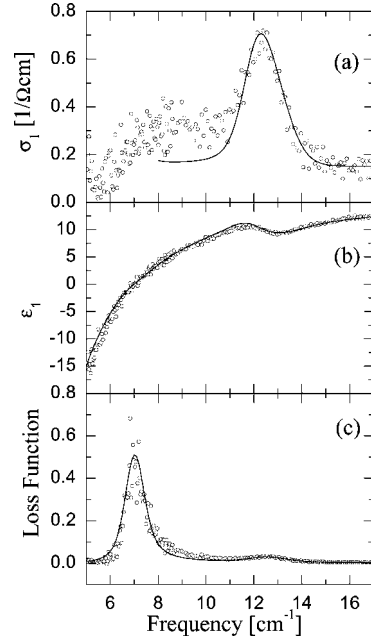


Fig. 13. Fit using Eq. (24), with the parameters defined in Eqs. (25) and (22) (solid line) to (a) the real part of the c -axis optical conductivity, (b) Real part of the c -axis dielectric function, (c) the loss function of $\text{SmLa}_{0.8}\text{Sr}_{0.2}\text{CuO}_{4-\delta}$ at 3 K. The open circles are the experimental data. The data are from Ref. [68]. Copyright (2001) by the American Physical Society.

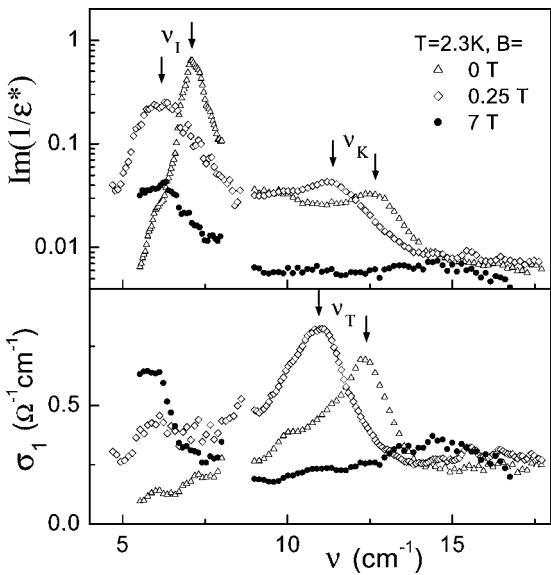


Fig. 12. Real part of the complex conductivity $\sigma_1(\omega)$ and loss function $\text{Im}(-1/\epsilon(\omega))$ of $\text{SmLa}_{0.8}\text{Sr}_{0.2}\text{CuO}_{4-\delta}$ along the c -axis for different magnetic fields. The transverse plasmon ν_T is seen as a peak in σ_1 , the longitudinal plasmons $\nu_{L,K}$ as peaks in $\text{Im}(-1/\epsilon(\omega))$. The data are from Ref. [80]. Copyright (2001) by the American Physical Society.

is the lattice constant, which is twice the spacing between the layers (see Fig. 14). Note, that the second factor under the denominator of Eq. (22) is just $d_K/(2d\gamma) \simeq 1.4$, close to the estimate given earlier in the discussion. Using the value of $\epsilon_\infty = 23$ in this compound, and $a = 0.38 \text{ nm}$ for the copper-copper distance along the planes, we can use the experimental value of γ to calculate, that $\kappa n_0^2 a^2 = 0.80 \text{ eV}^{-1}$. In

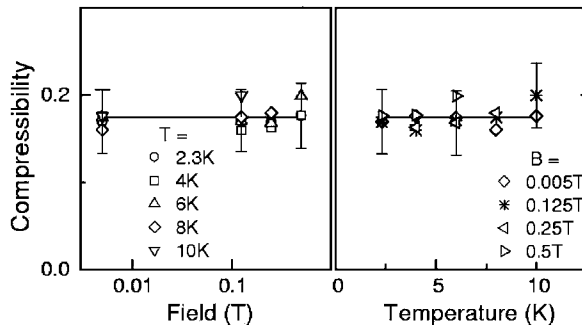


Fig. 14. Upper panels: magnetic field (left) and temperature (right) dependence of the electronic compressibility, $\gamma = \epsilon_\infty / (4\pi d_e^2 \kappa n_0^2)$ $\text{SmLa}_{0.8}\text{Sr}_{0.2}\text{CuO}_{4-\delta}$. The data are from Ref. [80]. Copyright (2001) by the American Physical Society.

a Fermi liquid picture $\kappa n_0^2 a_2$ is exactly the density of states at E_F per CuO_2 unit, $N(0)$. For the cuprates $N(0) = 0.8 \text{ eV}^{-1}$ is a very reasonable value.

15. TRANSVERSE OPTICAL PLASMON AND BI-LAYER SPLITTING IN HIGH T_c CUPRATES

The c -axis optical conductivity $\sigma_1(\omega)$ of YBCO shows several remarkable features [83–87]: (1) A very low value compared to band structure calculations, reflecting the large ρ_c . (2) A suppression of spectral weight at low frequencies already above T_c in underdoped samples referred to as the opening of a “pseudogap” (which agrees with the upturn in ρ_c). (3) The appearance of an intriguing broad “bump” in the FIR at low T in underdoped samples. The c -axis optical conductivity of YBCO is one order of magnitude larger than for LSCO near optimal doping. As a result the relative importance of the optical phonons in the spectra is diminished. c -axis optical conductivity of underdoped [83] and optimally and overdoped [69] YBCO are shown in Fig. 15. Above T_c the optical conductivity is weakly frequency dependent, and does not resemble a Drude peak. Below T_c the conductivity is depleted for frequencies below 500 cm^{-1} , reminiscent of the opening of a large gap, but not an s -wave gap, since a relatively large conductivity remains in this range.

There is a slight overshoot of the optical conductivity in the region between 500 and 700 cm^{-1} , and the normal state and superconducting state curves cross at 600 cm^{-1} . Most of the above mentioned issues can be clarified by modelling the cuprates, or in particular YBCO, as a stack of coupled CuO_2 layers with alternating weaker and stronger links. Indeed, the transverse mode in the infrared spectrum of optimally and overdoped YBCO and the above mentioned “bump” in underdoped YBCO are well fitted by the multilayer model. Hence also the “bump” in the YBCO c -axis spectra may be regarded as a realization of the “excitons” first considered by Leggett [14], which involve the relative phase fluctuations of the condensates formed in two different bands crossing the Fermi surface [58–60,69,94–98].

This assignment is complicated by the fact, that experimentally the peaks at $\tilde{\omega}_T$ and $\tilde{\omega}_K$ appear at a temperature higher than the superconducting phase transition. For the underdoped samples the intensity of these features has been shown to correlate with the intensity of the spin-flip resonance at (π, π) seen

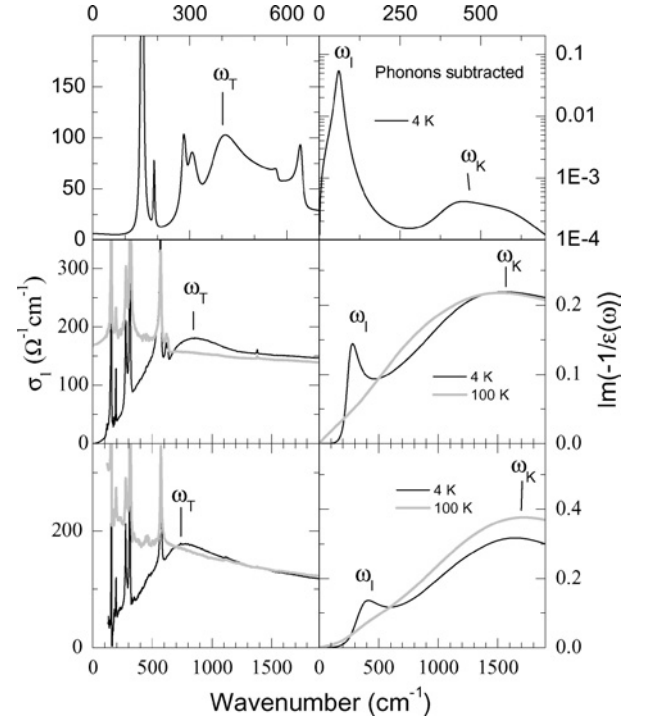


Fig. 15. c -axis optical conductivity (left) and energy loss function (right) as a function of wavenumber (in cm^{-1}) of underdoped ($x = 6.6$, top panels), optimally doped ($x = 6.93$, middle) and overdoped ($x = 7.0$, bottom panel) $\text{YBa}_2\text{Cu}_3\text{O}_{7-x}$. The optical phonons have been subtracted from the loss-functions for clarity. See Refs. [69,83] for details.

in neutron spectroscopy [88], which is quite far above T_c . On the other hand it appears to be another manifestation of the phenomenon that a strong reduction of dissipation reveals collective modes, which are otherwise overdamped. In the optimally and overdoped cuprate a wide peak is visible in the loss-function around 1600 cm^{-1} for all temperatures. The only effect of the transition into the superconducting state is in this case, that the peak becomes somewhat narrower. This behavior is reminiscent of a difficulty which we already encountered in the discussion relating to Figs. 8 and 7: The single-particle coupling term t between the layers, Fig. 8a, should in principle be revealed in the optical spectrum of the normal state as a transition between the bands consisting of the symmetric and antisymmetric combinations of the two layers [89–93]. In the underdoped YBCO this process appears to be overdamped. On the other hand, the type of process depicted in Fig. 8b can still contribute at low frequencies, at temperatures where the dissipation becomes sufficiently small. The coherent bi-layer splitting is gradually

restored as we move to the optimally and overdoped region. In this case the two types of interlayer transport indicated in Fig. 8 work in parallel, but there is still a temperature dependence, like in the other cases. Note that this does not imply nor require the simultaneous presence of both single electrons and pairs: These are just two different forms of charge transport.

Additional studies of the bi-layer (and trilayer) materials have provided confirmation of the transverse optical plasmon in these materials. The spectra of the far-infrared *c*-axis conductivity exhibit dramatic changes of some of the phonon peaks, which correlates with the temperature dependence of the transverse optical plasmon. The most striking of these anomalies can be naturally explained by the local fields acting on the ions arising from the transverse optical plasmon oscillations [58–60,69,94–97,99].

It is not difficult to extend Eq. (23) for the dielectric function, to cases where the sequence along the *c*-axis is extended to three or more different junctions per period [16]

$$\frac{1}{\epsilon(\omega)} = \sum_m \frac{z_m \omega^2}{\epsilon_\infty(\omega^2 - \omega_{J,m}^2) + 4\pi i \omega \sigma_m} \quad (26)$$

where z_m is the effective volume fraction of the m th junction, and σ_m is a parallel dissipative conductivity of the m th junction. In trilayer materials such Bi2223 two of the three junctions are identical because one of the CuO₂-layers is a mirror plane. Consequently the expression above has a degeneracy between two of the three terms in the summation, and the *c*-axis spectrum should still have one transverse optical plasmon. Interestingly in this case an additional mode exists where the charge oscillations have even parity around the mirror-plane [100]. This electronic mode is observable with Raman spectroscopy [100].

If one introduces a single planar defect layer in an otherwise perfectly periodic stack of Josephson coupled layers, this results in a pronounced satellite line in the real part of the complex resistivity, whose position and amplitude depend on the critical current density and on the parameters of the interlayer coupling [101]. The extreme narrowness of this plasma-peak could in principle be used to probe the pairing symmetry using a twist grain boundary configuration.

Random variations of the potential barrier, e.g. due to chemical disorder, can be taken into account by replacing the summation over m with a weighted integration over $\omega_{J,m}$. If one assumes for example a

gaussian distribution, a peak appears in the optical conductivity, which coincides with the center-value of the *c*-axis plasma frequency [16]. This effect is present in all published data of the optical conductivity of LSCO, for example also in Fig. 6. The effect has a strong doping dependence with its maximum at exactly 1/8 doping [102], suggesting an intriguing correlation between disorder in the interlayer Josephson coupling and the tendency toward stripe-formation. This appears to be a manifestation of a more general tendency where disorder allows optical absorption by “forbidden” collective modes. Similar phenomena have been observed [103] along the *ab*-planes of the cuprates in the THz regime and explained with a model of a planar disordered array of Josephson junctions [104].

An alternative way to introduce a more complicated pattern of Josephson couplings along the *c*-axis is obtained by the application of a magnetic field parallel to the CuO₂ planes, which for YBa₂Cu₃O_{6.6} results in inequivalent insulating layers with and without Josephson vortices. As a result one optical (transverse) mode appears at around 40 cm⁻¹, corresponding to the antiphase Josephson current oscillations between two inequivalent junctions [105].

16. SUMMARY

In superconductors a rich spectrum of collective modes can be observed using optical techniques. The simplest case is where there is one layer per unit cell, for example La_{2-x}Sr_xCuO₄. Here the Josephson-coupling gives rise to a single *c*-axis plasmon. This plasmon is an collective mode of the phase of the superconducting order parameter. Their coupling to the electromagnetic field causes a mass-gap of the photons coupled to the superconductor, providing a small energy scale (and small budget) demonstration of the Anderson–Higgs mechanism for generating massive particles. These modes can be described in the context of the Lawrence–Doniach model. However from the optical experiments on SmLa_{0.8}Sr_{0.2}CuO_{4-δ} we have seen that it is important to take into account the fact that the compressibility of the charge-fluid in the layers is finite. The compressibility term establishes the connection to the model considered by Leggett for Josephson coupled bands. A directly observable consequence is the appearance of several additional collective modes in the optical spectrum, which are related to the relative

phase excitons predicted by Leggett. However, their energy and optical oscillator strength is strongly affected by the interlayer Coulomb interaction. These excitons have been observed for light polarized along the c-axis in a number of cuprate superconductors. If the number of layers per unit cell is 3 or more, collective modes of even symmetry appear, which can be observed with Raman spectroscopy. In addition to chemical modulation of the interlayer Josephson-coupling, magnetic field parallel to the planes can result in inequivalent insulating layers with and without Josephson vortices.

ACKNOWLEDGMENTS

This work was supported by the Swiss National Science Foundation through the National Center of Competence in Research Materials with Novel Electronic Properties-MaNEP.

REFERENCES

1. N. N. Bogoliubov, V. V. Tolmachev, and D. V. Shirkov, *A New Method in the Theory of Superconductivity* (Consultants Bureau, New York, 1959).
2. Y. Nambu, *Phys. Rev. Lett.* **4**, 380 (1960).
3. J. Goldstone, *Nuovo Cim.* **19**, 154 (1961).
4. P. W. Anderson, *Phys. Rev.* **112**, 1900–1916 (1958).
5. P. W. Anderson, *Phys. Rev.* **110**, 985–986 (1958).
6. P. W. Anderson, *Phys. Rev.* **110**, 827–835 (1958).
7. P. W. Anderson, *Phys. Rev.* **130**, 439–442 (1963).
8. P. W. Higgs, *Phys. Rev. Lett.* **13**, 509 (1964).
9. P. W. Higgs, *Phys. Rev. Lett.* **145**, 1156 (1967).
10. D. M. Ginsberg, P. L. Richards, and M. Tinkham, *Phys. Rev. Lett.* **3**, 337 (1959).
11. A. Bardasis and J. R. Schrieffer, *Phys. Rev.* **121**, 1050 (1960).
12. V. G. Vaks, V. M. Galitskii, and A. I. Larkin, *Sov. Phys. JETP* **14**, 1177 (1962).
13. D. van der Marel, *Phys. Rev. B* **51**, 1147 (1995).
14. A. J. Leggett, *Prog. Theor. Phys.* **36**, 901 (1966).
15. D. van der Marel and A. A. Tsvetkov, *Phys. Rev. B* **64**, 024530 (2001).
16. D. van der Marel and A. Tsvetkov, *Czech J. Phys.* **46**, 3165 (1996).
17. E. Demler, S.-C. Zhang, N. Bulut, and D. J. Scalapino, *Int. J. Mod. Phys. B* **10**, 2137 (1996).
18. E. Demler and S.-C. Zhang, *Phys. Rev. Lett.* **75**, 4126 (1995).
19. P. A. Lee and N. Nagaosa, *Phys. Rev. B* **68**, 024516 (2003); V. G. Vaks, V. M. Galitskii, and A. I. Larkin, *Sov. Phys. JETP* **14**, 1177 (1962).
20. H.F. Fong *et al.*, *Phys. Rev. Lett.* **75**, 316 (1995).
21. D. Vollhardt and P. Wolfe, *The Superfluid Phases of Helium 3* (Taylor and Francis, 1990).
22. H. Goldstein, *Classical Mechanics* (Addison-Wesley, Reading, MA, 1980).
23. G. D. Mahan, *Many-Particle Physics*, 2nd ed. (Plenum, New York, 1990).
24. K. S. Singwi, M. P. Tosi, R. H. Land, and A. Sjölander, *Phys. Rev.* **176**, 589 (1968).
25. A. vom Felde, J. Sprösser-Prou, and J. Fink, *Phys. Rev. B* **40**, 10181 (1968).
26. V. Z. Kresin and H. Morawitz, *Phys. Rev. B* **37**, 7854 (1988).
27. S. M. Bose and P. Longe, *J. Phys. Condens. Matter* **4**, 1799 (1992).
28. A. L. Fetter *Ann. Phys.* **88**, 1 (1974).
29. K. Schulte, M. A. James, P. G. Steeneken, G. A. Sawatzky, R. Suryanarayanan, G. Dhalenne, A. Revcolevschi, cond-mat/0010475.
30. M. Tachiki, T. Koyama, and S. Takahashi, *Phys. Rev. B* **50**, 7065 (1994).
31. H. A. Fertig and S. Das Sarma, *Phys. Rev. Lett.* **65**, 1482 (1990).
32. E. H. Hwang and S. Dassarma, *Phys. Rev. B* **52**, R7010 (1995).
33. L. N. Bulaeviskii, M. P. Maley, and M. Tachiki, *Phys. Rev. Lett.* **74**, 801 (1995).
34. K. Tamasaku, Y. Nakamura, and S. Uchida, *Phys. Rev. Lett.* **69**, 1455 (1992).
35. O. K. C. Tsui, N. P. Ong, Y. Matsuda, Y. F. Yan, and J. B. Peterson, *Phys. Rev. Lett.* **73**, 724 (1994).
36. Y. Matsuda, M. B. Gaifullin, K. Kumagai, K. Kadowaki, and T. Mochiku, *Phys. Rev. Lett.* **75**, 4512 (1995).
37. D. van der Marel, A. Tsvetkov, M., Grüninger, D. Dulic, and H. J. A. Molegraaf, *Physica C* **341–348**, 1531 (2000).
38. Maria Krawczyk, *Acta Phys Polon. B* **29**, 3543 (1998).
39. K. Kadowaki, I. Kakeya, M. B. Gaifullin, T. Mochiku, S. Takahashi, T. Koyama, M. Tachiki, *Phys. Rev. B* **56**, 5617 (1997).
40. K. Kadowaki, I. Kakeya, and K. Kindo, *Europhys. Lett.* **42**, 203–208 (1998).
41. M. Tinkham and R. A. Ferrell, *Phys. Rev. Lett.* **2**, 331 (1959).
42. R. E. Glover and M. Tinkham, *Phys. Rev.* **108**, 243 (1957).
43. R. E. Glover and M. Tinkham, *Phys. Rev.* **110**, 778 (1958).
44. P. L. Richards and M. Tinkham, *Phys. Rev. Lett.* **1**, 318 (1958).
45. S. Chakravarty, A. Sudbo, P. W. Anderson, and S. Strong, *Science* **261**, 337 (1993).
46. P. W. Anderson, *Science* **268**, 1154 (1995).
47. A. J. Leggett, *Science* **274**, 587 (1996).
48. D. van der Marel, H. S. Somal, B. J. Feenstra, J. E. van der Eb, J. Schuetzmann, and J. H. Kim, in *Proceedings of 10th Annual HTS Workshop on Physics, Houston*, World Science Publications, Singapore, 1996, p. 357.
49. J. Schuetzmann, H. S. Somal, A. A. Tsvetkov, D. van der Marel, G. Kooops, N. Koleshnikov, Z. F. Ren, J. H. Wang, E. Brueck, and A. A. Menovski, *Phys. Rev. B* **55**, 11118 (1997).
50. K. A. Moler, J. R. Kirtley, D. G. Hinks, T. W. Li, and Ming Xu, *Science* **279**, 1193 (1998).
51. A. Tsvetkov, D. van der Marel, K. A. Moler, J. R. Kirtley, J. L. de Boer, A. Meetsma, Z. F. Ren, N. Koleshnikov, D. Dulic, A. Damascelli, M. Grüninger, J. Schützmman, J. W. van der Eb, H. S. Somal, and J. H. Wang, *Nature* **395**, 360 (1998).
52. S. Chakravarty, *Eur. Phys. J. B* **5**, 337 (1998).
53. J. R. Kirtley, K. A. Moler, G. Villard, A. Maignan, *Phys. Rev. Lett.* **81**, 2140 (1998).
54. M. B. Gaifullin, Yuji Matsuda, N. Chikumoto, J. Shimoyama, K. Kishio, and R. Yoshizaki, *Phys. Rev. Lett.* **83**, 3928 (1999).
55. D. N. Basov, S. I. Woods, A. S. Katz, E. J. Singley, R. C. Dynes, M. Xu, D. G. Hinks, C. C. Homes, M. Strongin, *Science* **283**, 49 (1999).
56. S. Chakravarty, H. Kee, and E. Abrahams, *Phys. Rev. Lett.* **82**, 2366 (1999).
57. D. N. Basov, C. C. Homes, E. J. Singley, M. Strongin, T. Timusk, G. Blumberg, and D. vander Marel, *Phys. Rev. B* **63**, 134514 (2001).
58. D. Munzar, C. Bernhard, T. Holden, A. Golnik, J. Humlicek, and M. Cardona, *Phys. Rev. B* **64**, 024523 (2001).

59. D. Munzar, T. Holden, and C. Bernhard, *Phys. Rev. B* **67**, R020501 (2003).
60. A. V. Boris, D. Munzar, N. N. Kovaleva, B. Liang, C. T. Lin, A. Dubroka, A. V. Pimenov, T. Holden, B. Keimer, Y.-L. Mathis, and C. Bernhard, *Phys. Rev. Lett.* **89**, 277001 (2002).
61. J. E. Hirsch, *Physica C* **199**, 305 (1992).
62. J. E. Hirsch, *Physica C* **201**, 347 (1992).
63. H. J. A. Molegraaf, C. Presura, D. van der Marel, P. H. Kes, and M. Li, *Science* **295**, 2239 (2002).
64. A. F. Santander-Syro, R. P. S. M. Lobo, N. Bontemps, Z. Konstantinovic, Z. Z. Li, and H. Raffy, *Europhys. Lett.* **62**, 568 (2003).
65. D. van der Marel, in *Strong Interactions in Low Dimensions*, D. Baeriswyl and L. Degiorgi, eds. (Kluwer, Dordrecht, The Netherlands, in press); cond-mat/0301506.
66. D. van der Marel, H. J. A. Molegraaf, C. Presura, and I. Santoso, in *Concepts in Electron Correlation*, A. Hewson and V. Zlatic, eds. (Kluwer, Dordrecht, The Netherlands, 2003), p. 7–16; cond-mat/0302169.
67. A. B. Kuzmenko, N. Tombros, H. J. A. Molegraaf, M. Grueninger, D. van der Marel, and S. Uchida, *Phys. Rev. Lett.* **91**, 037004 (2003).
68. D. Dulic, A. Pimenov, D. van der Marel, D. M. Broun, S. Kamal, W. N. Hardy, A. A. Tsvetkov, I. M. Sutjaha, R. Liang, A. A. Menovsky, A. Loidl, and S. S. Saxena, *Phys. Rev. Lett.* **86**, 4144 (2001).
69. M. Grueninger, D. van der Marel, A. A. Tsvetkov, and A. Erb, *Phys. Rev. Lett.* **84**, 1757 (2000).
70. D. F. Agterberg, E. Demler, and B. Janko, *Phys. Rev. B* **66**, 214507 (2002).
71. A. Brinkman, S. H. W. van der Ploeg, A. A. Golubov, H. Rogalla, T. H. Kim, and J. S. Moodera, in *Proceedings of SNS04*, Sitges, Spain, 2004).
72. Y. G. Ponomarev, S. A. Kuzmichev, M. G. Mikheev, M. V. Sudakova, S. N. Tchesnokov, N. Z. Timergaleev, A. V. Yargin, E. G. Maksimov, S. I. Krasnosvobodtsev, A. V. Varlashkin, M. A. Hein, G. Müller, H. Piel, L. G. Sevast'yanova, O. V. Kravchenko, K. P. Burdina, and B. M. Bulychev, *Solid State Commun.* **129**, 85 (2004).
73. W. E. Lawrence and S. Doniach in *Proceedings of the 12th International Conference on Low Temperature Physics, Kyoto, 1970*, Keigaku, Tokyo, 1970.
74. C. H. Ahn, J. M. Triscone, and J. Mannhart, *Nature* **424**, 1015 (2003).
75. S. Wehrli, D. Poilblanc, and T. M. Rice, *Eur. Phys. J. B* **23**, 345 (2001).
76. H. Shibata and T. Yamada, *Phys. Rev. Lett.* **81**, 3519 (1998).
77. T. Kakeshita, S. Uchida, K. M. Kojima, S. Adachi, S. Tajima, B. Gorshunov, and M. Dressel, *Phys. Rev. Lett.* **86**, 4140 (2001).
78. H. Shibata, *Physica C* **362**, 92 (2001).
79. H. Shibata, *Phys. Rev. Lett.* **86**, 21225 (2001).
80. A. Pimenov, A. Loidl, D. Dulic, D. van der Marel, I. M. Sutjaha, and A. A. Menovsky, *Phys. Rev. Lett.* **87**, 177003 (2001).
81. H. Shibata, *Phys. Rev. B* **65**, 180507 (2002).
82. H. Shibata, *Physica C* **367**, 360 (2002).
83. C. C. Homes, T. Timusk, D. A. Bonn, R. Liang, and W. N. Hardy, *Can. J. Phys.* **73**, 663 (1995).
84. J. Schützmann, S. Tajima, S. Miyamoto, Y. Sato, and R. Hauff, *Phys. Rev. B* **52**, 13665 (1995).
85. S. Tajima, J. Schützmann, S. Miyamoto, I. Terasaki, Y. Sato, and R. Hauff, *Phys. Rev. B* **55**, 6051 (1997).
86. R. Hauff, S. Tajima, W.-J. Jang, and A. I. Rykov, *Phys. Rev. Lett.* **77**, 4620 (1996).
87. C. Bernhard, R. Henn, A. Wittlin, M. Klser, Th. Wolf, G. Müller-Vogt, C. T. Lin, and M. Cardona, *Phys. Rev. Lett.* **80**, 1762 (1998).
88. T. Timusk and C. C. Homes, *Solid State Commun.* **126**, 63 (2003).
89. Y. N. Gartstein, and M. J. Rice, and D. van der Marel, *Phys. Rev. B* **49**, 6360 (1994).
90. F. Forsthofer, S. Kind, and J. Keller, *Phys. Rev. B* **53**, 14481 (1996).
91. W. A. Atkinson and J. P. Carbotte, *Phys. Rev. B* **55**, 3230 (1997).
92. S. V. Dordevic, E. J. Singley, J. H. Kim, M. B. Maple, S. Komiya, S. Ono, Y. Ando, T. Rößm, R. Liang, D. A. Bonn, W. N. Hardy, J. P. Carbotte, C. C. Homes, M. Strongin, and D. N. Basov, *Phys. Rev. B* **69**, 094511 (2004).
93. N. Shah and A. J. Millis, *Phys. Rev. B* **65**, 024506 (2002).
94. V. Zelezny, S. Tajima, T. Motohashi, J. Shimoyama, K. Kishio, and D. van der Marel, *J. Low Temp. Phys.* **117**, 1019 (1999).
95. D. Munzar, C. Bernhard, A. Golnik, J. Humlicek, and M. Cardona, *J. Low Temp. Phys.* **117**, 1049 (1999).
96. D. Munzar, C. Bernhard, A. Golnik, J. Humlicek, and M. Cardona, *Solid State Commun.* **112**, 365 (1999).
97. D. Munzar, C. Bernhard, A. Golnik, J. Humlicek, and M. Cardona, *Phys. Status Solidi B* **215**, 557 (1999).
98. C. Bernhard, D. Munzar, A. Golnik, C. T. Lin, A. Wittlin, J. Humlicek, and M. Cardona, *Phys. Rev. B* **61**, 618 (2000).
99. N. N. Kovaleva, A. V. Boris, T. Holden, C. Ulrich, B. Liang, C. T. Lin, B. Keimer, C. Bernhard, J. L. Tallon, D. Munzar, A. M. Stoneham, *Phys. Rev. B* **69**, 054511 (2004).
100. D. Munzar and M. Cardona, *Phys. Rev. Lett.* **90**, 077001 (2003).
101. A. Gurevich and M. Tachiki, *Phys. Rev. Lett.* **83**, 183 (1999).
102. S. V. Dordevic, S. Komiya, Y. Ando, and D. N. Basov, *Phys. Rev. Lett.* **91**, 167401 (2003).
103. J. Corson, J. Orenstein, S. Oh, *et al.*, *Phys. Rev. Lett.* **85**, 2569 (2000).
104. S. V. Barabash and D. Stroud, *Phys. Rev. B* **67**, 144506 (2003).
105. K. M. Kojima, S. Uchida, Y. Fudamoto, and S. Tajima, *Phys. Rev. Lett.* **89**, 247001 (2002).
106. P. Bourges, B. Keimer, L. P. Regnault, and Y. Sids, *J. Supercond.* **13**, 735 (2000).
107. P. Bourges, Y. Sidis, H. F. Fong, L. P. Regnault, J. Bossy, A. Ivanov, and B. Keimer, *Science* **288**, 1234 (2000).
108. J. H. Kim, H. S. Somal, M. T. Czyzyk, D. van der Marel, A. Wittlin, A. M. Gerrits, V. H. M. Duijn, N. T. Hien, and A. A. Menovsky, *Physica C* **247**, 297 (1995).
109. T. Koyama, *J. Phys. Soc. Jpn.* **71**, 2986 (2002).
110. C. Helm and L. N. Bulaevskii, *Phys. Rev. B* **66**, 094514 (2002).
111. C. Helm, L. N. Bulaevskii, E. M. Chudnovsky, and M. P. Maley, *Phys. Rev. Lett.* **89**, 057003 (2002).
112. L. N. Bulaevskii and C. Helm, *Phys. Rev. B* **66**, 174505 (2002).
113. L. N. Bulaevskii, Ch. Helm, 2, A. R. Bishop, and M. P. Maley, *Europhys. Lett.* **58**, 415 (2002).
114. V. Zelezny, S. Tajima, D. Munzar, T. Motohashi, J. Shimoyama, and K. Kishio, *Phys. Rev. B* **63**, 060502 (2001).
115. R. Sooryakumar and M. V. Klein, *Phys. Rev. Lett.* **45**, 660 (1980).
116. P. B. Littlewood and C. M. Varma, *Phys. Rev. Lett.* **47**, 811 (1981).
117. C. M. Varma, *J. Low Temp. Phys.* **126**, 901–909. (2001).

Decay of Supercurrents in Condensates in Optical Lattices

Anatoli Polkovnikov,¹ Ehud Altman,¹ Eugene Demler,¹
Bertrand I. Halperin,¹ and Mikhail D. Lukin¹

Received August 15, 2004; accepted September 4, 2004

In this paper we discuss decay of superfluid currents in boson lattice systems due to quantum tunneling and thermal activation mechanisms. We derive asymptotic expressions for the decay rate near the critical current in two regimes, deep in the superfluid phase and close to the superfluid-Mott insulator transition. The broadening of the transition at the critical current due to these decay mechanisms is more pronounced at lower dimensions. We also find that the crossover temperature below which quantum decay dominates is experimentally accessible in most cases. Finally, we discuss the dynamics of the current decay and point out the difference between low and high currents.

KEY WORDS: Optical lattices; condensates; decay.

1. INTRODUCTION

Some of the most intriguing questions in low-temperature physics concern the ways in which superconductors lose their superconducting properties, because of thermal or quantum fluctuations. Mike Tinkham has long been fascinated with these issues, and has done much to advance our understanding of the subject.

An early contribution in this area was the work of Newbower *et al.* on effects of fluctuations on the superconducting transition of tin whisker crystals [1]. Experimental data were compared with theories of thermally activated phase slips, both in the linear regime and in the nonlinear regime of finite current flows. More recently, Tinkham and collaborators studied the loss of superconductivity in very thin wires of MoGe, deposited on carbon nanotubes, where quantum fluctuations are involved [2–4]. Related work from Tinkham's laboratory, in recent years, has elucidated the breakdown of superconductivity in ultrasmall metallic grains, measured by the even–odd alternation of Coulomb-blockade en-

ergies [5,6], vortex motion, and resistance in high-temperature superconductors [7,8], and critical currents in frustrated arrays of Josephson junctions [9].

The decay of supercurrents in liquid ⁴He and in Bose-Einstein condensates of ultracold atoms has much in common with the decay of superconductivity. Concepts of flux-line motion, and of phase slips due to thermal or quantum fluctuations, appear in both cases. A new dimension has been added to the subject by recent experimental advances, where cold atoms have been trapped in a region that contains a spatially periodic potential, produced by optical standing waves (see for example [10]). The ability to vary continuously the parameters of the system, by changing the strength of the periodic potential, as well as by varying the number of trapped atoms and the shape of the overall confining potential, allows one to explore new regimes of parameters and to make more precise confrontations between theory and experiment. In turn, these developments give added urgency to the theoretical study of supercurrent decay.

In the present paper, we discuss similarities and differences between the decay of supercurrents in superconductors and systems of trapped atoms, and we present some new results for the latter. Specifically

¹Physics Department, Harvard University, Cambridge, Massachusetts 02138.

we consider certain experimental procedures which have become standard in systems of ultra cold atoms. In the first scheme, a condensate is prepared on a lattice with a specified intensity, when the lattice is suddenly accelerated to a finite velocity. In other words, a moving condensate is prepared in the lattice frame, essentially fixing the phase gradient. A similar experiment in superconductors would involve threading a flux through a closed superconducting loop. Such sudden lattice boosts were applied by several groups to demonstrate a dynamical instability of the superfluid when the imposed phase gradient exceeds $\pi/2$ per unit cell [11]. A related experiment involves tilting the lattice, thus subjecting the atoms to a linear potential. This is equivalent to imposing a constant voltage on a superconductor. The technique was used, for example, to demonstrate Bloch oscillations of a condensate [12]. In a third experimental sequence, one can prepare a moving condensate, then continuously increase the depth of the lattice toward the superfluid-Mott insulator transition.

The response of the atomic system to the perturbations, can be measured, by direct observation of the time evolution. Decay of the current, for example, is observed by repeated experiments, where atoms are released from the trap after varying waiting periods. The phase gradient in the superfluid at the time of release may be inferred from a *time of flight* measurement of the momentum distribution. This should be contrasted with superconductors, where measurements probe I-V characteristics.

Besides the differences in the experimental observation procedures, there are unique features of trapped atom systems which influence the physics of supercurrent decay. First, to a very good approximation such systems can be considered perfectly clean. Supercurrents decay only due to breaking of Galilean invariance by the periodic potential.

A second feature that distinguishes the dynamics of ultra cold atoms is their nearly perfect isolation from the environment. Strictly speaking they are always underdamped. However, we are usually interested in the dynamics of a subset of the system degrees of freedom, such as the super-current. How much the dynamics of the the interesting variables is damped, depends solely on the remaining system degrees of freedom rather than on external dissipation sources. In superconductors, effects of quenched disorder, phonons, fermion degrees of freedom, and coupling to a substrate can complicate the situation greatly, and the order parameter dynamics is most frequently overdamped.

2. CRITICAL CURRENT IN THE SUPERFLUID PHASE

Ultra cold atoms in an optical lattice, confined to the lowest Bloch band are described by the well known Bose-Hubbard Hamiltonian:

$$H = -J \sum_{\langle ij \rangle} (a_i^\dagger a_j + \text{h.c.}) + \frac{U}{2} \sum_i n_i (n_i - 1), \quad (1)$$

where J and U are the hopping amplitude and the on-site repulsive interaction, $\langle ij \rangle$ denotes pairs of nearest neighbor sites. Another implicit parameter in this Hamiltonian is the average number of bosons per site, N . In this paper we shall be primarily concerned with the case where N is a large integer. We shall address two separate regimes: the first is defined by the conditions $UN^2 \gg JN \gg U$, while the second regime corresponds to the superfluid near the transition to a Mott insulator ($UN^2 \gg JN \sim U$).

If the condition $UN \gg J$ holds, then the interactions are sufficiently strong to suppress amplitude fluctuations of the order parameter, and (1) can be mapped to the quantum rotor model:

$$H = -JN \sum_{\langle ij \rangle} \cos(\varphi_i - \varphi_j) - \frac{U}{2} \sum_i \left(\frac{\partial}{\partial \varphi^i} \right)^2 \quad (2)$$

The additional condition $JN \gg U$ ensures that the system is far from the superfluid-insulator transition, and facilitates a semiclassical approximation because fluctuations in φ as well as in the density, are small. In the classical limit the boson creation and annihilation operators can be treated as complex numbers subject to discrete Gross-Pitaevskii equations [13]:

$$i \frac{d\psi_j}{dt} = -J \sum_{k \in O} \psi_k + U |\psi_j|^2 \psi_j, \quad (3)$$

where the set O contains the nearest neighbors of site j . In the quantum rotor limit $UN \gg J$ the number fluctuations can be integrated out leaving us with only the equations of motion for the phase $\phi_j = \arg \psi_j$:

$$\frac{d^2 \phi_j}{dt^2} = -2UJN \sum_{k \in O} \sin(\phi_k - \phi_j). \quad (4)$$

Alternatively Eq. (4) immediately follows from the Hamiltonian (2). Both Eqs. (3) and (4) can support stationary current carrying states, $\psi_j \propto \exp(ipx_j)$. A simple linear stability analysis of (3) or (4), shows [14,15] that these states become unstable toward small perturbations when the phase twist exceeds a critical value of $\pi/2$ per unit cell. The onset of this

instability is signaled by appearance of imaginary frequencies. This instability was recently observed experimentally [12].

In principle, one can identify another type of instability, characterized by appearance of negative frequencies, in systems described by Eq. (3) [14]. In general this occurs at a phase twist $p^* < \pi/2$. However, in the quantum rotor limit $UN \gg J$, where we work, the two instabilities coincide.

While the modulational instability occurs precisely at $p = \pi/2$ for $JN \gg U$, we expect that the current can decay at smaller momenta due to either quantum or thermal fluctuations (see also Ref. 16). We envision the following experimental scheme to observe this. The condensate is either boosted to a state with a certain phase gradient or gradually accelerated. Following the boost or while the system is accelerating we probe the evolution of the phase gradient. If the system is sufficiently close to the modulational instability, i.e. p is slightly below $\pi/2$, the coherent motion of the condensate is expected to decay. The larger the phase gradient, the faster this decay will occur.

The other regime we shall address, is that of the superfluid close to the quantum phase transition to a Mott insulator at commensurate filling (i.e. $JN \sim U$, and for simplicity we still assume that $N \gg 1$). Now the phase fluctuations are large, and (2) cannot be treated semiclassically. However, one can use the semiclassical description after coarse graining the system. Since the coherence length ξ diverges at the transition, one can use a continuum description of the static and dynamic properties of the condensate. At commensurate filling the appropriate quantum action written in terms of the superfluid order parameter reads [17,18]:

$$S = C \int d^d x dt \left\{ \left| \frac{d\psi}{dt} \right|^2 - |\nabla\psi|^2 + |\psi|^2 - \frac{1}{2}|\psi|^4 \right\}, \quad (5)$$

where length is measured in units of ξ and time in units of ξ/c , with c the sound velocity, C is a numerical prefactor. The bare parameters ξ , c , and C can be found using a mean-field approximation [19]. For the cubic d-dimensional lattice they read:

$$\xi = \frac{1}{\sqrt{2d(1-u)}}, \quad c = 2JN\sqrt{2d},$$

$$C = \frac{1}{2(2d)^{d/2}}(1-u)^{\frac{3-d}{2}}, \quad (6)$$

where we introduced the dimensionless interaction $u = U/U_c$ with $U_c = 8JNd$ being the critical interac-

tion strength in the mean field approximation. The action (5) correctly describes low-energy dynamics of the system in the vicinity of the phase transition, only if the couplings ξ , c , U_c , and C are properly renormalized. While in three dimensions the effects of such renormalization should be weak, in two- and especially one-dimensional cases they strongly modify the couplings and the critical exponents. The bare mean field parameters can then be used only as an estimate. Note that the dimensionless part of the action (5) is general, and so are the conclusions we reach in this paper, once the renormalized, rather than mean field parameters are used. The action (5) is obviously extremized by stationary current-carrying states: $\psi_p(x) = \sqrt{1 - (p\xi)^2} e^{ipx\xi}$. It is easy to check [19] that these states are stable with respect to small fluctuations for $p < p_c = 1/(\xi\sqrt{3})$. Since ξ diverges at the phase transition, the critical phase twist vanishes at that point as it should.

A possible experimental procedure to measure the decay rate at low currents follows. A condensate with a specified phase gradient is prepared in a weak lattice (small u). Then, the lattice potential is gradually increased in time, driving the system closer to the Mott phase. This, in turn, results in the increase of the correlation length ξ and in decrease of the critical momentum p_c . As p_c approaches p the superfluid current is expected to decay either due to quantum or thermal fluctuations.

3. DECAY OF THE SUPERFLUID CURRENT

In this section we describe how the superfluid current decays in a lattice when p is below p_c . We shall consider first the Gross-Pitaevskii regime $JN \gg U$ in the quantum rotor limit $UN \gg J$ and then turn to the situation in the vicinity of the superfluid insulator transition $JN \sim U$. In each case we shall address the effects of both quantum and thermal fluctuations.

3.1. Gross-Pitaevskii Regime

3.1.1. Quantum Decay

The action corresponding to the quantum rotor model (2) is given by

$$S = \int dt \left[\sum_j \frac{1}{2U} \left(\frac{d\phi_j}{dt} \right)^2 - \sum_{\langle j,j' \rangle} 2JN \cos(\phi_j - \phi_{j'}) \right], \quad (7)$$

or after the rescaling $\tau \rightarrow \tau/\sqrt{UNJ}$:

$$S = (JN/U)^{1/2} s, \quad (8)$$

where

$$s = \int d\tau \left[\sum_j \frac{1}{2} \left(\frac{d\phi_j}{d\tau} \right)^2 - \sum_{(j,j')} 2 \cos(\phi_j - \phi_{j'}) \right]. \quad (9)$$

To leading order in $\sqrt{U/JN}$, which plays the role of the effective Planck's constant for this problem [20], the tunneling rate depends on the action S_b , associated with the bounce solution of the classical equations of motion in the inverted potential [21]:

$$\Gamma \propto e^{-S_b}, \quad (10)$$

Clearly the action should vanish at $p = \pi/2$, since at this point the spectrum becomes unstable and the tunneling barrier disappears. Deep in the superfluid regime $U/JN \ll 1$, the tunneling is effective only if p is close to $\pi/2$, where the product $s(JN/U)^{1/2}$ is not too large. In this case one can make further progress in calculating the tunneling action by expanding (9) up to cubic terms in phase differences $\phi_j - \phi_{j'}$:

$$s \approx \sum_{j,\mathbf{k}} \int d\tau \left[\frac{1}{2} \left(\frac{d\phi_{j,\mathbf{k}}}{d\tau} \right)^2 + \cos(p)(\phi_{j+1,\mathbf{k}} - \phi_{j,\mathbf{k}})^2 + (\phi_{j,\mathbf{k}+1} - \phi_{j,\mathbf{k}})^2 - \frac{1}{3}(\phi_{j+1,\mathbf{k}} - \phi_{j,\mathbf{k}})^3 \right]. \quad (11)$$

Here we explicitly split the site index into longitudinal (j) and transverse (\mathbf{k}) components. Also, for convenience, we shifted the phase $\phi_{j,\mathbf{k}} \rightarrow \phi_{j,\mathbf{k}} + pj$ so that the metastable state now corresponds to $\phi_{j,\mathbf{k}} = 0$. Note that at $p \rightarrow \pi/2$ only longitudinal modes become soft, due to the prefactor p in front of the quadratic term in the action. This implies that we can safely apply a continuum approximation for the phases along the transverse directions. Then instead of (11) we derive:

$$s \approx \sum_j \int d\tau d^{d-1}x \left[\frac{1}{2} \left(\frac{d\phi_j}{d\tau} \right)^2 + \left(\frac{d\phi_j}{dx} \right)^2 + \cos(p)(\phi_{j+1} - \phi_j)^2 - \frac{1}{3}(\phi_{j+1} - \phi_j)^3 \right]. \quad (12)$$

In this equation \mathbf{x} denotes transverse coordinates which reside in a $d-1$ dimensional space. Upon rescaling

$$\phi = \cos(p)\tilde{\phi}, \quad \tau = \frac{\tilde{\tau}}{\sqrt{\cos(p)}}, \quad x = \frac{\tilde{x}\sqrt{2}}{\sqrt{\cos p}}, \quad (13)$$

the action (12) simplifies further:

$$s \approx (\pi/2 - p)^{\frac{6-d}{2}} \tilde{s}_d, \quad (14)$$

where

$$\tilde{s}_d = 2^{\frac{d-1}{2}} \sum_j \int d^d\xi \left[\frac{1}{2} \left(\frac{d\tilde{\phi}_j}{d\xi} \right)^2 + (\tilde{\phi}_j - \tilde{\phi}_{j+1})^2 - \frac{1}{3}(\tilde{\phi}_j - \tilde{\phi}_{j+1})^3 \right] \quad (15)$$

is just a number, which is determined only by the dimensionality d . We will provide its detailed variational derivation elsewhere [19] and here just quote the results: $\tilde{s}_1 \approx 7$, $\tilde{s}_2 \approx 25$, $\tilde{s}_3 \approx 90$. From the scaling (13) it is obvious that the characteristic transverse dimension of the instanton x scales as $(\pi/2 - p)^{-1/2} \gg 1$, justifying the continuum approximation. Above $d=6$ the tunneling action would experience a discontinuous jump at $p = \pi/2$. However, since we deal with $d \leq 3$, the action always continuously vanishes at $p \rightarrow \pi/2$. In this way we derive the asymptotic decay rate of a uniform current state near the modulation instability:

$$\Gamma \propto \exp \left[-\tilde{s}_d (JN/U)^{1/2} (\pi/2 - p)^{\frac{6-d}{2}} \right] \quad (16)$$

3.1.2. Thermal Decay

To calculate the exponent characterizing the thermal decay rate, one has to compute the difference of energies of the metastable state and the saddle-point which separates two adjacent metastable minima [22–24]. Both saddle-point and metastable configurations are the stationary solutions of the equations of motion (4):

$$\sum_{k \in \mathcal{O}} \sin(\phi_k - \phi_j) = 0. \quad (17)$$

The metastable state corresponds to the uniform phase twist: $\phi_{j,\mathbf{k}} = jp$. The saddle-point state relevant for the current decay can be easily found in one dimension:

$$\phi_j = \begin{cases} p'j, & j < 0 \\ \pi + p'(j-2), & j \geq 1, \end{cases} \quad (18)$$

where $p' \approx p - (\pi - 2p)/M$ if we use periodic boundary conditions for the system with M sites. The energy difference between the two states in the limit $M \rightarrow \infty$ is

$$\Delta E = 2JN(2 \cos p - \sin p(\pi - 2p)). \quad (19)$$

Correspondingly, the decay rate is proportional to

$$\Gamma \propto e^{-\beta \Delta E} = e^{-2JN\beta(2\cos p - (\pi-2p)\sin p)}. \quad (20)$$

In particular when $p \rightarrow \pi/2$ we have:

$$\Gamma \propto e^{-\frac{4}{3}NJ\beta(\pi/2-p)^3}. \quad (21)$$

In higher dimensions we cannot find the energy of the saddle-point explicitly for all values of p . However, in analogy with the quantum case, at p close to $\pi/2$ we can expand the energy functional up to cubic terms in phase differences.

$$E_d \approx JN \sum_j \int d^{d-1}x \left[\left(\frac{d\phi_j}{dx} \right)^2 + \cos(p) \times (\phi_{j+1} - \phi_j)^2 - \frac{1}{3}(\phi_{j+1} - \phi_j)^3 \right], \quad (22)$$

where $\phi_j(x)$ is the nontrivial solution of the corresponding Euler-Lagrange equations vanishing at $x \rightarrow \infty$. We again shifted the phase $\phi_j \rightarrow \phi_j + p_j$. After rescaling $\phi_j = \cos(p)\tilde{\phi}_j$ and $x = \tilde{x}\sqrt{2}/\sqrt{\cos p}$ we find:

$$E_d \approx JN 2^{\frac{d-1}{2}} (p_c - p)^{\frac{7-d}{2}} \sum_j \int d^{d-1}\tilde{x} \left[\frac{1}{2} \left(\frac{d\tilde{\phi}_j}{d\tilde{x}} \right)^2 + (\tilde{\phi}_{j+1} - \tilde{\phi}_j)^2 - \frac{1}{3}(\tilde{\phi}_{j+1} - \tilde{\phi}_j)^3 \right]. \quad (23)$$

Note that the integral in the expression above coincides with \tilde{s}_{d-1} up to a number $2^{\frac{d-1}{2}}$. So we immediately conclude that

$$E_d \approx \tilde{s}_{d-1} JN \sqrt{2} (\pi/2 - p)^{\frac{7-d}{2}}. \quad (24)$$

Note that the activation energy characterizing the thermal decay vanishes faster than the tunneling action as $p \rightarrow \pi/2$. It implies that thermal fluctuations become increasingly important and dominate the decay of superfluid current as the system approaches the dynamical instability. Comparing the ratio E_d/T and the tunneling action in (16) we obtain the crossover temperature:

$$T^* \approx c \left(\frac{\tilde{s}_{d-1}}{\tilde{s}_d} \right) \sqrt{\pi/2 - p} \quad (25)$$

at which the quantum and thermal decay rates coincide. Here $c = \sqrt{2UJN}$ is the sound speed in equilibrium (i.e. $p = 0$). Alternatively, we can fix the temperature to obtain the momentum crossover scale p^* at which thermal and quantum decay rates coincide:

$$\pi/2 - p^* \approx \left(\frac{\tilde{s}_d}{\tilde{s}_{d-1}} \right)^2 \left(\frac{T}{c} \right)^2. \quad (26)$$

At phase gradients larger than p^* , thermal decay dominates. The tunneling action in (16), at this value of momentum is given by

$$S_d^* = \tilde{s}_d \left(\frac{\tilde{s}_d}{\tilde{s}_{d-1}} \right)^{6-d} \sqrt{\frac{JN}{U}} \left(\frac{T}{c} \right)^{6-d}. \quad (27)$$

If $S_d^* \gg 1$, then at the crossover momentum the current decay is exponentially suppressed and will be nonzero only at p closer to $\pi/2$. Then the thermally activated phase slips will dominate the decay process and quantum tunneling can be ignored. In the opposite limit $S_d^* \ll 1$ the current will decay at $p < p^*$ due to quantum process and the temperature effects are unimportant. The characteristic crossover temperature separating quantum and thermal decay regimes is thus:

$$T_q \approx A c \tilde{s}_d^{-\frac{7-d}{6-d}} \tilde{s}_{d-1} \left(\frac{U}{JN} \right)^{\frac{1}{2(6-d)}}, \quad (28)$$

where A is a numerical constant of the order of one. Note that for all relevant dimensions $d \leq 3$ the last multiplier is always of the order of one because of the small exponent $1/(12-2d)$. Therefore, the crossover temperature T_q is of the order of the sound velocity (or equivalently, the Josephson energy).

4. CURRENT DECAY IN THE VICINITY OF THE MOTT TRANSITION

Let us now address decay of supercurrents in the regime where $JN \sim U$ and large integer filling N . As we already argued, in the vicinity of the Mott-insulator phase transition the correlation length ξ becomes large compared to the lattice constant. One can therefore use a continuum description of the problem (5). The relativistic dynamics of (5) is a special feature of the commensurate transition. Ordinary superfluids are described by a similar action, but with a kinetic term including first time derivative.

The Euler Lagrange-equations derived from (5) admit stationary current carrying solutions of the form

$$\psi = \sqrt{1 - (p\xi)^2} e^{ip\xi x}, \quad (29)$$

We emphasize again that x is measured in units of the correlation length ξ . The current state becomes unstable at $p > p_c = 1/(\xi\sqrt{3})$. Below p_c , the current can still decay due to quantum or thermal fluctuations.

For the thermal decay, only the static part of the action needs to be considered. Then there is no difference between our problem and the current decay in ordinary superfluids described by the Ginzburg-Landau free energy. In particular, in the context of super-conducting wires, the exponent characterizing the current decay rate in one dimension was computed by Langer and Ambegaokar [23], and the prefactor setting the time scale was later found by McCumber and Halperin [24]. In three dimensions, the asymptotic behavior of the corresponding exponent at $p \rightarrow 0$ was obtained by Langer and Fisher [25]. However, here we are interested in the opposite limit $p \rightarrow p_c$.

For both the thermal and the quantum cases we will use the scaling approach, successfully applied above for the quantum phase model in the Gross-Pitaevskii regime. We expand the action to cubic order in the amplitude (η) and phase (ϕ) fluctuations, about the metastable minimum, and integrate out the gapped amplitude mode. After the rescaling:

$$\begin{aligned} x &\rightarrow \frac{x}{2^{3/4} \sqrt{\xi} \sqrt{p_c - p}}, & z &\rightarrow \frac{z}{6\xi(p_c - p)}, \\ \phi &\rightarrow \phi 3^{3/4} : 2\sqrt{\xi} \sqrt{p_c - p} \end{aligned} \quad (30)$$

the action to leading order in $p_c - p$ becomes:

$$\begin{aligned} S &= C3^{9/4-d} : 2^d \xi^{5/2-d} (p_c - p)^{5/2-d} \int dz dx (\nabla \phi)^2 \\ &+ (\partial_x^2 \phi)^2 - (\partial_x \phi)^3 \approx A_d (1 - u)^{1/4} (p_c - p)^{5/2-d} \end{aligned} \quad (31)$$

where \mathbf{z} denotes all the transverse coordinates relative to the current direction, including time. $\nabla = (\partial_{\mathbf{z}}, \partial_x)$ is the gradient in $d + 1$ dimensions. Accordingly, the quantum decay rate is given by $\Gamma_Q \propto \exp(-A_d (1 - u)^{1/4} (p_c - p)^{5/2-d})$. A variational calculation [19], yields $A_1 \approx 18.4$ and $A_2 \approx 8.4$. As before, to calculate the thermal decay rate one simply has to substitute $d \rightarrow d - 1$, so that

$$\begin{aligned} \Gamma_T(d) &\propto \\ &\exp\left(-\frac{JN}{T} (2d)^{-3/4} (1 - u)^{1/4} A_{d-1} (p_c - p)^{7/2-d}\right). \end{aligned} \quad (32)$$

In the one-dimensional case the relevant constant $A_0 \approx 12.56$. It is interesting to contrast these results with the asymptotic decay rate (16), found in the Gross-Pitaevskii regime. First we observe that the tunneling action close to the Mott insulator vanishes

as a smaller power of $p_c - p$. Moreover, for $d = 3$, the scaling hypothesis for the quantum decay rate breaks down, suggesting that S is discontinuous at the critical current and is dominated by fluctuations of a finite (rather than diverging as $p \rightarrow p_c$) length scale. We therefore expect, that in three dimensions at zero temperature, the instability marks a sharp localization transition. At finite T , thermal fluctuations broaden this transition, because the activation energy barrier vanishes at p_c for $d < 7/2$.

The quantum-to-thermal crossover for a given dimensionless interaction and phase gradient is found by comparing the two decay rates. In one and two dimensions we find

$$T^*(p) = \frac{JN}{(2d)^{3/4}} \frac{A_{d-1}}{A_d} (p_c - p). \quad (33)$$

In three dimensions $T^* = 0$ because the quantum decay is effectively suppressed. As discussed above for the quantum rotor model, there is a more useful, p -independent, crossover temperature scale. Using the same arguments as in the Gross-Pitaevskii limit, we can find the temperature separating the quantum and thermal decay regimes in one and two dimensions:

$$T_q \sim JN A_{d-1} A_d^{-\frac{7-2d}{5-2d}} (1 - u)^{-\frac{1}{10-4d}}. \quad (34)$$

We see that near the Mott transition the crossover temperature strongly depends on interaction u . Thus as $u \rightarrow 1$, in one and two dimensions $T_q \rightarrow \infty$, and therefore the quantum decay always dominates over the thermal. In particular, in two dimensions we find $T_q \sim 0.03 JN / \sqrt{1 - u}$, and in the one-dimensional case $T_q \sim 0.1 JN / (1 - u)^{1/6}$; i.e., the crossover temperature is very high and the thermal decay is unimportant.

5. DYNAMICS OF THE CURRENT DECAY

We have seen that except for one case, corresponding to the three-dimensional relativistic model at $T = 0$, there is no sharp transition between the superfluid current-carrying state and the insulating state with no current. Indeed, in all other cases the tunneling action and the energy barrier vanish continuously as the system approaches the modulation instability. Thus, instead of a sharp transition boundary we can define a broad crossover region, defined roughly by $1 < S_d < 3$, which separates the superfluid phase with a relatively slow current decay and the insulating phase with a fast decay. The fact that the transition is broad does not imply, however, that within a single experiment a gradual current decay

will be detected as the system is slowly tuned through the crossover region. The tunneling and thermal decay rate define a probability of creating a single phase slip per lattice site. The subsequent evolution, after a single phase slip has been created, can take one of two general routes. In the overdamped scenario, the phase slip rapidly dissipates its energy into phonon (Bogoliubov) modes and brings the system to the next metastable minimum with slightly lower current. In the second, underdamped scenario, the phase slip continues to unwind, triggering complete decay of the current in a single step.

In a closed system, i.e. with no coupling to the environment, these two regimes are well defined because the damping of the phase slip comes from the internal degrees of freedom, which are completely described by the equations of motion. Furthermore, near the critical current, whether the phase slip was thermally activated or induced by quantum tunneling, should make little difference for the dynamics that follow. This is because the energy barrier is very small, so the classically allowed motion following the tunneling event starts very close to the metastable maximum, where it would start following thermal activation. To see what type of decay modes are realized in the Gross-Pitaevskii regime, we solve the classical equations of motion (3) numerically. We start from a uniform current state in a periodic lattice. To allow for current decay we add small fluctuations to the initial values of the classical fields $\psi_j(t=0)$. This mimics the effect of thermal fluctuations. In Fig. 1 we plot the computed current versus time for a one-dimensional array of $M = 200$ sites. Initially the system is assumed to be noninteracting ($U = 0$) and prepared in an eigenstate with a given phase gradient p (specifically we consider $p = 2\pi/5$ and $p = \pi/10$). Then, the interaction is gradually increased in time reaching a constant value, and we follow the time evolution of the current. It is clear from the figure that the phase slips in the smaller current case ($p = \pi/10$) are overdamped leading to gradual decay. There are initially 10-phase twists in the system, and indeed, it is evident that each phase slip decreases the current by roughly 10%. On the other hand for the larger current ($p = 2\pi/5$) a single phase slip generates immediate current decay in the whole sample consistent with the underdamped regime. We will not attempt here to find the precise boundary between the two scenarios. However, we stress that near the instability the system is always in the underdamped regime. We checked that a similar overdamped to underdamped crossover occurs in

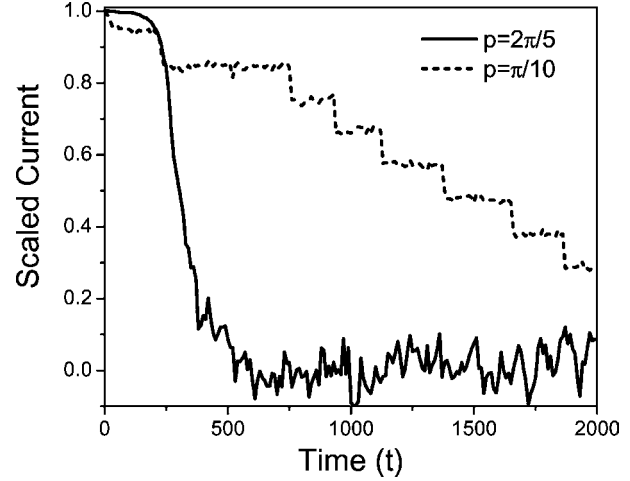


Fig. 1. Current (scaled to 1 at $t = 0$) versus time for a one-dimensional periodic array of 200 sites with two different initial phase gradients. The evolution is determined solving equations of motion (3) with constant hopping amplitude $J = 1$ and interaction increasing in time $U = 0.01 \tanh 0.01t$ for $p = 2\pi/5$ and $U = \tanh 0.01 t$ for $p = \pi/10$. To get the current decay we add small fluctuations to the initial values of the classical fields $\psi_j(t = 0)$.

other spatial dimensions. So if p is not too small, then in a given experimental run, one will always see a sharp transition from the superfluid to the insulating regime. However the precise point, where the current decays will vary from run to run. The broadened transition below the critical current, which was the subject of this paper, will be evident from accumulated statistics of the point where the rapid decay occurred. On the other hand, in the absence of any fluctuations the transition would seem very sharp, and always occurs at $p = \pi/2$.

We did not carry out a similar numerical analysis for small currents close to the Mott transition. There are some reasons to anticipate that the decay will be overdamped in this case even close to the critical current. In particular, because the size of the phase slip in this case is large, it should be able to easily dissipate energy into phonon modes.

It is worth mentioning, that if the motion of phase slips is underdamped, then in a truly infinite system the current state is always unstable. Indeed the probability of a phase slip in the whole system is proportional to its size M . If a single phase slip triggers the current decay in the whole sample, then obviously a state with a uniform phase gradient cannot exist. However, in finite size systems these effects are not so crucial, because the decay probability depends exponentially on the couplings and current, but only linearly on the system size.

6. CONCLUSIONS

The modulational instability can be observed either by accelerating the condensate or by increasing the lattice potential and driving the system closer to the Mott transition, while the condensate is in motion. We showed that because of quantum or thermal effects, the current decays before the system becomes classically unstable. Therefore instead of a sharp transition, there is a crossover region where the decay rate grows from being exponentially small to large. The crossover region becomes narrower either deep in the superfluid regime (i.e. $JN \gg U$) or in higher dimensions. In particular, in the three-dimensional case we always expect a very sharp boundary separating the regions with very weak and very strong decay rates.

We found that deep in the superfluid regime the crossover temperature separating quantum and thermal decay is of the order of plasma frequency in all dimensions. At small currents, close to the Mott phase, the decay occurs predominantly through thermal fluctuations in three dimensions and through quantum tunneling in one and two dimensions. In the two-dimensional case the quantum tunneling becomes appreciable only at extremely low temperatures or very close to the Mott transition.

We argue that both overdamped and underdamped dynamics of the current decay can be realized in these systems. The underdamped regime corresponds to high currents close to $p = \pi/2$, while at low currents the dynamics is overdamped.

ACKNOWLEDGMENTS

We acknowledge useful discussions with D.-W. Wang. This work was supported by ARO and NSF

under Grants DMR-0233773, DMR-0231631, and DMR-0213805.

REFERENCES

1. R. S. Newbower, M. R. Beasley, and M. Tinkham, *Phys. Rev. B* **5**, 864 (1972).
2. A. Bezryadin, C. N. Lau, and M. Tinkham, *Nature* **404**, 971–974 (2000).
3. C. N. Lau, N. Markovic, M. Bockrath, A. Bezryadin, and M. Tinkham, *Phys. Rev. Lett.* **87**, 217003 (2001).
4. M. Tinkham and C. N. Lau, *Appl. Phys. Lett.* **80**, 2946–2948 (2002).
5. F. Braun, J. von Delft, D. C. Ralph, and M. Tinkham, *Phys. Rev. Lett.* **79**, 921–924 (1997).
6. M. T. Tuominen, J. M. Hergenrother, T. S. Tighe, and M. Tinkham, *Phys. Rev. Lett.* **69**, 1997–2000 (1992).
7. M. Tinkham, *Physica B* **169**, 66–71 (1991).
8. L. Ji, M. S. Rzchowski, and M. Tinkham, *Phys. Rev. B* **42**, 4838–4841 (1990).
9. S. P. Benz, M. S. Rzchowski, M. Tinkham, and C. J. Lobb, *Phys. Rev. B* **42**, 6165–6171 (1990).
10. M. Greiner, O. Mandel, T. Esslinger, T. W. Hänsch and I. Bloch, *Nature* **415**, 39 (2002).
11. L. Fallani, L. De Sarlo, J. E. Lye, M. Modugno, R. Saers, C. Fort, and M. Inguscio, cond-mat/0404045.
12. M. Ben Dahan, E. Peik, J. Reidhel, Y. Castin, and C. Salomon, *Phys. Rev. Lett.* **76**, 4508 (1996).
13. A. Polkovnikov, S. Sachdev, and S. M. Girvin, *Phys. Rev. A* **66**, 053607 (2002).
14. B. Wu and Q. Niu, *Phys. Rev. A* **64**, 061603(R) (2001).
15. A. Smerzi, A. Trombettoni, P. G. Kevrekidis, and A. R. Bishop, *Phys. Rev. Lett.* **89**, 170402 (2002).
16. A. Polkovnikov and D.-W. Wang, *Phys. Rev. Lett.* **93**, 070401 (2004).
17. E. Altman and A. Auerbach, *Phys. Rev. Lett.* **89**, 250404 (2002).
18. S. Sachdev, *Quantum Phase Transitions* (Cambridge University Press, Cambridge, 1999).
19. A. Polkovnikov, E. Altman, E. Demler, B. I. Halperin, and M. D. Lukin, in press.
20. A. Polkovnikov, *Phys. Rev. A* **68**, 033609 (2003); A. Polkovnikov, *Phys. Rev. A* **68**, 053604 (2003).
21. S. Coleman, *Phys. Rev. D* **15**, 2929 (1977); C. G. Callan and S. Coleman, *Phys. Rev. D* **16**, 1762 (1977).
22. J. S. Langer, *Phys. Rev. Lett.* **21**, 973 (1968).
23. J. S. Langer and V. Ambegaokar, *Phys. Rev.* **164**, 498 (1967).
24. D. E. McCumber and B. Halperin, *Phys. Rev. B* **1**, 1054 (1970).
25. J. S. Langer and M. E. Fisher, *Phys. Rev. Lett.* **19**, 560 (1967).

The Strong Impact of the Weak Superconductivity

Antonio Barone¹

Received August 15, 2004; accepted September 4, 2004

The Josephson effect offers an unparalleled tool to shed light on aspects of the underlying physics of phenomena which go also far beyond the field of superconductivity. Some considerations on a few examples of the highlights concerning both exciting achievements and challenging perspectives of this fascinating topic are briefly outlined “sharing” the attention on both possible applications and intriguing implications.

KEY WORDS: Macroscopic quantum tunneling; Josephson effect; superconductivity.

1. INTRODUCTION

Seventy-five years ago two important events took place in the field of Physics: . . . the second one was the birth of quantum electrodynamics.

In this paper I shall dwell with aspects related to the development of superconductivity [1], confining the attention on the precious combination of the role of the Josephson effect [2] in the investigations of a few fundamental issues and on peculiar examples of realized and potential applications. In doing so I shall focus on examples that I hope will reflect the two sides of the coin.

In the next section a brief discussion is given on just a few aspects of macroscopic quantum phenomena such as Macroscopic Quantum Tunneling (MQT) and Macroscopic Quantum Coherence.

Section 3 deals with the important issue concerning the role of the Josephson effect as a probe of essential features of the superconducting state. Fundamental in this context, is the identification of the nature of the order parameter in new classes of superconductors using proper Josephson structure configurations. Some of the “historical” and quite recent results are briefly discussed. As for the applications based on the Josephson effect a few examples of great interest and quite different in nature are discussed in Section 4. Comments and conclusions will follow.

2. MACROSCOPIC QUANTUM PHENOMENA

Let us discuss some aspects of the Josephson effect of great importance in the context of macroscopic quantum phenomena [3,4]. Quantum tunnelling on a macroscopic scale was considered by Sidney Coleman [5] as an essential ingredient of “ground state metastability” in the cosmological frame. The fate of the “false vacuum,” namely its decay through barrier penetration is a fascinating, though a, hopefully unlikely, dramatic “small bang” perspective, toward a more stable state of the Universe.

I shall not dwell here with underlying concepts of quantum phenomena “at large” [6] nor with a variety of subtle concepts and detailed analysis which go far beyond the limits of space of the present article and those, even narrower, of its author.

Let us refer to experiments dealing with phenomena stemming from the quantum nature of a single macroscopic degree of freedom which are quite different [7] from those resulting in the superposition of a large number of microscopic variables. In our frame the macroscopic degree of freedom is the relative phase φ of the two weakly coupled superconductors of a Josephson junction or the trapped magnetic flux [$\Phi(\varphi = 2\pi(\Phi/\Phi_0))$] in a rf SQUID superconducting loop.

Let us refer to the usual junction washboard potential $U(\varphi)$ (Fig. 1) resulting from the sum of the free energy associated to the junction barrier and a term $\alpha = I/I_c$ due to the feeding current I which

¹INFM—Coherentia—Dipartimento di Scienze Fisiche, Università di Napoli “Federico II,” Napoli, Italy.

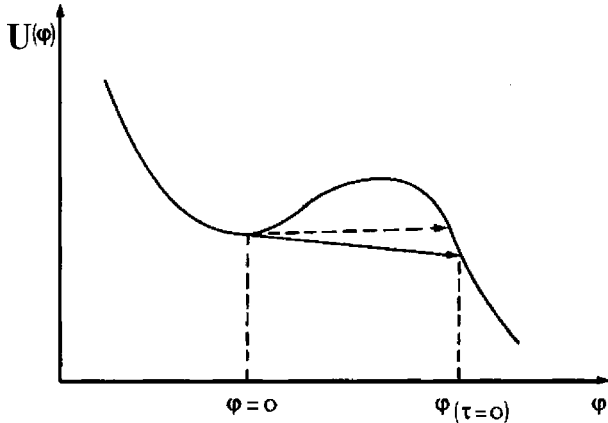


Fig. 1. Qualitative sketch of potential vs. phase. Two values of the imaginary time $\phi(\tau = -\infty)$ and $\phi(\tau = 0)$ are indicated. Dashed and solid arrows indicate tunnelling paths for small dissipation ($B \ll 1$) and large dissipation ($B \gg 1$), respectively.

determines the average slope of $U(\phi)$ (e.g. Chapter 6 [2]):

$$U(\phi) = -(\Phi_0 I_c / 2\pi)(\alpha\phi - \cos\phi - 1).$$

The decay probability for thermal activation out of a potential well (see also [1], Chapter 7) can be expressed by the classical Kramer theory as

$$\tau_c^{-1} = A \exp\left[\frac{\Delta U}{k_B T}\right]$$

where ΔU is the potential barrier height, which depends on the bias current. There are different expressions of the prefactor A for the various damping regimes.

At very low temperature, a regime of quantum activation can occur [8] and Josephson junctions offer the possibility to investigate intriguing aspects of quantum mechanics at a macroscopic level. From the experimental point of view a first fundamental signature of the macroscopic quantum nature of the system lies in the existence of quantized energy levels (ELQs). Unambiguous evidence of such a feature was provided by the experiments based on the microwave irradiation with consequent energy level hopping [3]. As for the Macroscopic Quantum Tunneling (MQT), the particle can now escape from one local minimum by tunnelling through the potential barrier, and a variety of situations can occur.

At $T = 0$, the tunnelling probability (WKB) is $\tau_q^{-1} = A \exp(-B)$, where $A = \omega_p / 2\pi$ and $B = 7.2\Delta U / \hbar\omega_p$, ω_p being the plasma frequency. The factor 7.2 accounts for the cubic shape of the potential $U(\phi)$ at current values close to the critical (thinner

barrier) where quantum tunnelling more likely occurs. Comparing this expression with the thermal decay in the underdamped regime, thermal and quantum activation are equal for $k_B T_0 = \hbar\omega_p / 7.2$ which defines thereby a “crossover temperature,” T_0 , below which quantum effects are dominant over thermal ones. In the full quantum mechanical description of the macroscopic variable it is mandatory to take into account interactions with the other degrees of freedom, the irreversible energy transfer between the system and the environment, namely the dissipation.

Caldeira and Leggett [9] have investigated such a problem and have found that dissipation produces a reduction of the tunnelling rate by a factor $\exp(-A\eta\Delta_q^2)$ where η is the friction coefficient and $\Delta_q \equiv \Delta_\phi$ the “distance in the barrier” (the tunnel length).

A sketch of $U(\phi)$ and turning points in the case of small and large dissipation [10] is given in Fig. 1. The influence of dissipation on the prefactor in the expression of the decay via MQT is of interest (see [11] and references reported therein). The correction to the prefactor due to the viscosity is smaller than the correction to the exponent by a factor $1/N$ (N is the number of levels in the well). However, the number of levels in a potential well in actual experimental conditions for MQT (low temperature) is quite small ($N \sim 1$). Thus, it is necessary to take into account the correction to the prefactor which is known only in some special cases (for large viscosity near the crossover temperature T_0 , and when the viscosity is equal to zero, at temperature T larger than the crossover temperature).

A macroscopic quantum phenomenon of great interest lies in the occurrence of MQT between levels in neighboring wells with very close energy. This Resonant Macroscopic Quantum Tunneling (RMQT) effect [12] results in sharp-voltage peaks as experimentally observed by Rouse *et al.* [13] in a SQUID structure.

Going back to the MQT, it is interesting to recall that such a macroscopic quantum phenomenon has been observed [14] also at temperature larger than the crossover temperature by playing on a combination of a high current bias sweeping rate (400 kHz) and low dissipation. Indeed, in these conditions, within the characteristic measurement time, incoherent mixing of eigenstates is negligible since the rate of change of the external energy, measured in terms of the energy level spacing, is fast compared to thermally activated transition rate between such levels.

It is important to stress that the effect of temporally modulated barriers on MQT is an extremely intriguing subject on which it is focused a great attention from both theoretical and experimental side. Mechanisms of barrier penetration in non-stationary field, such as, phenomena belonging to photon-assisted tunnelling and Euclidean resonance deserve great attention [15]. Recently, possible influence of current bias modulation on the dynamics of Josephson junctions has been also discussed [16] in connection with the quantum Zeno (QZE) and anti-Zeno (AZE) effects [17], namely slowdown and speedup respectively of the decay of quantum states into an energy continuum due to frequent measurements.

A further very stimulating topic which has attracted the attention of the scientific community is the Macroscopic Quantum Coherence. Evidence of a coherent superposition of states which differ by the transfer of a single Cooper pair was obtained in an ultra small capacitance tunnel junction device by Nakamura *et al.* ([18] and references reported therein) and quantum coherent charge oscillations by Nakamura *et al.* [19].

As for the experimental observation of coherent quantum superposition of macroscopic distinct quantum states, let us recall the results obtained by Lukens group at the State University of New York, Stony Brook [20]. The states were identified with two magnetic flux states of a SQUID, corresponding to a pair of excited states $|0\rangle$ and $|1\rangle$ of the individual well (see Fig. 2a). Excitation of the $|0\rangle$ state from the lower one $|1\rangle$ is realized by microwave irradiation. A series of measurements is performed reaching a condition when the two states in the wells are in a coherent regime identifying the symmetric and antisymmetric superpositions of the $|0\rangle$ and $|1\rangle$ state. Locations of resonant transitions between the fluxoid states of a SQUID are reported in Fig. 2b with a shift of 96 GHz between the excited and the ground state. Of great relevance is also the observation of the coherent superposition of persistent current quantum states in SQUID systems [21].

Furthermore, evidence of Rabi oscillations [21] between such macroscopic quantum states have been found in Josephson junctions [22] and on the “quantronium” [23] circuit configuration. The stimulating perspective of a quantum computer makes these types of circuitry quite promising. Indeed the implementation of proper quantum bits includes the single [19,24] and coupled [25] Cooper pair box configurations, flux qubits [26], and phase-qubit [21,27].

Among the other relevant results let us mention the use of rf-sets to probe the island charge performing thereby the qubit readout [28] and the charge-flux Josephson qubit discussed in [29]. Let us remember that also HTS superconductors circuits have been proposed in the context of a possible implementation of qubits (e.g. [30]). Potential and drawbacks of these structures deserve great attention.

3. UNCONVENTIONAL ORDER PARAMETER SYMMETRY

The potential of the Josephson effect as a probe of the order parameter symmetry has provided one of the main breakthrough in the investigations of unconventional superconductors. The basic idea of such a possibility was first proposed in Ref. [31] as a probe for a possible axial p -wave symmetry in heavy-fermion systems. It was independently considered in the following [32] in the context of high- T_c cuprate superconductors to explain properties of these materials as due to d -wave pairing. A detailed discussion of the following quite interesting experiments and the related extensive bibliography can be found in the excellent review by Van Harlingen [33]. A vortex state characterized by half-flux quantization, as a consequence of the unconventional symmetry of the order parameter, was proposed in Ref. [31]. It is interesting to observe that at the end of that article it was also stated: “It would be of great interest to consider the possibility of a direct experimental observation of such a vortex structure by using a suitable *microscopy* technique as any other possible probe which could be envisaged.” It is indeed what was achieved at the IBM Laboratory by using SQUID scanning microscopy (SSM) in a series of brilliant experiments on the flux quantization in high- T_c rings including two- and three-grain boundary Josephson junctions (for an extensive review and bibliography See [34]). Recently, further experiments which appear to confirm unambiguously the d -wave order parameter symmetry in high- T_c superconductors have been realized using biepitaxial YBCO Josephson structures with “tunnel-like” features and low barrier transparency [35]. The importance of these new results, obtained by anisotropy measurements, lies in the “intrinsic” character of the d -wave effects since observed in a Josephson junction not inserted in any loop configuration (see also Ref. [36]). In Fig. 3, the dependence of the Josephson critical current in a c -axis tilt biepitaxial grain boundary

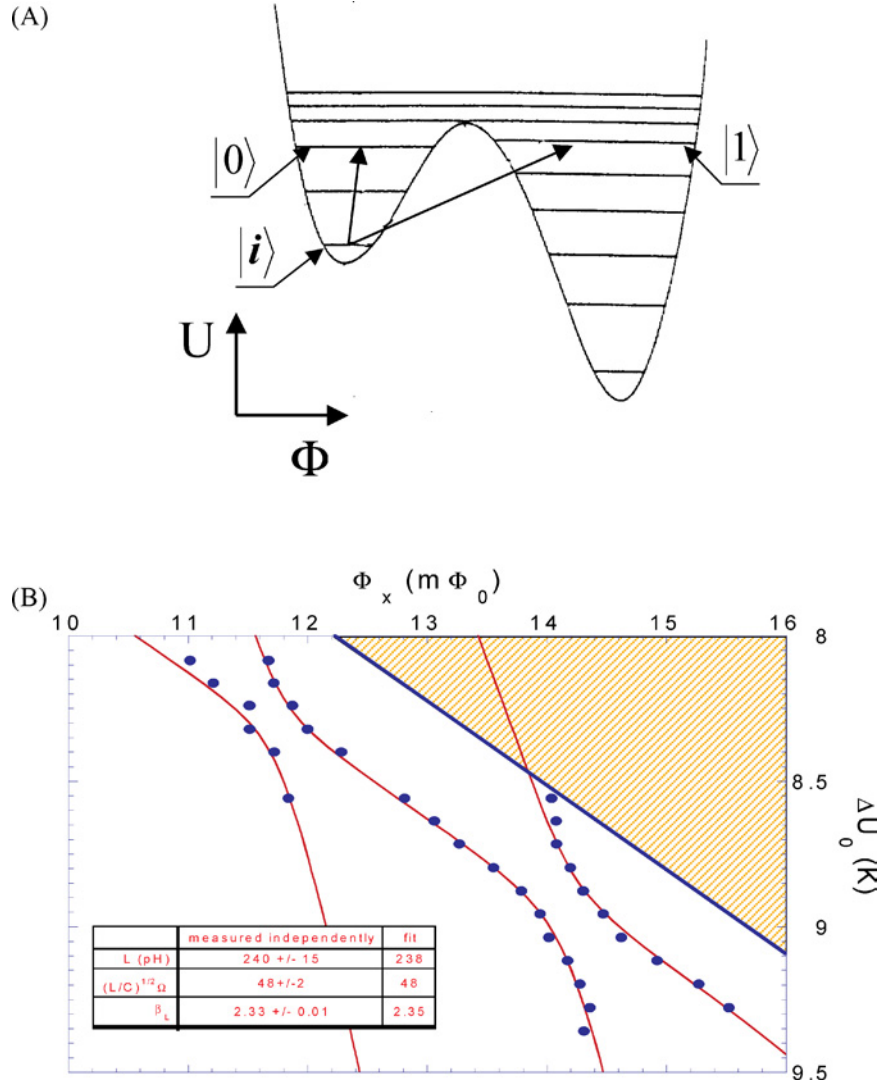


Fig. 2. (a) $U(\Phi)$ SQUID potential with the two left and right wells corresponding to the zero and one-fluxoid state, respectively. (b) Observed Peak Locations Compared to Best Fit Level Positions (see text). Data from Prof. Lukens group at SUNY Stony Brook [J. Friedman *et al.*, *Nature* **406**, 43 (July 2000)].

YBCO junction is reported (dots) as a function of the angle between the grain boundary line and the (001) in-plane direction of the substrate. The inset shows the grain boundary structure with different interface orientations. The excellent agreement with theoretical prediction of Sigrist and Rice model [32] (open circles) for a Josephson junction with a predominantly d -wave order parameter symmetry of the superconductors electrodes is impressive. For details see Ref. [35] and references reported therein. There is a vast literature concerning the debate of d -wave versus s -wave symmetry in cuprate superconductors

including the possibility of differences in probing surface (d -wave) or bulk (s -wave) properties [37].

4. DEVICE APPLICATIONS AND IMPLICATIONS

I still remember that during the conference on Superconducting Devices, held at Charlottesville in 1967, Michel Thinkam, belying the often assumed abstractness of a theoretician, gave a quite unambiguous definition: “A device is an object which can be

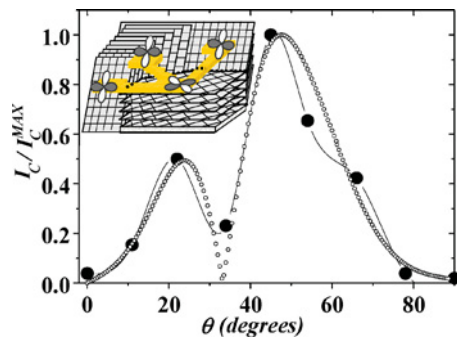


Fig. 3. I_c dependence on the angle is reported; experimental data (filled circles) are compared with theoretical predictions based on $d_{x^2-y^2}$ wave pairing symmetry (open circles) [35]. Inset—Sketch of the grain boundary structure with different interface orientations.

sold at a profit.” Accordingly, I shall proceed with due caution. Actually, I shall confine myself just to a brief comment on some applications and a short account of a specific example to stress a few intriguing implications.

4.1. Some Applications Based on the Josephson Effect

Although there is a number of stimulating realized and potential applications of the Josephson effect, it is wise to stress that, so far, these belong mainly to the so-called niche-type applications. The impression of some drawbacks in the diffusion of this technology could be also ascribed, in my opinion, to the circumstance that, often, tempting promises largely exceed cautious premises. A more concrete obstacle which affects superconductivity applications in general, obviously lies in the associated cryogenic requirements. In this respect the combination of research toward higher critical temperature materials and the significant improvements of cryocoolers technologies is quite promising. In any case, the widely celebrated existing “cryofobia” should not be justified for devices of unparalleled performances for which the benefit/cost ratio remains necessarily quite favorable. Among the best examples of superconductive devices based on the Josephson effect, magnetic flux sensors, namely the SQUIDs, represent a cornerstone of this technology (e.g. [38]). SQUIDs allow an unparalleled tool in the field of biomagnetism. Indeed, this is an area of growing importance, especially for the magnetoencephalography (MEG) which provides functional imaging of fundamental importance for medical implications. Clinical valida-

tions of the developed techniques and methodologies legitimate the concreteness of SQUIDs biomedical applications. For an updating on the trend of the developments in SQUID-based MEG instrumentation see [39] and enclosed references.

Another important area of application of SQUID circuits lies in the nondestructive evaluation (NDE) [40] which can be performed to investigate the presence of cracks and corrosion in different materials and structures (motors, airplanes, cables, etc.). The magnetic field sensitivity of such sensors over a wide frequency range and large dynamic range allows to collect informations often unobtainable by conventional electromagnetic probes. Magnetotellurics is also a field which has attracted great interest since long time (e.g. [41]).

SQUID read out circuitry in different context is also of great interest. An important role of SQUIDs can be envisaged also in the implementation of magnetic qubits. Finally, let us just mention the use of a SQUID in the context of the detection of gravitational waves and the early attempts in the search for the magnetic monopole (e.g. see B. Cabrera review in Ref. [38]).

It is well known that Josephson effect versus “applications” to fundamental physics has a long history in determining fundamental physical constants (see [1,2] and references reported therein). As for the implementation of superconductive electronics, Josephson junction circuitry has been widely investigated. Active components have been realized through the years employing conventional superconductors. As for high- T_c superconductors, the perspective is very stimulating although reproducibility and large scale integration still represent a hard issue. The potential of superconducting electronics remains however an extremely challenging issue [42].

4.2. Superconductive Radiation Detectors

Let us now briefly discuss a few peculiar aspects in the investigations of superconductive junction radiation detectors involving a variety of challenging implications. The small energy gap values of conventional superconductors (~ 1 meV) compared with that of a semiconductor (~ 1 eV) is the main reason of interest in superconductive tunnel junction (STJ) detectors [43]. Indeed, crudely speaking, this implies smaller values of the minimum energy to create “free carriers” (elementary excitations). Consequently, for a given released energy, in the case

of a superconductor a larger number of excitations is produced. This leads to reduced fluctuations and thus improvement of energy resolution. The elementary excitations are the quasiparticles created by the Cooper pairs breaking produced by the absorbed radiation.

Thus, STJ structures employed for high resolution energy spectroscopy work in the quasiparticle tunnelling regime. The junction is therefore biased at voltage values of the I–V characteristics in the subgap region. The necessity of high quasiparticle collection requires a high transparency of the tunnelling barrier leading to the occurrence of Josephson tunnelling. In this context however the Josephson current (and Josephson resonant modes) is an undesired additional feature which has to be eliminated. This is ordinarily achieved by applying a proper magnetic field. A possible clever alternative solution is to use an annular junction, i.e. a ring-shaped electrode junction. In this case, in fact one can take advantage of the ability of a ring made of superconducting material to stably trap flux quanta. Once magnetic flux quanta have been trapped in such a way that the magnetic field lines thread the tunnel barrier, the Josephson critical current is suppressed, and resonant modes are strongly reduced. Figure 4a reports an I–V characteristic obtained under these circumstances and illustrates how any presence of Josephson effect is completely disappeared. Figure 4b shows a pulse height spectrum from the same junction irradiated by X-rays and demonstrates the capability to detect photons in this configuration still maintaining a good spectroscopic response [45].

Annular Josephson junctions deserve a special place in the context of Josephson effect. In these structures, the fluxoid quantization phenomenon manifests in that magnetic flux quanta (fluxons) can irreversibly be trapped in one electrode during the normal/superconducting transition. This causes the superconductive order parameter phases of the two electrodes to differ by an integer number n of 2π for the entire time the device remains at a temperature below the critical temperature. This is an example of *topological* quantum number, i.e. a number characterizing a macroscopic physical system or device, which does not depend on the particular realization of the system itself, its defects, the particular shape, the presence of leads, and so on. In particular, if no trapping occurs, n is zero. In this case fluxons can still be excited in the annular junction (provided that the junction is enough extended) in the form

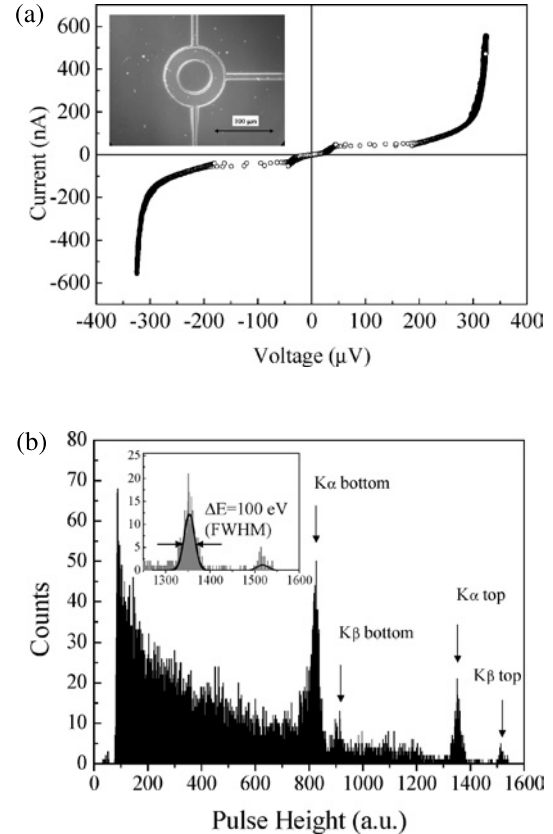


Fig. 4. (a) I–V characteristic of an annular Al STJ at $T = 70$ mK after trapping flux quanta. The inset shows a photograph of the junction. No external magnetic field is applied. The Josephson critical current appears to be completely suppressed and there is no trace of resonant structures [45]. (b) Pulse height spectrum from an annular STJ irradiated by a ^{55}Fe radioactive source emitting two lines at $E(K\alpha) = 5.9$ KeV, and $E(K\beta) = 6.5$ KeV, respectively. The spectrum was obtained in the same conditions described in Fig. 4a [45].

of fluxon–antifluxons, such that value of n remains untouched and equal to zero. Much of the physics of fluxon propagation in Josephson junctions (i.e. the sine Gordon soliton physics [46]) has been derived by experiments performed on annular junctions [47]. The main reason is certainly the circumstance that fluxons, as well as electromagnetic waves, propagate in these structures without suffering boundary collisions. Features in the I–V characteristic of these devices, steps, current peak branches, jumps, mirror exactly the dynamics of the superconductive order parameter phases of the two electrodes. They can be mapped one to one to the presence and the motion of fluxons, and waves, inside the device. The kind of nonlinear dynamics characterizing the fluxon motion in the junctions can be very complex (also in the

absence of collisions at the boundaries). However, there are broad classifications, which correspond to well understood mechanisms. Examples of these are *Fiske steps* and *zero-field steps*. A deep understanding of the rich phenomenology related to the soliton dynamics is of fundamental relevance.

In fact annular junctions have been considered as a possible physical system suitable for experiments dealing with a variety of intriguing aspects of fundamental physics. Among these we remind the demonstration of the macroscopic quantum nature of Josephson vortex dynamics related to the tunneling in real space of vortices and the quantum dissociation of vortex antivortex pairs [48]. This also in view of the realization of a flux qubit device [49]. Another potentiality offered by annular-shaped Josephson junctions lies in the possible observation of a direct influence of the Berry's geometric phase on Josephson vortex dynamics [50]. Investigations on these ring-shaped structures have been considered even toward the intriguing issue concerning the onset of second order phase transitions in the early universe scenario. The spontaneous flux generation in annular Josephson junctions is approached, in this contest, by resorting the "Kibble-Zurek" mechanism [51]. Finally, let us recall that detectors "based" on the Josephson effect were proposed as ultra fast threshold detectors [52] and, recently, excellent results have been obtained on a Josephson device and are able to provide a simultaneous time and energy radiation detection [53].

5. CONCLUSIONS

A few examples of important issues concerning the Josephson effect and its potential for both fundamental physics and practical "applications" have been briefly discussed. The attention has been addressed to the Josephson effect as a probe of macroscopic quantum phenomena and of the order parameter symmetry of high- T_c superconductors. As for the applications, just few examples have been mentioned, considering both those of practical impact and those which allow investigations of fundamental issues in different fields of physics. The occurrence of possible stimulating links between the two kinds of "applications" have been briefly analyzed.

Indeed, uniqueness of science does not contradict the combined process of "science push-technology pull." Rather, it is of interest how, for instance, the request of advanced solutions posed by

severe technological constrains can produce a sort of "spin-off" of importance for fundamental issues even in completely different fields. An example can be that discussed in Section 4.1 where optimization of a device geometry for a radiation detector touches problems concerning even cosmological issues. Incidentally, about the universe in the . . . laboratory, during the preparation of this article, I learned about a proposal [54] of dark energy to be measured replicating early measurements of spectral density of current noise in Josephson junctions performed by Koch *et al.* [55].

Finally, I wish to stress that among the various topics not considered in this paper, I have fully omitted the fundamental one of mesoscopic superconductivity, an issue of paramount importance [56] for the deep theoretical implications and the consequences in the advance of microelectronics. I confined myself in giving thereby, rather than a contribution on superconductive nanostructures, a nanocontribution on superconductive structures.

REFERENCES

1. M. Tinkham, *Introduction to Superconductivity*, 2nd edn. (Mc Graw-Hill, New York, 1996).
2. A. Barone and G. Paternò, *Physics and Applications of the Josephson Effect 2* (Wiley, New York, 1982).
3. J. Clarke, A. N. Cleland, M. H. Devoret, D. Esteve, and J. M. Martin Sci. **29**, 992 (1988) and references reported therein.
4. A. J. Leggett, in *Quantum Tunnelling in Condensed Media*, Yu. Kagan and A. J. Leggett, eds. (Elsevier Science, Amsterdam, 1992); in *Proceedings of the Nobel Jubilee Symposium*, T. Claeson and P. Delsing, eds., Goteborg, Sweden, December 4–7, 2001, *Phys. Scrip.* **T102**.
5. S. Coleman, *Phys. Rev. D* **15**, 2929 (1977).
6. J. M. Levy-Leblond, *Advances in Quantum Phenomena*, E. G. Beltrametti and J. M. Levy-Leblond, eds. (Plenum Press, New York, 1995).
7. A. J. Leggett, *Suppl. Prog. Theor. Phys.* **69**, 80 (1980); *Con-temp. Phys.* **25**, 583 (1984).
8. P. W. Anderson, in *Lectures on the Manybody Problem*, Vol. II, E. R. Caianiello, ed., (Academic Press, Ravello, 1963, pp. 113–115, Yu. M. Ivanchenko and L. A. Zil'berman, *Sov. Phys. JETP* **28**, 1272 (1969).
9. A. O. Caldeira and A. J. Leggett, *Phys. Rev. Lett.* **46**, 211 (1981); see also A. J. Leggett *et al.*, *Rev. Mod. Phys.* **59**, 1 (1987).
10. A. Barone and Yu. N. Ovchinnikov, *J. Low Temp. Phys.* **55**, 297 (1984).
11. Yu. N. Ovchinnikov and A. Barone, *J. Low Temp. Phys.* **67**, 323 (1987).
12. A. V. Zhuvalev and A. B. Zorin, *Sov. J. Low Temp. Phys.* **16**, 102 (1990); J. M. Shmidt, A. N. Cleland, and J. Clarke, *Phys. Rev. B* **43**, 229 (1991).
13. R. Rouse, S. Han, and J. L. Lukens, *Phys. Rev. B* **75**, 1614.
14. P. Silvestrini, V. G. Palmieri, B. Ruggiero, and M. Russo, *Phys. Rev. Lett.* **79**, 3046 (1997).
15. B. I. Ivlev, *Phys. Rev. A* **62**, 62102 (2000); *Phys. Rev. A* (in press); B. I. Ivlev, arXiv:quant-ph/0407163 (2004), and references reported therein.

16. A. Barone, G. Kurizki, and G. Kofman, *Phys. Rev. Lett.* **92**, 200403-1 (2004).
17. G. Kurizki and G. Kofman, *Nature* **405**, 546 (2000).
18. Y. Nakamura, C. D. Chen, and J. S. Tsai, *Phys. Rev. Lett.* **79**, 2328 (1997); See also D. Averin, *Nature* **398**, 749 (1999); C. D. Tesche, *Phys. Rev. Lett.* **64**, 2358 (1999); C. Cosmelli *et al.*, *Appl. Phys. Lett.* **80**, 2928 (1999).
19. Y. Nakamura, Y. Pashkin, and J. S. Tsai, *Nature* **398**, 786 (1999).
20. J. R. Friedman, V. Patel, W. Chen, S. K. Tolpygo, and J. E. Lukens, *Nature* **406**, 43 (2000).
21. I. Chiorescu, Y. Nakamura, C. J. P. M. Harmans, and J. E. Mooij, *Science* **299**, 1896 (2003).
22. Y. Yu, S. Han, X. Chu, S. I. Chu, and Z. Wang, *Science* **296**, 889 (2002); J. M. Martinis, S. Nam, J. Aumentado, and C. Urbina, *Phys. Rev. Lett.* **89**, 117901 (2002).
23. D. Vion *et al.*, *Science* **296**, 886 (2002).
24. V. Bouchiat, D. Vion, P. Joyez, D. Esteve, and M. H. Devoret, *Phys. Scr. T* **76**, 165 (1998).
25. Yu. A. Pashkin *et al.*, *Nature* **421**, 823 (2003).
26. C. H. Van der Wal *et al.*, *Science* **290**, 773 (2000).
27. Siyuan Han, Yang Yu, Xi Chu, Shih-I Chu, and Zhen Wang, *Science* **296**, 889 (2002).
28. K. Lehnert *et al.*, *Phys. Rev. Lett.* **88**, 047901 (2002).
29. E. Collin *et al.*, Proc. EUCAS 2003, A. Andreone, R. Cristiano, G. Pepe, and G. Masullo, eds., (IOP publishing, Bristol, U.K., 2004).
30. L. B. Joffe *et al.*, *Nature* **398**, 679 (1999); G. Blatter, V. G. Geshkenbein, and L. B. Joffe, *Phys. Rev. B* **63**, 174 (2001); A. Barone, J. R. Kirtely, F. Tafuri, and C. C. Tsuei, *Phys. Scrip. T* **102**, 51 (2002), and references reported therein.
31. V. B. Geshkenbein, A. I. Larkin, and A. Barone, *Phys. Rev. B* **36**, 235 (1987), and references reported therein.
32. M. Sigrist and T. M. Rice, *J. Phys. Soc. Jpn.* **61**, 4283 (1992); *Rev. Mod. Phys.* **67**, 503 (1995).
33. D. J. van Harlingen, *Rev. Mod. Phys.* **67**, 515 (1995).
34. C. C. Tsuei and J. R. Kirtley, *Rev. Mod. Phys.* **72**, 969 (2000).
35. F. Lombardi *et al.*, *Phys. Rev. Lett.* **89**, 207001 (2002).
36. C. C. Tsuei *et al.*, *Phys. Rev. Lett.* **73**, 593 (1994); J. Mannhart *et al.*, *Phys. Rev. Lett.* **77**, 2782 (1996); H. Hilgenkamp, J. Mannhart, and B. Mayer, *Phys. Rev. B* **53**, 14586 (1996); H. J. H. Smilde *et al.*, *Phys. Rev. Lett.* **88**, 057004 (2002); V. Z. Kresin, *Pair Correlations in Many-Fermion Systems*, Plenum Press (1998).
37. K. A. Müller, *Philosophical Magazine Lett.* **82**, 279 (2002); F. Iachello, *Philosophical Magazine Lett.* **82**, 289 (2002).
38. A. Barone, ed., *Principles and Applications of Superconducting Quantum Interference Devices*, (World Scientific, Singapore, 1992); see also J. Clarke, in "SQUID," Scientific American, 1994.
39. S. Della Penna and G. L. Romani, in *Proceedings of the EUCAS 2004*, A. Andreone, R. Cristiano, G. Pepe, and G. Masullo, eds. (IOP Publishing, Bristol, UK, 2003).
40. W. J. Jenks, S. S. H. Sadeghi, and J. P. Wikswo, *J. Phys. D* **30**, 293 (1997); J. Clarke and R. H. Koch, *Science* **242**, 217 (1988).
41. J. Clarke, *IEEE Trans. Mag.* **19**, 288 (1983).
42. H. Weinstoch, ed., in *Proceedings of NATO ASI, Nato Sciences Series: E 365* (Kluwer Academic, Dordrecht, 2000); *IEEE Trans. Appl. Sup.* **13**, 2 (2003); *Supercond. Sci. Technol.* **16**, 12 (2003).
43. A. Barone, *Nucl. Phys. B* **44**, 645 (1995); *J. Supercond.* **13**, 809 (2000); A. Barone *et al.*, *Int. Conf. Toward the controllable quantum states*, H. Takayanagi and J. Nitta, eds. (World Scientific, Singapore, 2002).
44. C. Nappi and R. Cristiano, *Appl. Phys. Lett.* **70**, 1320 (1997); R. Cristiano *et al.*, *Appl. Phys. Lett.* **74**, 3389 (1999).
45. M. P. Lissitski *et al.*, *Appl. Phys. Lett.* **84**, 5464 (2004).
46. A. Barone, F. Esposito, C. J. Magee, and A. C. Scott, *Riv. Nuovo Cimento* **1**, 227, (1971).
47. A. Davidson, B. Duellhom, B. Kryger, and N. F. Pedersen, *Phys. Rev. Lett.* **55**, 2059 (1985). For a recent account see: C. Nappi, M. P. Lissitskiy, G. Rotoli, R. Cristiano, and A. Barone *Phys. Rev. Lett.* **93**, 187001 (2004).
48. A. Wallraff, A. Lukashenko, J. Lisenfeld, A. Kemp, M. V. Fistul, Y. Koval, and A. V. Ustinov, *Nature* **425**, 155 (2003).
49. A. Kemp, A. Wallraff, and A. V. Ustinov, *Phys. Status Solid: B* **233**, 472, (2002).
50. F. Gaitan and S. R. Shenoy, *Phys. Rev. Lett.* **76**, 4404 (1996).
51. R. Monaco, J. Mygind, and R. J. Rivers, *Phys. Rev. B* **67**, 104506 (2003); E. Kavoussanaki, R. Monaco, and R. J. Rivers, *Phys. Rev. Lett.* **85**, 3452 (2000); C. Nappi, R. Cristiano, M. P. Lissitski, R. Monaco, and A. Barone, *Physica C* **367**, 241 (2002), and references reported therein.
52. A. Barone and S. De Stefano, *Nucl. Instr. Met. Phys. Res.* **202**, 513 (1982).
53. E. Esposito, M. Ejrnaes, S. Pagano, D. Perez de Lara, and R. Cristiano, *Appl. Phys. Lett.* **82**, 2109 (2003).
54. C. Beck and M. C. Mackey, arxiv: astro-ph/0406504 (2004).
55. R. H. Koch, D. van Harlingen, and J. Clarke, *Phys. Rev. Lett.* **45**, 2132 (1980).
56. M. Tinkham, in *Quantum Mesoscopic Phenomena and Mesoscopic Devices in Microelectronics*, I. O. Kulik and R. Ellialtioglu, eds. (Kluwer Academic, The Netherland, 2000), pp. 349–360; *J. Supercond.* **13**, 801 (2000).

Proximity Effect From an Andreev Perspective

T. M. Klapwijk¹

Received August 15, 2004; accepted September 4, 2004

The current understanding of the superconducting proximity effect is reviewed taking into account recent experimental and theoretical results obtained for mesoscopic normal metal-superconductor junctions as well as superconducting weak links. Although known for 40 years the phenomenon remained poorly understood. Current insights are the result of theoretical developments leading to the nonequilibrium quasiclassical theory, getting experimental access to proximity structures on a submicron scale as well as by combining it with the knowledge developed in the 80s on quantum transport in disordered and ballistic systems.

KEY WORDS: proximity-effect; Andreev reflection; mesoscopic superconductivity; Michael Tinkham.

1. INTRODUCTION

The proximity-effect is a well-known phenomenon in superconductivity and part of the standard vocabulary. A summary of early work [1] starts with the following defining line: *If a normal metal N is deposited on top of a superconductor S, and if the electrical contact between the two is good, Cooper pairs can leak from S to N.* In some cases a more specific analysis has emerged in particular for tunnel-junctions using a NS double-layer as one electrode [2], which has also entered the standard niobium junction technology [3]. Nevertheless, despite its familiarity, the subject hardly appears in textbooks on superconductivity. In an often-used textbook written by Tinkham, *Introduction to Superconductivity* [4] one finds, searching the index for *proximity effect*, a single sentence: *in which Cooper pairs from a superconducting metal in close proximity diffuse into the normal metal.* According to the author [private communication] a more extensive treatment of the subject is absent because in his view the phenomenon remained poorly understood. Another textbook by Waldram [5] puts the subject in a Chapter titled *Further theory and properties* in a paragraph *The proximity effect*. Interestingly, this paragraph is followed by one with the title *Andreev reflection* although no

connection is made between the two topics. Due to the more recent studies of transport in mesoscopic structures it has now become common wisdom that Andreev reflection and the proximity effect are intimately connected and certainly not two distinct phenomena [6]. The most-cited research paper of Tinkham [7], coauthored with G. E. Blonder and the present author, is on the subject of Andreev reflections. In a recent citation-study [8] this article appears as “hot,” meaning that it has been cited at a remarkable rate in the past few years and belongs to a group of which some soon might join the top-100 citation-impact articles. Within this context it seems appropriate to use this celebratory occasion to summarize some recent work on the proximity-effect from an Andreev perspective.

In retrospect a number of developments have contributed to the present level of understanding. First, in the 80s a substantial body of knowledge has been developed on quantum coherent transport in disordered normal systems. It has elucidated the role played by the Thouless length and the inelastic scattering length. Conductors have been studied which are small compared to those length scales even down to the Fermi wavelength. The crucial role is played by the single particle phase and the correlation between electrons in the disordered systems. Secondly, various experiments have been performed which probe the penetration of the superconducting properties on submicron length scales and objects are

¹Kavli Institute of Nanoscience, Faculty of Applied Sciences, Delft University Technology, Delft, The Netherlands.

constructed which are smaller than the characteristic lengths. Thirdly, various successful attempts have been made to bridge the gap between the heavy theoretical framework of the quasi-classical equations and the more accessible conceptual framework based on transmission matrices which assists experimentalists in designing and interpreting their experiments.

The aim of this contribution is to sketch a development since the original Blonder-Tinkham-Klapwijk article from ballistic Andreev toward diffusive normal metal-superconductor systems. On our way we highlight a few conceptually important experimental results. We apologize that the selection has some personal bias. To correct for that extensive reference is made to a number of important recent review articles. We hope that this contribution can serve as an introduction to the subject to newcomers in the field. We close with a historical note.

2. EARLY KNOWLEDGE

Most of the early knowledge about the proximity effect has been summarized by Deutscher and De Gennes [1] in 1969. It is based on the theoretical treatment developed by De Gennes [9,10] valid close to the critical temperature. In Fig. 1 the results are shown for two different NS interfaces and for a so-called SNS contact. On the vertical axis the pair

potential $\Delta(\vec{r})$ is shown defined as:

$$\Delta(\vec{r}) = V_N F(\vec{r}) = V_N \langle \psi(\vec{r} \uparrow) \psi(\vec{r} \downarrow) \rangle \quad (1)$$

with $F(\vec{r})$ the condensation amplitude, the probability amplitude of finding two electrons in the condensed state at a point \vec{r} and V_N the electron-electron interaction constant which may be either negative (repulsive) or positive (attractive). Obviously, Fig. 1 shows that $\Delta(\vec{r})$ is expected to have a finite value in N and is depressed in S. The full normal state value of $\Delta = 0$ and the full superconducting state of $\Delta = \Delta_0$ are recovered far away from the interface over some characteristic length.

The basic experimental facts on a NS interface are:

- The observation that the critical temperature of a bilayer of a low T_{cl} superconductor such as Al and a higher T_{ch} superconductor, such as Pb, gradually increases from T_{cl} to T_{ch} with increasing thickness of the Pb on the Al film. The same experiment could be done with a fully normal metal such as Cu covered by Pb. The effectiveness of the proximity effect could be influenced by adding magnetic impurities to the normal metal.
- The second observation regards tunneling experiments through which one can measure the excitation spectrum in a normal metal N backed by a superconducting film S.
- The third observation is the Meissner effect which accounts for the diamagnetic screening realized by a “proximitized” normal metal.

An additional body of knowledge results from the Josephson-effect. It has already been shown by De Gennes [9] in 1964 that as a consequence of the proximity-effect a supercurrent should flow through a normal metal of thickness d_N . The maximum supercurrent carried by such a normal metal would depend exponentially on thickness with the normal metal coherence length ξ_N as the characteristic length scale. This prediction has been confirmed in early experiments by Clarke [11] including its relationship to the Josephson-effect [12]. However, unlike the Josephson-effect in tunnel junctions, a detailed comparison with the microscopic theory has only been made recently [13]. This is partially due to lack of practical interest. Josephson junctions based on SNS junctions have a relatively low impedance, far below 1Ω , and are not very useful in any practical application where usually $50\text{-}\Omega$ impedances are required.

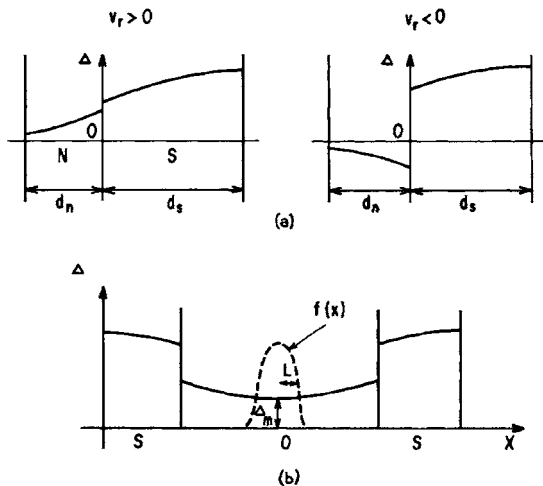


Fig. 1. Figure taken from DeGennes [9]. Spatial dependence of the pair potential $\Delta(x)$ at temperatures close to the critical temperature in a NS sandwich (a) and in an SNS junction (b). For the NS sandwich two cases, one for a repulsive and one for an attractive electron-electron interaction in N are shown (we ignore the $f(x)$ curve).

Due to the recent advances in microfabrication-techniques these experimental systems are much more accessible.

A more fundamental reason is that the original proximity-effect theory was much too simple. An SNS junction forms a problem of inhomogeneous superconductors. A current is driven from S to N and *vice versa* and high-frequency time-dependent processes may take place. In the early 60s one relied on the full Gorkov equations or used the simplified version of the Ginzburg-Landau equations only valid close to T_c . Subsequent theoretical developments have provided a much more advanced theoretical framework [14]. The equilibrium theory, known as the quasi-classical equations, was developed by Eilenberger [15] and for dirty superconductors by Usadel [16]. In this approach it is assumed that all relevant variations occur on a length scale larger than the Fermi wavelength. Hence, dependences on the scale of the Fermi wavelength can be averaged out. Usadel simplified the equations further by assuming that the system is dirty and impurity-averaged Green's functions can be defined.

This approach came to its full maturity in the early 70s to describe transport problems and time-dependent processes by Larkin and Ovchinnikov [17–19], Eliashberg [20], and Schmid and Schön [21]. We will refer to this theoretical approach as the “quasi-classical theory,” also when it includes the nonequilibrium version. In its application to inhomogeneous problems, such as the proximity-effect, these equations have to be supplemented by suitable boundary conditions. An example are those introduced by Zaitsev [22].

Many of the experimental problems studied recently can be understood with the help of the quasi-classical equations. However, some of these problems, in particular those where one could assume, ballistic electron transport could be understood more readily by using the Bogoliubov-De Gennes equations and using the concept of Andreev reflection [23]. The current understanding of the proximity effect focuses on the following aspects. At the boundary between a normal metal and a superconductor Andreev reflection occurs. In this process electrons above the Fermi level are converted into holes below the Fermi level and a Cooper pair is formed inside the superconductor. This is one crucial ingredient of the proximity effect and describes how the two electronic reservoirs are communicating at the boundary itself. The second ingredient is how in the normal metal this electron-hole pair loses

its correlated properties. The electron and the hole form phase-conjugated pairs, a property which will be lost at a certain distance from the interface. The proximity-effect is now understood as a process at the interface itself, in essence Andreev reflection, and how this coherence is propagated and lost due to dephasing processes in the normal metal. The latter are in principle identical to processes known from phase-coherent transport in normal metals. However, the presence of disorder in the normal metal influences also the processes at the boundary itself because incident electron waves may make repeated attempts which must be added phase-coherently to find the probability for Andreev reflection. Hence, the proximity effect is on a microscopic level the intimate connection between Andreev reflection at the interface and the phase coherence maintained over a certain length scale in the normal metal.

3. BALLISTIC ANDREEV INTERFACE

As a starting point it is appropriate to recall the results of Blonder *et al.* [7] for a ballistic Andreev interface. The microscopic description of the superconducting state starts with the Bogoliubov-De Gennes equations [11]. The wave-function ψ is defined as a 2-component wavefunction:

$$\psi = \begin{pmatrix} u \\ v \end{pmatrix} e^{\frac{i2Et}{\hbar} + \phi_s} \quad (2)$$

with u and v representing the electron-like ($k > k_F$) and the hole-like ($k < k_F$) component, E the energy with respect to the Fermi-level, and ϕ_s the macroscopic phase of the superconducting state.

The Bogoliubov-De Gennes equations, written in one dimension, are two coupled Schrödinger equations:

$$\begin{aligned} E\psi(x) &= \left(-\frac{\hbar^2}{2m} \frac{d}{dx^2} - \mu \right) u(x) + \Delta(x)v(x) \\ E\psi(x) &= \left(\frac{\hbar^2}{2m} \frac{d}{dx^2} + \mu \right) v(x) + \Delta(x)u(x) \end{aligned} \quad (3)$$

with $\Delta(x)$ the pair potential of Eq. (1) and μ the chemical potential, which serves as a reference for the energy E .

In general Eq. (3) allows for four types of quasiparticle waves for a given energy:

$$\psi_{\pm k^+} = \begin{pmatrix} u \\ v \end{pmatrix} e^{\pm ik^+ x} \quad (4)$$

and

$$\psi_{\pm k} = \begin{pmatrix} u \\ v \end{pmatrix} e^{\pm ik^- x} \quad (5)$$

where ψ is the position space representation of the BCS quasiparticles.

We assume that we will analyze a NS interface at which plane waves arrive from infinity and return to infinity. In addition it will be understood that any real interface of two dissimilar materials will have different Fermi-momenta, leading to an unavoidable electronic mismatch. In addition it is very likely that a practical interface has some level of elastic scattering due to lattice mismatch or excess impurities due to the fabrication process. The consequence is that any interface will have some elastic scattering. In addition we will assume that there is no elastic scattering in the superconductor nor in the normal metal itself and only at the interface. This is modelled by a delta-function potential at the interface: $V(x) = H\delta(x)$. The direction of the particle flow is determined by the group velocity. At the interface the appropriate boundary conditions are continuity of ψ at $x = 0$ i.e. $\psi_S(0) = \psi_N(0)$ and in view of the δ function potential $\hbar/2m(\psi'_S(0) - \psi'_N(0)) = H\psi(0)$, with $\psi'_{S,N}$ the spatial derivatives.

With these assumptions we may distinguish an incident plane wave ψ_{inc} , a reflected wave ψ_{refl} consisting of an electron part due to elastic scattering and a hole part due to interaction with the superconductor, and a transmitted wave ψ_{trans} into the superconductor with two possible solution:

$$\begin{aligned} \psi_{\text{inc}} &= \begin{pmatrix} 1 \\ 0 \end{pmatrix} e^{iq^+ x} \\ \psi_{\text{refl}} &= a \begin{pmatrix} 0 \\ 1 \end{pmatrix} e^{iq^- x} + b \begin{pmatrix} 1 \\ 0 \end{pmatrix} e^{-iq^+ x} \\ \psi_{\text{trans}} &= c \begin{pmatrix} u \\ v \end{pmatrix} e^{ik^+ x} + d \begin{pmatrix} v \\ u \end{pmatrix} e^{-ik^- x} \end{aligned} \quad (6)$$

with

$$\hbar k^\pm = \sqrt{2m}[\mu \pm (E^2 - \Delta^2)^{1/2}]^{1/2} \quad (7)$$

and

$$\hbar q^\pm = \sqrt{2m}[\mu \pm E]^{1/2}. \quad (8)$$

These three waves have to be matched with the given boundary conditions to determine the amplitudes. Working out the algebra the following expressions are found for the amplitudes (with

$$\gamma = u^2 + (u^2 - v^2)Z^2):$$

$$\begin{aligned} a &= \frac{uv}{\gamma} \\ b &= -\frac{(u^2 - v^2)(Z^2 + iZ)}{\gamma} \\ c &= \frac{u(1 - iZ)}{\gamma} \\ d &= \frac{ivZ}{\gamma} \end{aligned} \quad (9)$$

In determining Eqs. (9) it is assumed that the normal state Fermi velocities are identical for N and S. A possible difference is absorbed in the adjustable parameter Z , defined as $Z \equiv H/\hbar v_F$. In the absence of elastic scattering at the interface, $Z = 0$, we observe that both b and d are zero. Hence, the only existing reflection is Andreev reflection, conversion from electron to hole, a condition which can only be realized with two dissimilar materials with identical normal state densities of states. The amplitude depends on the energy since u and v are given by:

$$u^2 = 1 - v^2 = \frac{1}{2} \left\{ 1 + \frac{(E^2 - \Delta^2)^{1/2}}{E} \right\}. \quad (10)$$

This energy-dependence will be one of the important ingredients in understanding the relationship between the proximity-effect and Andreev reflection. The interaction at an interface cannot be represented by single parameter Δ , as in Fig. 1, because the effects at the interface are different for different energies.

A very important discovery of Blonder *et al.* [7] was that the properties of a ballistic Andreev interface can be measured *directly* in pointcontact experiments. In the current concepts of quantum transport a mesoscopic conductor, a scatterer, is distinguished from the equilibrium reservoirs where thermalization and phase-randomization occurs. An early example is the so-called Sharvin pointcontact, in which a short narrow conductor is connected to two large electronic reservoirs. Electrical transport is the difference between electrons originating from a reservoir at voltage V to a reservoir at voltage $V = 0$ and vice versa:

$$I = \frac{G_0}{e} \int_0^\infty dE [f(E) - f(E + eV)] \quad (11)$$

with $f(E)$ the Fermi-function and G_0 a quantity which counts the number of modes depending on the dimensionality of the sample. For 3-dimensional reservoirs connected by a small hole of area S it is

given by:

$$G_0 = \frac{2e k_F^2 S}{h^2 4\pi} \quad (12)$$

with k_F the Fermi momentum. Returning to the important case of a short channel of zero length Eq. (12) is now better known as the multichannel Landauer formula developed for mesoscopic conductors:

$$G_0 = \frac{2e^2}{h} \sum_{n=0}^m T_n \quad (13)$$

with T_n the transmission coefficient per mode n and m the number of modes. Each mode carries a current e/h , the factor 2 takes care of the two different spin directions. Equation (11) follows from the Landauer formula assuming that each mode has a transmission coefficient equal to unity, the number of modes follows from the area S compared to k_F .

The same reasoning used to derive Eq. (11) leads to the current-voltage characteristics for a pointcontact between a normal metal and a superconductor. The probabilities A , B , C , and D are determined from the amplitudes, Eq. (9), and used to calculate their contribution to the currents for a given applied voltage. Hence the current-voltage characteristic is given by:

$$I = \frac{G_0}{e} \int_0^\infty dE [f(E) - f(E + eV)] [1 + A(E) - B(E)] \quad (14)$$

with A the extra current per incident electron wave due to the Andreev process and B the reflected electron current due to elastic scattering. For low temperatures the 1st term in square brackets reduces to a δ -function around eV . Hence, scanning the voltage is also a direct probe of the energy-dependent reflection coefficients:

$$\frac{dI}{dV} = G_{NS} = G_0 [1 + A(eV) - B(eV)] \quad (15)$$

and the conductivity of the pointcontact is a direct measure of the reflection coefficients. Note the similarity with the conventional expression for a NIS tunneljunction in which the 2nd term within brackets is replaced by the BCS density of states, $E/\sqrt{E^2 - \Delta^2}$, in the superconductor. Indeed this term reduces to the BCS density of states for large values of Z i.e. for the tunnelbarrier regime. It is sometimes convenient to re-express the quantity Z in terms of a transmission coefficient for the normal state T_n . Evaluating

Eq. (15) for $\Delta = 0$ one finds for the conductance:

$$G_N = G_0 (1 - B(E)) = G_0 \frac{1}{1 + Z^2} \quad (16)$$

which means that T_n is equal to $1/(1 + Z^2)$ and the conductance in the normal state is given by:

$$G_N = G_0 T_n \quad (17)$$

for finite Z .

In the past 20 years Eq. (14) has been used extensively to study new superconducting materials with pointcontacts. From Eq. (14) one finds the superconducting energy gap allowing for various interface imperfections with the adjustable parameter Z , using the relatively simple technique of a point contact. Previously, the superconducting gap had to be determined by developing a suitable tunnel barrier [2]. The discovery of many new superconducting materials and the pointcontact technique accounts for much of the success of Eq. (14). A recent example is the application to the new superconductor MgB_2 with a critical temperature of 38 K [24,25]. In Fig. 2 temperature-dependent pointcontact conductance measurements are shown for a single-crystal MgB_2 and comparison with Eq. (14) assuming the

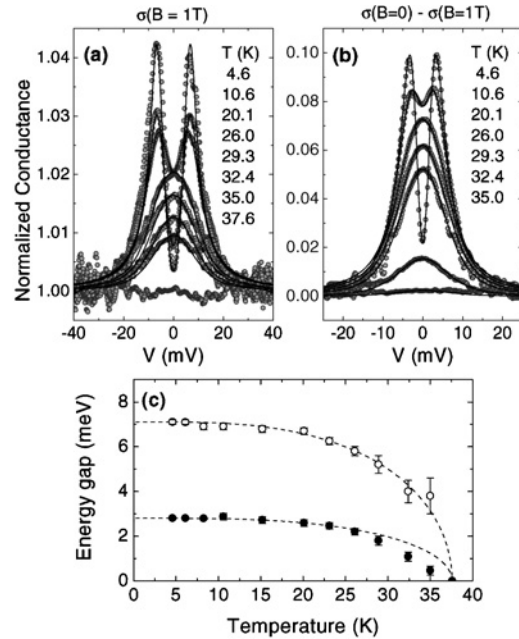


Fig. 2. (a) Temperature dependence of the conductance of a c-axis junction at a magnetic field of 1 T. (b) Comparison of conductance at $B = 0$ T and at 1 T. The full lines are fits to Eq. (14). The bottom panel shows the two energy gaps as a function of temperature. Taken from Ref. [25].

existence of two gaps in different crystal directions. Note the excellent agreement between data and theory over a large temperature range.

A 2nd important extension has been in the field of spin polarization. De Jong and Beenakker [26] pointed out that Andreev reflection should be suppressed at an interface between a ferromagnet and a superconductor. Since one has in general in a ferromagnet both spin-up and spin-down channels and Andreev reflection should still be partially possible and can become a measure of the degree of spin-polarization of a ferromagnet. This was recognized and successfully used by Soulen *et al.* [27] and Upadhyay *et al.* [28]. A further theoretical basis of the technique has been developed by Mazin *et al.* [29].

Clearly, rather than being an artificial model system the ballistic Andreev interface can be accessed directly by point contact spectroscopy. This application has turned out to be very flexible and useful for a large range of new superconducting materials and also useful for the determination of the degree of spin-polarization in ferromagnets or half-metals.

4. SPATIAL EXTENT OF THE ANDREEV PROCESSES

In a point contact geometry it is assumed that the reservoirs are three dimensional. The Andreev interface represents a weak link between the reservoirs. The one-dimensional solution of Eq. (3) can be used provided translational invariance is assumed in the plane parallel to the interface. In addition the choice for this geometry made it acceptable to ignore an important equation which in principle should be added to Eq. (3):

$$\Delta(\vec{r}) = V_N(\vec{r}) \sum_{E>0} v^*(\vec{r}) u(\vec{r}) [1 - 2f(E)] \quad (18)$$

with $\Delta(\vec{r})$ the pair potential which couples the two Schrodinger equations. It is called the self-consistency-equation while it is dependent on the solutions found from Eq. (3). In three-dimensional reservoirs the induced values for u and v are diluted by solutions for the unconnected reservoirs and therefore one can ignore the spatial decay of Δ at both the N and the S-side. In comparison with Fig. 1 Δ is a step-function rising from 0 to a finite bulk-value Δ_0 over a very short distance. To simplify this problem further one can choose the electron-electron interaction constant $V_N = 0$.

However, let us now return to the hypothetical situation of a ballistic system in a true one-dimensional model. The first thing to notice is that Eq. (18) with Eqs. (6) leads to a finite value for Δ in N assuming a finite value for the electron-electron interaction $V_N \neq 0$. For each energy E the coherence gets lost over a characteristic decay length $\hbar v_F/E$. For a given energy E above the Fermi energy E_F the wave vector for the electron $q_e = q_F + \delta k/2$ differs slightly from the Fermi wave vector. The reflected hole also has a slightly smaller value $q_h = q_F - \delta k/2$. The difference in momentum of δk is given by $q_F(E/E_F)$ which leads to a dephasing length depending on energy. Equation 18 clearly shows that to determine the spatial extent of the quantity Δ one needs to know u and v , which both are energy-dependent and the distribution-function. Each energy weighs differently into the sum and therefore one cannot define a characteristic decay length, except for the limit close to the critical temperature [9]. The same applies to the superconducting side, where a gradual rise of Δ is expected but again the energy dependence and the occupation numbers will play a role.

Another quantity of interest is the current carried by quasiparticles. At a normal metal-superconductor interface current carried by quasiparticles is converted into current carried by Cooper-pairs. The charge current carried by Bogoliubov quasiparticles is the sum of the part carried by the electron part u and the part carried by the hole part v :

$$J_Q = \frac{e\hbar}{m} [Im(u^* \nabla u) + Im(v^* \nabla v)] \quad (19)$$

For $E < \Delta$ both k^+ and k^- have small imaginary parts which lead to an exponential decay of the quasiparticle amplitude in the superconductor on a length scale λ given by:

$$\lambda = \frac{\hbar v_F}{2\Delta} \left[1 - \left(\frac{E}{\Delta} \right)^2 \right]^{1/2} \quad (20)$$

of which the leading term is $\hbar v_F/2\Delta \approx \xi(T)$. These evanescent waves carry quasiparticle current, which is taken over by an increasing supercurrent of this energy. To determine the full value of the quasiparticle current the fraction carried by each energy should be taken together with the probability of these states to be occupied.

In closing this section we return to the self-consistency equation. If we assume that in N $V_N = 0$ we will have also $\Delta(\vec{r}) = 0$. However, since we find at any point close to the interface a finite value for

the amplitudes of electrons and holes, we will obtain a finite value for the condensation amplitude F :

$$F = \langle \psi(\vec{r} \uparrow) \psi(\vec{r} \downarrow) \rangle = \sum_{E>0} v^*(\vec{r}) u(\vec{r}) [1 - 2f(E)] \quad (21)$$

which is known as the order parameter or alternatively the ‘‘Cooper pair density.’’ Hence, we find that in the absence of any attractive interaction there is still a finite probability of finding Cooper pairs in N, which is equivalent to stating that the Andreev-reflected electrons and holes maintain phase-coherence over a certain length leading to a finite contribution to F . This is the ‘‘leakage of Cooper pairs’’ alluded to in various textbooks on superconductivity.

5. IMPURITY-SCATTERING AND TRANSMISSION MATRIX APPROACH

In Section 3 the equivalent of a transmission matrix for a quantum-coherent scattering problem was used. A great deal of quantum-coherent transport theory has been developed to understand quantized conductance, Aharonov-Bohm oscillations and universal conductance fluctuations in, for example, metallic rings [30]. In recent years a similar approach has evolved for NS interfaces in which elastic scattering in N occurs. This approach has been developed and summarized by Beenakker [31,32] and Lambert [33]. To appreciate the nature of the problem we recall the early work of Van Wees *et al.* [34].

In Fig. 3 three relevant elements of the geometry are shown. We will assume that the inelastic scattering length L_{inel} is always smaller than the device size. Hence, the single particle phase is conserved

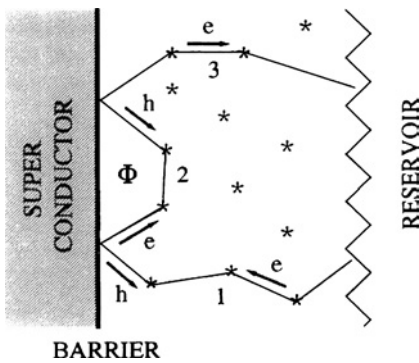


Fig. 3. Interface between a superconductor and a normal metal reservoir separated by a diffusive scattering region and an interface scatterer (barrier). Φ is the applied magnetic flux.

in crossing the object while being scattered by impurities. An equilibrium superconductor is separated from a normal metal by an interface barrier as used in Section 3. In the normal metal a contact is indicated, called a reservoir from which waves will emit and which will absorb waves. The middle region is the scattering region. It is assumed that $\Delta = 0$ ($V_N = 0$). An incident electron wave will scatter from the impurities and eventually reach the interface with the superconductor undergoing Andreev reflection. Since the hole wave is essentially phase-conjugate with the incident electron wave it will retrace the original path. However, since the incident electron wave is also partially reflected as an electron wave impurity scattering might scatter the partial electron wave again to the superconductor and so forth. The scattered wave will be the coherent superposition of the various contributions and since for small energy differences phase coherence is maintained the addition of impurities to the scattering problem of Section 3 is the enhancement of the Andreev reflection probability and hence, enhanced conductance (‘‘reflectionless tunneling’’ [31]). Depending on the path length and the magnetic field a total phase shift of

$$\Delta\phi = \frac{2eL}{\hbar v_F} + 4\pi \frac{BS}{\phi_0} \quad (22)$$

is accumulated with L the path length, B the applied magnetic field, S the enclosed area, and Φ_0 the flux quantum. For increased voltages (increased energies) or applied magnetic field phase coherence is destroyed and the enhanced conductance is suppressed. Such a behavior had been first reported by Kastalsky *et al.* [35]. In calculating the actual conductance an energy-average over the available occupied states is taken. The correlations of these electrons is determined by the Thouless energy $E_{\text{Th}} = \hbar D/L^2$. Or one can define for a particular energy value E a decay length $\Lambda_T = \sqrt{\hbar D/E}$, which is analogous to the phase-correlation length identified in the previous Section, but now for a dirty system. The correlation between an electron and an Andreev-reflected hole in a diffusive system is given by the normal metal coherence length $\xi_N = \sqrt{\hbar D/kT}$ if kT would be the dominant energy.

For small voltages very simple expressions have been derived by Beenakker [31]. For small voltages the probabilities of Section 3 $A(E)$ reduces to $1/(1 + 2Z^2)^2$ and $B(E)$ to $2(1 + Z^2)/(1 + 2Z^2)^2$ and hence

$$G_{\text{NS}} = G_0 \frac{2}{(1 + 2Z^2)^2} \quad (23)$$

which by using our previous observation that $T_n = 1/(1 + Z^2)$ leads to

$$G_{\text{NS}} = G_0 \frac{2T_n^2}{(2 - T_n)^2} \quad (24)$$

Subsequently Beenakker has generalized this expression for any arbitrary scatterer such as a mesoscopic phase-coherent conductor containing elastic impurities:

$$G_{\text{NS}} = \frac{2e^2}{h} \sum_{n=1}^m \frac{2T_n^2}{(2 - T_n)^2} \quad (25)$$

which is a generalization of the Landauer formula to the NS case with T_n the transmission coefficients applicable to the particular distribution of transmission channels.

Evidently, impurity scattering has a strong influence on the Andreev scattering probability and will also lead to a spatial dependence of the Cooper-pair density. It is the result of phase-coherent scattering processes, which interact with a nearby phase-coherent superconductor. An interesting extension has been the introduction of so-called Andreev interferometry. In Fig. 4 an example is shown. A T-shaped phase coherent conductor is connected at the two ends of the T-bar with a superconductor. The superconductor is part of a loop, which allows the application of a well-defined macroscopic phase-difference at both ends of the T-bar. In the Andreev reflection process the macroscopic superconducting phase ϕ_s appears. The transmitted wave in Eq. (2)

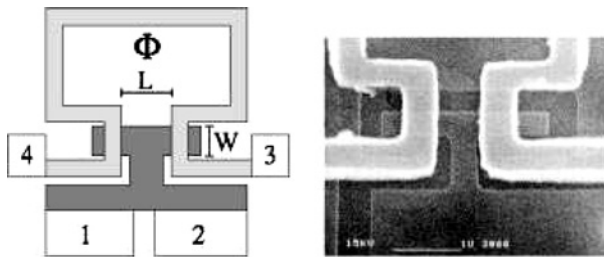


Fig. 4. At the left hand side a schematic picture of a T-shaped 2-dimensional electron gas with an interrupted superconducting niobium loop. The contacts 1 and 2 are connected to the T-shaped conductor and the contacts 3 and 4 to the superconducting niobium loop. The indicated dimensions L and W are $0.7 \mu\text{m}$ and $0.3 \mu\text{m}$ respectively. The right hand side picture shows a scanning electron microscope image of the actual device. Taken from Den Hartog *et al.* [36]

should read:

$$\psi_{\text{transm}} = c \begin{pmatrix} ue^{i\phi_{s1}} \\ v \end{pmatrix} e^{ik^+x} + d \begin{pmatrix} ve^{i\phi_{s1}} \\ u \end{pmatrix} e^{-ik^-x} \quad (26)$$

and analogously for the 2nd superconductor with ϕ_{s1} replaced by ϕ_{s2} . Consequently, the reflected wave amplitude a and b carry the information of the superconducting phase. The diffusive scattering leads to coherent superposition of wavelets which interact with both superconductors and the conductance will depend on their phase-difference $\phi_{s1} - \phi_{s2}$. Den Hartog *et al.* [36] observed a conductance which depends on the macroscopic phases of the superconducting loop, changed by the enclosed magnetic field. The amplitude of these Aharonov-Bohm oscillations is shown in Fig. 5. With increasing magnetic field the main contribution decays until a field of about 120 G is reached. Subsequently a random fluctuating amplitude continues to be visible up to the highest field measured. These two regimes mark the difference between ensemble-averaged and sample-specific resistance oscillations, which have been discussed in detail by Beenakker [31].

Andreev-interferometry has also been used to identify a phase coherent contribution to the conductance in normal metal-superconductor tunnel junctions. For low values of the transmission coefficient the conductance at low voltages or the subgap

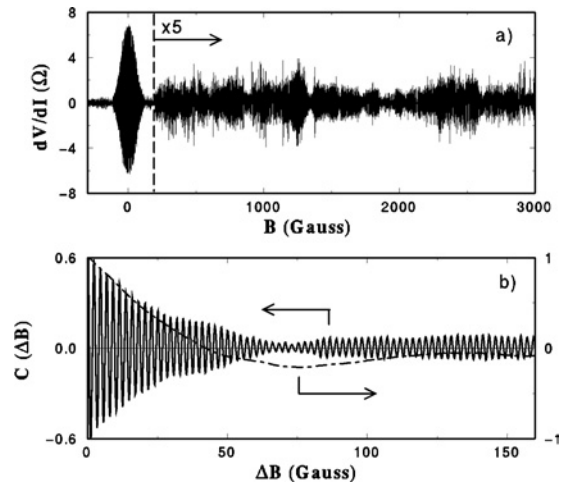


Fig. 5. (a) Magnetoresistance $R_{13,24}$ minus the background resistance at $T = 50 \text{ mK}$. (b) Autocorrelation function $C(\Delta B) \equiv \langle \delta R(B)\delta R(B + \Delta B) \rangle / \langle \delta R(B)^2 \rangle$ between 200 and 3000 G for the Andreev-mediated conductance oscillations of the trace shown in (a) (solid line) and for the fluctuations in the background resistance (dashed line). Taken from Den Hartog *et al.* [36].

current in a tunnel junction is small. An Andreev component will be present, although small since it is 2nd order in the transmission coefficient. Hekking and Nazarov [37] recognized that the probability for these 2nd order processes would depend on the impurity scattering in the metals used in the experiments. Pothier *et al.* [38] studied two closely spaced NIS tunneljunctions with the S electrodes connected by a superconducting loop. They demonstrated that the subgap current has a contribution which depends on the applied magnetic flux, which therefore could be identified as the Andreev-contribution, in perfect agreement with the theory of Hekking and Nazarov.

6. DIFFUSIVE USADEL-EQUATIONS

The previous Sections have demonstrated that a full understanding of the interactions between a normal metal and a superconductor must face the *spatial dependence*, the *energy dependence*, the *impurity scattering*, the *dependence on the macroscopic superconducting phase*, and on the *occupation-numbers*. This theoretical complexity is dealt with in the theory of nonequilibrium superconductivity based on impurity averaged Green's functions. A relatively accessible introduction has been developed by Estève *et al.* [39,40]. Further details of this approach can also be found in Guéron [41] and Anthore [42].

Rather than by using two-component plane waves with u and v , the diffusive superconducting state is described by the impurity-averaged Green functions introduced by Usadel [16]: \hat{g}_S^R , \hat{g}_S^A and \hat{g}_S^K . The first two, \hat{g}_S^R , and \hat{g}_S^A describe the equilibrium states of the system, whereas the third one \hat{g}_S^K describes the occupation of the states. A convenient way to proceed with these quantities, first introduced by Nazarov [43], is the parameterization by two complex parameters $\theta(x, E)$ and $\varphi(x, E)$, both being position dependent and energy dependent. Each of the functions \hat{g}_S^R and \hat{g}_S^A is now given by:

$$\hat{g}_S^R = \begin{pmatrix} \cos \theta & \sin \theta e^{i\varphi} \\ \sin \theta e^{-i\varphi} & -\cos \theta \end{pmatrix} \quad (27)$$

and

$$\hat{g}_S^A = \begin{pmatrix} -\cos \theta^* & \sin \theta^* e^{i\varphi^*} \\ \sin \theta^* e^{-i\varphi^*} & \cos \theta^* \end{pmatrix} \quad (28)$$

where $\theta(x, E)$ represents the complex superconducting order and $\varphi(x, E)$ is an energy-dependent super-

conducting phase. The third (Keldysh) function \hat{g}_S^K is given by:

$$\hat{g}_S^K = \hat{g}_S^R \hat{h} - \hat{h} \hat{g}_S^A \quad (29)$$

with the distribution matrix \hat{h} defined as:

$$\hat{h} = \begin{pmatrix} 1 - 2f_e & 0 \\ 0 & 2f_h - 1 \end{pmatrix} \quad (30)$$

with f_e and f_h the distribution functions for electrons and holes.

Once $\theta(x, E)$ and $\varphi(x, E)$ are known a set of expressions can be used to determine several quantities characteristic for the superconducting state. The density of states follows from:

$$n(x, E) = N(0) \text{Re}[\cos \theta(x, E)] \quad (31)$$

with $N(0)$ the density of states in the normal state. For a normal metal $\theta = 0$ and for a bulk superconductor $\sin \theta_{\text{BCS}}(E) = \Delta / \sqrt{\Delta^2 - E^2}$. As argued by Estève *et al.* [39] $\text{Im}[\sin^2 \theta]$ can be interpreted as an effective energy dependent pair density.

Finally, the self-consistency equation for $\Delta(x)$ depends on θ and φ according to:

$$\Delta(x) = N(0) V_N \int_0^{\hbar\omega_D} dE \tanh \frac{E}{2k_B T} \text{Im}(\sin \theta) e^{i\varphi} \quad (32)$$

which can be compared to Eq. (18).

For a normal metal-superconductor interface θ follows from solving the Usadel-equation:

$$\frac{\hbar D}{2} \nabla^2 \theta + \left(iE - \frac{\hbar}{\tau_{\text{sf}}} \cos \theta \right) \sin \theta + \Delta(x) \cos \theta = 0 \quad (33)$$

allowing for spin-flip scattering. In N it is assumed that $\Delta = 0$ with no electron-electron interaction, whereas in S $\Delta(x)$ is given by Eq. (32).

6.1. Induced Local Density of States

This analysis has been performed by Guéron *et al.* [44] and applied to experimental results. Figure 6 shows a superconducting wire (aluminium) connected to a normal wire (copper). The contacts labeled F_1 , F_2 , and F_3 are tunnelcontacts, which enable the measurement of the local density of states of Eq. (31).

Experimental results are shown in the upper panel of Fig. 7. The inset shows, for reference, a standard BCS density of states measurement. In the lower panel the results from the Usadel theory are

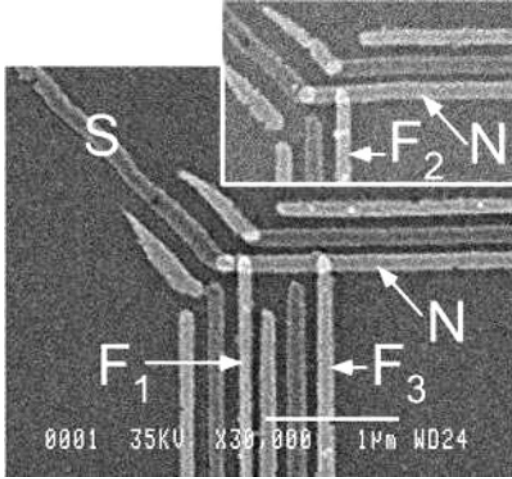


Fig. 6. SEM photograph of a sample used by Guéron *et al.* [44] to measure the local density of states in a normal metal in contact with a superconductor. F_1 , F_2 , and F_3 are tunnel junctions to measure the density of states.

shown. These results clearly show how the pairing-correlations manifest themselves over a length of about $1 \mu\text{m}$ and are visible in the density of states. In this experiment, in which equilibrium properties are measured the agreement between theory and experiment is strikingly good.

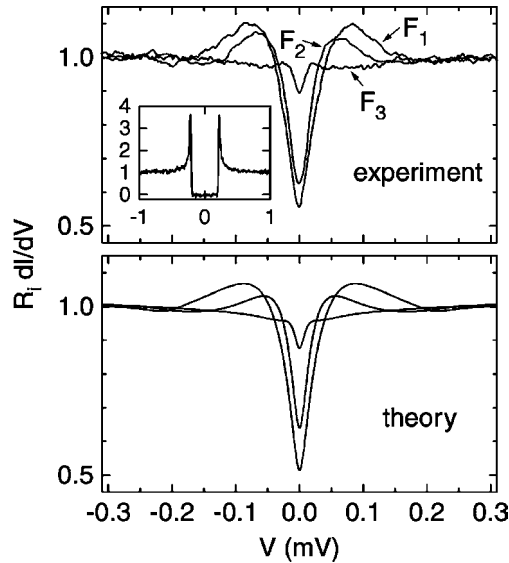


Fig. 7. Differential conductance of the tunnel junctions at the locations F_1 , F_2 , and F_3 . The inset shows the differential conductance of a reference tunnel junction on a BCS superconductor. The lower panel shows the calculated density of states, assuming a small degree of spin flip scattering in the normal metal. Taken from Guéron *et al.* [44].

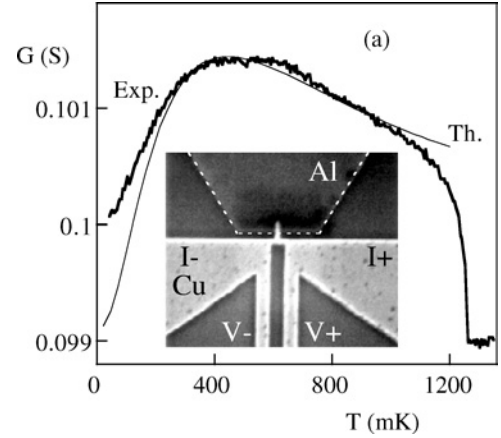


Fig. 8. Conductance of a normal metal wire in direct contact with a superconductor. Upon approaching $T = 0$ the full normal resistance is reestablished. The inset shows the actual sample. Taken from Ref. [45].

6.2. Reentrant Resistance

The position-dependent density of states implies that the normal metal wire has properties reminiscent of a superconductor. It is natural to expect that a normal wire in contact with a superconductor will with decreasing temperature become gradually less resistive. An example of such an experiment is shown in Fig. 8, which clearly shows counterintuitive non-monotonous behavior. A short normal metal wire of copper is attached to the superconductor aluminium. At the T_c of aluminium the conductance increases sharply reaching a maximum around 400 mK and then decreasing again. This reentrant resistivity was first pointed out by Artemenko *et al.* [46] and more recently treated by Stoof and Nazarov [47,48].

Transport is a nonequilibrium problem, which means that the occupation-numbers f_e and f_h need to be determined. In terms of θ (θ_1 and θ_2 are the real and imaginary part, respectively) the following equations need to be solved:

$$\nabla[\cos^2\theta_1 \nabla f_{\text{odd}}] = 0 \quad (34)$$

and

$$D\nabla[\cosh^2(\theta_2) \nabla f_{\text{even}}] - 2\delta f_{\text{even}} \text{Re}[\sin\theta] = 0 \quad (35)$$

in which f_{even} and f_{odd} represent the symmetric and asymmetric parts of the distribution-function. The 2nd term in Eq. (35) is only present in a superconductor and is needed when there is conversion from normal current to supercurrent (Section 6.3). In N the

normal current is given by:

$$J_N(x) = \frac{\sigma}{e} \int_0^\infty dE \nabla f_{\text{even}} \cosh^2(\theta_2) \quad (36)$$

which determines the conductivity for a given voltage. The result of such a calculation is shown in Fig. 8.

6.3. Resistance of the Superconductor Near the Interface

In Section 4 the decay of quasiparticle waves in a superconductor appeared. These evanescent waves can scatter from elastic impurities and contribute to a finite resistance of the superconducting wire. We have recently studied this resistive contribution [49]. We chose to study samples (Fig. 9) made of superconducting (S) aluminium (Al) because of its long coherence length. Thick and wide normal (N) contacts are used with a negligible contribution to the normal state resistance. To minimize interface resistances due to electronic mismatch of both materials bilayers of aluminium covered with thick normal metal (Cu) are used. In such a geometry the superconducting aluminium wire is directly connected to normal aluminium.

Figure 10 shows typical $R - T$ measurements. Samples with different RRR values show qualitatively identical behavior. All wires show a finite remaining resistance down to low temperatures as the most striking result. Similar results have been obtained by Siddiqi *et al.* [50] in studying hot-electron bolometers. Obviously, despite the differences in

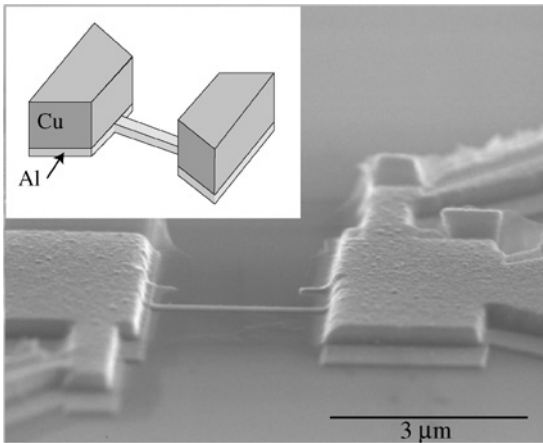


Fig. 9. SEM picture of a device (slightly misaligned), showing the coverage of the thin aluminium film with the thick Cu layer (except for one the measured devices are carefully lined up). The inset shows a schematic picture of an ideal device.

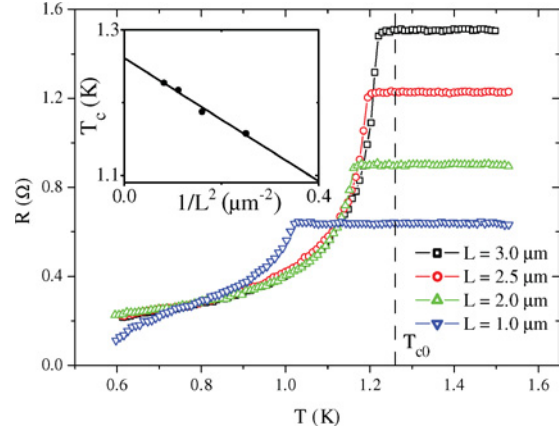


Fig. 10. Measured $R - T$ curves for four different bridge lengths. The intrinsic T_{c0} is indicated by the vertical dashed line. The inset shows the measured critical temperature of the wire vs. $1/L^2$, which is used to determine T_{c0} by letting $L \rightarrow \infty$.

length, the resistances at low temperatures have identical values and follow the same trace. It indicates that the origin of this remaining resistance is due to the region in the S-wire attached to the interface with the normal reservoir. The resistance at 600 mK is equal to a normal segment of the superconductor with a length of about 200 nm. Given the resistivity of the superconductor the coherence length $\xi = \sqrt{(\hbar D)/(2\pi k_B T_c)} = 124$ nm. Figure 10 (Inset) also shows that the critical temperature of the wire decreases linearly with increasing the inverse square of the wire length, as expected from a straightforward Ginzburg-Landau analysis.

Since the studied nanowires show diffusive transport the Usadel equations should apply to the system. It is convenient to calculate the normal current for a given applied voltage difference (assuming linear response). The strength of the pairing interaction, the proximity angle θ is determined by solving Eq. (33) together with the self-consistency equation Eq. (32). The density of states as a function of position is determined with Eq. (31).

Our main interest is the question how the current conversion process contributes to the resistance. First of all, the presence of decaying normal electron states suppresses the gap in the density of states.

In Fig. 11, the calculated density-of-states $N_1(E) = n(E)$ is shown given for several positions along the wire of $L = 2 \mu\text{m}$, $D = 160 \text{ cm}^2/\text{s}$, $\Delta_0 = 192 \mu\text{eV}$, and $T/T_c = 0.4$. Clearly, moving away from the normal contacts the density of states resembles more and more the well-known BCS density of states. Note however, that a finite subgap value

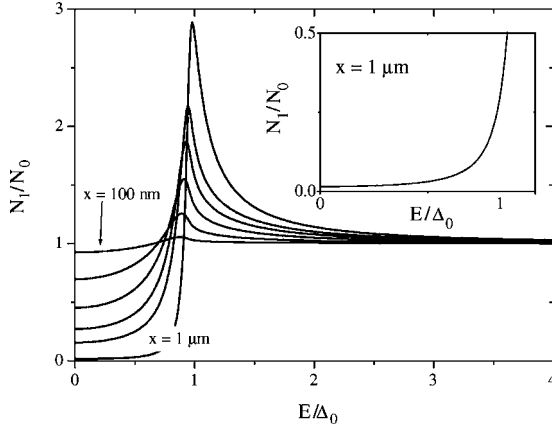


Fig. 11. The calculated density-of-states N_1 at various distances from the reservoirs ($x = 100, 200, 300, 400, 500, 1000$ nm) for a $2\text{-}\mu\text{m}$ long wire ($t = 0.4$, $D = 160$ cm^2/s and $\Delta_0 = 192$ μeV). Note the exponentially small but finite subgap density-of-states in the middle (at $x = 1$ μm ; see inset).

remains in the middle ($x = 1$ μm) even for very long wires. This is an intrinsic result for any NSN system.

The normal current in S is found using Eq. (36) with the distribution function determined from the Boltzmann-like Usadel equation Eq. (35). The applied voltage V , is taken into account via the boundary conditions for Eq. (35):

$$\delta f(0, L; E) = \frac{\pm eV/2}{4k_B T \cosh^2(E/2k_B T)}. \quad (37)$$

Hence, the normal metal leads are taken as equilibrium reservoirs.

The local voltage is calculated using:

$$eV(x) = \int_0^L dE f_{\text{even}}(E, x) \text{Re}[\cos \theta(x, E)] \quad (38)$$

In Fig. 12, we show the results of such a calculation as a function of position along the wire for two different temperatures: $t = 0.4$. and $t = 0.9$ with $D = 160$ cm^2/s , and $\Delta_0 = 192$ μeV . At the temperature close to the transition temperature, the electric field penetrates the sample completely and the resistance is close to the normal state value. At low temperatures, the electric field still penetrates the superconductor over a finite length, leaving a middle piece with hardly any voltage drop. The penetration length is of the order of the coherence length. The inset shows the position dependent normal currents (full line) and supercurrents (dashed line) illustrating the current conversion processes.

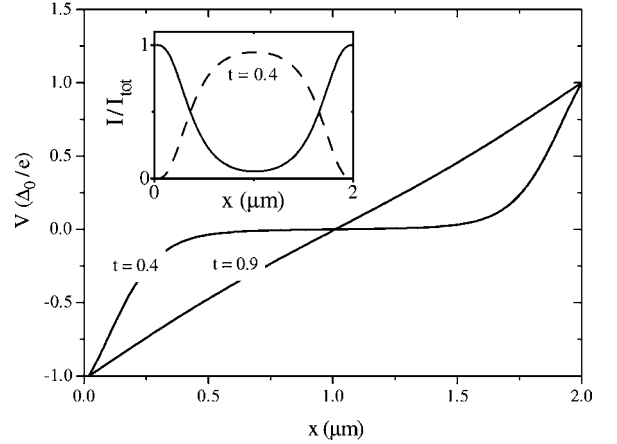


Fig. 12. The voltage in the superconducting wire as a function of position for two different temperatures ($t = 0.4$ and 0.9). At $t = 0.9$ the wire behaves as a normal metal and for $t = 0.4$ the voltage is clearly present to a depth ξ (wire length 2 μm with $D = 160$ cm^2/s and $\Delta_0 = 192$ μeV). The inset shows the position dependent normal currents and supercurrents.

In Fig. 13, a comparison is made between the calculated resistance as a function of temperature and the measurement for a $L = 2$ μm wire. The calculation is done with parameters $D = 160$ cm^2/s , as determined from the impurity resistivity, and $\Delta(0) = 1.764 k_B T_c = 192$ μeV with $T_c = 1.26$ K determined from the length dependence. Without any fitting parameter, the agreement between the model (dots) and the experiment (data points: open symbols) is

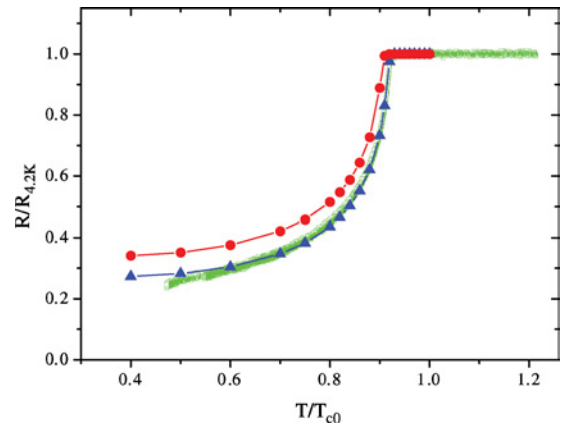


Fig. 13. The measured $R - T$ curve for the $2\text{-}\mu\text{m}$ bridge together with the model calculation using the boundary condition $\theta(x = 0, L) = 0$ (dots), and using the boundary condition $\partial_x \theta(x = 0, L) = \theta(x = 0, L)/a$ (triangles) with $a = 75$ nm. The value for $T = 0$ is found from Eq. (8) to be 0.323 and numerically 0.3255 for the hard boundary conditions (dots). For the soft boundary conditions we have numerically 0.2609 (triangles).

encouragingly good. Only at the lower temperatures the observed resistance is slightly less than the theoretically predicted values. The most likely cause is that the rigid boundary conditions imposed at the interfaces should be relaxed. There is a finite possibility for superconducting correlations to extend into the normal metal reservoirs, which would mean that the boundary condition $\theta(x=0, L) = 0$ is too rigid. Since the correlations will extend into a 3-dimensional volume we assume that using the boundary conditions $\partial_x \theta(x=0, L) = \theta(x=0, L)/a$ *i.e.* a decay over a fixed characteristic length a , is a realistic assumption. It assumes a geometric dilution of the correlations. The result is shown in Fig. 13 by filled triangles. The best agreement between measurement and calculation model is obtained for $a = 75$ nm. This value appears reasonable for a decay length since it is comparable to the dimensions (100 nm \times 250 nm) of the wire which emits into the reservoirs.

7. BALLISTIC SUPERCURRENTS

In Section 2 it was pointed out that DeGennes [9] in 1964 recognized that a Josephson supercurrent could flow through a normal metal sandwiched between two superconductors. The strength of the Josephson supercurrent was found to be exponentially dependent on the length reflecting the finite correlation length for penetrating Cooper pairs. In some of the experiments described above two superconductors were used to perform Andreev-interferometry and by doing that it was demonstrated that the normal conductance has a component which is phase-dependent. However, a phase-coherent component should be the Josephson-current. Apparently the normal conductance discussed so far can be studied without having to consider the supercurrent. The reason is that the characteristic length L_T plays its role differently. The supercurrent decays exponentially with L_T , whereas the conductance is proportional to L_T . If the length of the normal domain is short enough the supercurrent will appear. For larger lengths only the phase-coherent normal conductance is observable. Experimentally, this dependence has been clearly demonstrated in experiments by Dimoulas *et al.* [51] and in subsequent work.

In the spirit of Section 3 the supercurrent through SNS systems has been studied by starting with the concept of Andreev reflections. The early work was based on a normal domain free of any elastic scattering, a condition reachable in cur-

rent 2-dimensional semiconductors. The early work was done by Kulik [52], Ishii [53], and Bardeen and Johnson [54]. It is assumed that we have perfect interfaces between N and S leading to perfect Andreev-reflection at the interfaces *i.e.* determined by Eq. (9) and Eq. (26) with $Z = 0$. For simplicity a one-dimensional system is assumed. Because of the finite length of N discrete energy levels are formed.

For $E < \Delta$ the continuity conditions for the wavefunctions and their derivatives at $x = \pm L/2$ we obtain the dispersion relation:

$$\exp(2i\alpha(E)) \exp[i(k^+ - k^-)L] \exp(\pm i\phi) = 1 \quad (39)$$

where k^+ and k^- are the wave vectors of the electron and the hole respectively. The phase-factor ϕ is equal to the differences of the macroscopic phases of the two superconductors ($\phi_{s1} - \phi_{s2}$). The energy-dependent phase factor $\alpha(E)$ is given by $\arccos(E/\Delta)$. Since the considered energy E is usually much less than the Fermi-energy, the energy eigenvalues can be calculated by using the relation $\hbar\delta k = \hbar(k^+ - k^-) = 2E/v_F$. Under this condition the dispersion relation becomes:

$$E_n^\pm = \frac{\hbar v_F}{2L} [2(\pi n + \alpha) \pm \phi], \quad n = 0, 1, 2, \dots \quad (40)$$

If we specify for the case of low energies $E \ll \Delta$ we find:

$$E_n^\pm = \frac{\hbar v_F}{2L} \left[2\pi \left(n + \frac{1}{2} \right) \pm \phi \right] \quad (41)$$

Hence we have a set of equally spaced energy levels until the levels approach Δ . Note that the position of the energy level is set by the phase difference ϕ .

In recent years this approach has been extensively studied for the limit of very short contacts. The availability of mechanical break junctions has led to very detailed studies of both the supercurrent as well as the voltage carrying state in single-atom point contacts [55]. These junctions consist of adjustable point contacts in which the distance between the outermost atoms can be adjusted with a precision in the order of 0.001 Å. It has therefore become feasible to study continuously the transition from tunneling to metallic contact in superconducting junctions. These ballistic contacts are short compared to $\xi_0 = \hbar v_F/\Delta_0$. Since we are weakly connecting two bulk superconductors the contact-region itself can be viewed as a normal metal part. Hence, the dispersion relation (Eq. (39)) has only one solution within the bound $E < \Delta$:

$$\alpha = \arccos(E/\Delta) = \pm(\phi/2) \quad (42)$$

which leads to the very simple relation that

$$E = \pm \Delta \cos(\phi/2) \quad (43)$$

All these expressions have been derived for the case that elastic scattering is negligible. Beenakker [56] has extended this approach to the case with finite transmission eigenvalues. He finds that the energy levels are given by:

$$E_n = \Delta[1 - T_n \sin^2(\phi/2)]^{1/2} \quad (44)$$

with $n = 1, 2, \dots, m$ the number of allowable modes. The values for T_n might range between 1 and 0.

The most important aspect of these expressions in the various limits is that the allowed energy levels depend on the macroscopic phase difference between the two superconductors. The position of the levels mediate the information about the different phases of the two superconductors and form the core of the Josephson-effect.

Despite their importance a direct experimental demonstration of these energy-levels is difficult to provide. Several unpublished attempts have been made using far-infrared spectroscopy. Alternatively one would like to use a tunneljunction as a spectroscopic tool. The need for ballistic transport is practically incompatible with needed geometrical extension to fabricate a tunneljunction on top of the device. Morpurgo *et al.* [57] have been able to demonstrate the precursor of the formation of an Andreev bound state.

Each energy level carries a contribution to the current of ev_F/m either in positive or negative direction. For $\phi = 0$ there is an equal number of left and right-movers and the net current is zero. However, if we now allow a phase-difference between the two superconductors the energy of the levels changes. Some move upwards and others move downwards. For a given temperature these energy levels are occupied determined by the Fermi-Dirac distribution function. Hence, some levels move out of the occupied range of energies others move deeper inwards. As a consequence a net supercurrent flows in either the positive or the negative direction dependent on the applied phase-difference. The supercurrent carried by these bound states is determined by the contribution of the electron- and the hole-component:

$$I = \sum_{n=0}^m [I^+(E_n)f^+(E_n) + I^-(E_n)f^-(E_n)] \quad (45)$$

with I^+ and I^- the contribution of the hole and the electron respectively, which are identical with op-

posite sign. In addition by definition $f^+(E_n) = 1 - f^-(E_n)$, which leads to:

$$I = \sum_{n=0}^m I(E_n)[1 - 2f(E_n)] \quad (46)$$

The charge current carried by the allowable energy states follow from the probability-current-density:

$$\mathbf{J}_q = \frac{\hbar}{m} \text{Im}(u^*(\mathbf{r})\nabla u(\mathbf{r}) - v^*(\mathbf{r})\nabla v(\mathbf{r})) \quad (47)$$

Using this expression one finds for the supercurrent, taking the equilibrium Fermi-functions for the occupations:

$$I(\phi) = \frac{2e}{\hbar} \sum_{n=0}^m \frac{\partial E_n}{\partial \phi} \tanh \frac{E_n}{2kT} \quad (48)$$

which for a short junction with a transmission coefficient 1 using Eq. (43) we find:

$$I(\phi) = \frac{e}{\hbar} N \Delta(T) \sin(\phi/2) \tanh \frac{\Delta(T) \cos(\phi/2)}{2kT} \quad (49)$$

Knowing the number of modes one also knows the normal state conductance, the Sharvin-conductance $G_0 = N(e^2/\pi\hbar)$, which leads to the expression first derived by Kulik and Omelyanchuk [58]:

$$I(\phi) = \pi G_0 \frac{\Delta(T)}{e} \sin(\phi/2) \tanh \frac{\Delta(T) \cos(\phi/2)}{2kT} \quad (50)$$

In the same spirit one finds [58] for systems with a finite transmission coefficient using Eq. (44) that the supercurrent is governed by:

$$I(\phi) = \frac{e\Delta^2}{2\hbar} \sin(\phi) \sum_{n=0}^m \frac{T_n}{E_n} \tanh \frac{E_n}{2kT} \quad (51)$$

In many cases the transmission coefficients are energy dependent. For the well-known case of a tunneljunction we have a single transmissioncoefficient for all energies and one obtains $E_n = \Delta$ and hence:

$$I(\phi) = \frac{\pi G_0}{4e} \sin \phi \tanh \frac{\Delta}{2kT} \quad (52)$$

the well-known expression first derived by Ambegaokar and Baratoff [59] with $G_0 = e^2 N T_n$.

This set of equations clearly shows that starting with the Andreev bound states one obtains well-known expressions for the supercurrent carried by these systems. It also shows that the total supercurrent is determined by the relative contribution of the electron and the hole-like component.

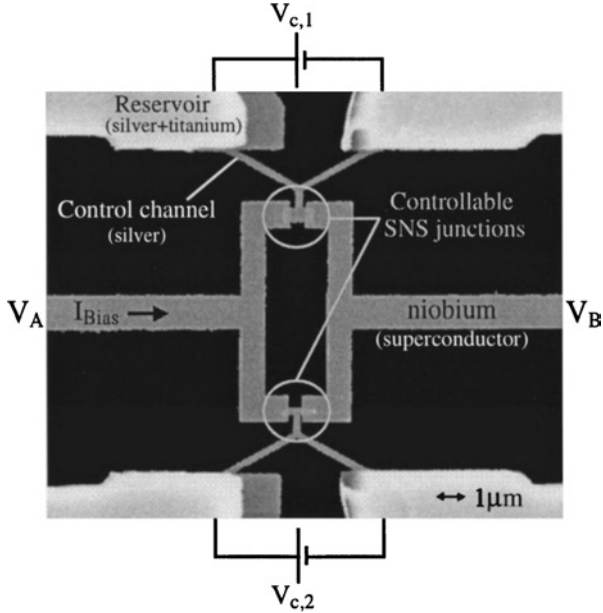


Fig. 14. Two SNS junctions in parallel. Each SNS junction can be individually controlled with a normal control wire in which a nonequilibrium electron distribution can be realized. Taken from Baselmans *et al.* [61].

8. DIFFUSIVE AND CONTROLLABLE SUPERCURRENTS

An important ingredient of the supercurrent-carrying capacity appearing in Eq. (46) is the dependence on the distribution-function $f(E)$. It controls the temperature dependence and it might enable the control through a nonequilibrium distribution function [60]. Figure 14 shows a recently studied sample lay-out consisting of two SNS junctions in parallel in which each of them can be individually controlled with a nonequilibrium distribution function [61,62]. In earlier work a thermal control was realized with hot electrons by Morpurgo *et al.* [60]. This led Wilhelm *et al.* [63] to a nonequilibrium analysis, using a nonequilibrium distribution as measured by Pothier *et al.* [64].

In a diffusive system the proximity-effect is again expressed in the two parameters θ and ϕ introduced in Section 6. The supercurrent is given by:

$$\vec{J}_s(x) = \frac{\sigma}{e} \int_0^\infty dE [1 - 2f(E)] \text{Im}(\sin^2 \theta(\nabla\varphi)) \quad (53)$$

By solving the Usadel equations for θ and ϕ with the appropriate boundary conditions at the interfaces one finds \vec{J}_s . This program has been carried out by Wilhelm *et al.* [63] in which a supercurrent-carrying

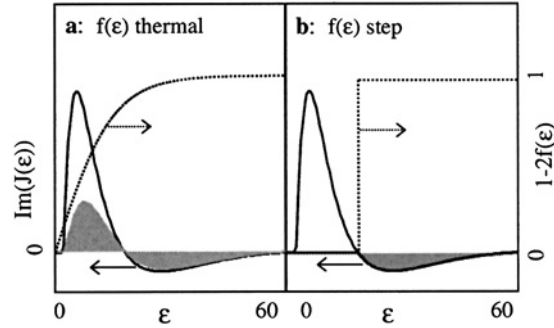


Fig. 15. Supercurrent-carrying density of states and distribution function. Left panel for thermal distribution and right panel for a steplike nonequilibrium function. The shaded area indicates the contribution to the integral Eq. (54).

density of states is introduced $\text{Im}(j_E)$.

$$I_s = \frac{d}{2R_d} \int_{-\infty}^{+\infty} dE [1 - 2f(E)] \text{Im}(j_E) \quad (54)$$

It means that for a dirty superconductor the energy dependent spectral current $\text{Im}(j_E)$ replaces the discrete Andreev bound states of Eq. (46). It is also dependent on the phase difference ϕ . For $\phi = 0$ there is a minigap E_g given by $E_g \simeq 3.2E_{\text{Th}}$ with E_{Th} the Thouless energy associated with the length of N. This energy-dependent current rises sharply at this minigap and oscillates for increasing energy around zero with an exponentially decaying amplitude (Fig. 15). For increasing phase-difference the mini-gap closes for $\phi = \pi$. Evidently one way to vary the supercurrent is to increase the temperature, which is modeled by replacing $1 - 2f(E)$ by $\tanh(E/2kT)$.

Wilhelm *et al.* [63] predicted that a suitably chosen distribution function would lead to a reversal of the direction of the supercurrent. In essence the left-moving parts of the contribution to the supercurrent weigh more heavily in the integral than the right-moving parts as illustrated in Fig. 15. This reversal of the direction of the supercurrent was demonstrated by Baselmans *et al.* [65]. The reversal of the supercurrent implies a shift of the phase-difference by π and the device is therefore called a controllable π -junction. A detailed comparison of experiment and theory [66] is shown in Fig. 16. As a function of control voltage (dots) the supercurrent-amplitude decreases, passes through zero, and continues with a small negative amplitude. The Inset shows the distribution-functions assumed in the comparison with theory. This experiment clearly illustrates the importance of the distribution-function in controlling the superconducting state in N.

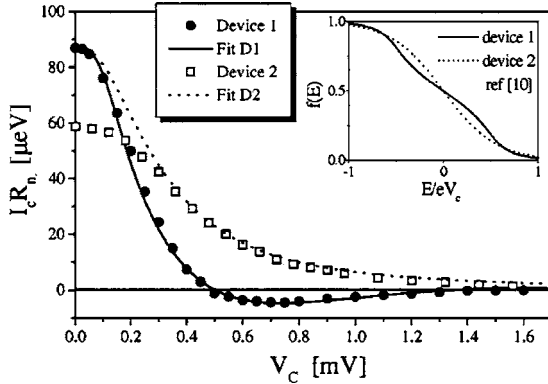


Fig. 16. Reversal of the direction of the supercurrent induced by a nonequilibrium distribution function and comparison with theory. The inset shows the two-step distribution-functions used in the fits.

9. CONCLUDING HISTORICAL NOTE

The examples shown above illustrate the intricate interplay between energies, correlation-lengths, phase-dependence, and distribution-functions. Collectively they constitute the relationship between the proximity-effect and Andreev-reflections. For me this interplay started in 1980 when I was a postdoc in Mike Tinkham's group.

When I arrived in Tinkham's group in 1979 he had just returned from a sabbatical in Karlsruhe. During this sabbatical he had also travelled to Moscow to visit the Institute of Radio Engineering and Electronics (IREE), in particular Anatoly Volkov, Sergey Artemenko, and Sacha Zaitsev. From this visit he had picked up the understanding that in their difficult to digest theoretical work Andreev reflection was an important concept to understand constrictions between superconductors and between superconductors and normal metals. In Josephson contacts the voltage-carrying state was mostly dominated by time-averaged quantities such as in the celebrated resistively-shunted-junction (RSJ) model. However, the fact that quantities like an excess current appeared in both S-c-S as well as S-c-N contacts was attributed to a static process like Andreev reflection. Tinkham had written a note for discussion in which he summarized his thinking on this subject by starting with charge imbalance and how that would be changed at lower temperatures.

My experimental work at Harvard was initially directed to make and study one of the first Josephson-arrays, in collaboration with Chris Lobb,

to mimic the Kosterlitz-Thouless phase transition. It was to be based on SNS junctions using a commercially available mesh as a shadow mask [67]. As a family we kept a diary during our stay in the US to remember the responses of our kids to the new environment. In this diary I find that Chris reports on our work in a Tinkham-group seminar on January 29, 1980. But more importantly I write for the first time about the "bouncing ball picture." That day I had been chatting with Greg Blonder who was trying to measure niobium point contacts as a function of temperature. And again, as in so many previous experiments including my own thesis work on microbridges, a phenomenon called "subharmonic gap structure" popped up abundantly. It had been reported extensively since at least 1964 and was never conclusively explained. In retrospect multiparticle tunnelling was the correct track but there were no experimental systems which allowed us to study this phenomenon in sufficient isolation, neither was the theory sufficiently developed. This experimental problem was eventually resolved when the mechanical break junctions [55] became available, which also stimulated a thorough theoretical treatment which still continues to the present day [68].

During my ride home on the Harvard Express Bus to Lexington on the 29th I realized suddenly that with two superconductors connected by a little Sharvin-like hole Andreev-reflection should take place at both superconductors and electron/hole particles should bounce back and forth picking up the voltage difference at each passage. With our kids I shared my enthusiasm over dinner referring to balls changing color upon reflection of the walls and rising higher and higher until they would go over the roof. The next day on the 30th the discussion with Greg started followed by a discussion over lunch with Mike, both of them swallowing the elementary idea rather quickly.

We worked out the idea in more details by making lots of pictures illustrating various bias conditions and illustrating what would happen for $2\Delta/n$. It was obvious that the transition from higher order to lower order multiple transitions was at the heart of the observed subharmonic gap structure. Most satisfying was the application to asymmetric junctions, contacts between superconductors with different gaps. The experiments had shown a peculiar series of structure at the large gap, the sum gap and *only* the even series of the smaller gap. The pictures clearly showed that this was naturally explained with

the concept of multiple Andreev reflections. This was completely convincing even without any mathematical formulation.

It was our hope to get a paper written before my return to The Netherlands, early July 1980. Several attempts were made, mostly descriptive and unsatisfying. Computer simulations with an *ad hoc* reflection coefficient at the interfaces looked encouraging but we were not sure how much of the Josephson-effect one could throw out and the concept of different chemical potentials associated with the charge imbalance was still confusing us. We had been gradually looking more and more into the Bogoliubov-De Gennes equations, which had been the vehicle to introduce the concept of Andreev reflections back in 1964. We realized that we were using a reflection-coefficient for number current and not for charge current.

A note was written by Greg Blonder, dated Aug. 20, 1980, which summarized the relevant aspects under the title *A Bogoliubov Equation Primer*. To this note he added an Appendix where he showed how the matching of the wave functions at an interface with a δ -function worked (Section 3). This was used to perform a computercalculation using the bouncing-ball picture, which we subsequently called the “trajectory method.” Everything worked fine and beautiful, except for the fact that the subharmonic gap structure disappeared at low temperatures. In the computer calculations the reflection-coefficients without the δ -function were used and therefore there was no cut-off for higher order processes. All orders weighed equally heavy. But the δ -function was introduced to find some mechanism to cut off these higher order processes. Since we modelled the SS contact with S-c-S with c a normal metal like constriction we had two δ -functions at each interface. With the trajectory method this led to the impossible task to keep track of multiple elastic scattering paths and multiple Andreev scattering paths. So we were stuck except that we were able to correctly describe in its full glory the NS contact with the trajectory method and also the SS contacts provided we were willing to accept that there was no cut-off for higher order processes. Having been impressed by the depth of the Russian theoretical work we were extremely pleased to obtain for NS contacts exactly the same result as Zaitsev had published in the course of 1980, even being able to point out that his expressions must contain a mistake. Moreover we were able to describe the NS contacts with an arbitrary transmission coefficient, an

accomplishment which Zaitsev [22] stimulated to develop his boundary conditions.

These results were included in a submitted contribution to LT16, in early 1981. The contribution got upgraded to an invited talk held during this conference in Los Angeles (Aug. 19–25, 1981) and published in the Proceedings [69]. On Oct. 19, 1981 the BTK paper was submitted. In parallel Mike developed the Boltzmann equation approach to attack the SNS problem with elastic scattering at the interfaces for which the trajectory method had turned out to be too clumsy. The original note on this issue was dated Feb. 18, 1981. It was further worked out with the help of Miguel Octavio and submitted on Feb. 18, 1983.

We believed that we had solved the last remaining puzzle in understanding superconducting contacts and that the subject was now closed. In retrospect we did not anticipate that the BTK paper would become so popular because of pointcontact spectroscopy of superconducting and magnetic materials. We neither did realize that it was an early example of dealing with quantum transport problems in the spirit of the Landauer-Büttiker formalism [31]. We also did not realize that the mechanical break junctions [55] would provide such rich and detailed experimental data, which stimulated a lot of theoretical work and which also clearly connected the multiple Andreev concept with multiparticle tunneling. The idea of multiple charge quanta have found strong support through recent shot noise measurements [70,71]. In view of the historical account in which experimental results on subharmonic gap structure between dissimilar superconductors played such an encouraging role it would be nice to see experiments with controllable break junctions of two dissimilar superconductors.

ACKNOWLEDGMENTS

The author likes to express his gratitude to Michael Tinkham for his very personal style of doing experimental research in superconductivity with a sharp eye for the essential physics. In addition he acknowledges the stimulating interactions with students and collaborators: J. J. A. Baselmans, W. Belzig, G. E. Blonder, G. R. Boogaard, A. Dimoulas, S. G. den Hartog, J. P. Heida T. T. Heikkillä, D. R. Heslinga, W. M. van Huffelen, A. T. Filip, R. S. Keizer, P. H. C. Magnée, A. F. Morpurgo, Yu. V.

Nazarov, M. Octavio, S. Russo, A. H. Verbruggen, A. F. Volkov, B. J. van Wees, F. K. Wilhelm, and A. V. Zaitsev. Financial support has been provided by the *Nederlandse Organisatie voor Wetenschappelijk Onderzoek* (NWO) through the *Stichting voor Fundamenteel Onderzoek der Materie* (FOM).

REFERENCES

1. G. Deutscher and P. G. de Gennes, in *Superconductivity*, R. D. Parks, ed. (Marcel Dekker, New York, 1969), Vol. 2, p. 1005.
2. E. L. Wolf and G. B. Arnold, *Phys. Rep.* **91**, 31 (1982).
3. M. Gurvitch, M. A. Washington, and H. A. Huggins, *Appl. Phys. Lett.* **42**, 472 (1983).
4. M. Tinkham, *Introduction to Superconductivity* (McGraw-Hill, New York, 1996).
5. J. R. Waldram, *Superconductivity of Metals and Cuprates* (Institute of Physics Publishing, London, 1996).
6. B. Pannetier and H. Courtois, *J. Low Temp. Phys.* **118**, 599 (2000).
7. G. E. Blonder, M. Tinkham, and T. M. Klapwijk, *Phys. Rev. B* **25**, 4515 (1982).
8. S. Redner, *Citation Statistics From More Than a Century of Physical Review*, physics/040713/v1, July **27**, 2004.
9. P. G. de Gennes, *Rev. Mod. Phys.* **36**, 225 (1964).
10. P. G. de Gennes, *Superconductivity of Metals and Alloys* (Benjamin, New York, 1966).
11. J. Clarke, *Proc. R. Soc. Lond. Ser. A: Math. Phys. Sci.* **308**, 447 (1969).
12. J. Clarke, *Phys. Rev. B* **4**, 2963 (1971).
13. P. Dubos, H. Courtois, B. Pannetier, F. K. Wilhelm, A. D. Zaikin, and G. Schön, *Phys. Rev. B* **63**, 064502 (2001).
14. J. Rammer and H. Smith, *Rev. Mod. Phys.* **58**, 323 (1986).
15. G. Eilenberger, *Z. Phys.* **214**, 195 (1968).
16. K. D. Usadel, *Phys. Rev. Lett.* **25**, 507 (1970).
17. A. I. Larkin and Yu. N. Ovchinnikov, *Zh. Eksp. Theor. Fiz.* **55**, 2262 (1968); [*Sov. Phys. JETP* **28**, 1200 (1969)].
18. A. I. Larkin and Yu. N. Ovchinnikov, *Zh. Eksp. Theor. Fiz.* **68**, 1915 (1975); [*Sov. Phys. JETP* **41**, 960 (1975)].
19. A. I. Larkin and Yu. N. Ovchinnikov, *Zh. Eksp. Theor. Fiz.* **73**, 299 (1977); [*Sov. Phys. JETP* **46**, 155 (1977)].
20. G. M. Eliashberg, *Zh. Eksp. Theor. Fiz.* **61**, 1254 (1971); [*Sov. Phys. JETP* **34**, 668 (1972)].
21. A. Schmid and G. Schön, *J. Low Temp. Phys.* **20**, 207 (1975).
22. A. V. Zaitsev, *Zh. Eksp. Theor. Fiz.* **86**, 1742 (1984); [*Sov. Phys. JETP* **59**, 1015 (1984)].
23. A. F. Andreev, *Zh. Eksp. Theor. Fiz.* **46**, 1823 (1964); [*Sov. Phys. JETP* **19**, 1228 (1964)].
24. R. S. Gonnelli, D. Daghero, G. A. Ummarino, V. A. Stepanov, J. Jun, S. M. Kazakov, and J. Karpinski, *Phys. Rev. Lett.* **89**, 247004 (2002).
25. P. Szabo, P. Samuely, J. Kacmarcik, T. Klein, J. Marcu, D. Fruchart, S. Miraglia, C. Marcenat, A. G. M. Jansen, *Phys. Rev. Lett.* **87**, 137005 (2001).
26. M. J. M. de Jong and C. W. J. Beenakker, *Phys. Rev. Lett.* **74**, 1657 (1995).
27. R. J. Soulen, Jr., J. M. Byers, M. S. Osofsky, B. Nadgorny, T. Ambrose, S. F. Cheng, P. R. Broussard, C. T. Tanaka, J. Nowak, J. S. Moodera, A. Barry, and J. M. D. Coey, *Science* **282**, 85 (1998).
28. S. K. Updhyay, A. Palanisami, R. N. Louie, and R. A. Buhrman, *Phys. Rev. Lett.* **81**, 3247 (1998).
29. I. I. Mazin, A. A. Golubov, and B. Nadgorny, *J. Appl. Phys.* **89**, 7576 (2001).
30. Y. Imry, *Introduction to Mesoscopic Physics* (Oxford University Press, Oxford, 2002).
31. C. W. J. Beenakker, *Rev. Mod. Phys.* **69**, 731 (1997).
32. C. W. J. Beenakker, *Andreev Billiards*, cond-mat/0406018.
33. C. J. Lambert and R. Raimondi, *J. Phys.: Condens. Matter* **10**, 901 (1998).
34. B. J. van Wees, P. de Vries, P. Magnée, and T. M. Klapwijk, *Phys. Rev. Lett.* **69**, 510 (1992).
35. A. Kastalsky, A. W. Kleinsasser, L. H. Greene, R. Bhat, F. P. Milliken, and J. P. Harbison, *Phys. Rev. Lett.* **67**, 3026 (1991).
36. S. G. Den Hartog, C. M. A. Kapteyn, B. J. van Wees, and T. M. Klapwijk, *Phys. Rev. Lett.* **76**, 4592 (1996).
37. F. W. J. Hekking and Yu. V. Nazarov, *Phys. Rev. Lett.* **71**, 1625 (1993).
38. H. Pothier, S. Guéron, D. Estève, and M. H. Devoret, *Phys. Rev. Lett.* **73**, 2488 (1994).
39. D. Estève, H. Pothier, S. Guéron, Norman O. Birge, and M. H. Devoret, in L. L. Sohn et al. (eds.), *Introduction to Mesoscopic Electron Transport* (Kluwer Academic, Amsterdam, 1997).
40. D. Estève, H. Pothier, S. Guéron, Norman O. Birge, and M. H. Devoret, in *Correlated Fermions and Transport in Mesoscopic Systems*, T. Martin, G. Montambaux, and J. Trân Vãn, eds. (Editions Frontières, Paris, 1996).
41. S. Guéron, *Quasiparticles in a Diffusive Conductor: Interaction and Pairing*, Thesis, CEA-Saclay, 1997.
42. A. Anthore, *Decoherence Mechanisms in Mesoscopic Conductors*, Thesis, CEA-Saclay, 2003.
43. Yu. N. Nazarov, *Phys. Rev. Lett.* **73**, 1420 (1994).
44. S. Guéron, H. Pothier, N. O. Birge, D. Estève, and M. H. Devoret, *Phys. Rev. Lett.* **96**, 3025 (1996).
45. H. Courtois, Ph. Gandit, B. Pannetier, and D. Mailly, *Superlattices Microstruct.* **25**, 721 (1999).
46. S. N. Artemenko, A. F. Volkov, and A. V. Zaitsev, *Solid State Commun.* **30**, 771 (1979).
47. Yu. V. Nazarov and T. H. Stoof, *Phys. Rev. Lett.* **76**, 823 (1996).
48. T. H. Stoof and Yu. V. Nazarov, *Phys. Rev. B* **53**, 14496 (1996).
49. G. R. Boogaard, A. H. Verbruggen, W. Belzig, and T. M. Klapwijk, *Phys. Rev. B* **69**, R220503 (2004).
50. I. Siddiqi, A. Verevkin, D. E. Prober, A. Skalare, W. R. McGrath, P. M. Echternach, and H. G. LeDuc, *J. Appl. Phys.* **91**, 4646 (2002).
51. A. Dimoulas, J. P. Heida, B. J. van Wees, T. M. Klapwijk, W. van de Graaf, and G. Borghs, *Phys. Rev. Lett.* **74**, 602 (1995).
52. I. O. Kulik, *Zh. Eksp. Theor. Fiz.* **57**, 1745 (1969); [*Sov. Phys. JETP* **30**, 944 (1970)].
53. C. Ishii, *Prog. Theor. Phys.* **44**, 1525 (1970).
54. J. Bardeen and J. L. Johnson, *Phys. Rev. B* **5**, 72 (1972).
55. N. Agrait, A. Levy Yeyati, and J. M. van Ruitenbeek, *Phys. Rep.* **377**, 81 (2003).
56. C. W. J. Beenakker, in *Transport Phenomena in Mesoscopic Systems*, H. Fukuyama and T. Ando, eds. (Springer, Berlin, 1992).
57. A. F. Morpurgo, B. J. van Wees, T. M. Klapwijk, and G. Borghs, *Phys. Rev. Lett.* **79**, 4010 (1997).
58. I. O. Kulik and A. N. Omel'yanchuk, *JETP Lett.* **21**, 96 (1975); *Sov. J. Low Temp. Phys.* **3**, 459 (1978).
59. V. Ambegaokar and A. Baratoff, *Phys. Rev. Lett.* **10**, 486 [1963; erratum **11**, 104 (1963)].
60. A. F. Morpurgo, T. M. Klapwijk, and B. J. van Wees, *Appl. Phys. Lett.* **72**, 966 (1998).
61. J. J. A. Baselmans, B. J. van Wees, and T. M. Klapwijk, *Appl. Phys. Lett.* **79**, 2940 (2001).
62. J. J. A. Baselmans, T. T. Heikkilä, B. J. van Wees, and T. M. Klapwijk, *Phys. Rev. Lett.* **89**, 207002 (2002).
63. F. K. Wilhelm, G. Schön, and A. D. Zaikin, *Phys. Rev. Lett.* **81**, 1682 (1998).
64. H. Pothier, S. Guéron, N. O. Birge, D. Estève, and M. H. Devoret, *Phys. Rev. Lett.* **79**, 3490 (1997).

65. J. J. A. Baselmans, A. F. Morpurgo, B. J. van Wees, and T. M. Klapwijk, *Nature* **397**, 43 (1999).
66. J. J. A. Baselmans, B. J. van Wees, and T. M. Klapwijk, *Phys. Rev. B* **63**, 094504 (2001).
67. D. W. Abraham, C. J. Lobb, M. Tinkham, and T. M. Klapwijk, *Phys. Rev. B* **26**, 5268 (1982).
68. S. Pilgram and P. Samuelsson, cond-mat/0407029.
69. T. M. Klapwijk, G. E. Blonder, and M. Tinkham, *Physica B +C* **109–110**, 1657 (1982).
70. P. Dieleman, H. G. Bukkems, T. M. Klapwijk, M. Schicke, and K. H. Gundlach, *Phys. Rev. Lett.* **79**, 3486 (1997).
71. R. Cron, M. F. Goffman, D. Estève, and C. Urbina, *Phys. Rev. Lett.* **86**, 4104 (2001).

Pancake Vortices

John R. Clem¹

Received August 15, 2004; accepted September 4, 2004

I describe the magnetic-field and current-density distributions generated by two-dimensional (2D) pancake vortices in infinite, semi-infinite, and finite-thickness stacks of Josephson-decoupled superconducting layers. Arrays of such vortices have been used to model the magnetic structure in highly anisotropic layered cuprate high-temperature superconductors. I show how the electromagnetic forces between pancake vortices can be calculated, and I briefly discuss the effects of interlayer Josephson coupling.

KEY WORDS: pancake vortices; layered superconductors; high-temperature superconductors; films; forces; Josephson coupling.

1. INTRODUCTION

Since this paper is intended for publication in a special Festschrift issue honoring Mike Tinkham, I have been invited to include some personal reflections in the introduction. I believe I first heard his name when I was a graduate student in the early 1960s at the University of Illinois-Urbana, working on extensions of the BCS theory [1] to include anisotropy of the superconducting energy gap [2,3]. A paper by Ginsberg, Richards, and Tinkham [4] had reported results on the far-infrared absorption in superconducting lead, which showed a precursor hump in the real part of the complex conductivity, $\sigma_1(\omega)/\sigma_N$. I tried to explain this feature in terms of gap anisotropy but was unsuccessful.

Throughout subsequent years, I have followed Mike Tinkham's career with considerable interest. I have admired his research style, which consistently has resulted in new and interesting experimental results and theoretical interpretations that advance the theory. I also admire anyone who can write carefully prepared books, and I have found his books on superconductivity (in both editions [5,6]) to be particularly useful. I have asked students beginning research with me to work diligently through these books to learn the fundamentals of superconductivity.

One of the topics that Mike Tinkham finds interesting is vortex physics, and since this has been one of my main research interests, I would like to focus here on one aspect: two-dimensional (2D) pancake vortices. This is a favorite subtopic of mine, partly because I coined the name and partly because my 1991 paper on this subject [7] has been so well received by the superconductivity community (over 600 citations to date). Incidentally, although I wanted to put "2D pancake vortex" in the title of this paper, the editors of *Physical Review B* forbid this but did allow me to use these words in the abstract and the rest of the paper. I first reported on my work on 2D pancake vortices at a Gordon Research Conference chaired by Mike Tinkham in June 1989, but (as has too often been the case with me) I was slow to publish, and some of the key results were published in 1990 by Artemenko and Kruglov [8] and by Buzdin and Feinberg [9]. I later discovered that the basic solution had even been published in 1979 by Efetov [10], but his work unfortunately had gone largely unnoticed.

This paper is organized as follows. In Sec. 2, I calculate the properties of 2D pancake vortices in an infinite stack of Josephson-decoupled superconducting layers, first by considering all the layers as being very thin and then by considering the layers above and below the pancake layer as a continuum [11]. In Sec. 3, I use the continuum approach to calculate the properties of 2D pancake vortices in a semi-infinite stack of Josephson-decoupled superconducting

¹Ames Laboratory and Department of Physics and Astronomy, Iowa State University, Ames, Iowa 50011-3160.

layers. In Sec. 4, I again use the continuum approach to calculate the properties of 2D pancake vortices in a finite stack of Josephson-decoupled superconducting layers [12], first for arbitrary thickness and then for a thickness much less than the in-plane penetration depth, where the results bear some similarities to those of Pearl [13–15] for vortices in thin films. In Sec. 5, I show how to calculate the electromagnetic forces between pancake vortices, and in Sec. 6, I discuss some consequences of Josephson coupling. I conclude with a brief summary in Sec. 7.

2. PANCAKE VORTEX IN AN INFINITE STACK OF SUPERCONDUCTING LAYERS

The chief motivation for my work that led to the idea of the 2D pancake vortex was the question of how to describe the vortex structure of highly anisotropic layered cuprate high-temperature superconductors, with Bi-2212 ($\text{Bi}_2\text{Sr}_2\text{CaCu}_2\text{O}_{8-\delta}$) being the best-known example. Applying the anisotropic Ginzburg-Landau equations [16–29] to this material, it could easily be seen that the calculated value of the coherence length ξ_c (the length scale describing spatial variation of the order parameter in the c direction perpendicular to the layers) was less than the center-to-center distance s between the CuO_2 bilayers. Since the Ginzburg-Landau theory assumes that all the characteristic lengths of superconductivity are large by comparison with atomic length scales, this fact indicated that some other theory was needed to describe details of the vortex structure in the most anisotropic high- T_c superconductors.

The natural way to incorporate the existence of discrete layers was to make use of the Lawrence-Doniach theory [30], which treats the intralayer behavior using Ginzburg-Landau theory but interlayer coupling via the Josephson effect [31]. In this theory the coherence length ξ_c plays no role when its value is less than s , and the penetration depth λ_c describing the length scale of the spatial variation of supercurrents parallel to the c direction can be related to the maximum Josephson supercurrent J_0 via [32] $\lambda_c = (c\phi_0/8\pi^2sJ_0)^{1/2}$ in Gaussian units. The parameter usually used to characterize the degree of anisotropy is $\gamma = \lambda_c/\lambda_{ab}$, where λ_{ab} is the penetration depth describing the length scale of the spatial variation of supercurrents parallel to the layers (neglecting the anisotropy between the a and b directions, i.e., assuming for simplicity that $\lambda_a \approx \lambda_b \approx \lambda_{ab}$). For Bi-2212, the value of γ is so large that it is difficult

to measure [33]; γ was found in Ref. [34] to be larger than 150, but a more recent quantitative determination [35] has yielded $\gamma = 640 \pm 25$.

For such highly anisotropic materials, it seemed sensible to me to take the limit $\gamma \rightarrow \infty$ ($\lambda_c = \infty$ or $J_0 = 0$) as the starting point to describe vortex structure. The essential idea was that in a model of identical superconducting layers separated by insulating layers, one could solve for the magnetic field and current density generated by a 2D pancake vortex in one of the superconducting layers when the other layers contained no vortices but served only to screen the magnetic field generated by the pancake vortex. With this solution as a building block, one could then find the magnetic field produced by a stack of such pancake vortices, even if misaligned, by the process of linear superposition. This was basically the approach I had used in developing the theory that quantitatively explains the coupling forces between misaligned vortices in just two layers [36,37], the primary and secondary superconducting layers of the dc transformer studied experimentally first by Giaever [38,39], and later by Solomon [40], Sherrill [41], Deltour and Tinkham [42], and Cladis *et al.* [43,44], but in greatest detail by Ekin *et al.* [45,46].

2.1. Model of Very Thin Discrete Superconducting Layers

To calculate the magnetic-field and current-density distributions generated by a pancake vortex in an infinite stack of Josephson-decoupled superconducting layers, in Ref. [7] I used the model in which the superconducting layers, all of thickness d , are centered on the planes $z = z_n = ns$ ($n = 0, \pm 1, \pm 2, \dots$), as sketched in Fig. 1. The London penetration depth within each layer is λ_s such that the average penetration depth for currents parallel to the layers is [32] $\lambda_{\parallel} = \lambda_s(s/d)^{1/2}$, which corresponds to the penetration depth λ_{ab} in the high-temperature superconductors. When the central layer ($z = 0$) contains a vortex at the origin but all other layers are vortex-free, the London fluxoid quantization condition [47] in layer n can be expressed as

$$2\pi\rho[a_\phi(\rho, z_n) + (2\pi\Lambda_s/c)K_\phi(\rho, z_n)] = \phi_0\delta_{n0}, \quad (1)$$

where in cylindrical coordinates $\mathbf{a}(\rho, z) = \hat{\phi}a_\phi(\rho, z)$ is the vector potential, $\mathbf{K}(\rho, z_n) = \hat{\phi}K_\phi(\rho, z_n) = \hat{\phi}\bar{j}_\phi(\rho, z_n)s$ is the sheet-current density in layer n averaged over the periodicity length s , $\Lambda_s = 2\lambda_{\parallel}^2/s = 2\lambda_s^2/d$ is the 2D screening length, and $\phi_0 = hc/2e$

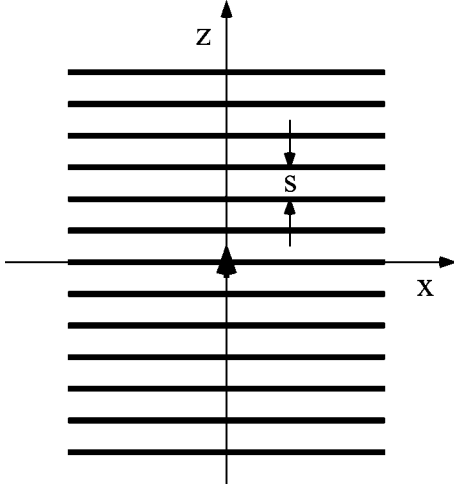


Fig. 1. Infinite stack of thin superconducting layers with a pancake vortex at the origin (bold arrow).

is the superconducting flux quantum. Equation (1) inevitably leads to a description of vortices in the London model [48], which is characterized by unphysical current-density and magnetic-field singularities on the vortex axis. The pioneering work on vortices by Abrikosov [49] showed that such singularities are cut off at a distance of the order of the in-plane coherence length ξ_{ab} . A simple model for the vortex core, employing a variational core-radius parameter $\xi_v \sim \xi_{ab}$, has been used to describe straight vortices in isotropic [50] and anisotropic [51] superconductors, as well as in films of arbitrary thickness, whether isolated [52] or in superconducting dc transformers [37]. This model also could be used to cure the vortex-core singularities that are present in all the following results of this paper.

If one takes the thickness d of each layer to be very small, as in Ref. [7], the vector potential can be expressed in the form

$$a_\phi(\rho, z) = \int_0^\infty dq A(q) J_1(q\rho) Z(q, z), \quad (2)$$

where $J_1(q\rho)$ is a Bessel function and $Z(q, z)$ has scallops as a function of z that are necessary to describe the discontinuities of $b_\rho(\rho, z)$ arising from the induced sheet currents $K_\phi(\rho, z_n)$ for $n \neq 0$. Note that $\mathbf{b}(\rho, z) = \nabla \times \mathbf{a}(\rho, z)$, such that

$$b_\rho(\rho, z) = -\frac{\partial a_\phi(\rho, z)}{\partial z} \quad (3)$$

and

$$b_z(\rho, z) = \frac{1}{\rho} \frac{\partial [\rho a_\phi(\rho, z)]}{\partial \rho}. \quad (4)$$

Inserting the exact expression for $A(q)$ into Eq. (2) yields a complicated integral that cannot be integrated analytically. However, a close approximation to the exact result can be obtained by writing $Z(q, z) = \exp(-Q|z|)$, where $Q = (q^2 + \lambda_\parallel^{-2})^{1/2}$ and $A(q) = \phi_0/2\pi\Lambda_s Q$; this approximation, which is valid for $s \ll \lambda_\parallel$, corresponds to retaining information on the scale of λ_\parallel but giving up detailed information on the finer scale of s . The resulting vector potential and magnetic field components are

$$a_\phi(\rho, z) = \frac{\phi_0 \lambda_\parallel}{2\pi \Lambda_s \rho} (e^{-|z|/\lambda_\parallel} - e^{-r/\lambda_\parallel}), \quad (5)$$

$$b_z(\rho, z) = \frac{\phi_0}{2\pi \Lambda_s r} e^{-r/\lambda_\parallel}, \quad (6)$$

$$b_\rho(\rho, z) = \frac{\phi_0}{2\pi \Lambda_s \rho} \left[\frac{z}{|z|} e^{-|z|/\lambda_\parallel} - \frac{z}{r} e^{-r/\lambda_\parallel} \right], \quad (7)$$

where $r = (\rho^2 + z^2)^{1/2}$. Since in the high-temperature superconductors $s/2\lambda_\parallel = \lambda_\parallel/\Lambda_s \approx 10^{-2}$, the vector potential term in Eq. (1) of order $\lambda_\parallel/\Lambda_s$ can be neglected in the central layer ($n = 0$) and we obtain to good approximation

$$K_\phi(\rho, z_0) = \frac{c\phi_0}{4\pi^2 \Lambda_s \rho}. \quad (8)$$

However, for all the other layers ($n \neq 0$) we obtain

$$K_\phi(\rho, z_n) = -\frac{c\phi_0 \lambda_\parallel}{4\pi^2 \Lambda_s^2 \rho} (e^{-|z_n|/\lambda_\parallel} - e^{-r_n/\lambda_\parallel}), \quad (9)$$

where $z_n = ns$ and $r_n = (\rho^2 + z_n^2)^{1/2}$. Note that the magnitude of the sheet-current density in the $n = 0$ central layer is much larger, by a factor of order 10^2 , than the sheet-current density in one of the $n \neq 0$ layers. It is for this reason that I gave the name pancake vortex to this field and current distribution.

An interesting property of the above solutions is that the pancake-vortex-generated magnetic flux $\Phi_z(\rho, z) = 2\pi\rho a_\phi(\rho, z)$ up through a circle of radius ρ at height z is (using $\Lambda_s = 2\lambda_\parallel^2/s$)

$$\Phi_z(\rho, z) = \phi_0 (s/2\lambda_\parallel) (e^{-|z|/\lambda_\parallel} - e^{-r/\lambda_\parallel}), \quad (10)$$

such that the magnetic flux up through a layer at height z is

$$\Phi_z(\infty, z) = \phi_0 (s/2\lambda_\parallel) e^{-|z|/\lambda_\parallel}, \quad (11)$$

and the magnetic flux up through the central layer at $z = 0$ is

$$\Phi_z(\infty, 0) = \phi_0 (s/2\lambda_\parallel). \quad (12)$$

When $s \ll \lambda_\parallel$, as in the high-temperature superconductors, we see that $\Phi_z(\infty, 0) \ll \phi_0$. This is at first

surprising until one realizes that fluxoids are quantized in superconductors but flux is not [47]. In the present problem, the fluxoid is the quantity on the left-hand side of Eq. (1), and since $(2\pi\Lambda_s/c)K_\phi(\rho, z_0)$ is proportional to $1/\rho$ and $a_\phi(\rho, z_0)$ is very small, the fluxoid is due almost entirely to the current term. Note also that $\Phi_z(\infty, \infty) = 0$; this occurs because all the magnetic flux up through the central layer $z = 0$ is directed radially outward by the screening currents in the layers with $z > 0$.

On the other hand, an infinite stack of pancake vortices, whether straight or not, has quite different magnetic-flux properties. If there is one pancake vortex in every layer at $z = z_n = ns$ ($n = 0, \pm 1, \pm 2, \dots$), then the magnetic flux up through the central layer (and by symmetry any other layer) is

$$\Phi_z(\infty, 0) = \phi_0(s/2\lambda_{\parallel}) \sum_{n=-\infty}^{\infty} e^{-|z_n|/\lambda_{\parallel}} = \phi_0, \quad (13)$$

where the last equality is obtained by evaluating the sum and making use of the property that $s \ll \lambda_{\parallel}$. Similarly, the radial magnetic field at $\rho = \infty$ and $z = 0$ is now zero, since the positive contributions from all the pancake vortices below the central layer are canceled by the negative contributions from the pancake vortices above this layer.

2.2. Continuum Model

The solutions given in Eqs. (5)–(9) can be obtained more easily by regarding the $n \neq 0$ layers as a continuum, characterized by the penetration depth λ_{\parallel} for currents parallel to the layers [11]. Moreover, for a realistic treatment of stacks of just a few superconducting layers, a model accounting for finite layer thickness s is needed. We therefore use the model sketched in Fig. 2 and write the London equation [47] in cylindrical coordinates in the form

$$2\pi\rho[a_\phi(\rho, z) + (4\pi\lambda_{\parallel}^2/c)j_\phi(\rho, z)] = \phi_0\delta_{n0}, \quad (14)$$

where the delta function on the right-hand side accounts for the presence of a vortex aligned along the z axis in the $n = 0$ layer ($|z| < s/2$). Combining this equation with Ampere's law, $j_\phi = (c/4\pi)(\partial b_\rho/\partial z - \partial b_z/\partial \rho)$, and making use of Eqs. (3) and (4), we obtain the partial differential equation

$$\frac{\partial^2 a_\phi}{\partial z^2} + \frac{\partial^2 a_\phi}{\partial \rho^2} + \frac{1}{\rho} \frac{\partial a_\phi}{\partial \rho} - \left(\frac{1}{\rho^2} + \frac{1}{\lambda_{\parallel}^2} \right) a_\phi = -\frac{\phi_0}{2\pi\lambda_{\parallel}^2\rho} \delta_{n0}, \quad (15)$$

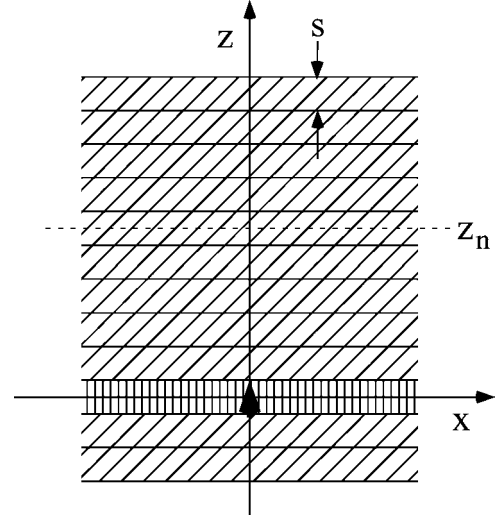


Fig. 2. Continuum model of an infinite stack of superconducting layers with a pancake vortex (bold arrow at the origin) in the layer at $z = z_0 = 0$.

which can be solved by writing $a_\phi(\rho, z)$ in the three regions $z > s/2$, $-s/2 < z < s/2$, and $z < -s/2$ in terms of Hankel components [53] as follows:

$$a_\phi(\rho, z) = \int_0^\infty dq A_a(q) J_1(q\rho) e^{-Qz}, \quad z \geq s/2, \quad (16)$$

$$a_\phi(\rho, z) = \int_0^\infty dq \left[\frac{\phi_0}{2\pi\lambda_{\parallel}^2 Q^2} + A_{0-}(q) e^{-Qz} + A_{0+}(q) e^{Qz} \right] J_1(q\rho), \quad -s/2 \leq z \leq s/2, \quad (17)$$

$$a_\phi(\rho, z) = \int_0^\infty dq A_b(q) J_1(q\rho) e^{-z}, \quad z \leq -s/2, \quad (18)$$

where $Q = (q^2 + 1/\lambda_{\parallel}^2)^{1/2}$. The four unknown functions $A_a(q)$, $A_{0-}(q)$, $A_{0+}(q)$, and $A_b(q)$ can be obtained by applying the boundary conditions of continuity of $a_\phi(\rho, z)$ and $b_\rho(\rho, z)$ [Eq. (3)] at the two interfaces $z = \pm s/2$, carrying out the Hankel transforms using [54]

$$\int_0^\infty d\rho \rho J_1(q\rho) J_1(q'\rho) = (1/q)\delta(q - q'), \quad (19)$$

and solving the four resulting linear equations. The results are

$$A_{0-}(q) = A_{0+}(q) = -\frac{\phi_0}{4\pi\lambda_{\parallel}^2 Q^2} e^{-Qs/2}, \quad (20)$$

$$A_a(q) = A_b(q) = \frac{\phi_0 \sinh(Qs/2)}{2\pi\lambda_{\parallel}^2 Q^2}. \quad (21)$$

Note that $s \ll \lambda_{\parallel}$, such that if we confine our attention to values of $\rho \gg s$, the integrals in Eqs. (16)–(18) are dominated by values of $q \ll 1/s$. We then may make the replacement $\sinh(Qs/2) \rightarrow Qs/2$, which makes $A_a = A_b = \phi_0/2\pi\lambda_{\parallel}^2 Q$, the same as $A(q)$ in Ref. [7] and Sec. 2.1.

The magnetic flux up through a circle of radius ρ in the plane with coordinate z is $\Phi_z(\rho, z) = 2\pi\rho a_{\phi}(\rho, z)$. Evaluating the integrals for $a_{\phi}(\rho, z)$ [Eqs. (16)–(18)] in the limit $\rho \rightarrow \infty$, we can show without making the approximation that $s \ll \lambda_{\parallel}$ that the pancake-vortex-generated magnetic flux through a layer at height z , where $|z| > s/2$, is

$$\Phi_z(\infty, z) = \phi_0 \sinh(s/2\lambda_{\parallel}) e^{-|z|/\lambda_{\parallel}}, \quad (22)$$

and the total magnetic flux up through the central layer at $z = 0$ is

$$\Phi_z(\infty, 0) = \phi_0(1 - e^{-s/2\lambda_{\parallel}}) \approx \phi_0(s/2\lambda_{\parallel}). \quad (23)$$

If there is one pancake vortex in every layer at $z = z_n = ns$ ($n = 0, \pm 1, \pm 2, \dots$), even if they are misaligned, then by summing the contributions given in Eqs. (22) and (23) we find that the magnetic flux up through the central layer (and by symmetry any other layer) is exactly ϕ_0 . If all the vortices are aligned along the z axis, the magnetic-field and current-density distributions reduce to those of the London model [48], for which

$$a_{\phi}(\rho) = \frac{\Phi_z(\rho)}{2\pi\rho} = \frac{\phi_0}{2\pi\rho} \left[1 - \frac{\rho}{\lambda_{\parallel}} K_1\left(\frac{\rho}{\lambda_{\parallel}}\right) \right], \quad (24)$$

$$b_z(\rho) = \frac{\phi_0}{2\pi\lambda_{\parallel}^2} K_0\left(\frac{\rho}{\lambda_{\parallel}}\right), \quad (25)$$

$$j_{\phi}(\rho) = \frac{c\phi_0}{8\pi\lambda_{\parallel}^3} K_1\left(\frac{\rho}{\lambda_{\parallel}}\right), \quad (26)$$

and $b_{\rho}(\rho) = 0$, where $K_n(x)$ is a modified Bessel function.

3. PANCAKE VORTEX IN A SEMI-INFINITE STACK OF SUPERCONDUCTING LAYERS

In Sec. 2, I reviewed the results found in Ref. [7] for a pancake vortex in an infinite stack of superconducting layers, where it is seen that the fields and currents decay exponentially on the scale of λ_{\parallel} above and below the layer containing the pancake vortex.

For a sample of thickness $D \gg \lambda_{\parallel}$ it is therefore clear that the fields and currents generated by pancake vortices that are many λ_{\parallel} from either surface are essentially the same as in Sec. 2. However, the fields and currents are significantly altered when a pancake vortex is less than λ_{\parallel} from the surface of a sample of thickness $D \gg \lambda_{\parallel}$ or when the sample thickness D is comparable with or smaller than λ_{\parallel} . In this section I use the continuum approximation described in Sec. 2.2 to obtain solutions describing the field and currents generated by a vortex in an arbitrary layer of a semi-infinite stack of superconducting layers. In the next section (Sec. 4) I present solutions for a pancake vortex in a finite stack of arbitrary thickness D .

Consider a semi-infinite stack of superconducting layers, with the top surface on the xy plane, such that all the layers are in the region $z < 0$, as sketched in Fig 3. We number the superconducting layers such that the layer $n = 0$ in the region $z_{0-} < z < z_{0+}$, centered at $z = z_0 < 0$, is the one containing the pancake vortex. The other layers are centered at $z = z_n = z_0 + ns$, where positive (negative) n labels layers above (below) the pancake vortex. If there are N_+ layers above the pancake vortex, then the top layer is centered at $z = z_0 + N_+s = D/2 - s/2$. By so numbering the layers, we still can use Eq. (14) as the London fluxoid quantization condition.

As in Sec. 2, we may write the vector potential in cylindrical coordinates as $a(\rho, z) = \hat{\phi}a_{\phi}(\rho, z)$. However, we now have different expressions for $a_{\phi}(\rho, z)$

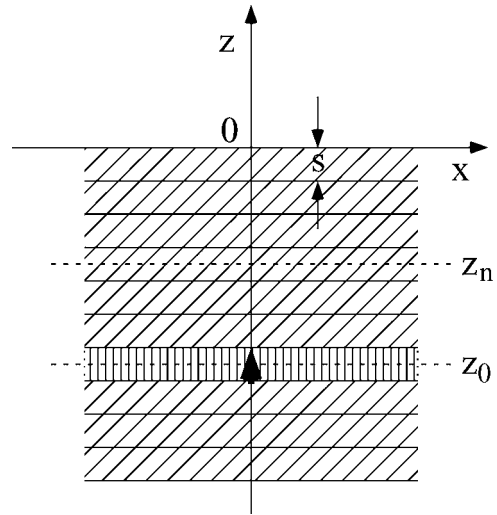


Fig. 3. Continuum model of a semi-infinite stack of superconducting layers in the space $z < 0$ with a pancake vortex (bold arrow) in the layer at $z = z_0$.

in four regions:

$$a_\phi(\rho, z) = \int_0^\infty dq A_>(q) J_1(q\rho) e^{-qz}, \quad z \geq 0, \quad (27)$$

$$a_\phi(\rho, z) = \int_0^\infty dq \left[A_{a-}(q) e^{-Q(z-z_0)} + A_{a+}(q) e^{Q(z-z_0)} \right] \times J_1(q\rho), \quad z_{0+} \leq z \leq 0, \quad (28)$$

$$a_\phi(\rho, z) = \int_0^\infty dq \left[\frac{\Phi_0}{2\pi\lambda_\parallel^2 Q^2} + A_{0-}(q) e^{-Q(z-z_0)} + A_{0+}(q) e^{Q(z-z_0)} \right] J_1(q\rho), \quad z_{0-} \leq z \leq z_{0+}, \quad (29)$$

$$a_\phi(\rho, z) = \int_0^\infty dq A_b(q) J_1(q\rho) e^{Q(z-z_0)}, \quad z \leq z_{0-}, \quad (30)$$

where $Q = (q^2 + \lambda_\parallel^{-2})^{1/2}$ and $z_{0\pm} = z_0 \pm s/2$. The six functions $A_>(q)$, $A_{a-}(q)$, $A_{a+}(q)$, $A_{0-}(q)$, $A_{0+}(q)$, and $A_b(q)$, obtained by applying the six boundary conditions of continuity of $a_\phi(\rho, z)$ and $b_\rho(\rho, z)$ [calculated from Eq. (3)] at $z = 0$, z_{0+} , and z_{0-} , are

$$A_>(q) = \frac{\phi_0 \sinh(Qs/2)}{\pi\lambda_\parallel^2 Q^2 (1 + q/Q)} e^{Qz_0}, \quad (31)$$

$$A_{a-}(q) = \frac{\phi_0 \sinh(Qs/2)}{2\pi\lambda_\parallel^2 Q^2}, \quad (32)$$

$$A_{a+}(q) = \frac{\phi_0 \sinh(Qs/2)}{2\pi\lambda_\parallel^2 Q^2} \left(\frac{1 - q/Q}{1 + q/Q} \right) e^{2Qz_0}, \quad (33)$$

$$A_{0-}(q) = -\frac{\phi_0}{4\pi\lambda_\parallel^2 Q^2} e^{-Qs/2}, \quad (34)$$

$$A_{0+}(q) = -\frac{\phi_0}{4\pi\lambda_\parallel^2 Q^2} \left[e^{-Qs/2} - 2 \sinh(Qs/2) \times \left(\frac{1 - q/Q}{1 + q/Q} \right) e^{2Qz_0} \right], \quad (35)$$

$$A_b(q) = \frac{\phi_0 \sinh(Qs/2)}{2\pi\lambda_\parallel^2 Q^2} \left[1 + \left(\frac{1 - q/Q}{1 + q/Q} \right) e^{2Qz_0} \right]. \quad (36)$$

Although the resulting integrals for $a_\phi(\rho, z)$ and those [via Eqs. (3) and (4)] for $b_\rho(\rho, z)$ and $b_z(\rho, z)$ can easily be calculated numerically, they are too complicated to evaluate analytically for arbitrary ρ and z . On the other hand, we can evaluate them approximately for large ρ . When $\rho \gg \lambda_\parallel$, the values of q that dominate the integrals in Eqs. (27)–(30) via the Bessel function $J_1(q\rho)$ are those of order $1/\rho \ll 1/\lambda_\parallel$,

such that we may replace all quantities under the integral except $J_1(q\rho)$ by their values at $q = 0$. Similarly, because of the factor $\exp(-qz)$ in Eq. (16) we may replace $A_>(q)$ by $A_>(0)$ to evaluate $a_\phi(\rho, z)$ when ρ is small but $z \gg \lambda_\parallel$.

The magnetic flux up through a circle of radius ρ in the plane with coordinate z is $\Phi_z(\rho, z) = 2\pi\rho a_\phi(\rho, z)$. Evaluating the integrals as indicated above for $a_\phi(\rho, z)$ in the limit as $\rho \rightarrow \infty$, we obtain for the total magnetic flux up through the plane with coordinate z :

$$\Phi_z(\infty, z) = 2\phi_0 \sinh(s/2\lambda_\parallel) e^{z_0/\lambda_\parallel}, \quad z \geq 0, \quad (37)$$

$$\Phi_z(\infty, z) = 2\phi_0 \sinh(s/2\lambda_\parallel) \cosh(z/\lambda_\parallel) e^{z_0/\lambda_\parallel}, \quad z_{0+} \leq z \leq 0, \quad (38)$$

$$\Phi_z(\infty, z) = \phi_0 \{ 1 - \cosh[(z - z_0)/\lambda_\parallel] e^{-s/2\lambda_\parallel} + \sinh(s/2\lambda_\parallel) e^{(z+z_0)/\lambda_\parallel} \}, \quad z_{0-} \leq z \leq z_{0+}, \quad (39)$$

$$\Phi_z(\infty, z) = 2\phi_0 \sinh(s/2\lambda_\parallel) \times \cosh(z_0/\lambda_\parallel) e^{z/\lambda_\parallel}, \quad z \leq z_{0-}. \quad (40)$$

When the pancake vortex is in the top layer (i.e., when $z_0 = -s/2$), the magnetic flux $\Phi_z(\infty, 0)$ up through the top surface is approximately $\phi_0(s/\lambda_\parallel)$, since $s/\lambda_\parallel \sim 10^{-2} \ll 1$. When the pancake vortex is in a layer much farther than λ_\parallel from the top surface, the amount of magnetic flux up through the top surface $\Phi_z(\infty, 0)$ [Eq. (37)] becomes exponentially small (recall that $z_0 < 0$). The precise magnetic field distribution generated in the space above the superconductor within λ_\parallel of the origin can be calculated numerically for a given pancake-vortex position z_0 from Eqs. (3), (4), and (27). However, at distances $r = \sqrt{\rho^2 + z^2}$ somewhat larger than λ_\parallel from the origin, we have to good approximation for $z \geq 0$,

$$a_\phi(\rho, z) = \frac{\Phi_z(\infty, 0)}{2\pi\rho} \left(1 - \frac{z}{r} \right), \quad (41)$$

$$b_\rho(\rho, z) = \frac{\Phi_z(\infty, 0)}{2\pi} \frac{\rho}{r^3}, \quad (42)$$

$$b_z(\rho, z) = \frac{\Phi_z(\infty, 0)}{2\pi} \frac{z}{r^3}. \quad (43)$$

In other words, the magnetic field generated by the pancake vortex appears as if generated by a magnetic monopole, with the flux $\Phi_z(\infty, 0)$ [Eq. (37)] spreading out evenly into the hemisphere above the surface. It is important to note that only pancake vortices

within about λ_{\parallel} (or λ_{ab} in the high-temperature superconductors) are visible using Bitter decoration, scanning Hall-probe microscopy, scanning SQUID microscopy, or magneto-optical techniques; pancake vortices deeper than this make an exponentially small contribution to the magnetic field above the surface.

From Eq. (39) we see that the magnetic flux up through the plane $z = z_0$ in the layer containing the pancake vortex is

$$\begin{aligned}\Phi_z(\infty, z_0) &= \phi_0[1 - e^{-s/2\lambda_{\parallel}} + \sinh(s/2\lambda_{\parallel})e^{2z_0/\lambda_{\parallel}}] \\ &\approx \phi_0(s/2\lambda_{\parallel})(1 + e^{2z_0/\lambda_{\parallel}}).\end{aligned}\quad (44)$$

When the pancake vortex is in the top layer (i.e., if $z_0 = -s/2$), the magnetic flux up through this layer is approximately $\phi_0(s/\lambda_{\parallel})$, and when the pancake vortex is deep inside the superconductor (i.e., if $-z_0 \gg \lambda_{\parallel}$), the magnetic flux up through the pancake layer is approximately $\phi_0(s/2\lambda_{\parallel})$, as found in Sec. 2 for the infinite superconductor [Eqs. (12) and (23)].

If there is a pancake vortex in every layer, even if they are misaligned, the total magnetic flux up through any plane with coordinate z is exactly equal to ϕ_0 . This can be shown by replacing z_0 by $z_n = z_0 + ns$, noting that the top layer is centered at $-s/2$, and summing over all n , using Eq. (37) if $z > 0$. On the other hand, if $z < 0$, one must use Eq. (40) for the top layers for which $z_n - s/2 \geq z$, Eq. (39) for the layer containing z for which $z_n - s/2 \leq z \leq z_n + s/2$, and Eq. (38) for the remaining layers for which $z_n + s/2 \leq z$. If all the pancake vortices are aligned along the z axis, the magnetic-field and current-density distributions reduce to those calculated by Pearl [11,53,55] for a vortex in a semi-infinite superconductor.

Scanning Hall-probe experiments visualizing vortices in underdoped, highly anisotropic $\text{YBa}_2\text{Cu}_3\text{O}_{6+x}$ (YBCO) single crystals, where $x = 0.35 - 0.375$, recently have been carried out by Guikema [56]. In the most underdoped crystals, the observations revealed what at first appeared to be ‘‘partial vortices’’ carrying magnetic flux less than ϕ_0 . Guikema concluded, however, that such images are caused by a full vortex that is partially displaced horizontally, i.e., a ‘‘split pancake-vortex stack.’’ The magnetic flux generated above the surface by the two parts of the vortex stack can be calculated as follows. Suppose the bottom portion, consisting of pancake vortices below the plane $z = -d$, is aligned along the z axis, and the top portion, consisting of pancake vortices above the plane $z = -d$, is aligned

parallel to the z axis but at $(x, y) = (x_0, 0)$. Using Eq. (37) to sum the contributions from the pancake vortices in the two portions, one finds that the magnetic flux $\Phi_{\text{bot}} = \phi_0 \exp(-d/\lambda_{\parallel})$ generated by the bottom portion emerges from the vicinity of the origin $(x, y, z) = (0, 0, 0)$, and the magnetic flux $\Phi_{\text{top}} = \phi_0[1 - \exp(-d/\lambda_{\parallel})]$ generated by the top portion emerges from the vicinity of the point $(x, y, z) = (x_0, 0, 0)$. The two flux contributions should be resolvable when the displacement x_0 exceeds the Hall-probe size and the probe’s field sensitivity allows detection of both contributions.

4. PANCAKE VORTEX IN A FINITE STACK OF SUPERCONDUCTING LAYERS

Since all laboratory samples of the high-temperature superconductors are of finite thickness, it is important to examine how the properties of pancake vortices discussed in Sec. 2 are modified when we take the finite thickness into account, including the possibility that the thickness D may be less than the penetration λ_{\parallel} . Let us begin by considering a pancake vortex centered on the z axis in a stack of superconducting layers, each of thickness s , in the region $-D/2 < z < D/2$, as sketched in Fig. 4. As in the previous section, we number the layers such that the layer $n = 0$ at $z = z_0$, where $|z_0| \leq (D/2 - s/2)$, is the one containing the pancake vortex. The other layers are centered at $z = z_n = z_0 + ns$, where positive (negative) n labels layers above (below) the pancake vortex. If there are N_+ layers above the

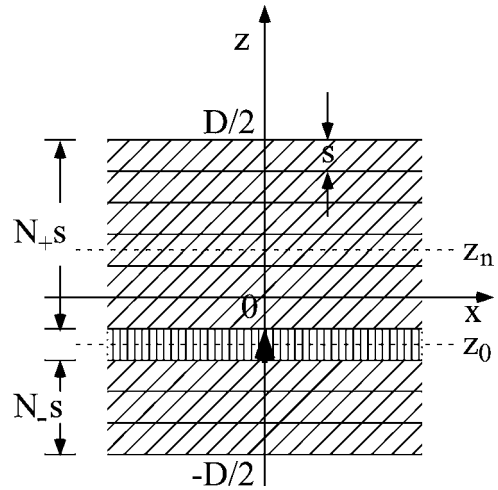


Fig. 4. Continuum model of a stack of superconducting layers in the space $|z| < D/2$ with a pancake vortex (bold arrow) in the layer at $z = z_0$.

pancake vortex, then the top layer is centered at $z = z_0 + N_+s = D/2 - s/2$, and if there are N_- layers below the pancake vortex, then the bottom layer is centered at $z = z_0 - N_-s = -D/2 + s/2$. As in Sec. 2.2, I treat all the layers using the continuum approximation and use Eq. (14) as the London fluxoid quantization condition. In Sec. 4.1, I show how to calculate the fields generated by a pancake vortex in a finite stack of Josephson-decoupled superconducting layers, each of thickness s , with an arbitrary total stack thickness D relative to λ_{\parallel} . In Sec. 4.2, I consider the simplifications that arise when $D \ll \lambda_{\parallel}$, which corresponds to the case of high-temperature superconducting samples consisting of roughly 10 or fewer unit cells along the c direction.

4.1. Finite Stack of Arbitrary Thickness

As in Secs. 2.2 and 3, we write the vector potential in cylindrical coordinates as $\mathbf{a}(\rho, z) = \hat{\phi}a_{\phi}(\rho, z)$. However, we now have different expressions for $a_{\phi}(\rho, z)$ in five regions:

$$a_{\phi}(\rho, z) = \int_0^{\infty} dq A_{>}(q) J_1(q\rho) e^{-q(z-D/2)}, \quad z \geq D/2, \quad (45)$$

$$a_{\phi}(\rho, z) = \int_0^{\infty} dq [A_{a-}(q) e^{-Q(z-D/2)} + A_{a+}(q) e^{Q(z-D/2)}] J_1(q\rho), \quad z_{0+} \leq z \leq D/2, \quad (46)$$

$$a_{\phi}(\rho, z) = \int_0^{\infty} dq \left[\frac{\phi_0}{2\pi\lambda_{\parallel}^2 Q^2} + A_{0-}(q) e^{-Q(z-z_0)} + A_{0+}(q) e^{Q(z-z_0)} \right] J_1(q\rho), \quad z_{0-} \leq z \leq z_{0+}, \quad (47)$$

$$a_{\phi}(\rho, z) = \int_0^{\infty} dq [A_{b-}(q) e^{-Q(z+D/2)} + A_{b+}(q) e^{Q(z+D/2)}] J_1(q\rho), \quad -D/2 \leq z \leq z_{0-}, \quad (48)$$

$$a_{\phi}(\rho, z) = \int_0^{\infty} dq A_{<}(q) J_1(q\rho) e^{q(z+D/2)}, \quad z \leq -D/2, \quad (49)$$

where $Q = (q^2 + \lambda_{\parallel}^{-2})^{1/2}$, the subscript a and (b) denotes the layered region above (below) the pan-

cake vortex, and $z_{0\pm} = z_0 \pm s/2$. The eight functions $A_{>}(q)$, $A_{a-}(q)$, $A_{a+}(q)$, $A_{0-}(q)$, $A_{0+}(q)$, $A_{b-}(q)$, $A_{b+}(q)$, and $A_{<}(q)$, obtained by applying the eight boundary conditions of continuity of $a_{\phi}(\rho, z)$ and $b_{\rho}(\rho, z)$ [calculated from Eq. (3)] at $z = D/2$, z_{0-} , z_{0+} , and $-D/2$, are

$$A_{>}(q) = \frac{\phi_0}{\pi\lambda_{\parallel}^2 Q^2} \sinh(Qs/2) G(q, z_0), \quad (50)$$

$$A_{a-}(q) = \frac{\phi_0}{2\pi\lambda_{\parallel}^2 Q^2} \sinh(Qs/2) (1 + q/Q) G(q, z_0), \quad (51)$$

$$A_{a+}(q) = \frac{\phi_0}{2\pi\lambda_{\parallel}^2 Q^2} \sinh(Qs/2) (1 - q/Q) G(q, z_0), \quad (52)$$

$$A_{0-}(q) = -\frac{\phi_0}{4\pi\lambda_{\parallel}^2 Q^2} [e^{Qs/2} - 2 \sinh(Qs/2) (1 + q/Q) \times G(q, z_0) e^{QD/2} e^{-Qz_0}] \\ = -\frac{\phi_0}{4\pi\lambda_{\parallel}^2 Q^2} [e^{-Qs/2} - 2 \sinh(Qs/2) (1 - q/Q) \times G(q, -z_0) e^{-QD/2} e^{-Qz_0}], \quad (53)$$

$$A_{0+}(q) = -\frac{\phi_0}{4\pi\lambda_{\parallel}^2 Q^2} [e^{-Qs/2} - 2 \sinh(Qs/2) (1 - q/Q) \times G(q, z_0) e^{-QD/2} e^{Qz_0}] \\ = -\frac{\phi_0}{4\pi\lambda_{\parallel}^2 Q^2} [e^{Qs/2} - 2 \sinh(Qs/2) (1 + q/Q) \times G(q, -z_0) e^{QD/2} e^{Qz_0}], \quad (54)$$

$$A_{b-}(q) = \frac{\phi_0}{2\pi\lambda_{\parallel}^2 Q^2} \sinh(Qs/2) (1 - q/Q) G(q, -z_0), \quad (55)$$

$$A_{b+}(q) = \frac{\phi_0}{2\pi\lambda_{\parallel}^2 Q^2} \sinh(Qs/2) (1 + q/Q) G(q, -z_0), \quad (56)$$

$$A_{<}(q) = \frac{\phi_0}{\pi\lambda_{\parallel}^2 Q^2} \sinh(Qs/2) G(q, -z_0), \quad (57)$$

where

$$G(q, z) = \frac{(1 + q/Q) + (1 - q/Q) e^{-QD} e^{-2Qz}}{(1 + q/Q)^2 - (1 - q/Q)^2 e^{-2QD}} \times e^{-QD/2} e^{Qz}, \quad (58)$$

Although the resulting integrals for $a_\phi(\rho, z)$ and those [via Eqs. (3) and (4)] for $b_\rho(\rho, z)$ and $b_z(\rho, z)$ can easily be calculated numerically, they are too complicated to evaluate analytically for arbitrary ρ and z . On the other hand, we can evaluate them approximately for large ρ . When $\rho \gg \lambda_\parallel$, the values of q that dominate the integrals in Eqs. (45)–(49) via the Bessel function $J_1(q\rho)$ are those of order $1/\rho \ll 1/\lambda_\parallel$, such that we may replace all quantities under the integral except $J_1(q\rho)$ by their values at $q = 0$. Similarly, because of the factors $\exp(-qz)$ and $\exp(qz)$ in Eqs. (45) and (49) we may replace $A_>(q)$ by $A_>(0)$ and $A_<(q)$ by $A_<(0)$ to evaluate $a_\phi(\rho, z)$ when ρ is small but $|z| - D/2 \gg \lambda_\parallel$.

The magnetic flux up through a circle of radius ρ in the plane with coordinate z is $\Phi_z(\rho, z) = 2\pi\rho a_\phi(\rho, z)$. Evaluating the integrals as indicated above for $a_\phi(\rho, z)$ in the limit as $\rho \rightarrow \infty$, we obtain for the total magnetic flux up through the plane with coordinate z [12]:

$$\Phi_z(\infty, z) = 2\phi_0 \sinh\left(\frac{s}{2\lambda_\parallel}\right) \cosh\left(\frac{D/2 + z_0}{\lambda_\parallel}\right) / \sinh\left(\frac{D}{\lambda_\parallel}\right), \quad z \geq D/2, \quad (59)$$

$$\Phi_z(\infty, z) = 2\phi_0 \sinh\left(\frac{s}{2\lambda_\parallel}\right) \cosh\left(\frac{D/2 + z_0}{\lambda_\parallel}\right) \times \cosh\left(\frac{D/2 - z}{\lambda_\parallel}\right) / \sinh\left(\frac{D}{\lambda_\parallel}\right), \quad z_{0+} \leq z \leq D/2, \quad (60)$$

$$\Phi_z(\infty, z) = \phi_0 \left\{ 1 - \left[e^{(D-s)/2\lambda_\parallel} \cosh\left(\frac{D/2 - z_0}{\lambda_\parallel}\right) - e^{-(D-s)/2\lambda_\parallel} \cosh\left(\frac{D/2 + z_0}{\lambda_\parallel}\right) \right] \times e^{z/\lambda_\parallel} / 2\sinh\left(\frac{D}{\lambda_\parallel}\right) - \left[e^{(D-s)/2\lambda_\parallel} \cosh\left(\frac{D/2 + z_0}{\lambda_\parallel}\right) - e^{-(D-s)/2\lambda_\parallel} \cosh\left(\frac{D/2 - z_0}{\lambda_\parallel}\right) \right] \times e^{-z/\lambda_\parallel} / 2\sinh\left(\frac{D}{\lambda_\parallel}\right) \right\}, \quad z_{0-} \leq z \leq z_{0+}, \quad (61)$$

$$\Phi_z(\infty, z) = 2\phi_0 \sinh\left(\frac{s}{2\lambda_\parallel}\right) \cosh\left(\frac{D/2 - z_0}{\lambda_\parallel}\right)$$

$$\times \cosh\left(\frac{D/2 + z}{\lambda_\parallel}\right) / \sinh\left(\frac{D}{\lambda_\parallel}\right), \quad -D/2 \leq z \leq z_{0-}, \quad (62)$$

$$\Phi_z(\infty, z) = 2\phi_0 \sinh\left(\frac{s}{2\lambda_\parallel}\right) \cosh\left(\frac{D/2 - z_0}{\lambda_\parallel}\right) / \sinh\left(\frac{D}{\lambda_\parallel}\right), \quad z \leq -D/2. \quad (63)$$

The magnetic flux $\Phi_z(\infty, D/2)$ up through the top surface is given by Eq. (59). When $D \gg \lambda_\parallel$ and a pancake vortex is in the top layer (i.e., when $z_0 = D/2 - s/2$), we obtain $\Phi_z(\infty, D/2) \approx \phi_0(s/\lambda_\parallel)$, which is a tiny fraction of ϕ_0 , since $s/\lambda_\parallel \sim 10^{-2} \ll 1$. As a function of the distance $D/2 - z_0$ of the pancake vortex from the top surface, we see that $\Phi_z(\infty, D/2) \approx \phi_0(s/\lambda_\parallel)\exp[-(D/2 - z_0)/\lambda_\parallel]$. When $D \ll \lambda_\parallel$, we find that $\Phi_z(\infty, D/2) \approx \phi_0(s/D) = \phi_0/N$, independent of the position z_0 of the pancake vortex within the stack, where $N = D/s$ is the number of layers in the sample. When $N = D/s = 1$, $\Phi_z(\infty, D/2) = \phi_0$, because our results then reduce to those of Pearl [13–15], who calculated the field and current distribution generated by a vortex in a film of thickness much less than the London penetration depth. The precise magnetic field distribution generated in the space above the superconductor can be calculated numerically for a given z_0 from Eqs. (3), (4), and (45). However, at distances $r_+ = \sqrt{\rho^2 + (z - D/2)^2}$ from the point on the surface directly above the pancake vortex that are larger than λ_\parallel when $D > 2\lambda_\parallel$ or larger than the two-dimensional screening length $\Lambda_D = 2\lambda_\parallel^2/D$ when $D < 2\lambda_\parallel$, we have to good approximation for $z \geq D/2$

$$a_\phi(\rho, z) = \frac{\Phi_z(\infty, D/2)}{2\pi\rho} \left[1 - \frac{(z - D/2)}{r_+} \right], \quad (64)$$

$$b_\rho(\rho, z) = \frac{\Phi_z(\infty, D/2)}{2\pi} \frac{\rho}{r_+^3}, \quad (65)$$

$$b_z(\rho, z) = \frac{\Phi_z(\infty, D/2)}{2\pi} \frac{(z - D/2)}{r_+^3}. \quad (66)$$

In other words, the magnetic field generated by the pancake vortex appears as if generated by a positive magnetic monopole, with the flux $\Phi_z(\infty, D/2)$ [Eq. (59)] spreading out into the hemisphere above the surface.

Similar statements can be made about the magnetic flux $\Phi_z(\infty, -D/2)$ up through the bottom surface [Eq. (63)]. At large distances $r_- = \sqrt{\rho^2 + (z + D/2)^2}$ from the point on the surface directly below the pancake vortex, the magnetic field

appears as if generated by a negative magnetic monopole.

From Eq. (61), we see that the magnetic flux up through the plane $z = z_0$ in the layer containing the pancake vortex is

$$\Phi_z(\infty, z_0) = \phi_0 \left\{ 1 - \left[\sinh\left(\frac{D-s/2}{\lambda_{\parallel}}\right) - \sinh\left(\frac{s}{2\lambda_{\parallel}}\right) \right] \times \cosh\left(\frac{2z_0}{\lambda_{\parallel}}\right) / \sinh\left(\frac{D}{\lambda_{\parallel}}\right) \right\}. \quad (67)$$

When $D \gg \lambda_{\parallel}$, the dependence of this magnetic flux upon the distance $(D/2 - |z_0|)$ from the top or bottom surface is given by $\Phi_z(\infty, z_0) \approx \phi_0(s/2\lambda_{\parallel})\{1 + \exp[-2(D/2 - |z_0|)/\lambda_{\parallel}]\}$. When the pancake vortex is in the top or bottom layer (i.e., if $|z_0| = D/2 - s/2$), the magnetic flux up through this layer is approximately $\phi_0(s/\lambda_{\parallel})$, and when the pancake vortex is deep inside the superconductor (i.e., if $D/2 - |z_0| \gg \lambda_{\parallel}$), the magnetic flux up through the pancake layer is approximately $\phi_0(s/2\lambda_{\parallel})$ as found in Sec. 2 for the infinite superconductor [Eqs. (12) and (23)]. When $D \ll \lambda_{\parallel}$, we see that $\Phi_z(\infty, z_0) \approx \phi_0(s/D) = \phi_0/N$, independent of the position z_0 of the pancake vortex within the stack, where $N = D/s$ is the number of layers in the sample.

If there is a pancake vortex in every layer, even if they are misaligned, the total magnetic flux up through any plane with coordinate z is exactly equal to ϕ_0 . This can be shown by replacing z_0 by $z_n = z_0 + ns$ and summing over all n , using Eq. (59) if $z > D/2$ or Eq. (63) if $z < -D/2$. On the other hand, if $|z| < D/2$, one must use Eq. (62) for the top layers for which $z_n - s/2 \geq z$, Eq. (61) for the layer containing z for which $z_n - s/2 \leq z \leq z_n + s/2$, and Eq. (60) for the remaining layers for which $z_n + s/2 \leq z$. If all the vortices are aligned along the z axis, the magnetic-field and current-density distributions reduce to those given in Ref. [52] when $\xi_v = 0$.

It is possible that scanning Hall-probe or magneto-optical experiments may be able to detect partial vortices or split pancake-vortex stacks [56] carrying magnetic flux less than ϕ_0 in samples of highly anisotropic layered superconductors of thickness $D < \lambda_{\parallel}$. The magnetic flux generated above the surface $z = D/2$ by the two parts of the vortex stack can be calculated as follows. Suppose the bottom portion, consisting of pancake vortices below the plane $z = D/2 - d$, is aligned along the z axis, and the top portion, consisting of pancake vortices above the plane $z = D/2 - d$, is aligned parallel to the z axis but at $(x, y) = (x_0, 0)$. Using Eq. (59) to sum

the contributions from the pancake vortices in the two portions, one finds that the magnetic flux $\Phi_{\text{bot}} = \phi_0 \sinh[(D-d)/\lambda_{\parallel}] / \sinh(D/\lambda_{\parallel})$ generated by the bottom portion emerges from the vicinity of the point $(x, y, z) = (0, 0, D/2)$, and the magnetic flux $\Phi_{\text{top}} = \phi_0\{1 - \sinh[(D-d)/\lambda_{\parallel}] / \sinh(D/\lambda_{\parallel})\}$ generated by the top portion emerges from the vicinity of the point $(x, y, z) = (x_0, 0, D/2)$. The two flux contributions should be resolvable when the displacement x_0 exceeds the Hall-probe size and the probe's field sensitivity allows detection of both contributions. Note that $\Phi_{\text{bot}} = \Phi_{\text{top}} = \phi_0/2$ when $d = D/2 \ll \lambda_{\parallel}$.

4.2. Finite Stack of Thickness $D \ll \lambda_{\parallel}$

Considerable simplifications occur when the thickness $D = Ns$ of the stack is much less than the in-plane penetration depth λ_{\parallel} [11]. It is well known from the work of Refs. [13] and [14] that when $D \ll \lambda_{\parallel}$ the characteristic screening length in isolated films is not λ_{\parallel} but rather the 2D screening length $\Lambda_D = 2\lambda_{\parallel}^2/D$. This is also true for the case of Josephson-decoupled stacks of total thickness D considered here. We may derive equations for $a_{\phi}(\rho, z)$, $b_{\rho}(\rho, z)$, and $b_z(\rho, z)$ valid for $D \ll \lambda_{\parallel}$ and $\rho \gg \lambda_{\parallel}$ by starting with Eqs. (45)–(49), applying Eqs. (3) and (4), and making the replacement $e^{\pm Qz} = \cosh(Qz) \pm \sinh(Qz)$. Since we are most interested in values of ρ of the order of Λ_D or larger, because of the presence of $J_1(q\rho)$ the dominant values of q in the resulting integrals are of the order of $q \sim 1/\Lambda_D \ll 1/\lambda_{\parallel}$, such that Q can be replaced by $1/\Lambda_D$, and small quantities of the order of D/λ_{\parallel} and $q\lambda_{\parallel}$ are of the same order of magnitude. Expanding in powers of the small quantities (D/λ_{\parallel} and $q\lambda_{\parallel}$), we find that both $a_{\phi}(\rho, z)$ and $b_z(\rho, z)$ are to lowest order independent of z , with small correction terms of the order of D/λ_{\parallel} , such that to good approximation we may write these quantities as

$$a_{\phi}(\rho, z) = \frac{\phi_0}{2\pi N} \int_0^{\infty} dq \frac{J_1(q\rho)}{1 + q\Lambda_D} e^{-q(z-D/2)}, \quad z \geq D/2, \quad (68)$$

$$a_{\phi}(\rho, z) = \frac{\phi_0}{2\pi N} \int_0^{\infty} dq \frac{J_1(q\rho)}{1 + q\Lambda_D}, \quad -D/2 \leq z \leq D/2, \quad (69)$$

$$a_{\phi}(\rho, z) = \frac{\phi_0}{2\pi N} \int_0^{\infty} dq \frac{J_1(q\rho)}{1 + q\Lambda_D} e^{q(z+D/2)}, \quad z \leq -D/2, \quad (70)$$

$$b_z(\rho, z) = \frac{\phi_0}{2\pi N} \int_0^\infty dq \frac{qJ_0(q\rho)}{1+q\Lambda_D} e^{-q(z-D/2)}, \quad z \geq D/2, \quad (71)$$

$$b_z(\rho, z) = \frac{\phi_0}{2\pi N} \int_0^\infty dq \frac{qJ_0(q\rho)}{1+q\Lambda_D}, \quad -D/2 \leq z \leq D/2, \quad (72)$$

$$b_z(\rho, z) = \frac{\phi_0}{2\pi N} \int_0^\infty dq \frac{qJ_0(q\rho)}{1+q\Lambda_D} e^{q(z+D/2)}, \quad z \leq -D/2. \quad (73)$$

On the other hand, the radial component of the magnetic field varies strongly with z :

$$b_\rho(\rho, z) = \frac{\phi_0}{2\pi N} \int_0^\infty dq \frac{qJ_1(q\rho)}{1+q\Lambda_D} e^{-q(z-D/2)}, \quad z \geq D/2, \quad (74)$$

$$b_\rho(\rho, z) = \frac{\phi_0}{2\pi N} \int_0^\infty dq \frac{qJ_1(q\rho)}{1+q\Lambda_D}, \quad z = D/2, \quad (75)$$

$$b_\rho(\rho, z) = b_\rho(\rho, D/2) + \frac{(D/2-z)a_\phi(\rho)}{(D/2)\Lambda_D}, \quad z_{0+} \leq z \leq D/2, \quad (76)$$

$$b_\rho(\rho, z) = b_\rho(\rho, D/2) + \frac{(D/2-z)a_\phi(\rho)}{(D/2)\Lambda_D} - \frac{(z_{0+}-z)\phi_0}{(D/2)2\pi\Lambda_D\rho}, \quad z_{0-} \leq z \leq z_{0+}, \quad (77)$$

$$b_\rho(\rho, z) = b_\rho(\rho, D/2) + \frac{(D/2-z)a_\phi(\rho)}{(D/2)\Lambda_D} - \frac{s}{(D/2)2\pi\Lambda_D\rho}, \quad -D/2 \leq z \leq z_{0-}, \quad (78)$$

$$b_\rho(\rho, z) = b_\rho(\rho, D/2) - \frac{2}{\Lambda_D} \left[\frac{\phi_0}{2\pi N\rho} - a_\phi(\rho) \right] = b_\rho(\rho, -D/2), \quad z = -D/2, \quad (79)$$

$$b_\rho(\rho, z) = -\frac{\phi_0}{2\pi N} \int_0^\infty dq \frac{qJ_1(q\rho)}{1+q\Lambda_D} e^{q(z+D/2)}, \quad \times z \leq -D/2, \quad (80)$$

where we use $a_\phi(\rho)$ to denote the vector potential in the region $|z| \leq D/2$, since $a_\phi(\rho, z)$ is very nearly independent of z . The sheet current $K_n(\rho) = K_\phi(\rho, z_n) = s j_\phi(\rho, z_n)$ in layer n can be obtained from either $j_\phi(\rho, z) = (c/4\pi)\partial b_\rho(\rho, z)/\partial z$ or the fluxoid quantization condition [Eq. (14)]:

$$K_n(\rho) = \frac{c}{2\pi\Lambda_s} \left[\frac{\phi_0}{2\pi\rho} \delta_{n0} - a_\phi(\rho) \right], \quad (81)$$

Table I. Results for One Pancake Vortex in a Stack of N Superconducting Layers of Total Thickness $D = N_s \ll \lambda_{||}$ in the Limits $D \ll \rho \ll \Lambda_D = 2\lambda_{||}^2/D$ and $\rho \gg \Lambda_D$ [Since D is very small, $r = (\rho^2 + z^2)^{1/2}$ may be regarded as the distance from the pancake vortex, and $|z|$ may be regarded as the distance from the top or bottom surface]

Physical quantity	$\rho \ll \Lambda_D$	$\rho \gg \Lambda_D$
$a_\phi(\rho, z)$	$\frac{\phi_0(r- z)}{2\pi N\Lambda_D\rho}$	$\frac{\phi_0(r- z)}{2\pi N\rho r}$
$a_\phi(\rho, 0)$	$\frac{\phi_0}{2\pi N\Lambda_D}$	$\frac{\phi_0}{2\pi N\rho}$
$\Phi_z(\rho, z) = 2\pi\rho a_\phi(\rho, z)$	$\frac{\phi_0(r- z)}{N\Lambda_D}$	$\frac{\phi_0(r- z)}{Nr}$
$\Phi_z(\rho, z) = 2\pi\rho a_\phi(\rho, 0)$	$\phi_0\rho/N\Lambda_D$	ϕ_0/N
$b_\rho(\rho, z), z = \pm z $	$\pm\frac{\phi_0(r- z)}{2\pi N\Lambda_D\rho}$	$\pm\frac{\phi_0\rho}{2\pi Nr^3}$
$b_\rho(\rho, \pm D/2)$	$\pm\frac{\phi_0}{2\pi N\Lambda_D\rho}$	$\pm\frac{\phi_0}{2\pi N\rho^2}$
$b_z(\rho, z)$	$\frac{\phi_0}{2\pi N\Lambda_D}$	$\frac{\phi_0 z}{2\pi Nr^3}$
$b_z(\rho, 0)$	$\frac{\phi_0}{2\pi N\Lambda_D}$	$\frac{\phi_0\lambda_D}{2\pi N\rho^3}$
$K_0(\rho) = K_\phi(\rho, z_0)$	$\frac{c\phi_0}{4\pi^2 N\Lambda_D\rho}$	$\frac{c\phi_0(N-1)}{4\pi^2 N^2\Lambda_D\rho}$
$K_n(\rho) = K_\phi(\rho, z_n), n \neq 0$	$-\frac{c\phi_0}{4\pi^2 N^2\Lambda_D^2}$	$-\frac{c\phi_0}{4\pi^2 N^2\Lambda_D\rho}$
$K_D(\rho)$	$\frac{c\phi_0}{4\pi^2 N\Lambda_D\rho}$	$\frac{c\phi_0}{4\pi^2 N\rho^2}$

where $\Lambda_s = 2\lambda_{||}^2/s = N\Lambda_D$. The net sheet current through the thickness D is the sum of the K_n :

$$K_D(\rho) = \sum_{n=-N}^{N+} K_n(\rho) = \frac{c}{2\pi\Lambda_D} \left[\frac{\phi_0}{2\pi N\rho} - a_\phi(\rho) \right]. \quad (82)$$

The integrals appearing in Eqs. (68)–(82), which are evaluated in the Appendix, have simple forms in the limits $D \ll \rho \ll \Lambda_D$ and $\rho \gg \Lambda_D$. The corresponding expressions for the physical quantities we have calculated in this section are given in Table I. The magnetic-field and current-density distributions reduce to the thin-film results of Pearl [13,14] when $N = 1$ and $D = s$ or when each of the N layers contains a pancake vortex on the z axis.

5. FORCES

The force on a second pancake vortex at the position (ρ, z_n) due to a pancake vortex centered on the z axis at $(0, z_0)$ can be calculated from the Lorentz force [57]. Since pancake vortices cannot move out of their planes, the force is directed parallel to the planes in the radial $\hat{\rho}$ direction:

$$F_\rho(\rho) = K_\phi(\rho, z_n)\phi_0/c, \quad (83)$$

where

$$K_\phi(\rho, z_n) = \frac{c}{2\pi\Lambda_s} \left[\frac{\phi_0}{2\pi\rho} \delta_{n0} - a_\phi(\rho, z_n) \right] \quad (84)$$

is the sheet-current density and $a_\phi(\rho, z_n)$ is the vector potential at (ρ, z_n) generated by the pancake vortex at $(0, z_0)$, and $\Lambda_s = 2\lambda_\parallel^2/s = N\Lambda_D$.

If both pancake vortices are in the same plane, the interaction force is always repulsive and in an infinite or semi-infinite stack of superconducting layers is given to excellent approximation by

$$F_\rho(\rho) = \frac{\phi_0^2}{4\pi^2\Lambda_s\rho} \quad (85)$$

for all ρ . The reason for this is that the vector potential in Eq. (84) obeys $a_\phi(\rho, z_0) \leq (s/\lambda_\parallel)(\phi_0/2\pi\rho) \ll \phi_0/2\pi\rho$, as shown in Secs. 2 and 3. However, for a finite stack of thickness $D \ll \lambda_\parallel$ consisting of N layers, Eq. (85) holds only for small ρ ($\rho \ll \Lambda_D$), where the vector potential in Eq. (84) is much smaller than $\phi_0/2\pi\rho$. As discussed in Sec. 4.1, the magnetic flux at infinite radius $\Phi_z(\infty, z_0)$ up through the pancake-vortex layer is approximately ϕ_0/N , which means that $a_\phi(\rho, z_0) \approx \phi_0/2\pi N\rho$ for large ρ , and

$$F_\rho(\rho) = \frac{(N-1)}{N} \frac{\phi_0^2}{4\pi^2\Lambda_s\rho}, \quad \rho \gg \Lambda_D. \quad (86)$$

In the special case when $N = 2$, the repulsive force given in Eq. (86) is half that in Eq. (85).

If the two pancake vortices are in different planes, the $\phi_0/2\pi\rho$ term in Eq. (84) is absent, and the interaction force is given by

$$F_\rho(\rho) = -\frac{\phi_0 a_\phi(\rho, z_n)}{2\pi\Lambda_s}. \quad (87)$$

Because $a_\phi(\rho, z_n)$ is always positive, the interaction force is always negative, i.e., in a direction so as to cause the two pancake vortices to become aligned along the same vertical axis. For the general case, it is not a simple matter to calculate the spatial dependence of the attractive force between pancake vortices in different layers, as can be seen from the expressions for $a_\phi(\rho, z)$ given in previous sections. However, we can say that for an infinite or semi-infinite stack of superconducting layers, the magnitude of this attractive force is orders of magnitude smaller than the repulsive force between pancake vortices in the same layer. The attractive force between vortices in different layers in an infinite stack (or deep inside a semi-infinite stack) has a range λ_\parallel in the z direction. Equation (5) shows that the attractive force in the infinite stack vanishes exponentially when the interplanar separation of the pancakes along the z direction exceeds λ_\parallel . For a finite stack of thickness $D = Ns \ll \lambda_\parallel$, we find that the attractive force between pancake vortices in different

layers is

$$F_\rho(\rho) = -\frac{\phi_0^2}{4\pi^2\Lambda_s^2} = -\frac{\phi_0^2}{4\pi^2N^2\Lambda_D^2}, \quad D \ll \rho \ll \Lambda_D, \quad (88)$$

which agrees with the force in the infinite stack calculated from Eq. (9) when $|z_n| \ll \rho \ll \lambda_\parallel$, and

$$F_\rho(\rho) = -\frac{\phi_0^2}{4\pi^2N^2\Lambda_D\rho}, \quad \rho \gg \Lambda_D. \quad (89)$$

For the special case of two layers ($N = 2$) and a separation $\rho \gg \Lambda_D$, the magnitude of the attractive force exerted by a pancake vortex in one layer upon a pancake vortex in the other layer [Eq. (89)] is equal to the magnitude of the repulsive force between two pancake vortices in the same layer [Eq. (86) with $\Lambda_s = N\Lambda_D$].

The energy per unit length of a uniformly tilted infinite stack of pancake vortices in an infinite stack of superconducting layers was calculated in Ref. [7]. The corresponding line tension $T(\theta)$ was calculated in Ref. [58] as a function of the angle θ relative to the z axis and found to be positive only for $\theta < 51.8^\circ$, indicating an instability beginning at 51.8° . Further calculations [58] showed that, because pancake vortices energetically prefer to line up parallel to the z axis, the energy for an infinite stack of pancake vortices with a large average tilt angle is reduced when the stack breaks up into shorter stacks parallel to the z axis with kinks between them. Pe *et al.* [59] calculated the equilibrium positions of a stack of pancake vortices in a finite stack of Josephson-decoupled layers when equal and opposite transport currents are applied to the top and bottom layers. They found that the pancake vortices in the top and bottom layers have large displacements to the left and right, while the other vortices all remain close to the z axis. Related model calculations were carried out in Ref. [60] for moving two-dimensional pancake vortex lattices in a finite stack of magnetically coupled superconducting thin films with transport current only in the top layer. For small currents, the entire electromagnetically coupled vortex array moves uniformly in the direction of the Lorentz force but with a large displacement of the pancake vortices in the top layer relative to the others, which remain in nearly straight lines perpendicular to the layers. Above a critical decoupling current, the 2D vortex array in the top layer periodically slips relative to the arrays in the other layers, and the dc current-voltage characteristics for

the top and bottom layers resemble those reported in Refs. [45] and [46] for the dc transformer.

6. JOSEPHSON COUPLING

The equations underlying the solutions presented in Secs. 2, 3, and 4 assume no interlayer Josephson coupling. Implicit in these solutions is the assumption that the component of the magnetic field parallel to the layers spreads out uniformly in the radial direction. This is consistent with the idea that if a magnetic field is applied parallel to a stack of Josephson-decoupled layers, the field will penetrate uniformly between the layers.

When the layers are Josephson-coupled, however, parallel magnetic fields penetrate the structure in the form of quantized Josephson vortices [61,62]. As discussed in Ref. [62], Josephson vortices in the high-temperature superconductors have highly elliptical current and field patterns. Since the decay length for currents perpendicular to the layers is λ_c and that for currents parallel to the layers is λ_{ab} , the ratio of the width of the pattern parallel to the layers to the height perpendicular to the layers is $\gamma = \lambda_c/\lambda_{ab}$ at large distances from the nonlinear Josephson core. For a high- κ Abrikosov vortex [49] in an isotropic superconductor, the decay length at large distances is the penetration depth λ , and the currents in the nonlinear core vary on the much smaller length scale of the coherence length ξ . The behavior in a Josephson vortex is analogous. The small length scale for spatial variation of the Josephson currents in the vortex core (whose axis is centered in the insulating layer between two adjacent superconducting layers) is the Josephson length [62,63] $\lambda_J = \gamma s$, while the corresponding length scale for the return of these currents parallel to the layers is s , such that the ratio of the width to the height of the Josephson core is $\gamma = \lambda_J/s = \lambda_c/\lambda_{ab}$.

In the presence of interlayer Josephson coupling, the magnetic-field and current-density distributions generated by a pancake vortex are unaltered at short distances but are strongly affected at distances of the order of λ_J and λ_c . To give an example, imagine an infinite stack of semi-infinite Josephson-coupled superconducting layers, all parallel to the xy plane, filling the half-space $x > 0$, such that the surface coincides with the plane $x = 0$. Imagine creating a pancake vortex at the origin in the superconducting layer $n = 0$ and moving it in to a distance x_0 . The magnetic-field and current-density distributions,

including the effects of a dipole-like stray field that leaks out into the space $x < 0$, have been calculated as a function of x_0 in Ref. [64] under the assumption of very weak Josephson coupling. In the presence of Josephson coupling, however, the component of the magnetic field parallel to the layers cannot penetrate with a power-law dependence to large distances but rather must decay exponentially with the decay length λ_c , because this component of the field induces Josephson currents to flow perpendicular to the layers. As the pancake vortex moves deeper into the stack, the Josephson coupling begins to play a greater role. When the pancake vortex is a distance λ_J or greater from the surface, a Josephson core region of width $2\lambda_J$ appears in the region between the vortex axis and the surface. Finally, at distances such that $x_0 \gg \lambda_c$, the current and field distribution can be characterized as a pancake vortex in which the fields at distances less than λ_J from the axis are nearly the same as in the Josephson-decoupled case, and the magnetic flux carried up through the pancake layer $z = 0$ is $\phi_0 (s/2\lambda_{\parallel})$. However, this magnetic flux does not flow radially outward to infinity as in the Josephson-decoupled case but instead is confined within a highly elliptical field distribution consisting of an overlapping Josephson vortex-antivortex pair, which links the pancake vortex to the surface. Recall that when a straight vortex is at a distance x from the surface of an isotropic superconductor of penetration depth λ , the magnetic flux inside the superconductor, calculated accounting for the image vortex at $-x$, is $\phi_0[1 - \exp(-x/\lambda)]$. As a pancake vortex moves from the surface to a position x_0 deep within the superconductor, it drags along a Josephson vortex (carrying magnetic flux in the $+x$ direction) whose axis is in the insulating layer at $z = -s/2$, and it also drags along a Josephson antivortex (carrying magnetic flux in the $-x$ direction) whose axis is in the insulating layer at $z = +s/2$. Accounting for the overlapping field distributions, which nearly cancel each other, we find that the magnetic flux carried in the $+x$ direction through the space $z < 0$ is $\phi_0[1 - \exp(-s/2\lambda_{\parallel})] \approx \phi_0(s/2\lambda_{\parallel})$; the same amount of magnetic flux is carried back in the $-x$ direction through the space $z > 0$.

To give another example, consider an infinite stack of pancake vortices initially aligned along the z axis in an infinite stack of Josephson-decoupled superconducting layers. As discussed at the end of Sec. 2, the field and current distributions reduce to those of a line vortex in an isotropic superconductor of penetration depth λ_{\parallel} [48]. The magnetic field is

everywhere perpendicular to the layers. Now imagine displacing all of the pancake vortices in the space $z > s/2$ by a distance x_0 in the x direction, such that the pancake vortex stack now has a kink at $z = s/2$. In the absence of Josephson coupling, the resulting field and current distributions can be obtained by superposing those given in Sec. 2. A component of the field parallel to the layers must arise in order to displace the magnetic flux ϕ_0 whose distribution is centered on the z axis for $z \ll -\lambda_{\parallel}$ to a distribution centered on the line $(x, y) = (x_0, 0)$ for $z \gg \lambda_{\parallel}$. The component of the field parallel to the layers has a dipole-like distribution in any plane $z = \text{const}$, with a power-law dependence at large distances, but it decreases exponentially for $|z| > \lambda_{\parallel}$ because of the screening currents that flow parallel to the layers. In the presence of interlayer Josephson coupling, the above picture is altered, and it is now useful to think of kinked vortices as stacks of pancake vortices connected by Josephson strings (short pieces of Josephson vortices). The axes of the Josephson strings are confined to the insulating regions between superconducting layers. As a consequence of the Josephson coupling, the radial component of the magnetic field is screened on the length scale of λ_c by the induced Josephson currents, which flow perpendicular to the layers. Although there is little perturbation of the original field distribution when $x_0 < \lambda_J$, the Josephson length, this situation is altered when $x_0 > \lambda_J$, because in this case a nonlinear Josephson core appears along the string connecting the two pancake vortices centered at $(x, y, z) = (0, 0, 0)$ and $(x, y, z) = (x_0, 0, s)$. The Josephson-energy cost of the Josephson string coupling the two semi-infinite stacks of pancake vortices is approximately (taking logarithmic terms to be of order unity) [11,63,65–68]

$$E_{\text{short}}(x_0) \approx (\phi_0/4\pi)^2 x_0^2 / s \lambda_c^2, \quad x_0 < \lambda_J = (\lambda_c / \lambda_{ab}) s, \quad (90)$$

when the Josephson string is short and its core is not fully formed. The Josephson-energy cost is of the order of [11,61–63,65–69]

$$E_{\text{long}}(x_0) \approx (\phi_0/4\pi)^2 x_0 / \lambda_{ab} \lambda_c, \quad x_0 > \lambda_J = (\lambda_c / \lambda_{ab}) s, \quad (91)$$

when the Josephson string is long and its core is more fully formed. However, it is not until $x_0 \gg \lambda_c$ that a fully formed Josephson vortex (with width $2\lambda_c$ and height $2\lambda_{ab}$) can stretch out between the upper and lower parts of the split stack of pancake vortices. In this case the energy cost of the Josephson string

coupling the two semi-infinite stacks of pancake vortices reduces to $(\phi_0 H_{c1,ab} / 4\pi) x_0$, where $\phi_0 H_{c1,ab} / 4\pi$ is the energy per unit length of an isolated Josephson vortex parallel to the layers [61,67,69,70] and

$$H_{c1,ab} = \frac{\phi_0}{4\pi \lambda_{ab} \lambda_c} \left[\ln \left(\frac{\lambda_{ab}}{s} \right) + 1.55 \right]. \quad (92)$$

is the lower critical field parallel to the layers.

In anisotropic superconductors consisting of Josephson-coupled superconducting layers, one may always regard the vortex structure as consisting of a superposition of 2D pancake vortices, which carry magnetic flux up through the layers, and Josephson vortices (or strings), which carry magnetic flux parallel to the layers but no net flux perpendicular to the layers. In transport experiments involving vortex motion, the voltages are given by the Josephson relations [31]. The dc voltage parallel to the layers is $V_{\parallel} = (h/2e)v_{\parallel}$, where v_{\parallel} is the time-averaged rate with which 2D pancake vortices cross a line between the contacts, and the dc voltage perpendicular to the layers is proportional to $V_{\perp} = (h/2e)v_{\perp}$, where v_{\perp} is the time-averaged rate with which the axes of Josephson vortices (or strings) cross a line between the contacts.

When the Josephson coupling is strong, vortex lines tilted with respect to the z (or c) axis can be described as tilted stacks of 2D pancake vortices or as a tilted lattice, where pancakes in adjacent layers are connected by Josephson strings. Such vortices, sometimes called kinked vortex lines [71,72] have been studied by numerous authors [70,73–76]. However, when the Josephson coupling is very weak, a magnetic field applied at a small angle relative to the layers can produce a structure consisting of two perpendicular interpenetrating lattices [63,77,78] (called a combined lattice [63] or crossing lattices [78]): a lattice of pancake vortices aligned nearly perpendicular to the layers and a lattice of Josephson vortices parallel to the layers. The interaction between the two kinds of vortices leads to striking chain-like vortex patterns in highly anisotropic Bi-2212, which have been observed by Bitter decoration [79,80] and scanning Hall-probe microscopy [35,81,82]. Both techniques reveal the positions of 2D pancake vortices within about λ_{ab} of the surface. As shown by Koshelev [83], in highly anisotropic layered superconductors the interactions between pancake vortices and Josephson vortices lead to deformations of both the pancake-vortex and Josephson-vortex crystals and to pinning of Josephson vortices by pancake vortices.

At high temperatures and applied magnetic fields, the vortex lattice melts [84–88], and this process has even been directly visualized in Bi-2212 by scanning Hall-probe microscopy [89,90]. The authors of Ref. [90] used the formalism of Sec. 4.1 A to infer the Lindemann parameter from the rms thermal fluctuations of pancake vortices versus magnetic field just below the melting transition. Much experimental and theoretical research has been devoted to vortex-lattice melting, and the reader is referred to reviews by Blatter *et al.* [91] and Brandt [92] for a more complete discussion of this topic.

The pinning of vortices by point defects is another topic where the interactions between pancake vortices and Josephson vortices play a key role. This difficult subject is further complicated by the effects of thermal fluctuations, especially in the high-temperature superconductors at the elevated temperatures where potential applications are most interesting. The reader is referred to the above reviews [91,92] and the recent paper by Kierfeld [93] for further details about this subject.

7. SUMMARY

In this paper, I have presented solutions that permit the calculation of the magnetic-field and current-density distributions generated by a single 2D pancake vortex in an infinite stack (Sec. 2), semi-infinite stack (Sec. 3), or a finite-thickness stack (Sec. 4) of Josephson-decoupled superconducting layers. I have shown in Sec. 5 how to calculate the electromagnetic forces between two pancake vortices, and in Sec. 6, I have discussed some of the ways that interlayer Josephson coupling modifies the results.

The results of this paper should be useful to those using probes (such as scanning Hall-probe microscopy, scanning SQUID microscopy, Bitter decoration, and magneto-optics) of the vortex-generated magnetic-field distributions above anisotropic high-temperature superconductors. If the sample surface is parallel to the cuprate planes, these probes measure chiefly the magnetic fields generated by pancake vortices within about λ_{ab} of the top surface. Although Josephson vortices (or strings) produce no net magnetic flux through the top surface, they can produce dipole-like stray fields if they are within λ_{ab} of the surface. On the other hand, if the sample surface is normal to the cuprate planes, such probes measure chiefly the magnetic fields generated by Josephson vortices within about λ_c of the sample

surface, although pancake vortices within λ_{ab} of the surface can produce dipole-like stray fields outside the sample [64].

The pancake-vortex field and current distributions given in Secs. 2–4 also could be useful in analyzing experiments such as Lorentz microscopy [94–100] that probe the magnetic-field distribution throughout the sample thickness.

Since the London model is at the heart of the above pancake-vortex calculations, the resulting theoretical field and current distributions have unphysical singularities at the pancake-vortex core, which is of size $\sim \xi_{ab}$. Such singularities should have no experimental consequences for the above probes, which have insufficient resolution to reveal details at this length scale. However, for probes of higher resolution it may be necessary to take into account the fact that the circulating current density reaches a maximum at $\rho \approx \xi_{ab}$, and vanishes linearly as $\rho \rightarrow 0$, such that the singularity of the magnetic field at the pancake-vortex core is removed. The core effects could be treated approximately by using a vortex-core model that employs a variational core-radius parameter $\xi_v \sim \xi_{ab}$, as in Refs. [37,50–52].

APPENDIX: INTEGRALS USEFUL FOR $D \ll \lambda_{\parallel}$

Several integrals appear in Sec. 4.2. All may be evaluated by starting from [101,102]

$$\int_0^{\infty} du \frac{J_0(zu)}{1+u} = \frac{\pi}{2} [\mathbf{H}_0(z) - Y_0(z)], \quad (\text{A.1})$$

where $\mathbf{H}_n(z)$ is the Struve function and $Y_n(z)$ is the Bessel function of the second kind (Weber's function), differentiating with respect to z , making use of recurrence relations, integrating by parts, and making use of the properties that [101,102]

$$\int_0^{\infty} du J_0(zu) = \int_0^{\infty} du J_1(zu) = \frac{1}{z}, \quad (\text{A.2})$$

$$\int_0^{\infty} du \frac{J_1(zu)}{u} = 1. \quad (\text{A.3})$$

The vector potential $a_{\phi}(\rho, 0)$ is proportional to

$$\int_0^{\infty} du \frac{J_1(zu)}{1+u} = \frac{1}{z} + 1 - \frac{\pi}{2} [\mathbf{H}_1(z) - Y_1(z)] \quad (\text{A.4})$$

$$\approx 1, \quad z \ll 1, \quad (\text{A.5})$$

$$\approx \frac{1}{z}, z \gg 1, \quad (\text{A.6})$$

where the limiting forms for $z \ll 1$ and $z \gg 1$ are obtained from expansions given in Refs. [101] and [102]. However, Eq. (A.5) may be obtained more simply by noting that, because of the properties of $J_1(uz)$, the integral when $z \ll 1$ is dominated by values of $u \gg 1$, such that $1+u$ may be replaced by u ; the resulting integral then takes the form of Eq. (A.3). Similarly, Eq. (A.6) may be obtained by noting that when $z \gg 1$ the integral is dominated by values of $u \ll 1$, such that $1+u$ may be replaced by 1; the resulting integral may be evaluated using Eq. (A.2). The limiting forms of the following integrals also may be obtained in a similar fashion.

The magnetic field component $b_z(\rho, 0)$ is proportional to

$$\begin{aligned} \int_0^\infty du \frac{uJ_0(zu)}{1+u} &= \frac{1}{z} \int_0^\infty du \frac{uJ_1(zu)}{(1+u)^2} \\ &= \frac{1}{z^2} \int_0^\infty du \frac{(1-u)J_0(zu)}{(1+u)^3} \end{aligned} \quad (\text{A.7})$$

$$= \frac{1}{z} - \frac{\pi}{2} [\mathbf{H}_0(z) - Y_0(z)] \quad (\text{A.8})$$

$$\approx \frac{1}{z}, \quad z \ll 1, \quad (\text{A.9})$$

$$\approx \frac{1}{z^3}, \quad z \gg 1, \quad (\text{A.10})$$

and the net sheet current $K_D(\rho)$ is proportional to

$$\int_0^\infty du \frac{uJ_1(zu)}{1+u} = \frac{1}{z} \int_0^\infty du \frac{J_0(zu)}{(1+u)^2} \quad (\text{A.11})$$

$$= \frac{\pi}{2} [\mathbf{H}_1(z) - Y_1(z)] \quad (\text{A.12})$$

$$\approx \frac{1}{z}, \quad z \ll 1, \quad (\text{A.13})$$

$$\approx \frac{1}{z^2}, \quad z \gg 1. \quad (\text{A.14})$$

ACKNOWLEDGMENTS

I thank S. J. Bending, P. G. Clem, J. W. Guikema, J. Hoffman, and V. G. Kogan for stimulating discussions and correspondence. This article has been authored in part by Iowa State University of Science and Technology under Contract No. W-7405-ENG-82 with the U.S. Department of Energy.

REFERENCES

1. J. Bardeen, L. N. Cooper, and J. R. Schrieffer, *Phys. Rev.* **108**, 1175 (1957).
2. J. R. Clem, *Phys. Rev.* **148**, 392 (1966).
3. J. R. Clem, *Ann. Phys. (N.Y.)* **40**, 268 (1966).
4. D. M. Ginsberg, P. L. Richards, and M. Tinkham, *Phys. Rev. Lett.* **3**, 337 (1959).
5. M. Tinkham, *Introduction to Superconductivity* (McGraw-Hill, New York, 1975).
6. M. Tinkham, *Introduction to Superconductivity*, 2nd edn. (McGraw-Hill, New York, 1996).
7. J. R. Clem, *Phys. Rev. B* **43**, 7837 (1991).
8. S. N. Artemenko and A. N. Kruglov, *Phys. Lett. A* **143**, 485 (1990).
9. A. Buzdin and D. Feinberg, *J. Phys. (Paris)* **51**, 1971 (1990).
10. K. B. Efetov, *Sov. Phys. JETP* **49**, 905 (1979).
11. R. G. Mints, V. G. Kogan, and J. R. Clem, *Phys. Rev. B* **61**, 1623 (2000).
12. J. R. Clem, *Physica C* **235–240**, 2607 (1994).
13. J. Pearl, *Appl. Phys. Lett.* **5**, 65 (1964).
14. J. Pearl, in *Proceedings of the Ninth International Conference on Low Temperature Physics*, J. G. Daunt, D. V. Edwards, F. J. Milford, and M. Yaquub, eds. (Plenum, New York, 1965), Part A, p. 566.
15. P. G. de Gennes, *Superconductivity of Metals and Alloys* (Benjamin, New York, 1966), p. 60.
16. M. von Laue, *Theory of Superconductivity* (Academic Press, New York, 1952).
17. C. Caroli, P. G. de Gennes, and J. Matricon, *J. Phys. Kondens. Mater.* **1**, 176 (1963).
18. L. P. Gor'kov and T. K. Melik-Barkhudarov, *Sov. Phys. JETP* **18**, 1031 (1964).
19. D. R. Tilley, G. J. Van Gorp, and C. W. Berghout, *Phys. Lett.* **12**, 305 (1964).
20. D. R. Tilley, *Proc. Phys. Soc. Lond.* **85**, 1977 (1965); **86**, 289 (1965).
21. E. I. Katz, *Sov. Phys. JETP* **29**, 897 (1969).
22. E. I. Katz, *Sov. Phys. JETP* **31**, 787 (1970).
23. K. Takanaka, *Phys. Status Solidi B* **68**, 623 (1975).
24. R. A. Klemm and J. R. Clem, *Phys. Rev. B* **21**, 1868 (1980).
25. V. G. Kogan, *Phys. Rev. B* **24**, 1572 (1981).
26. V. G. Kogan and J. R. Clem, *Phys. Rev. B* **24**, 2497 (1981).
27. V. G. Kogan and J. R. Clem, *Jpn. J. Appl. Phys.* **26** (Suppl. 26–3), 1159 (1987).
28. A. V. Balatskii, L. I. Burlachkov, and L. P. Gor'kov, *Sov. Phys. JETP* **63**, 866 (1986).
29. L. N. Bulaevskii, V. L. Ginzburg, and A. Sobyenin, *Sov. Phys. JETP* **68**, 1499 (1988).
30. W. E. Lawrence and S. Doniach, in *Proceedings of the Twelfth International Conference on Low Temperature Physics*, E. Kanda, ed. (Academic Press of Japan, Kyoto, 1971), p. 361.
31. B. D. Josephson, *Phys. Lett.* **1**, 251 (1962).
32. J. R. Clem, *Physica C* **162–164**, 1137 (1989).
33. P. H. Kes, J. Aarts, V. M. Vinokur, and C. J. van der Beek, *Phys. Rev. Lett.* **64**, 1063 (1990).
34. J. C. Martínez, S. H. Brongersma, A. Koshelev, B. Ivlev, P. H. Kes, R. P. Griessen, D. G. de Groot, Z. Tarnavski, and A. A. Menovsky, *Phys. Rev. Lett.* **69**, 2276 (1992).
35. A. N. Grigorenko, S. J. Bending, A. E. Koshelev, J. R. Clem, T. Tamegai, and S. Ooi, *Phys. Rev. Lett.* **89**, 217003 (2002).
36. J. R. Clem, *Phys. Rev. B* **9**, 898 (1974).
37. J. R. Clem, *Phys. Rev. B* **12**, 1742 (1975).
38. I. Giaever, *Phys. Rev. Lett.* **15**, 825 (1965).
39. I. Giaever, *Phys. Rev. Lett.* **16**, 460 (1966).
40. P. R. Solomon, *Phys. Rev. Lett.* **16**, 50 (1966).
41. M. D. Sherrill, *Phys. Lett. A* **24**, 312 (1967).
42. R. Deltour and M. Tinkham, *Phys. Rev.* **174**, 478 (1968).

43. P. E. Cladis, *Phys. Rev. Lett.* **21**, 1238 (1968).
44. P. E. Cladis, R. D. Parks, and J. M. Daniels, *Phys. Rev. Lett.* **21**, 1521 (1968).
45. J. W. Ekin, B. Serin, and J. R. Clem, *Phys. Rev. B* **9**, 912 (1974).
46. J. W. Ekin and J. R. Clem, *Phys. Rev. B* **12**, 1753 (1975).
47. F. London, *Superfluids*, Vol. 1 (Dover, New York, 1961).
48. M. Tinkham, *Introduction to Superconductivity*, 2nd edn. (McGraw-Hill, New York, 1996) p. 152.
49. A. A. Abrikosov, *Sov. Phys. JETP* **5**, 1174 (1957).
50. J. R. Clem, *J. Low Temp. Phys.* **18**, 427 (1975).
51. J. R. Clem, Z. Hao, L. Dobrosavljević-Grujić, and Z. Radović, *J. Low Temp. Phys.* **88**, 213 (1992). On p. 216 of this paper, the number 0.479 should be corrected to 0.497.
52. J. R. Clem, in *Inhomogeneous Superconductors—1979*, D. U. Gubser, T. L. Francavilla, S. A. Wolf, and J. R. Leibowitz, eds. (American Institute of Physics, New York, 1980), p. 245.
53. J. Pearl, *J. Appl. Phys.* **37**, 4139 (1966).
54. J. D. Jackson, *Classical Electrodynamics* (Wiley, New York, 1962), p. 77.
55. J. R. Clem, *Phys. Rev. B* **5**, 2140 (1970). The prefactor on the right-hand side of Eq. (3.11) of this paper should be corrected to $(\phi_0/4\pi\lambda^2)$.
56. J. W. Guikema, PhD dissertation, Stanford University, March 2004.
57. M. Tinkham, *Introduction to Superconductivity*, 2nd edn. (McGraw-Hill, New York, 1996), p. 155.
58. M. Benkraouda and J. R. Clem, *Phys. Rev. B* **53**, 438 (1996).
59. T. Pe, M. Benkraouda, and J. R. Clem, *Phys. Rev. B* **55**, 6636 (1997).
60. T. Pe, M. Benkraouda, and J. R. Clem, *Phys. Rev. B* **56**, 8289 (1997).
61. L. N. Bulaevskii, *Sov. Phys. JETP* **37**, 1133 (1973).
62. J. R. Clem and M. W. Coffey, *Phys. Rev. B* **42**, 6209 (1990).
63. L. N. Bulaevskii, M. Ledvij, and V. G. Kogan, *Phys. Rev. B* **46**, 355 (1992).
64. R. G. Mints, I. B. Snapiro, and E. H. Brandt, *Phys. Rev. B* **54**, 9458 (1996).
65. L. I. Glazman and A. E. Koshelev, *Physica C* **173**, 180 (1991).
66. A. Kapitulnik, in *Phenomenology and Applications of High-Temperature Superconductors*, K. S. Bedell, M. Inui, D. Meltzer, J. R. Schrieffer, and S. Doniach, eds. (Addison-Wesley, Reading, 1992), p. 34.
67. L. N. Bulaevskii, M. Ledvij, and V. G. Kogan, *Phys. Rev. B* **46**, 11807 (1992).
68. J. R. Clem, *Physica A* **200**, 118 (1993).
69. J. R. Clem, M. W. Coffey, and Z. Hao, *Phys. Rev. B* **44**, 2732 (1991).
70. A. E. Koshelev, *Phys. Rev. B* **48**, 1180 (1993) and private communication.
71. D. Feinberg and C. Villard, *Mod. Phys. Lett.* **4**, 9 (1990).
72. D. Feinberg and C. Villard, *Phys. Rev. Lett.* **65**, 919 (1990).
73. B. I. Ivlev, Y. N. Ovchinnikov, and V. L. Pokrovskii, *Mod. Phys. Lett.* **5**, 9 (1990).
74. S. S. Maslov and V. L. Pokrovskii, *Europhys. Lett.* **14**, 591 (1991).
75. S. S. Maslov and V. L. Pokrovskii, *JETP Lett.* **53**, 637 (1991).
76. D. Feinberg, *Physica C* **194**, 126 (1992).
77. D. A. Huse, *Phys. Rev. B* **46**, 8621 (1992).
78. A. E. Koshelev, *Phys. Rev. Lett.* **83**, 189 (1999).
79. C. A. Bolle, P. L. Gammel, D. J. Bishop, D. Mitzi, and A. Kapitulnik, *Phys. Rev. Lett.* **68**, 3343 (1991).
80. I. V. Grigorieva, J. W. Steeds, G. Balakrishnan, and D. M. Paul, *Phys. Rev. B* **51**, 3765 (1995).
81. A. Oral, S. J. Bending, and M. Henini, *Appl. Phys. Lett.* **69**, 1324 (1996).
82. A. N. Grigorenko, S. J. Bending, T. Tamegai, S. Ooi, and M. Henini, *Nature (London)* **414**, 728 (2001).
83. A. E. Koshelev, *Phys. Rev. B* **68**, 094520 (2003).
84. H. Safar, P. L. Gammel, D. A. Huse, D. J. Bishop, J. P. Rice, and D. M. Ginsberg, *Phys. Rev. Lett.* **69**, 824 (1992).
85. W. K. Kwok, S. Fleshler, U. Welp, V. M. Vinokur, J. Downey, G. W. Crabtree, and M. M. Miller, *Phys. Rev. Lett.* **69**, 3370 (1992).
86. R. Cubitt, E. M. Forgan, G. Yang, S. L. Lee, D. M. Paul, H. M. Mook, M. Yethiraj, P. H. Kes, T. W. Li, A. A. Menovsky, Z. Tarnavski, and K. Mortensen, *Nature (London)* **365**, 407 (1993).
87. E. Zeldov, D. Majer, M. Konczykowski, V. B. Geshkenbein, V. M. Vinokur, and H. Shtrikman, *Nature (London)* **375**, 373 (1995).
88. A. Schilling, R. A. Fisher, N. E. Phillips, U. Welp, D. Dasgupta, W. K. Kwok, and G. W. Crabtree, *Nature (London)* **382**, 791 (1996).
89. A. Oral, J. C. Barnard, S. J. Bending, I. I. Kaya, S. Ooi, T. Tamegai, and M. Henini, *Phys. Rev. Lett.* **80**, 3610 (1998).
90. S. J. Bending, A. Oral, J. R. Clem, I. I. Kaya, S. Ooi, T. Tamegai, and M. Henini, *IEEE Trans. Appl. Supercond.* **9**, 1820 (1999).
91. G. Blatter, M. V. Feigelman, V. B. Geshkenbein, A. I. Larkin, and V. M. Vinokur, *Rev. Mod. Phys.* **66**, 1125 (1994).
92. E. H. Brandt, *Rep. Prog. Phys.* **58**, 1465 (1995).
93. J. Kierfeld, *Phys. Rev. B* **69**, 144513 (2004).
94. S. Fanesi, G. Pozzi, J. E. Bonevich, O. Kamimura, H. Kasai, K. Harada, T. Matsuda, and A. Tonomura, *Phys. Rev. B* **59**, 1426 (1999).
95. T. Yoshida, J. Endo, K. Harada, H. Kasai, T. Matsuda, O. Kamimura, A. Tonomura, M. Beleggia, R. Patti, and G. Pozzi, *J. Appl. Phys.* **85**, 4096 (1999).
96. T. Matsuda, O. Kamimura, H. Kasai, K. Harada, T. Yoshida, T. Akashi, A. Tonomura, Y. Nakayama, J. Shimoyama, K. Kishio, T. Hanaguri, and K. Kitazawa, *Science* **294**, 2136 (2001).
97. O. Kamimura, H. Kasai, T. Akashi, T. Matsuda, K. Harada, J. Masuko, T. Yoshida, N. Osakabe, A. Tonomura, M. Beleggia, G. Pozzi, J. Shimoyama, K. Kishio, T. Hanaguri, K. Kitazawa, M. Sasase, and S. Okayasu, *J. Phys. Soc. Jpn.* **71**, 1840 (2002).
98. M. Beleggia, G. Pozzi, J. Masuko, K. Harada, T. Yoshida, O. Kamimura, H. Kasai, T. Matsuda, and A. Tonomura, *Phys. Rev. B* **66**, 174518 (2002).
99. A. Tonomura, *Physica C* **388–389**, 624 (2003).
100. A. Tonomura, *J. Low Temp. Phys.* **131**, 941 (2003).
101. I. S. Gradshteyn and I. M. Ryzhik, *Table of Integrals, Series, and Products*, 6th edn. (Academic Press, San Diego, 2000).
102. M. Abramowitz and I. A. Stegun, eds., *Handbook of Mathematical Functions* (National Bureau of Standards, Washington, 1967).

Superconductivity Through Intra-Atomic Excitations

P. Fulde¹ and G. Zwicknagl²

Received August 15, 2004; accepted September 4, 2004

It is demonstrated that the occurring of superconductivity in UPd₂Al₃ can be understood within the dual model for 5*f* electrons. Due to strong intra-atomic or Hund's rule correlations two of the 5*f* electrons remain localized while the remaining 5*f* part is delocalized and part of the conduction electrons. Cooper-pair formation of the latter takes place due to the exchange of magnetic excitations within the localized 5*f* subsystem. By solving Eliashberg's equations, it is shown that a consistent description can be obtained of the superconducting transition temperature and of the strong mass anisotropies of the semi-heavy quasiparticles.

KEY WORDS: superconductivity; 5*f* electrons; dual model.

1. INTRODUCTION

Since the work of Fröhlich [1] on electron-phonon interactions and the discovery of the isotope effect [2], this particular interaction has been considered the main source of electron-electron attraction and Cooper-pair formation. It is known that an effective electron attraction is not necessarily required for superconductivity to occur. Instead, what is required is that the BCS ground state has a lower energy than the normal state, i.e., a state without pair formation. As discussed, e.g., by Bogoliubov *et al.* [3], Cooper pairs may form even when the electron interactions are purely repulsive. They may lead to an energy gain, provided the variation of the repulsive interaction in momentum space is appropriate. Despite all these considerations, the general belief has been, at least until the discovery of heavy-fermion and high-temperature superconductivity, that electron-pair formation is caused by the exchange of phonons. The high superconducting transition temperatures observed in some of the cuprate perovskites have called that belief into question and have led to a number of suggestions as regards nonphononic pairing interactions. But they

have been mainly qualitative and not quantitative and therefore remained inconclusive.

The aim of the present paper was to draw attention to a particular nonphononic interaction which has led to quantitative and experimentally confirmed predictions as regards its influence on the formation of a superconducting state. It concerns intra-atomic or crystal field excitations of strongly correlated 4*f* or 5*f* electrons and applies in particular to systems with rare-earth or U ions. When those ions are put as impurities into a superconductor, the inelastic intra-atomic excitations caused by conduction electrons can be either pair-breaking or pair-forming, depending on the relative size of the respective matrix elements. When the latter involves time reversal invariant interactions between the conduction electrons and localized *f* electrons they act as pair formers [4]. But they act as pair breakers when the interactions break time-reversal symmetry [5]. This may change when, e.g., the U ions form a lattice. In that case, the intra-atomic excitations form a band of magnetic excitations, i.e., magnetic excitons. When the interactions of the conduction electrons with the magnetic excitations are largest near the zone-bounding (implying antiferromagnetic correlations) Cooper pairs can form even when the local interactions break time-reversal symmetry. But in this case, the resulting superconducting order parameter has necessarily to have node lines, i.e., it must be of an anisotropic form. We shall show that UPd₂Al₃

¹Max-Planck-Institut für Physik komplexer Systeme, Nöthnitzer Str. 38, 01187 Dresden, Germany.

²Inst. of Mathemat. Physik, Techn., Universität Braunschweig, Mendelssohnstraße 3, 38106 Braunschweig, Germany.

belongs to that category [6,7]. The superconducting transition temperature as well the enhanced quasi-particle mass can be well explained this way [6]. The same holds true for the observed node structure of the order parameter [8].

The paper is organized as follows: In the next section, we recapitulate the effects on superconductivity of impurities containing $4f$ electrons. Section 3 describes the dual model of $5f$ electrons as applied and tested for U ions in a given chemical environment and in Section 4 we apply that model to UPd_2Al_3 . A summary and the conclusions are contained in Section 5.

2. EFFECTS OF CRYSTAL-FIELD EXCITATION ON SUPERCONDUCTIVITY

We consider rare-earth impurities with crystalline electric field (CEF) split energy levels and study their effect on a superconducting matrix. According to Hirst [4], the different interactions between conduction electrons and such impurities can be classified with respect to their transformation properties under rotations and spin rotations. He showed that their total number is $2 \cdot (2\ell + 1)$ and equals 14, because for f electrons $\ell = 3$. Among them, the isotropic Coulomb interaction is of no interest. The most important interactions are the isotropic exchange interaction and the aspherical Coulomb charge scattering. The former is written in the form

$$H_{\text{ex}} = -2(g - 1)J_{\text{ex}} \sum_i \mathbf{s}(\mathbf{r}) \mathbf{J}_i \delta(\mathbf{r} - \mathbf{R}_i) \quad (1)$$

where g is the Landè factor, $\mathbf{s}(\mathbf{r})$ the conduction electron spin, \mathbf{J}_i the total angular momentum of the incomplete $4f$ shell of the i -th ion and \mathbf{R}_i is its position. The aspherical Coulomb scattering is of the form

$$H_{\text{AC}} = \sum_{\sigma} \sum_{m=-2}^{+2} I_2(k's; kd) \left(\frac{5}{4\pi} \right)^{\frac{1}{2}} \cdot Q_2 [Y_2^m(J) c_{k's\sigma}^+ c_{kdm\sigma} + h.c.]. \quad (2)$$

Here I_2 is a Coulomb integral, the explicit form of which is found in Ref. [4] and Q_2 is the quadrupole moment of the rare-earth ion. A list of Q_2 values for rare-earth ions is also found in Ref. [4]. The operators $Y_2^m(J)$ act on the incomplete $4f$ shell as

$$Y_2^{\pm 2} = (J^{\pm})^2 / N$$

$$Y_2^{\pm 1} = \mp (J_z J^{\pm} + J^{\pm} J_z) / N$$

$$Y_2^0 = \left(\frac{2}{3} \right)^{\frac{1}{2}} (3J_z^2 - J(J+1)) / N \quad (3)$$

where the normalization factor is $N = (2/3)^{1/2} (2J^2 - J)$. The conduction electrons are specified by the four quantum numbers k, ℓ, m, σ when a decomposition of their states in terms of spherical harmonics is used. For simplicity, we have included in Eq. (3) scattering of s- into d-waves only and *vice versa*. A complete expression for aspherical Coulomb charge scattering must also include p- into p-wave, d- into d-wave scattering, etc.

It is noticed that H_{ex} is not time-reversal invariant while H_{AC} is. Note that a time-reversal operation refers only to the conduction electrons and excludes the impurity ions. The latter are treated like an external perturbation. Otherwise, a time-reversal operation would be irrelevant for deciding which interactions lead to pair formation and which result in pair breaking.

A CEF-split incomplete $4f$ shell or, in the case of $U, 5f$ subshell (see later) gives rise to a frequency dependent magnetic or quadrupolar susceptibility, depending on the particular form of the interaction. In the finite temperatures formalism, it has the form

$$R(\omega_n, \omega_m) = - \sum_{ij} \frac{|M_{ij}|^2 \delta_{ij} (n_i - n_j) \text{sgn} \omega_n}{(\omega_n - \omega_m)^2 + \delta_{ij}^2}$$

$$= - \sum_{ij} |M_{ij}|^2 r_{ij}(\omega_n, \omega_m). \quad (4)$$

The different CEF states $|i\rangle$ have energies δ_i and $\delta_{ij} = \delta_i - \delta_j$. The thermal populations of the levels are given by n_i . The matrix elements M_{ij} describe transitions between states $|i\rangle$ and $|j\rangle$ caused by either H_{ex} or H_{AC} . Associated with them is a scattering rate of conduction electrons

$$\frac{1}{\tau_{ij}} = 2\pi n_1 N(E_F) |M_{ij}|^2 \quad (5)$$

where $N(E_F)$ is the conduction electron density of states per spin and n_1 is the impurity concentration. The Matsubara frequencies are $\omega_n = 2\pi T(n + 1/2)$ with n being an integer and T is the temperature. The dependence of the superconducting transition temperature T_c on impurity concentration n_1 is obtained from the following set of equations:

$$\ln \frac{T_c}{T_{c0}} = 2\pi T_c \sum_{\omega_n > 0} \left\{ \frac{1}{\Delta} \frac{\tilde{\Delta}_n}{\tilde{\omega}_n} - \frac{1}{\omega_n} \right\} \quad (6)$$

where T_{c0} denotes the transition temperature when $n_I = 0$ and

$$\tilde{\omega}_n = \omega_n + T_c \sum_{i,j,\omega_m} \frac{1}{\tau_{ij}} r_{ij}(\omega_n, \omega_m) \quad (7)$$

$$\tilde{\Delta}_n = \Delta + T_c \eta \sum_{i,j,\omega_m} \frac{1}{\tau_{ij}} \frac{\tilde{\Delta}_m}{\tilde{\omega}_m} r_{ij}(\omega_n, \omega_m). \quad (8)$$

The prefactor η is $\eta = 1$ when H_{AC} is considered while $\eta = -1$ when H_{ex} is used. The last terms in Eqs. (7) and (8) describe the effect of the impurities. They have the same sign when $\eta = 1$, i.e., when H_{AC} is acting and contribute to pairing. But when $\eta = -1$ they have different signs and lead to pair breaking and a reduction of T_c . This is the case when H_{ex} is considered.

For a better understanding of the solutions of Eqs. (6)–(8) we consider a CEF-level scheme consisting of two singlets only, with energy difference δ . This situation may occur in non-Kramers ions like Pr^{3+} with $4f^2$ and a $J = 4$ lowest multiplet. Those ions may have a number of singlet levels. When the remaining energy levels are sufficiently high, it may suffice to take only the lowest two singlets into account. A two-level description applies also to the localized $5f$ electrons of a U ion (see Section 3). In that case, the expression for the susceptibility simplifies to

$$R(\omega_n, \omega_m) = |M|^2 \frac{2\delta \tanh \delta/2T}{(\omega_n - \omega_m)^2 + \delta} \text{sgn } \omega_m \quad (9)$$

where $\tanh(\delta/2T)$ describes the difference in the thermal population of the two levels. The scattering rates τ_{ij}^{-1} reduce to $\tau^{-1} = 2\pi n_I N(E_F) |M|^2$, where $|M|$ is computed either from H_{AC} or H_{ex} . When the transitions between the two levels are caused by H_{AC} (or H_{ex}), the increase (or decrease) of the transition temperature as function of impurity concentration is determined by a function $y(\frac{\delta}{2T_c})$. The dependence $T_c(n_I)$ is obtained from the solution of the Eqs. (6)–(8)

$$\ln \frac{T_c}{T_{c0}} + \psi\left(\frac{1}{2} + \frac{2}{\pi^2 T_c \tau} \frac{y(\delta/2T_c)}{y(\delta/2T_{c0})}\right) - \psi\left(\frac{1}{2}\right) = 0 \quad (10)$$

where $\psi(x)$ is the digamma function. The function $y(\delta/2T)$ is plotted in Fig. 1a,b for the cases of pair formation due to H_{AC} (Fig. 1a) and pair breaking when H_{ex} is operative (Fig. 1b).

It is seen from Fig. 1a that CEF energy levels with an excitation energy much larger than T can contribute to pair formation, because the virtual pair

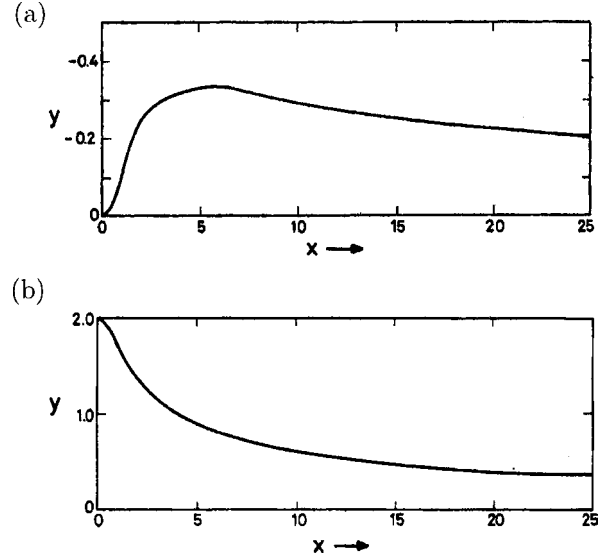


Fig. 1. (a) Function $y(x)$ vs. $x = \delta/2T$ for aspherical Coulomb scattering H_{AC} by a two-level system. (b) The same as in (a) but for exchange scattering H_{ex} (from Ref. [4]).

scattering of Cooper pairs involves states far from the Fermi surface. An analogy to optical phonons is apparent. Those phonons also can cause Cooper pairing when their excitation energy is much higher than the binding energy of a Cooper pair. A similar argument holds for pair breaking. High-lying CEF states can still break efficiently Cooper pairs. Usually, the pair-breaking processes dominate the pair-forming ones. Take Pr^{3+} ions as an example. When added to the superconductor LaPb_3 they reduce T_c despite the fact that through H_{AC} some pair-forming processes take place. But the effect of H_{ex} is stronger. This is shown in Fig. 2 where also the drop in T_c is shown which would take place without a CEF splitting [5]. (La, Pr) Sn_3 [11] is the only example where pair-forming processes have shown up.

The reason that we have discussed the known effects of CEF-split impurities on superconductivity in such details is that for a lattice of CEF split ions the situation is different. Then processes acting in the impurity case as pair breakers may cause pair formation. As we shall show later, that is precisely the situation met in UPd_2Al_3 . This has led to the explanation of a number of experiments for this intermetallic compound.

3. DUAL MODEL APPLIED TO UPd_2Al_3

There is growing evidence that actinide ions may have itinerant as well as localized $5f$ electrons.

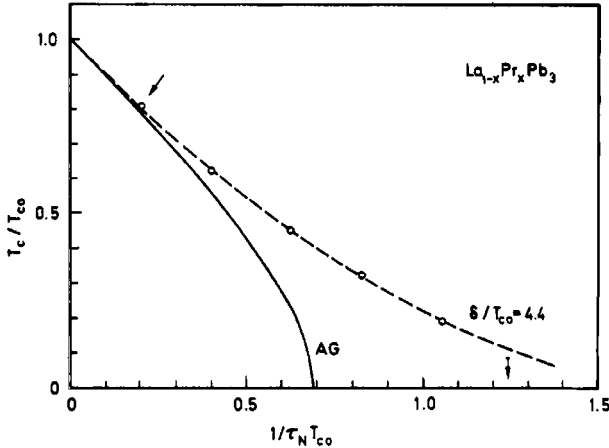


Fig. 2. T_c as function of Pr concentration for $\text{La}_{1-x}\text{Pr}_x\text{Sn}_3$ [9]. Solid line: Abrikosov–Gorkov theory [5]. The dashed line is the theoretical curve for $\delta/T_{c0} = 4.4$. The point marked by an arrow has been fitted (from Ref. [9]).

Model calculations show that the dual nature of the U $5f$ states ultimately arises from intra-atomic correlations as described by Hund’s rules [12]. The underlying physics can be understood as follows: The U compound under consideration is in the mixed-valent regime with $n_f \simeq 2.5$. Therefore, the low-energy states will be formed by the $5f^2$ and $5f^3$ configurations. As there should be either two or three $5f$ electrons at a site, there will be only one of them hopping from site to site. The selection of the delocalized orbital, on the other hand, is determined by intra-atomic correlations. To see how this happens, it is important to note that the energy gain due to multiplet formation exceeds the one obtained from the kinetic energy. As a consequence, a coherent $5f$ band will form only if the local intra-atomic correlations are preserved. This constraint selects the symmetry of the delocalized $5f$ orbital in an anisotropic crystal. To illustrate this point, we consider the elementary hopping process between two neighboring sites. For hopping to occur, one site has to be occupied by three $5f$ electrons (site a), while there are two at the other site b. We assume that the initial state locally satisfies Hund’s rules, i.e., the $5f$ shells are in their respective ground states. Transferring a $5f$ electron from site a to site b will usually lead to a final state where both i.e., the remaining doubly occupied $5f$ shell at site a as well as the triply occupied $5f$ shell at site b are in excited states. Depending on the initial state, Hund’s rule can be (approximately) preserved only for specific symmetries of the transferred orbital. The symmetry of the delocalized $5f$ orbital is finally selected

so as to maximize the energy gain due to band formation under the constraint that the local intra-atomic correlations are preserved. The localized and delocalized $5f$ subsystems interact which leads to the mass enhancement of the delocalized quasiparticles. The situation resembles that in Pr metal where a mass enhancement of the conduction electrons by a factor of 5 results from virtual crystal field (CEF) excitations of localized $4f^2$ electrons [13]. The underlying hypothesis is supported by a number of experiments including susceptibility measurements [14], photoemission and neutron inelastic scattering experiments on UPd_2Al_3 [15–17].

The dual nature of the $5f$ electrons is strongly evident in UPd_2Al_3 [18]. The presence of localized $5f^2$ configurations is suggested by the temperature dependence of the paramagnetic susceptibility and of the antiferromagnetic order which develops below $T_N = 14.3$ K and which is characterized by an almost atomic size ordered moment $\mu = 0.85\mu_B$. On the other hand, the itinerant $5f$ states forming bands by hybridization with the conduction electrons, give rise to a low-temperature specific heat $C \sim \gamma T$ with $\gamma = 120$ mJ/mol K^2 . At $T_c = 1.8$ K, the normal heavy Fermi liquid becomes unstable and a superconducting phase forms with Cooper pairs consisting of the heavy quasiparticles. The two ordering phenomena, i.e., superconductivity and antiferromagnetic order coexist down to lowest temperatures.

A direct confirmation of this dual nature of $5f$ electrons in UPd_2Al_3 was obtained from neutron inelastic scattering [17, 19–22]. The data exhibit a resonance-like structure in the dynamical structure function of localised moments which appears below T_c and is linked to the superconducting quasiparticles. The coupling between the heavy quasiparticles and the local magnetic moments give rise to structures in the tunneling DOS [23].

3.1. Normal State Quasiparticles

The dual model provides a method to microscopically calculate the heavy quasiparticle bands in real U-based heavy fermion compounds. The conjecture that the two localized atomic-like $5f$ electrons of the U ions coexist with an itinerant $5f$ electron suggests the following scheme which proceeds in three steps [24,25]. First, the dispersion of the itinerant $5f$ state is determined by solving Dirac’s equation for the selfconsistent LDA potentials but excluding two

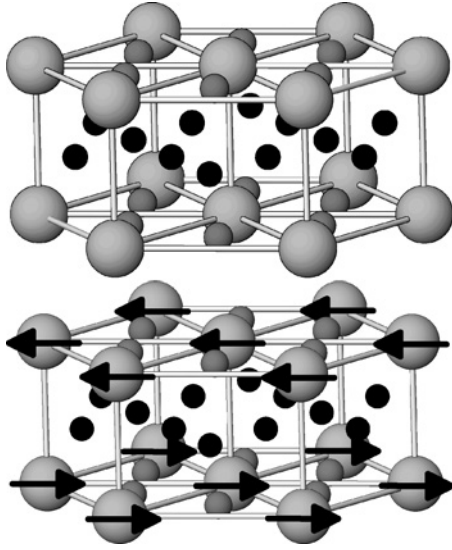


Fig. 3. Conventional unit cell of UPd_2Al_3 ((a), upper panel) and simple AF magnetic structure with propagation vector $\mathbf{Q} = (0, 0, \frac{1}{2})$ ((b) lower panel). Large and small spheres in hexagonal planes correspond to U and Pt atoms respectively, intercalated by Al atoms.

$U 5f$ ($j = \frac{5}{2}, j_z = \pm\frac{5}{2}$ and $j_z = \pm\frac{1}{2}$) states from forming bands. The choice of the itinerant and localized orbitals depends upon the symmetry of the crystal and the hybridization strengths. For UPd_2Al_3 , the f occupancy per U atom for the delocalized $5f$ electrons amounts to 0.65, indicating that we are dealing with a mixed valent situation. The density of states at the Fermi level $N(E_F) = 2.76$ states/(eV cell spin) corresponds to the one found in Ref. [26]. The LDA parameters will be used later in the calculation of the effective mass.

The *ab initio* calculations are performed for the paramagnetic state in the PrNi_2Al_3 structure displayed in Fig. 3. The relevant structural elements are the hexagonal UPd_2 -planes which are stacked along the hexagonal c -axis. These planes are intercalated with Al layers which play a minor role for the electronic bands in the vicinity of the Fermi surface. The quasi-two-dimensional character of the U-sublattice is reflected in the dispersion of the $5f$ bands. In the paramagnetic state, there are two bands intersecting the Fermi energy. The dHvA experiments which probe the topology of the Fermi surface are performed at very low temperatures, i. e., in the antiferromagnetic phase displayed in Fig. 3. The magnetic superstructure introduces small gaps in the planes $q_z = \pm\frac{\pi}{2c}$. Although the absolute values of these gaps are rather small, they nevertheless change

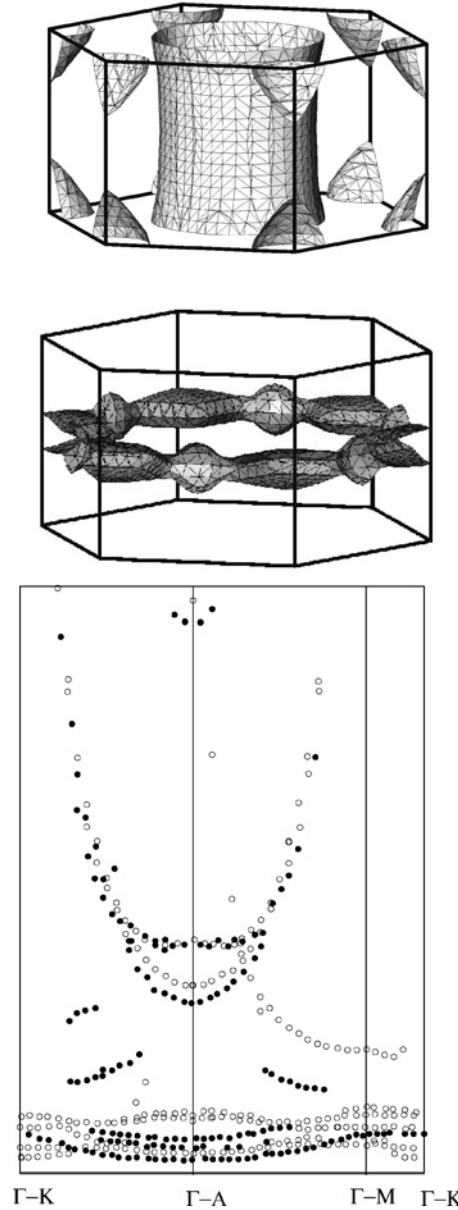


Fig. 4. Upper panel: Fermi surface of UPd_2Al_3 calculated within the dual approach. The main cylinder part has also a heavy mass with $m^* = 19\text{--}33 m$. The torus depends sensitively on the position of the Fermi energy. Lower panel: Comparison of experimental dHvA frequencies (black symbols) (from Ref. [27]) and calculated frequencies (open symbols) from the dual approach (from Ref. [25]). Large parabola corresponds to the main FS cylinder.

the topology of the Fermi surface dramatically. The thermodynamically most relevant parts displayed in Fig. 4 originate from a single paramagnetic band. In addition to these two sheets, there are small ellipsoids centered at K which are not shown here. The calculated variation of the dHvA frequencies with

the orientation of the magnetic field agree very well with experiment as shown in Fig. 4.

Having shown that the assumption of a single itinerant $5f$ electron reproduces the Fermi surface, we next turn to the localized $5f^2$ configurations. Accounting for the fact that the $5f$ state with $j = \frac{5}{2}, j_z = \pm \frac{3}{2}$ are hybridized away, we diagonalize the Coulomb matrix in the restricted subspace of the remaining localized $5f$ states. Assuming the jj -coupling scheme, the Coulomb matrix elements are calculated from the radial functions of the *ab initio* band structure potentials. The anisotropic hybridization lifts the rotational symmetry. As a consequence, the resulting eigenstates of the Coulomb matrix are not necessarily eigenstates of the total angular momentum J but remain eigenstates of J_z . We find a doubly degenerate ground state with $J_z = \pm 3$ which must be a simultaneous eigenstate of $J = 4$. In a crystal, the degeneracies of the ground state may be lifted by a CEF. This is in fact the case for UPd₂Al₃ where the resulting singlet ground state of the localized $5f^2$ is given by $|\Gamma_4\rangle = (1/\sqrt{2})(|J_z = 3\rangle - |J_z = -3\rangle)$ in the $J = 4$ subspace with a first excited state $|\Gamma_3\rangle = (1/\sqrt{2})(|J_z = 3\rangle + |J_z = -3\rangle)$. We neglect the next-higher excited eigenstates of the Coulomb matrix and consider the two singlets $|\Gamma_4\rangle$ and $|\Gamma_3\rangle$. For the energy splitting, we assume a value of $\tilde{\delta} \simeq 7$ meV in agreement with recent neutron experiments [28].

The matrix element for the transition between the localized states $|\Gamma_4\rangle$ and $|\Gamma_3\rangle$ due to the Coulomb interaction with the delocalized $5f$ state is directly obtained from the expectation values of the Coulomb interaction in the $5f^3$ states. From this we find the value $|M| = 0.19$ eV. This value calculated in the jj -coupling scheme can be expressed in terms of a usual exchange Hamiltonian. We first calculate the effective Landé factor $g_{\text{eff}}(f^2)$ of the localized jj -coupled $5f^2$ ground state $J = 4$ manifold by decomposing the states in terms of LS states. This yields

$$g_{\text{eff}}(f^2) = \frac{31}{49} \simeq 0.63. \quad (11)$$

The Landé factor of the itinerant $5f$ electron with $j = 5/2$ is $g_{5/2} = 6/7$. Inserting these numbers, we find the following matrix element for the exchange interaction between the localized $5f^2$ system and the delocalized $5f$ electron

$$|M| = |I_{\text{eff}}(g_{\text{eff}}(f^2) - 1)J_z(g_{5/2} - 1)j_z| \quad (12)$$

which implies for the effective exchange coupling

$$I_{\text{eff}} \simeq 0.8 \text{ eV}. \quad (13)$$

This is of the correct size for $5f$ electrons.

Finally, the renormalization of the effective masses which results from the coupling between the two $5f$ subsystems is determined. The enhancement of the band mass is calculated from the self-consistent solution of the self-energy equation [13] with the input taken from the *ab initio* electronic structure calculations for the delocalized and the localized $5f$ electrons. The renormalization of the band mass m_b is given by

$$\frac{m^*}{m_b} = 1 - \left. \frac{\partial \Sigma}{\partial \omega} \right|_{\omega=0} \quad (14)$$

where $\Sigma(\omega)$ denotes the local self-energy of the delocalized $5f$ states. The latter is obtained by analytic continuation from the Matsubara frequencies $\omega_n = \pi T(2n + 1)$ at the temperature T where it is given by

$$\Sigma(i\omega_n) = a^2 M^2 T \sum_{n'} \chi(i\omega_n - i\omega_{n'}) g(i\omega_{n'}) \quad (15)$$

in terms of the local susceptibility

$$\chi(i\omega_n - i\omega_{n'}) = -\tanh \frac{\tilde{\delta}}{2T} \frac{2\tilde{\delta}}{(i\omega_n - i\omega_{n'})^2 - \tilde{\delta}^2} \quad (16)$$

and the local propagator

$$g(i\omega_n) = \int dE \frac{N(E)}{i\omega_n - E - \Sigma(i\omega_n)}. \quad (17)$$

Here $2N(E)$ is the total density of states at the energy E as obtained from the bandstructure, when two $5f$ electrons are kept localized. The prefactor a denotes the $5f$ weight per spin and U atom of the conduction electron states near E_F . The local propagator reduces to $g(i\omega_n) \rightarrow -i\pi N(E_F) \text{sgn}(\omega_n)$ if the variation with energy of the DOS can be neglected. In the present case, however, this simplification cannot be justified.

The self-consistent calculation yields a mass enhancement of 9.6. The resulting calculated quasiparticle masses are in excellent agreement with experiment (see Table I).

Table I. Effective Masses for $\dot{H} \parallel c$. Notation for FS Sheets and Experimental values from Ref. [27]

FS sheet	m^*/m (exp.)	m^*/m (Theory)
ζ	65	59.6
γ	33	31.9
β	19	25.1
ϵ_2	18	17.4
ϵ_3	12	13.4
β	5.7	9.6

Note: Theoretical values from Ref. [25].

3.2. Superconductivity

Strong evidence for an interplay of CEF excitations and superconductivity comes from tunnelling [23] and inelastic neutron scattering experiments [19–22,28]. The pioneering tunnelling experiments were performed on UPd₂Al₃/Al₂O₃/Pb tunnel junctions. Thereby, a structure in the frequency-dependent order parameter $\Delta(\omega)$ was observed around 1 meV. This strong coupling feature can be related to dispersive spin-wave like excitations (magnetic excitons) in the AF phase of UPd₂Al₃. They are seen in inelastic neutron scattering experiments. The measured magnetic excitation energy at the antiferromagnetic zone center \mathbf{Q}_0 is only slightly larger than $2\Delta \simeq 6T_c$ and results in observable resonance structures when superconductivity sets in [28].

For a consistent description of superconductivity and the enhanced effective mass, a model calculation has been performed in Ref. [6] that uses a fit of the three-dimensional magnetic exciton dispersion derived from inelastic neutron scattering. The dispersion is most pronounced in the c -direction and we shall approximate it by [7]

$$\omega(q_z) = \omega_{\text{ex}}[1 + \beta \cos(cq_z)] \quad (18)$$

with $\omega_{\text{ex}} = 5$ meV, $\beta = 0.8$ and c denoting the lattice constant perpendicular to the hexagonal planes. The form (18) of the magnetic exciton spectrum simplifies solving Eliashberg's equations for the conduction electron self-energy $\Sigma(p_z, \omega_n)$ and order parameter $\Delta(p_z, \omega_n)$. They are of the form

$$\begin{aligned} \Sigma(p_z, \omega_n) &= \frac{T}{N_z} \sum_{p'_z, m} K(p_z - p'_z; \omega_n - \omega_m) \\ &\quad \int \frac{dp'_\perp}{(2\pi)^2} G(p'_\perp, p'_z, \omega_m) \\ \Delta(p_z, \omega_n) &= -\frac{T}{N_z} \sum_{p'_z, m} K(p_z - p'_z; \omega_n - \omega_m) \\ &\quad \Delta(p'_z, \omega_m) \int \frac{dp'_\perp}{(2\pi)^2} \\ &\quad |G(p'_\perp, p'_z, \omega_m)|^2 \end{aligned} \quad (19)$$

and the integration over dp'_\perp can be done first. Note that N_z is the number of lattice sites along the c -axis. Equation (19) assumes that the order parameter has even parity (singlet channel). The self-energy enters

Green's function in the well-known way

$$G^{-1}(\mathbf{p}, \omega_n) = i\omega_n - \epsilon_p + \mu - \Sigma(p_z, \omega_n). \quad (20)$$

The boson propagator $K(p_z, \omega_\nu)$ ($\omega_\nu = 2\pi T_\nu$, $\nu = \text{integer}$) describes the magnetic-exciton exchange between the quasiparticles which form Cooper pairs. It is of the form

$$K(q_z, \omega_\nu) = g \frac{\omega_{\text{ex}}^2}{(\omega(q_z))^2 + \omega_\nu^2} \quad (21)$$

with a coupling constant g given by

$$g = \frac{I^2}{4} \left(\frac{1}{c} \frac{p_0^2}{2\pi} \right) \frac{1}{\omega_{\text{ex}}}. \quad (22)$$

Here the coupling constant I refers to the interaction between the conduction electrons having partially $5f$ character and the localized $5f^2$ electrons. The two levels $|\Gamma_3\rangle_i$ and $|\Gamma_4\rangle_i$ at a uranium site i are described by a pseudospin τ_{iz} so that $\tau_{iz}|\Gamma_{3(4)}\rangle_i = \pm \frac{\delta}{2}|\Gamma_{3(4)}\rangle_i$. For the interaction Hamiltonian we assume a simple Ising-like form

$$H_{c-f} = I \sum_i \sigma_{iz} \tau_{ix} \quad (23)$$

where σ_i refers to the spin of the delocalized $5f$ electron which is part of the conduction electrons. Furthermore, in Eq. (22) p_0 is the radius of a circle in the (p_x, p_y) plane containing the same area as the hexagon and c is the lattice constant in z direction.

The Fermi surface of the antiferromagnetic ground state consists of a cylindrical part and a torus (see Fig. 4). In the paramagnetic state, both sheets result from the same band. For simplicity we will do the calculations for a paramagnetic state and approximate the Fermi surface by a weakly corrugated cylinder. The latter is described by a parabolic dispersion $\epsilon_{p_\perp} = \epsilon_\perp (p_\perp/p_F)^2$. This seems justified in view of the fact that AF order opens small gaps at the corresponding symmetry points which have a comparatively small influence on the superconducting transition temperature T_c . This was studied before on systems like TbMo₆S₈ [29] or HoNi₂B₂C [30].

After the dp'_\perp integrations are done, solving the Eliashberg equations reduces to a one-dimensional problem. The following point is essential and should be stressed: the kernel $K(q, \omega_\nu)$ is strongly peaked at $q_z = \pi/c$ and $\omega_\nu = 0$. Therefore, roughly speaking, for the singlet channel the gap equation is of the type [6]

$$\Delta(p_z, \pi T) = -C(p_z) \Delta\left(p_z - \frac{\pi}{c}, \pi T\right) \quad (24)$$

This suggests the form

$$\Delta(p_z) \sim \cos(cp_z) \quad (25)$$

with lines of nodes perpendicular to the c -axis. Note that they are situated at the AF Brillouin zone boundary. Such a node structure was recently found in experiments on the directional dependence of the thermal conductivity in an applied magnetic field [8].

We want to point out that rotational symmetry in spin space is broken in the case under consideration because of the Ising-like interaction (23). Solving the Eliashberg equations, one finds also an odd-parity solution with the same T_c

$$\Delta(p_z) \sim \sin(cp_z) \quad (26)$$

and a spin part $|\chi\rangle = (2)^{-1/2}(|\uparrow\downarrow\rangle + |\downarrow\uparrow\rangle)$. We discard this solution. For a spin rotational invariant interaction, it would be part of a spin triplet order parameter. The reader should realize that we obtain here superconducting pairing from an interaction H_{c-f} which is *not* time-reversal invariant. This is possible because of the dispersion of the magnetic excitations and a required sign change of the order parameter as expressed in Eq. (24). The order parameter (25) is conventional in the sense that it has the same symmetry properties as the AF ordered lattice while the one in Eq. (26) has a lower symmetry and therefore is unconventional.

3.3. Comparison of the Parameters

In the following we compare the parameters which were used in the calculation of the anisotropic effective mass in Section 3.1. and when Eliashberg's equations were solved.

First of all, there is a difference in the bare band-structure DOS at the Fermi level. In the calculation of the effective mass, the sum over the intermediate states in the self-energy Eq. (15) runs over *all* states in the vicinity of the Fermi energy, i.e., all sheets are included in the calculation. As a result, the full DOS of the paramagnetic state, $N(E_F) = 2.76$ states/(eV cell spin) was inserted into the self-consistency equation. The volume enclosed by the Fermi surface corresponds to one electron, the f content of the strongly hybridized states being ~ 0.65 . The solution of the Eliashberg equations for the superconducting transition, on the other hand, approximated the Fermi surface of the paramagnetic phase by a cylinder. This choice for the most relevant part of the Fermi surface was suggested by conventional band structure calcu-

lations based on the LDA [31] which assumes three $5f$ electrons to be itinerant. The DOS at the Fermi energy is chosen to be $N_P(E_F) \simeq 2$ state/(eV cell spin) which corresponds to the contribution of the cylinder plus torus in Fig. 4. In the paramagnetic state, these two pieces are joint. In Ref. [6] a value of $N_P(E_F) = 1$ state/(eV cell spin) was chosen which in retrospect seems too small.

The local excitations responsible for the mass enhancement and the quasiparticle interaction are characterized by the energies $\tilde{\delta} \simeq 7$ meV [25] and $\omega_{\text{ex}} \simeq 5$ meV [6], respectively, where I has been defined in Eq. (23). For *ab initio* calculations a value of [25]

$$(a_f M)^2 N(E_F) = 0.041 \text{ eV} \quad (27)$$

is derived. In the other hand, the product $I^2 N_P(E_F)$ is adjusted to reproduce the experimentally observed mass enhancement within the simplified scheme applied in solving Eliashberg's equations. This yields a value of [6]

$$I^2 N_P(E_F) = 0.026 \text{ eV}. \quad (28)$$

With it the superconducting transition temperature comes out by a factor 1.6 too large, i.e., $T_c = 2.9$ K instead of 1.8 K.

It is noticed that the two values (27) and (28), which should be the same, do not completely agree. This is not too surprising in view of the different approximations which were made in Sections 3.1 and 3.2. The agreement is better when the coupling constants $I = 0.16$ eV and $(a_f |M|) = 0.12$ eV are directly compared. Furthermore, it is unrealistic to expect that T_c can be accurately determined. But we have shown that the proposed non-phononic mechanism gives a value of the right size.

4. CONCLUSIONS

Based on the dual model for $5f$ electrons in U compounds our microscopic understanding of those materials has considerably improved. UPd_2Al_3 is a model example for that. Not only can the strong anisotropy of the semi-heavy quasiparticle mass be explained without adjustable parameter, but also the size of the superconducting transition temperature is obtained in good approximation. The latter is caused by the exchange of intra-atomic excitations between the conduction electrons leading to Cooper-pair formation. The intra-atomic excitations take place within the subsystem of localized $5f$ electrons. They

form a band of magnetic excitons which has been explored and characterized by inelastic neutron scattering. In most cases the exchange of magnetic excitations between conduction electrons is pair breaking. Here it is pair-forming as we have shown in detail. But this requires a superconducting order-parameter which has a line of nodes in the hexagonal plane. A node structure of this form was recently observed experimentally by studying the behavior of the anisotropic thermal conductivity in magnetic fields. Therefore, the indications are strong that UPd_2Al_3 is indeed a superconductor with a non-phononic interaction being the cause of pair formation.

ACKNOWLEDGMENTS

We thank Dr P. Thalmeier for helpful discussions and cooperation on Section 3.2. One of us (PF) had the privilege to work as a postdoc in the group of Mike Tinkham in Berkeley. He spent there an extremely interesting and stimulating period of time. Therefore we delight in devoting this paper to him on the occasion of his 75th birthday.

REFERENCES

1. H. Fröhlich, *Phys. Rev.* **79**, 845 (1950).
2. E. Maxwell, *Phys. Rev.* **78**, 477 (1950); C. A. Reynolds, B. Serin, W. H. Wright, and L. B. Nesbitt, *Phys. Rev.* **78**, 487 (1950).
3. N. N. Bogoliubov, V. V. Tolmachev, and D. V. Shirkov, *Fortschr. d. Phys.* **6**, 605 (1958).
4. P. Fulde, L. L. Hirst, and A. Luther, *Z. Phys.* **238**, 99 (1970).
5. A. A. Abrikosov and L. P. Gorkov, *Zh. Eksperion i Teor Fiz.* **39**, 1781 (1960) [English translation: *Sov. Phys. JETP* **12**, 1243 (1961)].
6. P. McHale, P. Thalmeier, and P. Fulde, *Phys. Rev. B*, **70**, 014513 (2004).
7. P. Thalmeier, *Eur. Phys. Journ. B* **27**, 29 (2002).
8. T. Watanabe, K. Izawa, Y. Kasahara, Y. Haga, Y. Onuki, P. Thalmeier, K. Maki, and Y. Matsuda, cond-mat/0405211.
9. E. Bucher, K. Andres, J. P. Maita, and G. W. Hull, *Helv. Phys. Acta* **41**, 723 (1968).
10. J. Keller and P. Fulde, *J. Low Temp. Phys.* **4**, 289 (1971); J. Keller and P. Fulde, *J. Low Temp. Phys.* **12**, 63 (1973).
11. R. W. McCallum, W. A. Fertig, C. A. Lu-engo, M. B. Maple, E. Bucher, J. P. Maita, A. R. Sweedler, L. Mattix, P. Fulde, and J. Keller, *Phys. Rev. Lett.* **34**, 1620 (1975).
12. D. V. Efremov, N. Hasselmann, E. Runge, P. Fulde, and G. Zwicky, *Phys. Rev. B* **69**, 115114 (2004).
13. R. White and P. Fulde, *Phys. Rev. Lett.* **47**, 1540 (1981).
14. J. Schoenes, O. Vogt, J. Löhle, F. Hulliger, and K. Mattenberger, *Phys. Rev. B* **53**, 14987 (1996).
15. T. Takahashi, N. Sato, T. Yokoya, A. Chainani, T. Morimoto, and T. Komatsubara, *J. Phys. Soc. Jpn.* **65**, 156 (1995).
16. N. Metoki, Y. Haga, Y. Koike, and Y. Onuki, *Phys. Rev. Lett.* **80**, 5417 (1998).
17. N. Bernhoeft, N. Sato, B. Roessli, N. Aso, A. Hiess, G. H. Lander, Y. Endoh, and T. Komatsubara, *Phys. Rev. Lett.* **81**, 4244 (1998).
18. C. Geibel, C. Schank, S. Thies, H. Kitazawa, C. D. Bredl, A. Böhm, M. Rau, A. Grauel, R. Caspary, R. Helfrich, U. Ahlheim, G. Weber, and F. Steglich, *Z. Phys. B* **84**, 1 (1991).
19. T. E. Mason and G. Aeppli, *Matematisk-fysiske Meddelelser* **45**, 231 (1997).
20. N. Sato, N. Aso, G. H. Lander, B. Roessli, T. Komatsubara, and Y. Endoh, *J. Phys. Soc. Jpn.* **66**, 1884 (1997).
21. N. Sato, N. Aso, G. H. Lander, B. Roessli, T. Komatsubara, and Y. Endoh, *J. Phys. Soc. Jpn.* **66**, 2981 (1997).
22. N. Bernhoeft, *Eur. Phys. J. B* **13**, 685 (2000).
23. M. Jourdan, M. Huth, and H. Adrian, *Nature* **398**, 47 (1999).
24. G. Zwicky, A. N. Yaresko, and P. Fulde, *Phys. Rev. B* **65**, 081103(R) (2002).
25. G. Zwicky, A. Yaresko, and P. Fulde, *Phys. Rev. B* **68**, 052508 (2003).
26. L. Petit, A. Svane, W. Temmermann, Z. Szotek, and R. Tyer, *Europhys. Lett.* **62**, 391 (2003).
27. I. Inada, H. Yamagami, Y. Haga, K. Sakurai, Y. Tokiwa, T. Honma, E. Yamamoto, Y. Onuki, and T. Yanagisawa, *J. Phys. Soc. Jpn.* **68**, 3643 (1999).
28. N. K. Sato, N. Aso, K. Miyake, R. Shiina, P. Thalmeier, G. Varelogiannis, C. Geibel, F. Steglich, P. Fulde, and T. Komatsubara, *Nature* **410**, 340 (2001).
29. M. Ishikawa, and Ø. Fischer, *Solid State Commun.* **24**, 747 (1977).
30. J. W. Lynn, S. Skanthakumar, Q. Huang, S. K. Sinha, Z. Hossain, L. C. Gupta, R. Nagarajan, and C. Godart, *Phys. Rev. B* **55**, 6584 (1997).
31. K. Knöpfle, A. Mavromaras, L. M. Sandratskii, J. Kübler, *J. Phys. Condens. Matter* **8**, 901 (1996).

When are Superconductors Really Superconducting?

C. J. Lobb¹

Received August 15, 2004; accepted September 4, 2004

While the most striking aspect of superconductivity is dissipation-free current flow, it is not straightforward to experimentally demonstrate whether the resistance is truly zero or “merely” immeasurably small. The distinction between zero or very small resistance is important, because the true superconducting state can be destroyed by thermodynamic fluctuations. This paper discusses a variety of different superconducting systems: two-dimensional superconductors, Josephson-junction arrays, and three-dimensional superconductors in zero and nonzero magnetic field, and the experiments conducted to determine which, and under what conditions, systems are *really* superconducting.

KEY WORDS: superconductivity; phase transitions; Kosterlitz-Thouless transition; vortex-glass transition.

1. INTRODUCTION

The hallmark of superconductivity, and the basis of its name, is zero resistance for temperature T below a transition temperature T_c . Since the discovery of superconductivity, much research has been done to understand the limits of this zero resistance state [1]. It is known, for example, that a magnetic field greater than the critical field $H_c(T)$ will destroy superconductivity in a type-I superconductor, as will a current density greater than the critical current density $J_c(T)$.

One other property that determines whether the resistance goes to zero, or is, perhaps, just very small, is the spatial dimensionality of the system, D . In zero magnetic field, and for small currents, we know that the resistance is not strictly zero for one-dimensional systems. The resistance is zero for $D = 3$, and for $D = 2$, some systems do not have zero resistance, while others will. Interestingly, the two-dimensional superconductors that have zero resistance also have zero critical current.

Roughly 50 years ago, two remarkable theories provided us with an understanding of superconductivity. The phenomenological Ginzburg-Landau

theory assumed a superconducting order parameter analogous to the order parameter in other second-order phase transitions. The Ginzburg-Landau theory has been very successful in describing the behavior of superconductors on the macroscopic level. The microscopic Bardeen-Cooper-Schrieffer theory showed that a weak attractive electron-electron interaction leads to a superconducting state. Both theories, however, make mean-field assumptions [1]. Because of this, thermal fluctuations are not taken into account, and fluctuations make the existence of zero resistance a subtle and interesting question.

At any nonzero temperature, fluctuations occur because a system can borrow an energy kT from its environment. For $T < T_c$, this makes it possible to temporarily increase the energy of a small volume of superconductor, perhaps enough to drive the small volume into the normal state. The effects of such fluctuations may be relatively benign, perhaps weakening superconductivity without destroying it. Under the right circumstances, however, fluctuations can destroy the superconducting state.

There are two key physical quantities, the correlation length ξ , and the correlation time τ , that together characterize the fluctuations [2]. In three dimensions, the correlation length diverges at T_c , varying as

$$\xi \sim \varepsilon^{-\nu} \quad (1)$$

¹Center for Superconductivity Research, Department of Physics, University of Maryland, College Park, Maryland 20742.

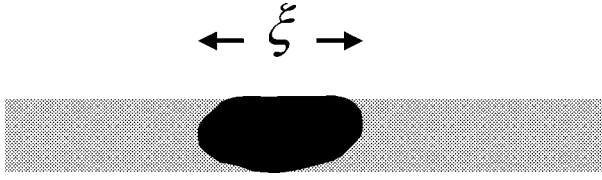


Fig. 1. Schematic picture of a superconducting wire, shown in gray. The fluctuation (shown in black) is large enough to cross the entire wire, making the system essentially one dimensional and destroying the superconductivity.

where $\varepsilon = |T - T_c|/T_c$ and ξ is the size of a typical fluctuation. Above T_c , ξ is the size of superconducting regions that occur as fluctuations in the normal background, and below T_c , ξ is the size of normal fluctuations in the superconducting background. The correlation time varies as

$$\tau \sim \xi^z \sim \varepsilon^{-z\nu} \quad (2)$$

and is a measure of the lifetime of fluctuations. Eqs. (1) and (2) contain the static and dynamic critical exponents ν and z which characterize the diverging length and time scales. Note that for the special case of $D = 2$, the correlation length diverges, but not as a power of ε . For $D = 2$, however, τ will still vary as ξ^z .

It is instructive to briefly consider the case where $D = 1$. In order to be in the one-dimensional limit, a superconducting wire must be close enough to T_c for the correlation length, $\xi(T)$, to be larger than the diameter of the wire. In this limit, at nonzero temperature there will be fluctuations that are large enough to drive the entire cross section of the sample normal, as shown schematically in Fig. 1. This will cause a nonzero resistance, and will destroy the long-range coherence in the sample. Since the probability of such a fluctuation is given by a Boltzmann factor, it is nonzero (although perhaps very small), so for $T > 0$ the resistance will be greater than zero. Mike Tinkham and his collaborators studied superconductors in $D = 1$ extensively, as discussed in Refs. 1 and 3.

I first worked on this type of problem in the early 1980s with David Abraham, Teun Klapwijk, and Mike Tinkham [4,5]. At the time, there was much interest in the Kosterlitz-Thouless transition, which was proposed as a theoretical description of the phase transition in $D = 2$ neutral superfluids [6]. While it was at first thought that the Kosterlitz-Thouless transition should not occur in superconductors, it was later shown theoretically that it should occur in large but finite samples if the two-dimensional

penetration depth were large enough [7]. As described in Section 2, we studied this problem in two-dimensional square lattices of Josephson junctions with zero external magnetic field, and were able to observe a key signature of the transition in our experiments.

The discovery of high-temperature superconductors brought about renewed interest in the Kosterlitz-Thouless transition. Many papers reported a Kosterlitz-Thouless transition in high-temperature superconductors. The transition was sometimes reported in quite thick samples, presumably because the materials are sufficiently anisotropic to decouple the Cu—O planes from each other, making even thick samples effectively two dimensional. Section 3 of this paper describes work done by Max Repaci and other members of my group at Maryland on single-unit-cell films of $\text{YBa}_2\text{Cu}_3\text{O}_{7-\delta}$ in zero magnetic field [8]. These samples are presumably as two dimensional as you can get in a cuprate, yet we showed that they did *not* undergo a Kosterlitz-Thouless transition. The resistance of these unit-cell thick films remained nonzero (but very small) to very low temperatures because their two-dimensional penetration depths are too small, in marked contrast with the Josephson arrays of Section 2.

It seemed natural to next study the $D = 3$ superconducting phase transition in thick high- T_c films. Because of their short coherence lengths, long penetration depths, and high-transition temperatures, fluctuations play a much greater role in high- T_c superconductors than in low- T_c superconductors [9]. Given our work in $D = 2$, the $D = 3$ transition in zero magnetic field seemed like a good place to start. Doug Strachan began this work, but found, surprisingly, that results disagreed with theory. We decided to try our experiment in a magnetic field, because there were a very large number of recent theoretical and experimental papers on the topic, with theory and experiment agreeing that a new type of phase transition (depending on the type of pinning in the sample, a vortex-glass [2] or a Bose-glass [10] transition) occurred in a field. Our experimental results in magnetic field were very similar to other people's results. When analyzing our data, however, our conclusions were *not* in agreement with most others': The resistance did not go to zero, suggesting that the superconducting phase transition does not occur in magnetic field for $D = 3$ [11]. These results are discussed in Section 4.

Building on the results obtained in magnetic field, we returned to the $D = 3$ zero field

experiments. The results were disturbing: The zero-field results were very similar to the nonzero field results. In particular, the resistance did not appear to be going to zero in the manner expected as temperature was lowered. Matt Sullivan showed [12] that our samples were not sufficiently three dimensional: Even in very thick films (0.32 μm), the experiment's length scales were limited by the film thickness. These results are discussed in Section 5.

2. KOSTERLITZ-THOULESS TRANSITION IN JOSEPHSON-JUNCTION ARRAYS

As discussed briefly in Section 1, thermal fluctuations will cause resistance below T_c in a superconductor if the correlation length, ξ , is larger than the diameter of a superconducting wire. The situation is subtler in two dimensions.

To study superconductivity in $D = 2$, one can make very thin films. While this approach works [13], it can be difficult to make films that are very thin and very uniform.

Another approach is to make square lattices of Josephson junctions. As discussed in Refs. 1, 5, 14, and 15, square Josephson-junction arrays are a discrete version of a two-dimensional superconductor, with the advantage that properties such as the penetration depth can be varied by changing the critical currents of the junctions.

As shown by Kosterlitz and Thouless (KT) [6], the essential fluctuations to consider are vortex-antivortex pairs. Since we are considering zero external magnetic field here, there will be an equal number of vortices and antivortices. KT showed that if the vortex-antivortex interaction is logarithmic in separation, a vortex-unbinding transition occurs. Below a characteristic temperature T_{KT} , each vortex is bound to an antivortex, while above T_{KT} , some vortices will thermally unbind.

In a two-dimensional Josephson-junction array, vortex-antivortex pairs interact via

$$U = \Phi_0 i_c \ln\left(\frac{r}{a}\right) \quad (3)$$

where $\Phi_0 = h/2e$ is the flux quantum, i_c is the temperature-dependent critical current of one junction, r is the distance between the vortex and the antivortex centers, and a is the lattice spacing of the array [15]. Eq. (3) is true only if

$$r < \lambda_{\perp}, \quad (4)$$

where λ_{\perp} is the penetration depth for two-dimensional samples, given by

$$\lambda_{\perp} = \frac{\Phi_0}{2\pi\mu_0 i_c}. \quad (5)$$

As long as the sample size is greater than λ_{\perp} , Eq. (4) will always be satisfied, and a KT transition can be observed, as first shown in Refs. 7. Note that, by making i_c smaller, λ_{\perp} can be made as large as needed to guarantee that Eq. (4) is true.

Given that the KT transition was predicted to occur, how would one observe it in a Josephson array? Since there are free vortices present for $T > T_{KT}$, there will be a flux-flow resistance. The prediction for this is

$$R_{HN} = c_1 R_n e^{-\left[\frac{c_2 T_{KT}}{T - T_{KT}}\right]^{1/2}}. \quad (6)$$

Here R_n is the normal-state resistance of the array, and c_1 and c_2 are constants of order unity [7,16]. (The formula for arrays is more complicated, but this thin-film Halperin-Nelson version is sufficient for the discussion here. See Ref. 15.) There are subtle problems with the formula, however: It is only correct for small currents, and for temperatures close to T_{KT} , though the definitions of "close to" and "small" are nontrivial. Nevertheless, as other people measuring thin films and arrays before us had found [17], Eq. (6) seemed to agree with the data. This is shown in Fig. 2.

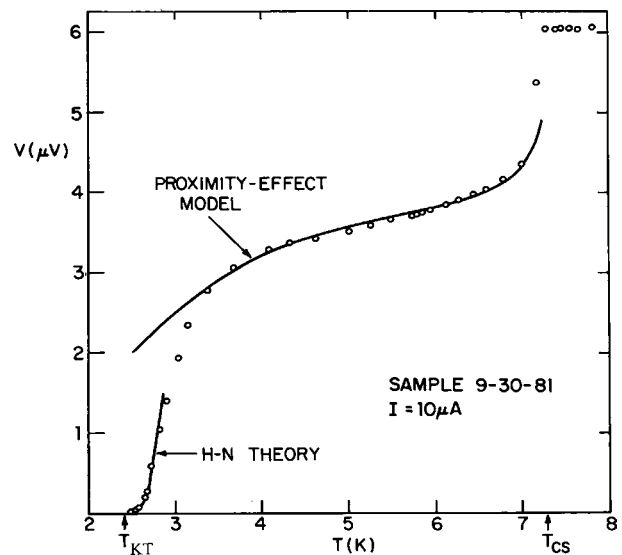


Fig. 2. Voltage vs. temperature at a constant $10 \mu\text{A}$ current for a 1000×1000 Josephson-junction array. Data are open circles, and solid labeled H-N (Halperin-Nelson) theory is a fit to the complete form of Eq. 6. From Ref. 4.

When we arrived at this point in the research, Mike Tinkham made a typical Tinkham comment. He told us that it is easy to fit data to reasonable three-parameter functions, and that Eq. (6) was reasonable: It predicted that the resistance should drop as the temperature was lowered. He reminded us that a single overdamped junction with small critical current would have a measurable resistance due to thermal fluctuations that also dropped rapidly as the temperature was lowered. In the limit of small current, the prediction for this is [18]

$$R_{AH} = R_n \left[I_0 \left(\frac{\Phi_0 i_c}{\pi k T} \right) \right]^{-2} \approx R_n \frac{2\Phi_0 i_c}{k T} e^{-\frac{2\Phi_0 i_c}{\pi k T}}. \quad (7)$$

Here I_0 is the zeroth-order-modified Bessel function, and the approximate version holds when the argument of the Bessel function is much greater than one.

While Eq. (7) is nonzero for $T > 0$, it does predict a rapid drop in resistance as the temperature is lowered. At first sight, in fact, it was hard to prove that Eq. (7) did not explain the data, especially since i_c depended on T in a manner that was not precisely known from experiment.

Fortunately, Ref. 16 provided a more demanding way to test the KT theory. For $T \leq T_{KT}$, they showed that the voltage should be a power of the current, of the form

$$V \propto I^{a(T)}. \quad (8)$$

where Eq. (8) is also restricted to small currents. A striking prediction of the Halperin-Nelson theory is that just below T_{KT} ,

$$a(T_{KT-}) = 3. \quad (9)$$

Eq. (6) predicts ohmic behavior just above T_{KT} , so that V is proportional to I , or

$$a(T_{KT+}) = 1. \quad (10)$$

The KT transition should thus cause a *discontinuous* change in the power-law behavior at T_{KT} . By contrast, Eq. (7) predicts ohmic behavior for *all* temperatures.

The way to see this behavior is to plot current-voltage (IV) curves on a log-log plot, as is done in Fig. 3. Since $\log(V) = a(T) \log(I) + \text{constant}$, the slope of the log-log IV curves should change from 3 to 1 at T_{KT} . The result of this is shown in Fig. 4, where a slightly broadened jump from 3 to 1 can be seen around $T = 2.4$ K. Note that Eq. (8) not only

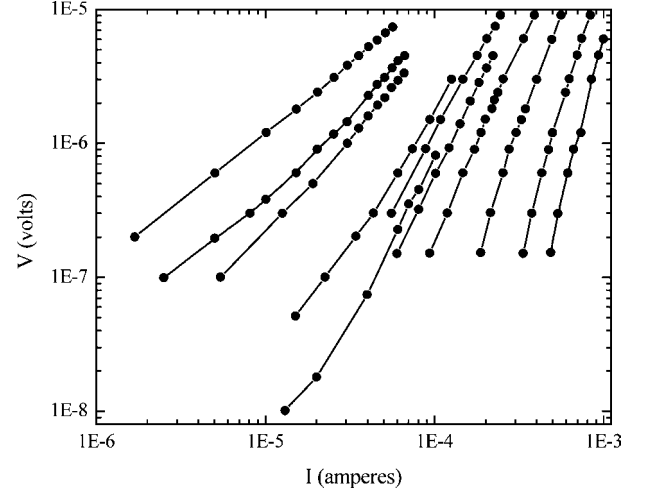


Fig. 3. Log voltage vs. log current for a square Josephson-junction array. These data represent a small subset of the actual data, and were generated by reading points off of continuous IV curves originally made on an XY plotter. Curve at upper left has $T = 2.75$ K, right most curve has $T = 1.95$ K.

implies zero resistance, but also zero critical current, for $T < T_{KT}$.

As further proof that Eq. (7) does not account for the data, Ref. 5 shows that $R_{AH}(T_{KT}) = 0.82R_n$, while, of course, $R_{HN}(T_{KT}) = 0$. The evidence for a KT transition in our arrays was thus very strong, indicating that these two-dimensional samples are indeed superconducting.

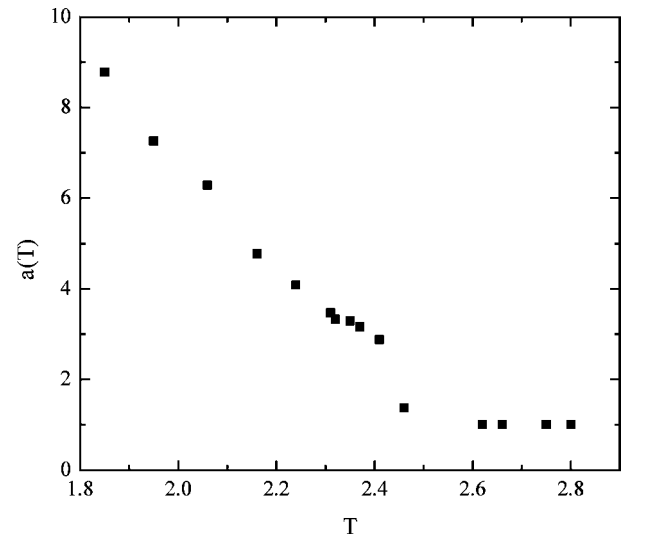


Fig. 4. $a(T)$ vs. T taken from the slopes of $\log I$ - $\log V$ plots for voltages in the 10-nV range. From data in Ref. 4.

3. ABSENCE OF A KOSTERLITZ-THOULESS TRANSITION IN CUPRATE SUPERCONDUCTORS

At the University of Maryland, Max Repaci made and measured single-unit-cell-thick films of $\text{YBa}_2\text{Cu}_3\text{O}_{7-\delta}$ to see if a Kosterlitz-Thouless transition occurred [8]. In such films, vortex–antivortex pairs interact via a potential

$$U = 2\pi n_s^* \frac{\hbar^2}{m^*} \ln\left(\frac{r}{\xi}\right) \quad (11)$$

where n_s^* is the number of Cooper pairs per unit area [5]. Note that Eq. (11) is of the same form as Eq. (3). Like Eq. (3), Eq. 11 is true only if $r < \lambda_\perp$, where in a superconductor of thickness d ,

$$\lambda_\perp = \frac{\lambda^2}{d}, \quad (12)$$

where λ is the bulk penetration depth for the material [18].

The passage of a decade allowed us the significant advantage of easily acquiring data with a computer. IV curves for a typical sample are shown in Fig. 5. (The advantages of Fig. 5 over Fig. 3 are very great indeed!)

Figure 5 certainly appears to show a superconducting transition. At the highest temperatures, the IV curves are ohmic, with slope 1 on a log–log plot. At the lowest temperatures, the voltage drops very rapidly as a function of current, with no indication of ohmic behavior. At intermediate temperatures, the voltage drops rapidly as a function of current at high currents, and is ohmic at low currents. The low-current ohmic “tails” are no longer visible for temperatures below about 22 K on the plot.

The question is, do the ohmic tails disappear because the sample becomes superconducting (presumably by undergoing a KT transition), or do they continue to occur at voltages below the resolution of the voltmeter? A good way to explore this issue is to plot $d\log(V)/d\log(I)$ vs. $\log(I)$, as is done in Fig. 6. From Eqs. (6) and (8), we expect that $d\log(V)/d\log(I) = 1$ for $T > T_{KT}$, $d\log(V)/d\log(I) = 3$ for $T = T_{KT}$, and $d\log(V)/d\log(I) = a(T)$, with $a(T) > 3$, for $T < T_{KT}$, all at low currents.

Rather than showing a KT transition, Fig. (6) indicates that there is not a phase transition at all. At the highest temperatures, $d\log(V)/d\log(I) = 1$ for all currents, indicating the normal state. As the temperature is lowered, $d\log(V)/d\log(I) > 1$ at intermediate currents, but bends back down toward 1 at low

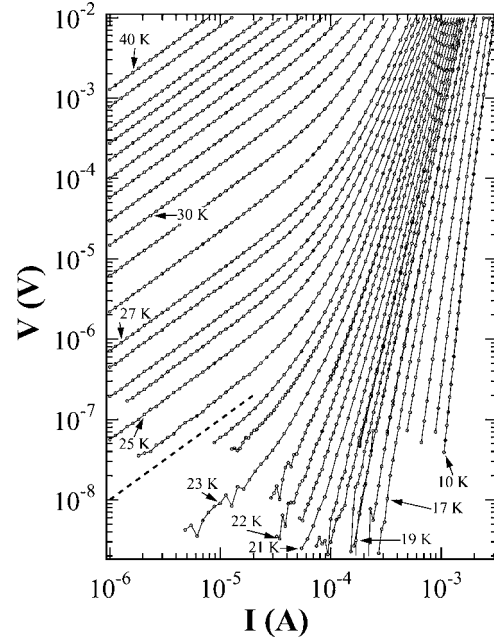


Fig. 5. Current–voltage characteristics plotted on a log–log scale for a unit-cell thick $\text{YBa}_2\text{Cu}_3\text{O}_{7-\delta}$ film in zero magnetic field. Lines connecting the points are guides for the eye. The dashed line near the bottom of the plot has a slope of 1, representing ohmic behavior. Temperatures range from 40 K at the top to 10 K at the bottom. From Ref. 8.

currents. As the temperature is lowered further, the trend down is still evident, but $d\log(V)/d\log(I)$ does not reach 1 because of limited voltmeter sensitivity. Furthermore, it is clear that there is no isotherm where $d\log(V)/d\log(I) = 3$ or any other larger constant over any appreciable range of current.

The simplest explanation for Fig. (6) is that there is not a KT transition, perhaps because λ_\perp is smaller than the sample size. As discussed in Ref. 8, the data imply that $\lambda_\perp(T = 0) \approx 160 \mu\text{m}$. Equation (12), combined with single-crystal measurements of $\lambda(0)$, imply a value of $\lambda_\perp(T = 0)$ which is a factor of 4 smaller than the estimate in Ref. 8, as might be expected given that single crystals are cleaner and have much higher transition temperatures than unit-cell films. Both estimates are smaller than the $200 \mu\text{m}$ sample width, so that Eq. (11) is not valid for all vortex–antivortex pairs in the sample. Indeed, when $r > \lambda_\perp$, the interaction energy approaches a constant, which guarantees that more widely separated vortex–antivortex pairs will be thermally unbound at *all* nonzero temperatures [8,15]. The absence of a KT transition, and the occurrence of nonzero resistance at low temperatures, are thus in agreement with theory.

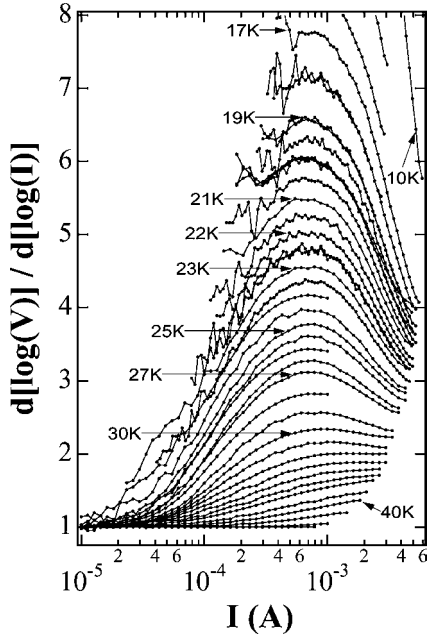


Fig. 6. $d\log(V)/d\log(I)$ as a function of current. Temperatures range from 10 K at the upper right to 60 K at the bottom. Lines connecting the points are guides for the eye. From Ref. 8.

Note that Eq. (12) implies that thicker samples are even less likely to undergo a KT transition. We concluded that $\text{YBa}_2\text{Cu}_3\text{O}_{7-\delta}$ does not undergo a KT transition—earlier work failed to distinguish between very small resistance and zero resistance.

4. THREE-DIMENSIONAL SUPERCONDUCTORS IN A MAGNETIC FIELD

Starting with the pioneering theoretical work of Fisher [19] and experimental work of Koch *et al.* [20], a new picture of the transition for bulk type-II superconductors in a magnetic field emerged in the early 1990s [21]. On the basis of work done on conventional superconductors, it had been believed that a magnetic field led to nonzero (although possibly extremely small) resistance [1]. The new consensus was that a transition to a true zero-resistivity state occurs in the presence of a magnetic field. Various theories have been proposed for this phase transition, including a vortex-glass transition [2,19], which is predicted to occur when disorder in the superconductor is uncorrelated, and a Bose-glass transition [10], which is predicted to occur in the presence of correlated disorder. While these theories apply to different situa-

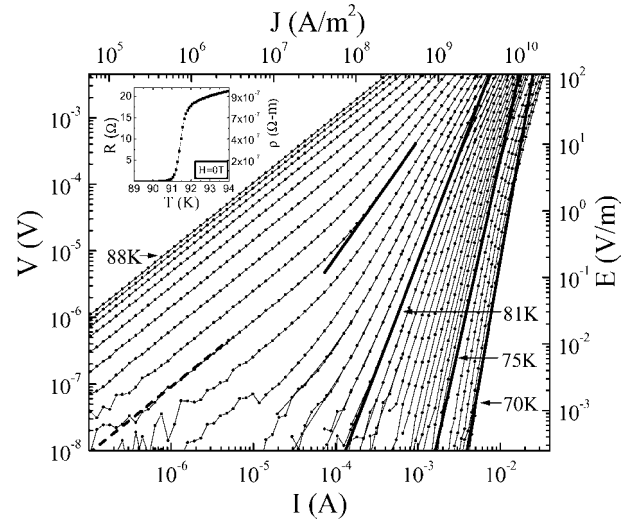


Fig. 7. Current-voltage characteristics plotted on a log-log scale for a 220-nm-thick $\text{YBa}_2\text{Cu}_3\text{O}_{7-\delta}$ film in 4 tesla magnetic field. The dashed line at the lower left has slope 1, while the solid lines at 81, 75, and 70 K are fits to simple power laws. The inset is $R(T)$ vs. T in ambient field. From Ref. 11.

tions, both predict that the resistivity should be zero below a transition temperature.

Doug Strachan at Maryland decided to take another look at this problem [11,21], based on difficulties in understanding our measurements of bulk samples in zero field. Figure 7 shows IV curves from a typical high-quality $\text{YBa}_2\text{Cu}_3\text{O}_{7-\delta}$ thick film. (This film was laser ablated onto a SrTiO_3 substrate and had a thickness of 220 nm.) The pinning in such samples is uncorrelated, so theory predicted, and many earlier experiments seemed to confirm, that a vortex-glass transition should occur.

Qualitatively, Fig. 7 is very similar to Fig. 5. We used the same approach to examine the data more carefully, by plotting a $d\log(V)/d\log(I)$ vs. $\log(I)$ plot, shown in Fig. 8. This graph is very similar to Fig. 6.

It is important, however, to remember that this is a three-dimensional sample, while the data shown in Figs. 5 and 6 come from a two-dimensional sample, so one cannot draw conclusions about the presence or absence of a phase transition based on Eqs. (8)–(10). Fortunately, scaling [2,21] leads to testable predictions for the behavior of IV curves.

The basic prediction is that

$$\frac{V}{I} = \xi^{D-2-z} \chi_{\pm} \left(\frac{I \xi^{D-1}}{T} \right), \quad (13)$$

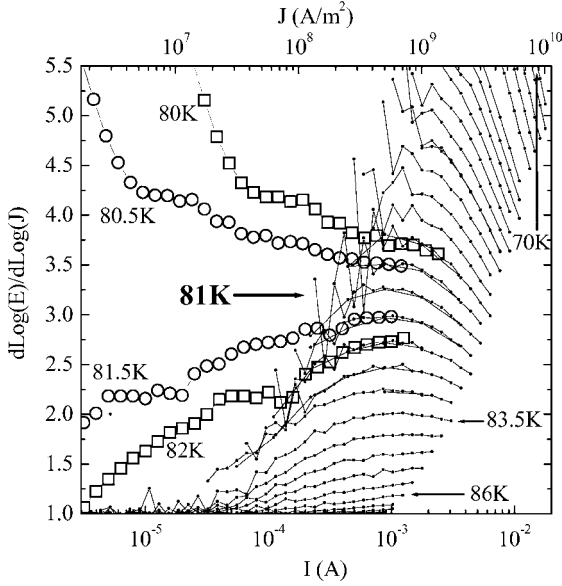


Fig. 8. Small solid circles are $d\log(V)/d\log(I)$ as a function of current. The open symbols are extrapolated data based on scaling showing a change in slope from positive to negative as temperature is lowered—a signature of the phase transition that is not present in the actual data. From Ref. 11.

where ξ and z are defined in Eqs. (1) and (2), and χ_{\pm} are two unknown functions, one (+) for above T_c , the other (−) below T_c .

Eq. (13) has two useful limiting forms. For small currents and $T \geq T_c$, it can be shown that

$$\frac{V}{I} \sim \xi^{D-2-z} \sim \varepsilon^{\nu(2+z-D)}, \quad (14)$$

where ε is defined below Eq. (1). We thus see that samples should be ohmic for small currents above T_c . Note that if $D = 2$ and $z = 2$, this reproduces Eq. (6) when the two-dimensional equation for ξ is used, see Refs. 5,7, and 16.

The second useful limiting form applies for $T = T_c$ (and only at $T = T_c$), where Eq. (13) implies that

$$V \sim I^{(z+1)/(D-1)}. \quad (15)$$

Note that, for $z = 2$ and $D = 2$, Eq. (15) agrees with the KT result, Eq. (8).

Standard scaling analysis assumes that a transition does occur. Assuming this to be correct for the time being, Eq. (15) predicts that the IV curve at $T = T_g$ should be a straight line on a log–log plot, with slope given by $(z + 1)/(D - 1)$. (I use T_g here in place of T_c to indicate that the measurements are in field.) The dark solid line drawn in Fig. 7 is a power-law fit to the IV curve at 81 K which looks closest to

a power law (i.e., it looks straight on a log–log plot.). Using $D = 3$ and Eq. (15), this determines a value of $z = 5.46$.

Following the standard analysis, we next use $T_g = 81$ K, $z = 5.46$, and Eq. (14) to determine ν . The resistances R_L are read off of the low-current tails in Fig. 7, and plotted on a log–log plot, as shown in the inset to Fig. 9a. It is seen that below about 87 K, a

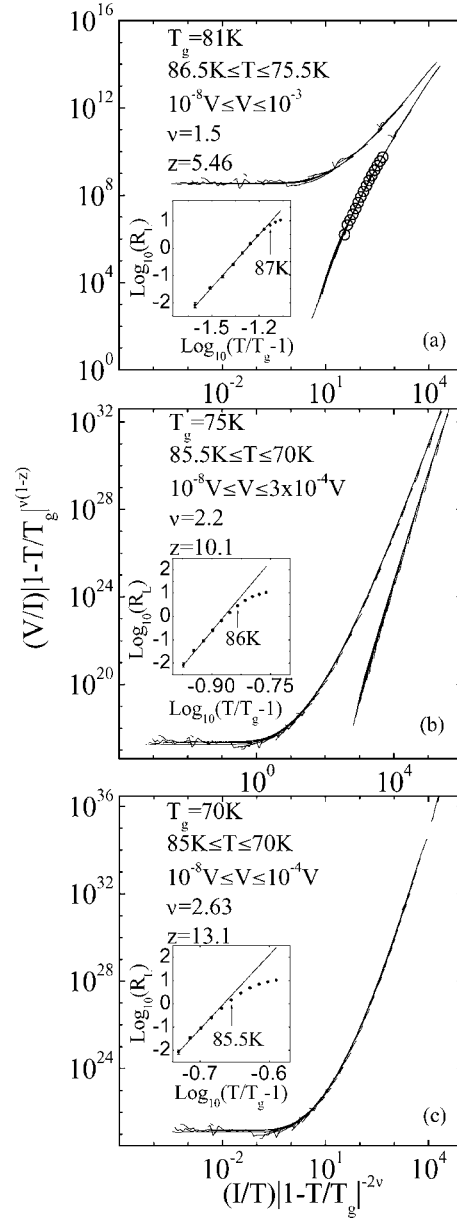


Fig. 9. Collapses of the data from Fig. 7 using Eq. (16), using different values for T_g . All of the data collapses look good, which demonstrates that the technique can be too flexible if used uncritically. From Ref. 11.

good fit is obtained, with deviations at higher temperatures. Equation (14) yields a value $\nu = 1.5$, again consistent with other values in the literature.

Equation (13) can be rewritten as

$$\frac{V}{I} \xi^{2+z-D} = \chi_{\pm} \left(\frac{I \xi^{D-1}}{T} \right). \quad (16)$$

Equation (16) predicts that a plot of $V \xi^{2+z-D}/I$ against $I \xi^{D-1}/T$ should “collapse” all of the data in the critical regime onto one of two curves, χ_+ for $T \geq T_g$ and χ_- for $T \leq T_g$. This data collapse is shown in Fig. 9a.

The data collapse shown in Fig. 9a is very impressive to the eye. The apparent success of the data collapse is widely taken to indicate the data scale. This, in turn, would indicate that a phase transition has taken place.

Unfortunately, Fig. 8 and Eq. (15) taken together indicate that a phase transition has not taken place. No nonnormal state data in Fig. 8 fall on a straight horizontal line, as predicted by Eq. (15).

The problem is that the scaling approach must be applied with more caution. Note that qualitatively, at least, *all* the isotherms with $T \leq 81$ K appear to be straight over some range in V in Fig. 7. (Note, however, that Fig. 8 indicates that this is not true.) They would thus all *appear* to satisfy Eq. (15), which suggests that T_g may not be uniquely determined by the standard procedure. To test this idea, we did the standard scaling analysis with a different value of $T_g = 75$ K. The result of this scaling analysis is graphed in Fig. 9b. Remarkably, this data collapse also looks very good.

Taking this to the extreme case, Fig. 9c shows the result of choosing $T_g = 70$ K, the lowest temperature measured in the experiment. Here, since all the data are from temperatures above the nominal T_g , all the data collapse onto only one curve, corresponding to χ_+ in Eq. (9). Once again, the collapse appears to be quite good.

The problem with the conventional scaling collapse approach is that it is too flexible, as Fig. 9 shows. A more stringent test of scaling is to use Eq. (13) to generate predictions based on extrapolation of the actual data, as is done in the open symbols in Fig. 8. These extrapolations show a clear signature of the phase transition which is not present in the actual data: All curves tend toward ohmic behavior at low currents for $T > T_g$, while all curves diverge for $T < T_g$, with a break at at the critical isotherm. On the basis of this analysis, we concluded that the data

are inconsistent with the occurrence of a superconducting phase transition.

5. THREE-DIMENSIONAL SUPERCONDUCTORS IN ZERO MAGNETIC FIELD

While the data discussed in the previous section strongly indicated that the resistance became small but not zero at lower temperatures, they did not tell us why there was no superconducting phase transition. Were the old theories, which predicted small but nonzero resistance in a magnetic field, correct after all? Or was something else going on?

It seemed like a good time to return to the $D = 3$ zero magnetic field experiment, which Matt Sullivan did [12]. The existence of a superconducting phase transition in this case is not in doubt, and furthermore, there are theoretical estimates for the critical exponents ν and z . Very close to T_c ($|T - T_c|$ smaller than about 2 K [9]), the transition is expected to be of the three-dimensional XY type, with $\nu \cong 0.67$ and $z = 2$ for diffusive dynamics [2]. Interestingly, however, researchers have found vortex-glass like exponents $\nu \cong 1.1$ and $z \cong 8.3$ in small fields (< 10 mT) [22] while others find three-dimensional XY exponents when extrapolating to zero field from higher fields [23] and in crystals [24].

Figure 10 is a $\log(V)$ – $\log(I)$ plot for a 210-nm-thick $\text{YBa}_2\text{Cu}_3\text{O}_{7-\delta}$ film in zero magnetic field

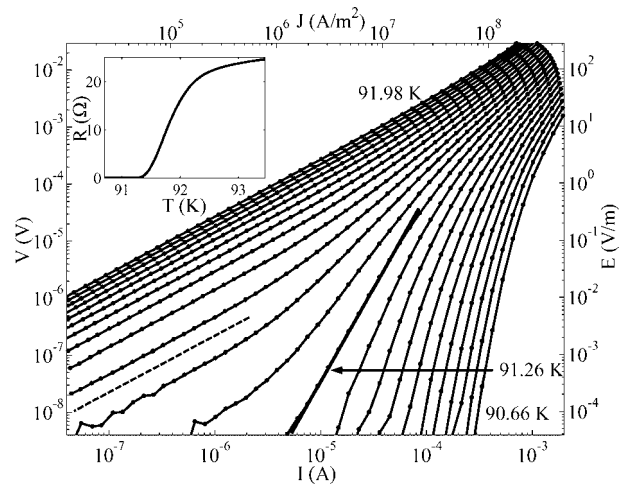


Fig. 10. Current–voltage characteristics for a 210-nm $\text{YBa}_2\text{Cu}_3\text{O}_{7-\delta}$ film in zero magnetic field. Curves are separated by 60 mK. The dashed line indicates a slope of 1, or ohmic behavior. Inset shows $R(T)$ at 10 μA . From Ref. 12.

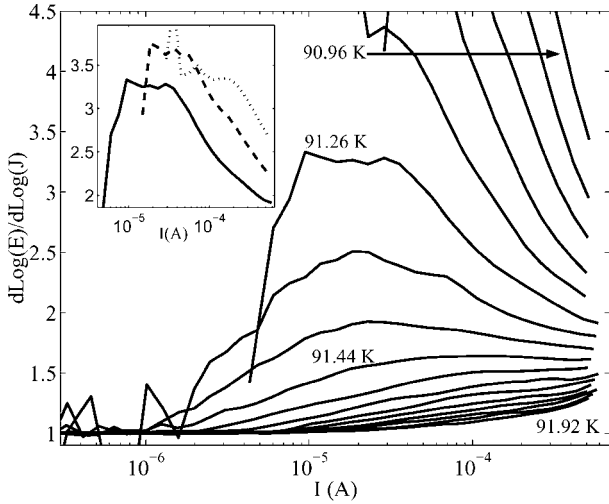


Fig. 11. $d\log(E)/d\log(J)$ vs. I for the IV curves of Fig. 10. The inset shows the 91.26 K isotherm for three-bridges widths on the same film, $20 \mu\text{m}$ (solid line), $50 \mu\text{m}$ (dashed line), and $100 \mu\text{m}$ (dotted line), which do not agree as a function of I . From Ref. 12.

[12]. Once again, the data are qualitatively consistent with a transition occurring, with ohmic low-current tails being visible for $T > 91.26$ K, and not being visible at lower temperatures.

Figure 11 is a derivative plot for the data in Fig. 10. It is qualitatively similar to Eqs. (6) and (8). In particular, if a phase transition were present, there would be one curve, at $T = T_c$, that is straight and horizontal, separating curves at higher temperature with positive derivative from those at lower temperature with negative derivative. As with the other derivative plots in this paper, this is not what is seen here: A simpler explanation of the data is that all of the underlying curves are the same, with the only differences being due to voltmeter resolution.

Earlier work had pointed out the possibility that in thin films, fluctuation dynamics can cross over from three-dimensional to two-dimensional behavior [2,25,26]. The idea is that a current density J probes fluctuations of a typical size L_J given by [2]

$$L_J = \left(\frac{ckT}{\Phi_0 J} \right)^{1/2} \quad (17)$$

where c is a constant of order the $\text{YBa}_2\text{Cu}_3\text{O}_{7-\delta}$ film anisotropy parameter, about 0.2. As long as $L_J < d$, the film thickness, the measurements will be probing three-dimensional fluctuations. Once $L_J > d$, however, the measurements will be probing two-dimensional fluctuations.

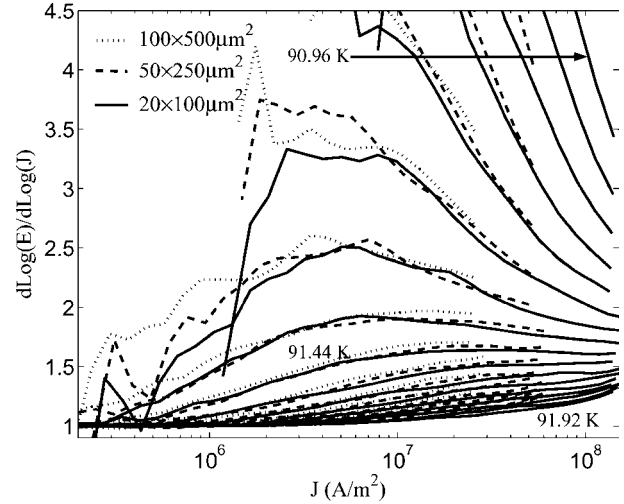


Fig. 12. $d\log(E)/d\log(J)$ vs. J for three different-width samples fabricated from the same film. The crossover from nonohmic to ohmic behavior clearly depends on J . From Ref. 12.

This crossover from three dimensions to two dimensions provides a qualitative explanation for the behavior seen in Fig. 11, and can also be checked quantitatively. The inset to Fig. 12 shows derivative plots taken on samples with three different widths made from the same film and measured at the same temperature, and it is seen that the curves do not lie on top of each other. (They would fall on top of each other if the effect depended on current instead of current density.) By contrast, Fig. 13 plots data

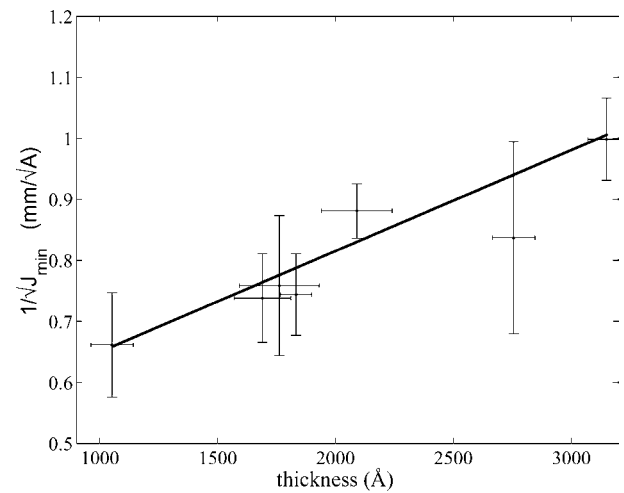


Fig. 13. $1/\sqrt{J_{\min}}$ vs. d for eight different thickness films. The straight line fit indicates quantitative agreement with Eq. (18). From Ref. 12.

from the same three samples using current density J as a variable, rather than current I . Within experimental uncertainty, all three curves at any given temperature lie on top of each other, in agreement with Eq. (17).

To further test Eq. (17), Matt Sullivan made films with thicknesses varying between 95 nm and 320 nm. Using a method described in Ref. 12, he inferred a value of the current, J_{\min} , at which deviations from three-dimensional behavior first occur. If this deviation occurs when $L_J = d$, then Eq. (17) predicts that

$$J_{\min} = \frac{ckT}{\Phi_0 d^2}. \quad (18)$$

Figure 13 shows that this is indeed the case. Quite remarkably, the IV curves are dominated by finite-thickness effects, even in quite thick films.

6. SUMMARY AND CONCLUSIONS

I have discussed a number of different systems—two-dimensional Josephson-junction arrays, two-dimensional unit-cell $\text{YBa}_2\text{Cu}_3\text{O}_{7-\delta}$ films, and three-dimensional thick (fractions of a micrometer) $\text{YBa}_2\text{Cu}_3\text{O}_{7-\delta}$ films. In two dimensions, whether or not the KT transition occurs depends on the width W of the sample relative to λ_{\perp} . In the arrays, $W < \lambda_{\perp}$, and the signature of the KT transition, a change from cubic to linear IV curves at T_{KT} , can be seen. In unit-cell $\text{YBa}_2\text{Cu}_3\text{O}_{7-\delta}$ films, $W > \lambda_{\perp}$, and the transition is not seen.

In three-dimensional samples, scaling provides a powerful tool for determining whether or not samples are truly superconducting. While a “by eye” data collapse such as those shown in Fig. 9 can lead to the mistaken conclusion that a transition has occurred, when the technique is used carefully it is very powerful. Our in-field data were not consistent with a transition to a state of zero resistance, which led us to suggest that a vortex-glass transition may not occur. Quite alarmingly, our zero-field data led us to a similar conclusion. In the latter case, however, we believe that ubiquitous finite-size effects interrupt the transition, even in our thickest films.

An important question is whether finite-thickness effects are causing the samples to not become superconducting in field, or something else is happening. This question is currently being pursued at Maryland. In addition, we are making measurements on single crystals, which are very much thicker than films. Our initial results indicate that finite size

effects are not visible in the crystals, but more work is needed. Finally, we are measuring other properties, such as microwave response and heat capacity, which are independent ways of studying whether or not samples are really superconducting.

ACKNOWLEDGMENTS

Mike Tinkham taught me a lot when I worked with him. There is no doubt in my mind that the work we did at Harvard was very good: His role in that work means that I am not being conceited by saying so. I hope that my subsequent work occasionally measures up to his high standards. I have had many other collaborators in the work described here, as well as in related work that could not be discussed due to space constraints; all of them have been a source of knowledge and inspiration. I especially acknowledge the primary authors of the work described here, David Abraham, Max Repaci, Doug Strachan, and Matt Sullivan. I had a lot of fun working with all of you.

REFERENCES

1. M. Tinkham, *Introduction to Superconductivity* (McGraw-Hill, New York, 1996).
2. D. S. Fisher, M. P. A. Fisher, and D. A. Huse, *Phys. Rev. B* **43**, 130 (1991); D. A. Huse, M. P. A. Fisher, and D. S. Fisher, *Nature* **358**, 553 (1992).
3. W. J. Skocpol and M. Tinkham, *Rep. Prog. Phys.* **38**, 1049 (1975).
4. D. W. Abraham, C. J. Lobb, M. Tinkham, and T. M. Klapwijk, *Phys. Rev. B* **26**, 5268 (1982).
5. C. J. Lobb, D. W. Abraham, and M. Tinkham, *Phys. Rev. B* **27**, 150 (1983).
6. J. M. Kosterlitz and D. J. Thouless, *J. Phys. C* **6**, 1181 (1973); J. M. Kosterlitz, *J. Phys. C* **7**, 1046 (1974).
7. M. R. Beasley, J. E. Mooij, and T. P. Orlando, *Phys. Rev. Lett.* **42**, 1165 (1979); S. Doniach and B. A. Huberman, *Phys. Rev. Lett.* **42**, 1169 (1979).
8. J. M. Repaci, C. Kwon, Q. Li, X. Jiang, T. Venkatesan, R. E. Glover, III, and C. J. Lobb, *Phys. Rev. B* **54**, R9674 (1996).
9. C. J. Lobb, *Phys. Rev. B* **36**, 3930 (1987).
10. D. R. Nelson and V. M. Vinokur, *Phys. Rev. Lett.* **68**, 2398 (1992).
11. D. R. Strachan, M. C. Sullivan, P. Fournier, S. P. Pai, T. Venkatesan, and C. J. Lobb, *Phys. Rev. Lett.* **87**, 067007 (2001).
12. M. C. Sullivan, D. R. Strachan, T. Frederiksen, R. A. Ott, M. Lilly, and C. J. Lobb, *Phys. Rev. B* **69**, 214524 (2004).
13. A. F. Hebard and A. T. Fiory, *Phys. Rev. Lett.* **50**, 1603 (1983).
14. M. Tinkham and C. J. Lobb, in *Solid State Physics Volume 42*, H. Ehrenreich and D. Turnbull, eds. (Academic Press, New York, 1989), pp. 91–134.
15. R. S. Newrock, C. J. Lobb, U. Geigenmuller, and M. Octavio, in *Solid State Physics Volume 54*, H. Ehrenreich and F. Spaepen, eds. (Academic Press, New York, 2000), pp. 266–512.

16. B. I. Halperin and D. R. Nelson, *J. Low Temp. Phys.* **36**, 599 (1979).
17. See references cited in Ref. 4.
18. J. Pearl, *Appl. Phys. Lett.* **5**, 65 (1964).
19. M. P. A. Fisher, *Phys. Rev. Lett.* **62**, 1415 (1989).
20. R. H. Koch, V. Foglietti, W. J. Gallagher, G. Koren, A. Gupta, and M. P. A. Fisher, *Phys. Rev. Lett.* **63**, 1511 (1989).
21. D. R. Strachan, M. C. Sullivan, and C. J. Lobb in *Proceedings of SPIE Vol. 4811, Superconductivity and Related Oxides: Physics and Nanoengineering V*, Ivan Bozovic and Davor Pavuna, eds. (International Society for Optical Engineering, Bellingham, Washington, DC 2002) pp. 65–77, and references cited therein.
22. J. M. Roberts, B. Brown, B. A. Hermann, and J. Tate, *Phys. Rev. B* **49**, 6890 (1994); T. Nojima, T. Ishida, and Y. Kuwasawa, *Czech. J. Phys.* **46** (Suppl. S3), 1713 (1996).
23. K. Moloni, M. Friesen, S. Li, V. Souw, P. Metcalf, L. Hou, and M. McElfresh, *Phys. Rev. Lett.* **78**, 3173 (1997).
24. N.-C. Yeh, W. Jiang, D. S. Reed, U. Kriplani, and F. Holtzberg, *Phys. Rev. B* **47**, 6146 (1992); N.-C. Yeh, D. S. Reed, W. Jiang, U. Kriplani, F. Holtzberg, A. Gupta, B. D. Hunt, R. P. Vasquez, M. C. Foote, and L. Bajuk, *Phys. Rev. B* **45**, 5654 (1992).
25. C. Dekker, R. H. Koch, B. Oh, and A. Gupta, *Physica C* **185–189**, 1799 (1991).
26. P. J. M. Wöltgens, C. Dekker, R. H. Koch, B. W. Hussey, and A. Gupta, *Phys. Rev. B* **52**, 4536 (1995).

Effect of Nuclear Field on Magnetotransport Quantum Oscillations in InSb¹

N. Gauss,^{2,3} A. G. M. Jansen,⁴ and P. Wyder²

Received August 15, 2004; accepted September 4, 2004

In combining magneto-transport investigations with NMR (nuclear magnetic resonance) we measured the effect of the nuclear hyperfine field B_{HF} on quantum oscillations in the transverse magneto-resistivity ρ_{xx} and in the Hall resistivity ρ_{xy} of metallicly doped n -InSb. Quantitative analysis of the B_{HF} -induced change in ρ_{xx} demonstrates that this experiment allows to separate spin splitting phenomena in magneto-transport from effects due to the external magnetic field B . This is used to show that an oscillatory structure in $R_{\text{H}} = \rho_{xy}/B$ is directly related to a redistribution in the occupation of the two spin states in the lowest Landau level.

KEY WORDS: magnetotransport; NMR; Shubnikov-de Haas effect; InSb.

1. INTRODUCTION

In metallicly doped n -InSb an effect of the nuclear spin on the resistivity has been measured in quantizing magnetic fields. Inversion of nuclear polarization by NMR (nuclear magnetic resonance) was shown to induce a change in the resistance of a sample [1,2]. Many years later the electron-nuclear hyperfine interaction could be measured even on a two-dimensional (2D) metallic system in performing resistively detected NMR under dynamic polarization of the nuclear spin system with ESR (electron spin resonance) [3]. At sufficiently low temperatures, this technique has been applied without the use of dynamic polarization for the study of the Quantum Hall Effect in a high mobility 2D system [4].

ESR investigations in bulk InSb show that in a magnetic field the electronic energy levels are split-

ted in spin by the electronic Zeeman effect and that the magnetic hyperfine interaction between electrons and nuclei produces a measurable effect on the energy splitting of the spin levels [5–7]. The hyperfine interaction is known to consist of three contributions: A dipolar part which reflects the potential energy of the magnetic moment of the electron in the magnetic field created by a nuclear magnetic dipole, a contact part due to the local interaction of electronic and nuclear spin moment (Fermi-contact interaction), and an orbital part given by the interaction of the nuclear magnetic moment with an electronic orbital current on an atomic scale whose origin lies in a slightly non s -wave character of electronic wavefunctions [8].

Conduction electrons are delocalized within the solid, so that for them only the ensemble average of the interaction with nuclear spins is retained [9,10]. The spatial means of a magnetic dipole field of nuclear origin is zero. There also is an orbital part of the nuclear hyperfine interaction which is due to a slight p -wave character of electrons in the conduction band [8,11]. As for InSb the ratio of the energies of the orbital hyperfine interaction to the Fermi contact interaction can be estimated to 0.4% [5,11], the dominating contribution to the hyperfine interaction is the Fermi-contact interaction.

¹In honour of Professor Michael Tinkham's 75th Birthday.

²Grenoble High Magnetic Field Laboratory, Max-Planck-Institut für Festkörperforschung and Centre National de la Recherche Scientifique, BP 166, 38042, Grenoble Cedex 9, France.

³Present address: Carl Zeiss AG, Carl-Zeiss-Strasse 22, 73447 Oberkochen, Germany.

⁴Service de Physique Statistique, Magnétisme, et Supraconductivité, Département de Recherche Fondamentale sur la Matière Condensée, CEA-Grenoble, 38054 Grenoble Cedex 9, France.

The effective spin Hamiltonian of a conduction electron in an external field applied in the z -direction is given by the static part of the averaged hyperfine interaction and reads [9]:

$$H_S = g\mu_B B S_z + \sum_i a_i A_i \langle I_z \rangle_i S_z. \quad (1)$$

$g \approx -50$ is the effective g -factor of the conduction band electrons in InSb [12], μ_B is the Bohr magneton, $\langle I_z \rangle_i$ denotes the spin polarization of different nuclear isotopes of abundance a_i with the hyperfine coupling constant

$$A_i = \frac{8\pi}{3} \frac{\mu_0}{4\pi} g_0 \mu_B \hbar \gamma_i |\Psi_i(0)|^2, \quad (2)$$

where $g_0 = 2.002310$ denotes the g -factor of the free electron, γ_i the gyromagnetic ratio and $|\Psi_i(0)|^2$ the probability density of the conduction electron at the site of a nucleus of species i . Introducing a nuclear hyperfine field B_{HF} , Eq. (1) can be formally rewritten in terms of an effective Zeeman interaction

$$H_S = g\mu_B (B + B_{\text{HF}}) S_z. \quad (3)$$

B_{HF} is expected to have no effect on the degeneracy of Landau levels and represents only an additional term in the electronic Zeeman spin splitting.

At low temperatures, the transverse magnetoresistivity ρ_{xx} in pure crystalline 3D metallic systems as e.g. InSb is characterized by magnetoquantum oscillations due to Landau quantization of the electron system (Shubnikov–de Haas effect). This is understood by that the resistivity ρ_{xx} is determined by the magnetic field-dependent electronic density of states at the Fermi level $D_B(E_F)$ via its influence on the electronic scattering, while the Hall resistivity ρ_{xy} is given by its classical value $\rho_{xy}^{\text{cl}} = B/ne$ and is independent of scattering [13,14]. Although excellent agreement between theory based on a lowest order scattering approach and experimental data of ρ_{xx} is found for n -InSb and n -InAs [15], magnetoquantum oscillations are also observed in ρ_{xy} in these metallicly doped semiconductors in the extreme quantum limit where only the lowest spin-split Landau levels are occupied [16–22]. These oscillations have been ascribed to higher-order scattering [17]. More recently they are related to the presence of disorder-induced localized electronic states in the tails of the lowest spin-split Landau levels (0^- and 0^+) [23].

Assuming that electronic Zeeman spin splitting is at the origin of a decoupling of the 0^+ - and 0^- -levels such that the transport in these states is independent from each other, localized 0^- - and extended

(free) 0^+ -states can coexist in the same energy range. In a first approximation this explains magnetoquantum oscillations in the Hall resistivity ρ_{xy} by a dominating mechanism of disorder-induced localization of charge carriers with minority spin. This mechanism leads to a reduced density of free carriers with the corresponding variation in the Hall resistivity at magnetic fields where localized minority spin states and extended majority spin states coexist. Experimental investigations of magnetoquantum oscillations in ρ_{xy} on InSb and InAs point to the presence of localized states in the lower energy tail of a broadened spin split Landau level [22,24].

For metallic InSb, we have measured and analysed the NMR induced change in both ρ_{xx} and ρ_{xy} in the extreme quantum limit where only the lowest spin splitted Landau levels 0^+ and 0^- are occupied [25]. Quantitative analysis of the change in ρ_{xx} shows that in this way the role of electronic spin splitting in transport can be studied while keeping the external magnetic field B fixed. This is of interest for investigating the magnetoquantum oscillations in the Hall resistivity ρ_{xy} at the extreme quantum limit, because different from the external field B , the nuclear hyperfine field B_{HF} is expected to play no role in the localization mechanism for charge carriers.

2. EXPERIMENT

Our InSb samples (MCP wafer technology, U.K.) were spark cut from Te-doped single crystal wafers into the standard Hall-bar geometry with four lateral contact legs and a size of about $9.0 \times 1.5 \times 1.0 \text{ mm}^3$. For electrical contact fine gold wires were attached with molten indium after surface etching in a bromo-methanol solution. For three samples with different metallic doping concentrations the transverse magneto-transport data were measured at liquid helium temperatures down to 1.2 K in superconducting solenoids or Bitter magnets up to 20 T. Transverse magnetoresistivity ρ_{xx} and Hall resistivity ρ_{xy} were derived from the corresponding resistances R_{xx} and R_{xy} in the classical way. Dingle temperature T_D and carrier concentration n determined from low-field magneto-transport data are presented in Table I. According to the Mott-criterion $na_B^3 \geq 0.027$ as a measure for a metallic system with sufficient overlap of the donor wavefunctions [26,27], where $a_B = 64 \text{ nm}$ is the electronic Bohr radius in InSb, all samples are found to be well in the metallic regime. In Fig. 1, we show the low-temperature

Table I. Parameters of the Measured Samples: n was Derived from the Low-Field Slope in ρ_{xy} . T_D was Determined from Shubnikov-de Haas Oscillations in ρ_{xx} at Fields Far Below the Extreme Quantum Limit in the Classical Way. B_{MI} , the Field of a B -Induced Metal-Insulator Transition, was Estimated from the Magnetic Field Dependent Mott Criterion. In the Bottom Row the Magnetic Field Dependent Mott Criterion has been Applied on the Population n^{0-} of the 0^- Landau Level (see Text for Explanation)

	Sample 1	Sample 2	Sample 3
n (cm $^{-3}$)	1.54×10^{15}	1.50×10^{16}	1.97×10^{16}
na_B^3	0.39	3.93	5.24
T_D ($^{\circ}$ K)	3.0	4.7	5.4
B_{MI} (T)	3.30	17.24	21.19
$(n_{loc}^{0-} a_{\parallel}^2 a_{\perp}^2)^{\frac{1}{3}}$	0.29	0.26	0.27

magneto-transport characteristics of sample 1. All the samples show well-resolved spin-splitting of the lower Landau levels in ρ_{xx} (see Landau level quantum numbers indicated in Fig. 1) while ρ_{xy} is characterized by a pronounced cusp in this field region. The latter is clearly separated from a steep nonlinear rise of ρ_{xy} at higher fields which sets in for sample 1 at $B \approx 2.9$ T and which may be ascribed to the onset of a magnetic-field induced MI-transition [28].

To study the NMR-induced change in magneto-transport ρ_{xx} and ρ_{xy} were measured in an rf coil at 1.95 ± 0.02 K with a resistance bridge providing up to $1 : 10^6$ resolution. By leaving the samples in a strong magnetic field ($B = 8.64$ T) for a long time (up to 20 h) at low temperature ($T = 1.95$ K) a nuclear polarization was generated. Since the nuclear spin-lattice relaxation time T_1 in InSb is known to be in

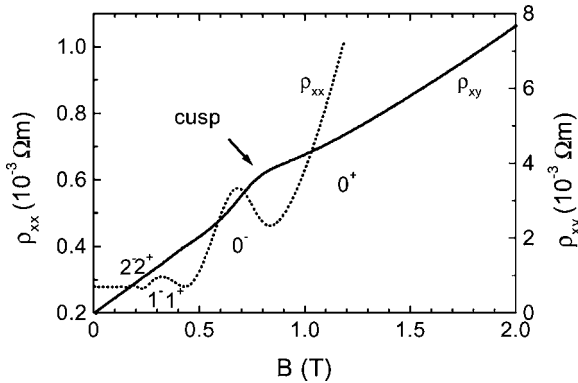


Fig. 1. Transverse magnetoresistivity ρ_{xx} and Hall resistivity ρ_{xy} at $T = 1.95$ K of sample 1 showing magnetoquantum oscillations with Zeeman spin splitted structure. The quantum numbers of the Landau levels which correspond to the local maxima of ρ_{xx} are indicated in the figure.

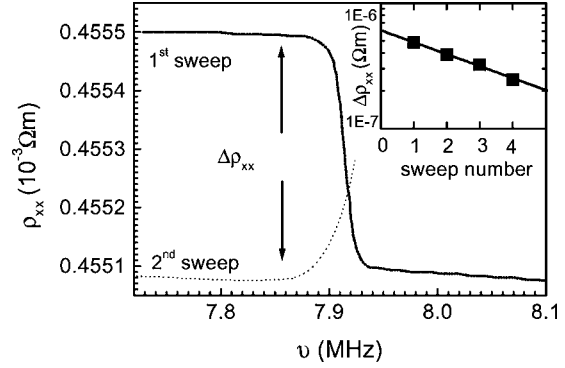


Fig. 2. B_{HF} -induced change in ρ_{xx} at $T = 1.95$ K measured in an adiabatic rf-signal passage over the resonance frequency of ^{115}In isotopes at $B = 0.85$ T with rf-field $B_1 \approx 1$ G and $\frac{d}{dt}v_{rf} \approx 6.7$ kHz/s. The inset shows the amplitudes for successive resonance passages causing a signal change of alternating sign.

the range of several hours for the investigated doping concentration [29], nuclear magnetization is expected to be conserved on the timescale of several minutes while B is cycled to a value where transport is measured. The sample was exposed to a rf-field B_1 ($B_1 \sim 1$ G), which could be estimated with a pick-up mechanism. In sweeping the radio frequency fast over the nuclear resonance (adiabatic rf-signal passage) the collective magnetization of the nuclei can be inverted [30,31]. This procedure changes the sign of B_{HF} at the nuclear resonance frequency. As shown in Fig. 2 this triggers a change in resistivity [1]. Although passing the rf-signal several times over the resonance line, the signal amplitude decayed exponentially with the number of frequency-sweeps carried out. This may be due to nuclear spin-spin interaction. We account for this effect by extrapolating our measured data to the “zero sweep” value in a logarithmic plot as shown in the inset of Fig. 2.

3. NMR-INDUCED CHANGE IN ρ_{xx}

In Fig. 3a, we show $\Delta\rho_{xx}$, i.e. the B_{HF} -induced change in ρ_{xx} measured on sample 1 in an adiabatic rf-signal passage over the resonance frequency of the ^{115}In , ^{121}Sb , and ^{123}Sb isotopes at different magnetic fields. Nuclear polarization was generated by leaving the sample for 2.5 h in $B_{pol} = 8.64$ T at $T = 1.95$ K. Then B was cycled to a value of interest at which first four frequency sweeps over the resonance of the ^{115}In -, then of the ^{121}Sb -, and at last of the ^{123}Sb nuclei were carried out. By linear

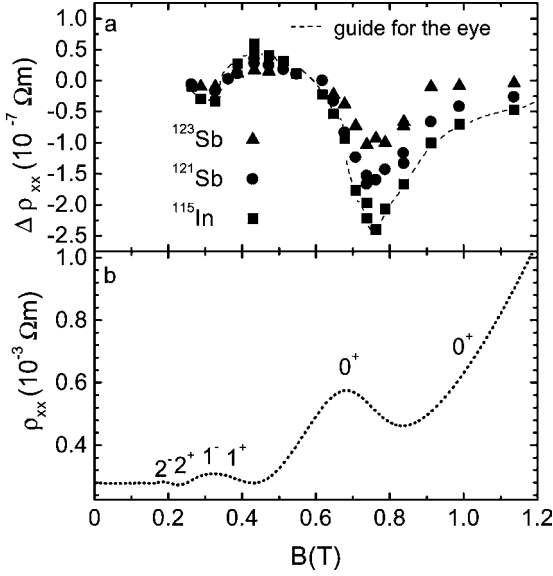


Fig. 3. Graph a: Data points for the B_{HF} -induced change in transverse magnetoresistivity $\Delta\rho_{xx}$ after 2.5 h of thermal polarization in $B_{\text{pol}} = 8.65$ T at $T = 1.95$ K for three different nuclear subsystems. Graph b: The transverse magnetoresistivity ρ_{xx} with the Landau levels indicated for comparison.

extrapolation in a logarithmic representation of the data, $\Delta\rho_{xx}$ was determined out of this series of four adiabatic resonance frequency sweeps. Before cycling B back to 8.64 T for thermal polarization, the remaining nuclear magnetization was destroyed in exposing each nuclear isotope to resonant rf-radiation. The NMR-induced change $\Delta\rho_{xx}$ is also characterized by magnetoquantum oscillations. However the oscillations are shifted in phase with respect to the oscillations in the transverse magnetoresistivity ρ_{xx} shown in Fig. 3b and $\Delta\rho_{xx}$ is about four orders of magnitude smaller than ρ_{xx} . $\Delta\rho_{xx}$ for the ^{121}Sb and ^{123}Sb nuclei was more difficult to measure than for the ^{115}In nuclei because of a higher signal loss with each rf-signal passage.

The nuclear hyperfine field related to electron nuclear hyperfine interaction acts only on the spin of the electrons [9] and can be deduced from known parameters of the InSb-sample:

$$B_{\text{HF}} = \frac{2}{3}\mu_0 \frac{g_0}{g} \hbar \sum_i a_i \gamma_i \hbar \langle I_z \rangle_i |\Psi_i(0)|^2, \quad (4)$$

with $g_0 = 2.002310$ being the g -factor of the free electron, $g = -50$ the effective g -factor in InSb [12], γ_i the gyromagnetic ratio, and $|\Psi_i(0)|^2$ the probability density of the conduction electron at the site of a nucleus of species i , a_i their relative abundance within

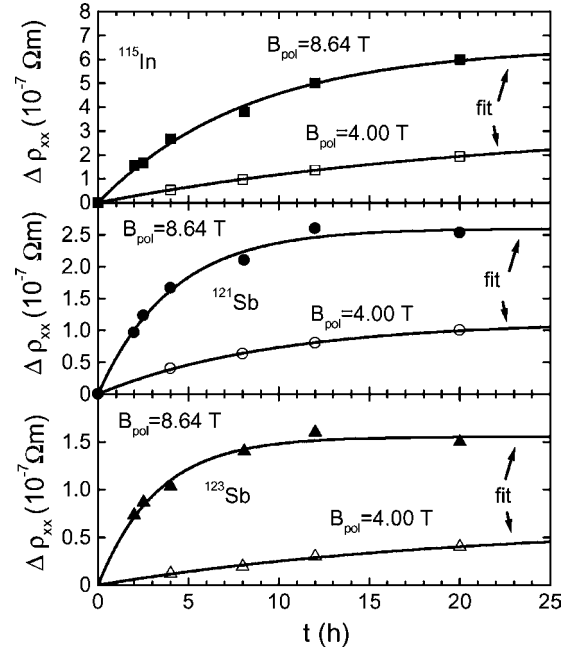


Fig. 4. Saturation behavior of the B_{HF} -induced change in ρ_{xx} as a function of thermal polarisation of nuclei at $T = 1.95$ K in $B_{\text{pol}} = 8.64$ T and $B_{\text{pol}} = 4$ T. A fit of the data points allows to estimate $\rho_{xx}(\infty)$ using Eq. (5).

the solid, and $\langle I_z \rangle_i$ the expectation value of their angular momentum in z -direction.

B_{HF} of different nuclear isotopes for our experimental conditions can be estimated based on Eq. (4), as $|\psi(0)|_{\text{In}}^2$ and $|\psi(0)|_{\text{Sb}}^2$ are known from the measurement of the Overhauser-shift in ESR-experiments [5–7]. The equilibrium nuclear spin polarization $\langle I_z \rangle_i$ at $B = 8.64$ T and $T = 1.95$ K has to be determined from the situation of thermal polarization of nuclei during only 2.5 h. We, therefore, measured $\Delta\rho_{xx}$ in the extreme quantum limit at $B_{\text{meas}} = 0.85$ T for polarization times t_{pol} varying from 1 to 20 h at $B_{\text{pol}} = 8.64$ and $B_{\text{pol}} = 4$ T. As shown in Fig. 4, $\Delta\rho_{xx}$ is characterized by an exponential saturation behavior for all nuclear subsystems which is more pronounced for the ^{121}Sb and ^{123}Sb isotopes than for the ^{115}In nuclei. $\Delta\rho_{xx}(\infty)$, i.e. the NMR-induced change in ρ_{xx} caused by inversion of a completely thermalized nuclear subsystem and the nuclear spin-lattice relaxation rate T_1 can be estimated in a two-parameter fit of the data to the following equation:

$$\Delta\rho_{xx}(t_{\text{pol}}) = \Delta\rho_{xx}(\infty)(1 - e^{-t_{\text{pol}}/T_1}). \quad (5)$$

T_1 was found to be of the order of 5 to 20 h depending on the nuclear isotope. It varied significantly

with the magnitude of the polarizing magnetic field B_{pol} . Thermal polarization of nuclei at $B = 4$ T leads to a reduction in $\rho_{xx}(\infty)$ as compared to polarization at $B_{\text{pol}} = 8.64$ T by a factor which coincides with the ratio of 8.64 to 4 T for the ^{121}Sb - and which is close to it for the ^{115}In - and ^{123}Sb nuclei. From this measurement we deduce that the degree of polarization of the ^{121}Sb (^{115}In , ^{123}Sb) subsystem after 2.5 h of thermal polarization at $B = 8.64$ T corresponds to 47% (25.5%, 53%) of the equilibrium value.

The nuclear-spin polarization in thermal equilibrium is determined by the Boltzmann distribution of magnetic energy levels and in our temperature regime given by the Curie law:

$$\langle I_z \rangle_i = \frac{\hbar \gamma_i B I_i (I_i + 1)}{3kT}. \quad (6)$$

For the ^{121}Sb (^{115}In , ^{123}Sb) nucleus with $I_{121\text{Sb}} = \frac{5}{2}$ ($I_{115\text{In}} = \frac{9}{2}$, $I_{123\text{Sb}} = \frac{7}{2}$) in $B = 8.64$ T at $T = 1.95$ K, one finds for the expectation value of the z-component of angular momentum $\langle I_z \rangle_{121\text{Sb}} = 6.25 \cdot 10^{-3}$ ($\langle I_z \rangle_{115\text{In}} = 1.53 \cdot 10^{-2}$, $\langle I_z \rangle_{123\text{Sb}} = 6.67 \cdot 10^{-3}$). With the natural abundance $a_{121\text{Sb}} = 57.25\%$ ($a_{115\text{In}} = 95.72\%$, $a_{123\text{Sb}} = 47.75\%$) and $\gamma_{115\text{In}}/2\pi = 0.93285$ KHz/G ($\gamma_{121\text{Sb}}/2\pi = 1.0189$ KHz/G, $\gamma_{123\text{Sb}}/2\pi = 0.55175$ KHz/G) from [32], taking the value of $|\Psi(0)|_{121\text{Sb}}^2 = 1.1 \pm 0.1 \times 10^{32} \text{m}^{-3}$ ($|\Psi(0)|_{115\text{In}}^2 = 6.8 \pm 0.7 \times 10^{31} \text{m}^{-3}$, $|\Psi(0)|_{123\text{Sb}}^2 = |\Psi(0)|_{121\text{Sb}}^2$) as determined in an Overhauser shift experiment in [7], we calculate the nuclear hyperfine field of the ^{121}Sb (^{115}In , ^{123}Sb) subsystem generated by thermal polarization of nuclei at $B_{\text{pol}} = 8.64$ T in $T = 1.95$ K for 2.5 h to $B_{\text{HF}}^{121\text{Sb}} = -0.42$ G ($B_{\text{HF}}^{115\text{In}} = -0.55$ G, $B_{\text{HF}}^{123\text{Sb}} = -0.23$ G). Due to its smallness in amplitude and a bigger signal loss with every adiabatic resonance passage compared to the other isotopes, ρ_{xx} of the ^{121}Sb -nuclei was most difficult to measure. The consistency of the fit according to Eq. (5) is best for the ^{121}Sb -isotopes where one reaches saturation for both polarizing magnetic fields.

We, therefore, estimate $B_{\text{HF}}^{115\text{In}}$ and $B_{\text{HF}}^{123\text{Sb}}$ generated by thermal polarization of nuclei at $B_{\text{pol}} = 8.64$ T in $T = 1.95$ K for 2.5 h from the corresponding resistivity ratios assuming $\Delta\rho_{xx}^{115\text{In}}/\Delta\rho_{xx}^{121\text{Sb}} = B_{\text{HF}}^{115\text{In}}/B_{\text{HF}}^{121\text{Sb}}$ and $\Delta\rho_{xx}^{123\text{Sb}}/\Delta\rho_{xx}^{121\text{Sb}} = B_{\text{HF}}^{123\text{Sb}}/B_{\text{HF}}^{121\text{Sb}}$, i.e. $B_{\text{HF}}^{115\text{In}} = -0.58$ G and $B_{\text{HF}}^{123\text{Sb}} = -0.28$ G. Within our experimental error both ways of estimating B_{HF} give the same results.

4. NMR-INDUCED CHANGE IN ρ_{xy}

$\Delta\rho_{xy}$, i.e. the NMR-induced change in ρ_{xy} after polarizing nuclei at $B_{\text{pol}} = 8.64$ T for 2.5 h at $T = 1.95$ K could be measured in the same way as for ρ_{xx} although the signal was by a factor of 2 to 5 smaller in absolute voltage drop. Due to its smallness in absolute voltage drop, quantitative evaluation of the B -independence of $\Delta\rho_{xy}$ was only possible for adiabatic resonance passages over the resonance frequencies of ^{115}In and ^{121}Sb nuclei. $\Delta\rho_{xy}$ shows a pronounced quantum oscillation in the magnetic field region of the extreme quantum limit where ρ_{xy} is characterized by a cusp. The sign of $\Delta\rho_{xy}$ depends on the direction of B in the same way as ρ_{xy} , i.e. the observed signal is odd in magnetic field. The amplitude of the quantum oscillation in $\Delta\rho_{xy}$ is about the same as for $\Delta\rho_{xx}$, however $\Delta\rho_{xy}$ is shifted in phase with respect to $\Delta\rho_{xx}$.

As shown in Fig. 5 we observe on sample 1 that the change of the Hall constant $R_{\text{H}} = \rho_{xy}/B$ with an increment in the external field of $\Delta B = 1$ G is about proportional to the B_{HF} -induced change $\Delta R_{\text{H}}|_{\Delta B_{\text{HF}}} = \Delta\rho_{xy}/B$, i.e. the following relation holds:

$$\Delta R_{\text{H}}|_{\Delta B} \propto \Delta R_{\text{H}}|_{\Delta B_{\text{HF}}}. \quad (7)$$

5. DISCUSSION OF NMR-INDUCED CHANGE IN ρ_{xx}

We discuss the effect of nuclear field on ρ_{xx} by a theoretical calculation of the NMR-induced change $\Delta\rho_{xx}$. In the case of a white noise scattering

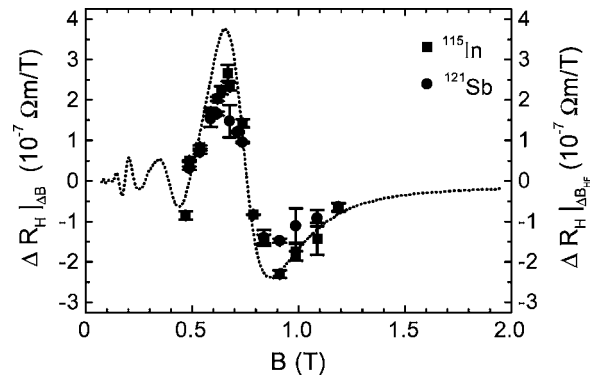


Fig. 5. The data points of the B_{HF} -induced change $\Delta R_{\text{H}} = \Delta\rho_{xy}/B$ in the Hall constant both for the ^{115}In - and ^{121}Sb isotopes after thermal polarisation for 2.5 h at $B_{\text{pol}} = 8.64$ T and at 1.95 K. For comparison the dotted line represents the change in the Hall constant R_{H} with an external field increment of $\Delta B = 1$ G.

potential without taking into account electronic spin Adams and Holstein obtain an exact expression for the relative change in the transverse magnetoresistivity ρ_{xx} [13]. Assuming independence between $+/-$ spin states this expression can be easily generalized to the case of finite electronic Zeeman spin splitting as follows:

$$\begin{aligned} \rho_{xx}(B)/\rho_0 &= \sum_{\pm} \frac{D_B^{\pm}(E_F) \left[(E_F \mp \frac{1}{2}g\mu_B B) D_B^{\pm}(E_F) - \frac{1}{2}n^{\pm} \right]}{n \frac{1}{2}D_0(E_F)}. \end{aligned} \quad (8)$$

The sum is taken over the two electronic spin-up (+) and spin down (-) subsystems. $D_B^{\pm}(E)$ denotes the density of states and n^{\pm} the concentration of carriers in the + (-) spin-state. g is the effective electronic g -factor, μ_B the Bohr magneton, $D_0(E_F)$ the zero-field density of states at the Fermi level, ρ_0 the resistivity at zero field, and $n = n^+ + n^-$ the total concentration of free charge carriers.

Calculation of transverse magnetoresistivity according to Eq. (8) requires the knowledge of the zero field density of states $D_0(E_F)$ and the magnetic field-dependent electronic density of states $D_B(E_F)$ at the Fermi energy E_F . Since, according to Table I, the experiments were carried out below the Dingle Temperature T_D , we neglect the effect of finite temperature in the following.

At $B = 0$ the density of states of a 3D free electron gas reads:

$$D_0(E) = \frac{1}{2\pi^2} \left\{ \frac{2m}{\hbar^2} \right\}^{\frac{3}{2}} \sqrt{E}. \quad (9)$$

Application of a finite magnetic field leads to Landau quantization combined with electronic Zeeman spin splitting so that the electronic density of states is:

$$\begin{aligned} D_B(E) &= D_B^+(E) + D_B^-(E) \\ &= \sum_{\pm} \frac{1}{2\sqrt{2}} \frac{1}{\pi^2} \left\{ \frac{m}{\hbar^2} \right\}^{\frac{3}{2}} \hbar\omega_c \sum_n \frac{1}{\sqrt{E - (n + \frac{1}{2})\hbar\omega_c \pm g\mu_B(B + B_{\text{HF}})}}. \end{aligned} \quad (10)$$

The hyperfine coupling is included as the B_{HF} -term in the electronic Zeeman spin splitting and has no effect on the degeneracy of Landau levels.

Unfortunately standard oscillatory formula derived from Eq. (8) in the limit of large Landau level

quantum numbers ($n \geq 2$) as given e.g. in [15] are no longer valid in the field region of the extreme quantum limit. Therefore, to calculate transport by means of Eq. (8) a broadening mechanism has to be assumed, because $D_B(E)$ in Eq. (10) is singular at the bottom of each Landau level.

In doped semiconductors the donor ions are statistically spread all over the solid. This causes spatial fluctuations in the mean energy of conduction band electrons. In the case of heavy doping this leads to a broadening of energy levels which may be shown to be Gaussian [33], so that the effective density of states D_0^{Γ} is found to be the convolution of the density of states of the free electron gas $D_0(E)$ given by Eq. (9) with a Gaussian distribution function of broadening parameter Γ :

$$D_0^{\Gamma}(E) = \int_0^{\infty} dE_0 D_0(E_0) \frac{e^{-\frac{(E-E_0)^2}{\Gamma^2}}}{\Gamma\sqrt{\pi}}. \quad (11)$$

Similarly, in a magnetic field the density of states $D_B(E)$ in Eq. (10) has to be convoluted with a Gaussian.

For given Γ both at $B = 0$ and at finite B the magnetic field-dependent Fermi energy E_F is determined by the integral equation

$$\int_{-\infty}^{E_F} dE D_B^{\Gamma}(E) = n, \quad (12)$$

for a fixed concentration n of charge carriers. Using a numerical procedure (for details see [37]) for the solution of this integral equation gives us the Fermi energy for arbitrary B in the expression for the density of states. From the density of states the transverse magnetoresistivity can be calculated using Eq. (8). To see the influence of the hyperfine field, these calculations were performed both for positive and negative B_{HF} .

For the parameters of sample 1, i.e. $n = 1.54 \times 10^{21} \text{ m}^{-3}$, $g = -50$ [12], $m_{\text{eff}}^{\text{InSb}} = 0.0145$ [34], $\epsilon_r^{\text{InSb}} = 17.7$ [34] and $\Gamma = k_B T_D$ with $T_D = 3.0 \text{ K}$, the thick lines in Fig. 6a show the calculated B -dependent relative change in the transverse magnetoresistivity due to inversion of the polarisation of different nuclear subsystems according to the equation:

$$\frac{\Delta\rho_{xx}(B)}{\rho_0} = \frac{\rho_{xx}^{B_{\text{HF}}}(B) - \rho_{xx}^{-B_{\text{HF}}}(B)}{\rho_0}, \quad (13)$$

while using the estimated B_{HF} -values given in Section 3. Both relative position and order of magnitude of the calculated $\Delta\rho_{xx}(B)/\rho_0$ with respect to the oscillatory field dependence of the calculated

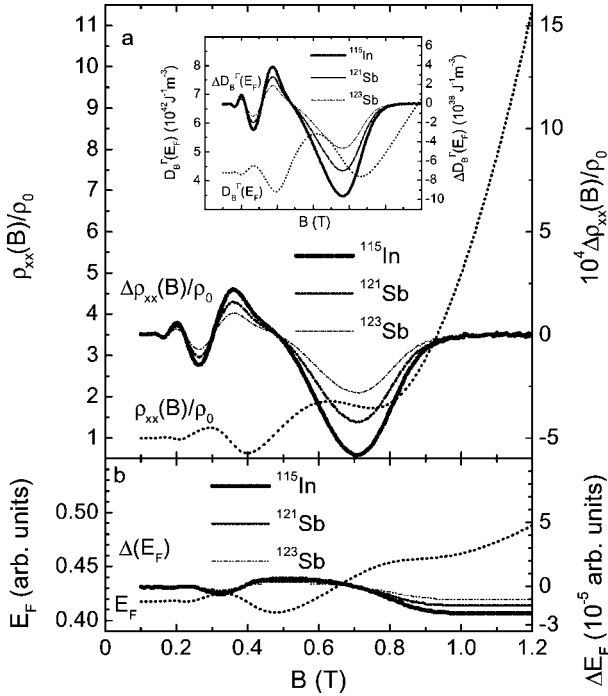


Fig. 6. Graph a: ρ_{xx}/ρ_0 as function of B for a free electron gas with the material parameters of InSb-sample 1 and Gaussian Landau level broadening calculated according to Eq. (8). The solid lines correspond to the difference ρ_{xx}/ρ_0 in the transverse magnetoresistivity due to an inversion of B_{HF} with the B_{HF} -values taken from section 3. Inset: Dotted curve: $D_B^r(E_F)$ as function of B . The solid lines show the corresponding B_{HF} -induced change in the density of states at the Fermi level $\Delta D_B^r(E_F)$ due to an inversion of B_{HF} . Graph b: Dotted curve: Fermi energy E_F as function of B . The solid lines present the B_{HF} -induced change in the Fermi energy ΔE_F .

$\rho_{xx}(B)/\rho_0$ may be well compared with the corresponding measured data shown in Fig. 3.

The oscillatory magnetic-field dependence of the density of states calculated is shown in the inset of Fig. 6a. The magnetoquantum oscillations in $D_B(E_F)$ and in $\Delta\rho_{xx}(B)/\rho_0$ coincide but slightly differ in shape. Comparing the B_{HF} -induced change in $D_B(E_F)$ with the B_{HF} -induced change in the magnetoresistivity, it can be seen that $\Delta\rho_{xx}(B)/\rho_0$ reflects the B_{HF} -induced change in the density of free charge carriers at the Fermi level.

The magnetic field dependence of the Fermi energy E_F and its change due to inversion of B_{HF} is presented in Fig. 6b. In the extreme quantum limit, E_F shows a pronounced magnetic field dependence which has been taken into account in our calculation of magneto-transport and cannot be neglected. However, the B_{HF} -induced change in E_F does play no role for the B_{HF} -induced change in ρ_{xx} .

The inversion of B_{HF} in InSb changes the electronic Zeeman spin splitting leading to a B_{HF} -induced rearrangement of the population of Landau levels. Our simulation of the transverse resistivity shows that the NMR-induced change of ρ_{xx} can be described satisfactorily by only including B_{HF} in the Zeeman term of the Hamiltonian.

6. DISCUSSION OF NMR-INDUCED CHANGE IN ρ_{xy}

In Fig. 7 we plot the normalized Hall-constant $R_H^N(B) = R_H(B)/R_H(0)$ of sample 1 over a wide range in B : R_H^N is constant at low-magnetic fields, it shows magnetoquantum oscillations at moderate fields for $B \geq 0.3$ T, and it has a pronounced cusp in the extreme quantum limit which peaks at $B_{cusp} = 0.75$ T as indicated by arrow 2 in Fig. 7. Before this cusp R_H^N is having a local minimum marked by arrow 3 in Fig. 1 where it is slightly smaller than its classical low magnetic field value. At higher fields R_H^N is characterized by a wide dip as indicated by arrow 1 in Fig. 7 and a sharp rise of R_H^N beyond $B = 2.5$ T. All these structures were observed on sample 2 and 3 as well and are reported elsewhere [17,19,20,22,35]. In the following we will concentrate on the cusp-like structure which for an increasing Hall constant would correspond to a decrease in the density of free charge carriers.

Interestingly the structures in the field-dependent Hall constant go hand in hand with critical

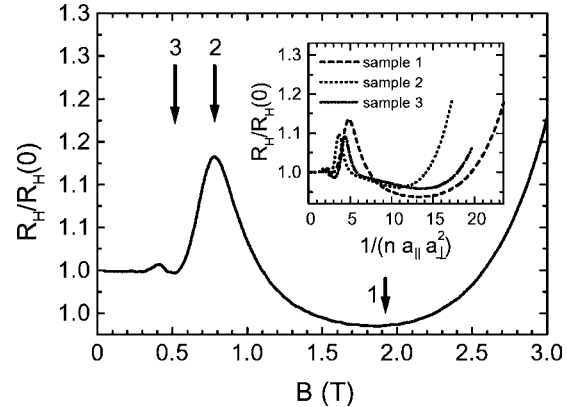


Fig. 7. Normalized Hall constant $R_H^N(B) = R_H(B)/R_H(0)$ of the metallic InSb-sample 1 as a function of the magnetic field. The arrows 1, 2 and 3 serve as a reference for features discussed in the text. In the inset $R_H^N(B)$ of sample 1, 2 and 3 is shown as a function of $(na_{||}a_{\perp}^2)^{-1}$ which is inversely proportional to the magnetic field-dependent volume of the rotationally symmetric ellipsoidal donor-wavefunction.

relations between the donor-wavefunction overlap and the doping concentration of the material. In a magnetic field the spatial extension of the donor ground-state wavefunction is given by the shape of a rotationally symmetric ellipsoid of half-axes a_{\parallel} and a_{\perp} with [36]:

$$a_{\parallel} = a_B \sqrt{\frac{E_B}{E_0}} \quad \text{for } l_B \ll a_B \quad \frac{a_B}{\ln[(a_B/l_B)^2]}, \quad (14)$$

$$a_{\perp} = 2l_B, \quad (15)$$

where E_B is the magnetic-field dependent binding energy of the s-like groundstate found by a direct variational calculation with an ellipsoidal trial wavefunction [36] and $l_B = \sqrt{\hbar/eB}$ is the magnetic length. Extending the Mott-criterium for the critical relation for metallic transport between the donor concentration n_c and the Bohr-radius a_B of donor-wavefunctions [26,27,38,39] on finite magnetic fields yields [28]:

$$na_{\parallel}a_{\perp}^2 = \delta^3. \quad (16)$$

Experimental findings of $\delta = 0.26$ [28] and $\delta = 0.34$ [35] in InSb are in reasonable agreement with the prediction of Mott [38] that a MI-transition will occur at a critical concentration of donor centers given by Eq. (16) while n is determined from the zero-field value of the Hall-constant R_H . In the inset of Fig. 7 we plot R_H^N of all three samples as a function of $(na_{\parallel}a_{\perp}^2)^{-1}$. For sample 1 the low-field approximation of a_{\parallel} according to Eq. (14) is used. a_{\parallel} for samples 2 and 3 was calculated taking the high-field expression of Eq. (14) while correcting the effective Bohr-radius a_B for a B -independent effective mass according to a two-band model [41]:

$$m(B) = m_0^{\text{InSb}} \sqrt{1 + \frac{4E_F(B)}{E_{\text{gap}}}}, \quad (17)$$

with $E_{\text{gap}} = 230$ meV and $m_0^{\text{InSb}} = 0.0145$ [34]. The magnetic field dependent Fermi energy $E_F(B)$ while neglecting energy level broadening for the magnetic field regime where only the lowest 0^+ Landau level is occupied is estimated by [40]:

$$E_F(B) = \frac{16}{9} \frac{E_{F_0}^3}{(\hbar\omega_c)^2} + \frac{\hbar\omega_c}{2}(1 - \nu), \quad (18)$$

where

$$\nu = \frac{2g\mu_B m}{\hbar e} \quad (19)$$

denotes the electronic spin splitting and

$$E_{F_0} = \frac{\hbar^2}{2m}(3\pi^2 n)^{\frac{2}{3}} \quad (20)$$

is the zero-field Fermi energy E_{F_0} . From the inset of Fig. 7 it is readily seen that R_H^N in all samples rises abruptly for $(na_{\parallel}a_{\perp}^2)^{-1} > 25$ as the field B_{MI} of a B -induced MI-transition is approached. B_{MI} in sample 1 according to Eq. (16) taking $\delta = 0.3$ is estimated to $B_{\text{MI}} = 3.30$ T. B_{MI} for samples 2 and 3 is much higher as their carrier concentration n , given in Table I, is by one order of magnitude bigger than compared to n of sample 1. A self-consistent estimation with $\delta = 0.3$ based on the high-field expression of Eq. (14) and Eqs. (15)–(20) taking into account the magnetic field dependence of the effective mass implies $B_{\text{MI}} = 17$ T (21 T) for sample 2 (sample 3).

The inset of Fig. 7 shows that the normalized Hall constant R_H^N of all three samples is characterized by a pronounced cusp at B_{cusp} between $4 < (na_{\parallel}a_{\perp}^2)^{-1} < 5$. On all samples this corresponds to the magnetic field regime of the extreme quantum limit where only the 0^- and 0^+ Landau levels are occupied. The variation of R_H which would be constant equal to $1/ne$ in the high-field limit has been explained in terms of localization effects in the tail of the 0^- Landau level of the carriers with minority spin [23], since the Mott criterium also holds for the concentration $n_{\text{loc}}^{0^-}$ of localized states in the 0^- Landau level derived on the basis of Eq. (16) [22]. Estimating the concentration $n_{\text{loc}}^{0^-}$ of localized carriers in the 0^- Landau level from the Hall-constant by:

$$\frac{n_{\text{loc}}^{0^-}}{n} = \frac{n - n_{\text{free}}^{0^+}}{n} = 1 - \frac{R_H(0)}{R_H(B_{\text{cusp}})}, \quad (21)$$

one finds that the value of $(n_{\text{loc}}^{0^-} a_{\parallel} a_{\perp}^2)^{\frac{1}{3}}$ for all three samples at the magnetic field where the cusp of R_H is peaked, as given in Table I, is close to 0.3. Thus, with reference to Fig. 7, the cusplike structure in R_H around $B = 0.75$ T may be explained by the localization of the 0^- -states while the 0^+ -levels are still extended [23,42].

In a picture of independent transport in spin-sublevels an inversion of the two-band model conductivity tensor for the 0^+ and 0^- levels around $B = 0.75$ T gives, neglecting terms of order of at most $(\rho_{xx}/\rho_{xy})^2$ (in our case smaller than 2 to 4%),

$$\rho_{xy} = (\sigma_{xy}^{0^+} + \sigma_{xy}^{0^-})^{-1}. \quad (22)$$

In this approximation, with $\sigma_{xy}^{0^+}$ given by its classical high field limit $n^{0^+} e/B$, the deviation of ρ_{xy} from ρ_{xy}^{cl}

is determined by the deviation of σ_{xy}^{0-} from $n^{0-}e/B$, where n^{0-} denotes the 0^- -population [23].

To explain the observed relation between the change of the Hall-constant $R_H = \rho_{xy}/B$ with an increment in the external field of $\Delta B = 1$ G and the B_{HF} -induced change $\Delta R_H|_{\Delta B_{\text{HF}}} = \Delta\rho_{xy}/B$ we define the quantity $\Delta_n^{0-}(n^{0-}, B)$ as a measure of the deviation of σ_{xy}^{0-} from its first order perturbation theory value $n^{0-}e/B$ for the minority-spin band 0^- by

$$\frac{e}{B}\{n^{0-} + \Delta_n^{0-}(n^{0-}, B)\} = \sigma_{xy}^{0-}(n^{0-}, B). \quad (23)$$

Eqs. (22) and (23) imply $R_H = 1/e(n + \Delta_n^{0-})$, while using that the total population of the respective spin states $n^{0+} + n^{0-} = n$ is a constant. Writing

$$\begin{aligned} \frac{d}{dB}\Delta_n^{0-}(n^{0-}, B) &= \left(\frac{\partial}{\partial n^{0-}}\Delta_n^{0-}\right) \left\{\frac{d}{dB}n^{0-}\right\} + \frac{\partial}{\partial B}\Delta_n^{0-} \\ &\approx \left(\frac{\partial}{\partial n^{0-}}\Delta_n^{0-}\right) \left\{\frac{d}{dB}n^{0-}\right\}, \end{aligned} \quad (24)$$

i.e. neglecting the explicit dependence of Δ_n^{0-} on B , one obtains for the magnetic-field induced change of R_H due to a variation ΔB in the magnetic field after successive partial differentiations

$$\begin{aligned} \Delta R_H|_{\Delta B} &\equiv \left(\frac{d}{dB}R_H\right) \Delta B \\ &= -eR_H^2 \left(\frac{\partial}{\partial n^{0-}}\Delta_n^{0-}\right) \Delta n_{\Delta B}^{0-}, \end{aligned} \quad (25)$$

where $\Delta n_{\Delta B}^{0-} \equiv \{ \frac{d}{dB}n^{0-} \} \Delta B$ is the ΔB -induced change in the 0^- -population. With the inversion of B_{HF} exclusively causing a change $\Delta n_{\Delta B_{\text{HF}}}^{0-}$, the B_{HF} -induced change of the Hall constant is

$$\Delta R_H|_{\Delta B_{\text{HF}}} = -eR_H^2 \left(\frac{\partial}{\partial n^{0-}}\Delta_n^{0-}\right) \Delta n_{\Delta B_{\text{HF}}}^{0-}. \quad (26)$$

Hence in the extreme quantum limit the observed change in the Hall constant R_H both by incrementing the external magnetic field B and by inverting the hyperfine field B_{HF} is determined by the corresponding changes in population $\Delta n_{\Delta B}^{0-}$ and $\Delta n_{\Delta B_{\text{HF}}}^{0-}$ of the 0^- Landau level.

This makes us conclude that the cusp-like structure showing up with rising magnetic field B in the Hall constant R_H at the extreme quantum limit is due to the change in population of the minority-spin Landau level corresponding to an electron transfer between localized states at the 0^- Landau level and extended states at the 0^+ Landau level.

7. CONCLUSION

We have observed NMR-induced changes in both ρ_{xx} and ρ_{xy} around the magnetic field regime of the extreme quantum limit. Due to the Fermi-contact hyperfine contribution to the electronic Zeeman spin splitting, inversion of the nuclear hyperfine field B_{HF} by NMR acts on the electronic density of states at the Fermi level $D(E_F)$ thus inducing a change in the transverse magnetoresistivity ρ_{xx} . Both inversion of the nuclear hyperfine field B_{HF} and rise in the external magnetic field B by $\Delta B = 2|B_{\text{HF}}|$ cause a similar change of the Hall constant $R_H = \rho_{xy}/B$ in the magnetic field range where only the two lowest spin splitted Landau levels are occupied. This makes us explain the cusp-like structure of R_H in the extreme quantum limit by the redistribution of the occupation between extended and localized spin-states. On two-dimensional samples, the spin-part of the influence of an external magnetic field can be separated from the orbital part by tilting the magnetic field. These investigations on bulk n -InSb show that the technique of NMR-induced magneto-transport can be used to separate spin and orbital term in the Hamiltonian for a three-dimensional sample.

ACKNOWLEDGMENTS

We wish to thank I. D. Vagner and U. Zeitler for stimulating discussions and M. H. Julien, Y. Fagot, J. A. Gillet, and M. Horvatic for their valuable advices in setting up the NMR part of the experiment.

P. W. had the privilege to be a post-doctoral fellow with Michael Tinkham in Berkeley and at Harvard, A. G. M. J. was a graduate student of P. W. and N. G. was a graduate student of A. G. M. J. . Therefore, for all of us some of our education goes back to Professor Tinkham and we are most grateful for everything we have been allowed to learn from him.

REFERENCES

1. B. Sapoval, D. Kaplan, and G. Lampel, *Proc. 10th Int. Conf. Physics of Semiconductors*, Cambridge Massachusetts, 1970, p. 387, S. P. Keller, J. C. Hensel and F. Stern, eds. (CONF-700801 U.S. A.E.C. Division of technical Information, Springfield, Va. 1970).
2. B. Sapoval, D. Kaplan, and G. Lampel, *Solid State Commun.* **9**, 1591 (1971).
3. M. Dobers, K. V. Klitzing, J. Schneider, G. Weimann, and K. Ploog, *Phys. Rev. Lett.* **61**, 1650 (1988).

4. W. Desrat, D. K. Maude, M. Potemski, J. C. Portal, Z. R. Wasilewski, and G. Hill, *Phys. Rev. Lett.* **88**, 256807 (2002).
5. M. Gueron, *Phys. Rev.* **135**, A200 (1964).
6. W. Hofmann, G. Denninger, and H. Pascher, *Phys. Rev. B* **48**, 17035 (1993).
7. W. Hofmann, *Untersuchung der Hyperfeinwechselwirkung zwischen Elektronen- und Kernspins mittels kohärenter Spin-flip Ramanstreuung*, Dissertation Universität Bayreuth (1993).
8. C. P. Slichter, *Principles of Magnetic Resonance*, Springer Series in Solid-State Sciences 1, M. Cardona, P. Fulde, K. von Klitzing, and H.-J. Queisser, eds. (Springer Verlag, Berlin, 1996).
9. G. Denninger, *Festkörperprobleme / Adv. Solid State Phys.* **30**, 113 (1990).
10. A. Abragam, *The Principles of Nuclear Magnetism*, Chap. 8 (Clarendon Press, Oxford, 1985).
11. Y. Yafet, *J. Phys. Chem. Solids* **21**, 99 (1961).
12. R. A. Isaacson, *Phys. Rev.* **169**, 312 (1968).
13. E. N. Adams and T. D. Holstein, *J. Phys. Chem. Solids* **10**, 254 (1959).
14. R. Kubo, S. J. Miyake, and N. Hashitsume, *Solid State Physics*, **17**, F. Seitz and D. Turnbull, eds. (Academic Press, New York and London, 1965).
15. D. G. Seiler and A. E. Stephens, *Modern Problems in Condensed Matter Sciences* **27.2**, G. Landwehr and E. I. Rashba, eds. (Elsevier Science Publishers B.V., Amsterdam, 1991), p. 1031.
16. H. P. R. Frederikse and W. R. Hosier, *Phys. Rev.* **108**, 1136 (1957).
17. S. T. Pavlov, R. V. Parfen'ev, Yu. A. Firsov, and S. S. Shalyt, *Zh. Eksp. Teor. Fiz.* **48**, 701 (1965) [*Sov. Phys. JETP* **21**, 1049 (1965)].
18. G. A. Antcliffe and R. A. Stradling, *Phys. Rev. Lett.* **20**, 119 (1966).
19. V. J. Goldman, M. Shayegan, and H. D. Drew, *Phys. Rev. Lett.* **57**, 1056 (1986).
20. Ramesh G. Mani, *Phys. Rev. B* **41**, 7922 (1990).
21. S. S. Murzin and A. G. M Jansen, *J. Phys.: Condens. Matter* **4**, 2201 (1992).
22. U. Zeitler, A. G. M. Jansen, P. Wyder, and S. S. Murzin, *J. Phys.: Condens. Matter* **6**, 4289 (1994).
23. O. Viehweger and K. B. Efetov, *Phys. Rev. B* **43**, 6840 (1991).
24. U. Zeitler, *Electronic Transport in Three-Dimensional and Two-Dimensional Metallic Semi-Conductors Under Extreme Quantum Conditions*, Dissertation Universität Konstanz (1994).
25. N. Gauss, A. G. M. Jansen, M. H. Julien, Y. Fagot-Revurat, M. Horvatic, and P. Wyder, *Europhys. Lett.* **49**, 75 (2000).
26. N. F. Mott, *Proc. Phys. Soc. A* **62**, 416 (1949).
27. N. F. Mott, *Can. J. Phys.* **34**, 1356 (1956).
28. S. Ishida and E. Otsuka, *J. Phys. Soc. Japan* **43**, 124 (1977).
29. F. Bridges and W. G. Clark, *Phys. Rev.* **182**, 463 (1969).
30. M. Goldman, *Spin Temperature and Nuclear Magnetic Resonance in Solids*, (Oxford University Press, London, 1970) p. 121.
31. A. Abragam, *The Principles of Nuclear Magnetism*, p. 34 (Oxford at the Clarendon Press, Oxford, 1985).
32. G. C. Carter, L. H. Bennett, and D. J. Kahan, *Progress in Materials Science*, Vol. 20, p. 122, B. Chalmers, J. W. Christian, and T. B. Massalski, eds. (Pergamon Press, Oxford, New York, 1976).
33. B. I. Shklovskii and A. L. Efros, *Electronic Properties of Doped Semiconductors*, Chapter 12 (Springer Verlag, Berlin, Heidelberg, New York, Tokio, 1984).
34. S. M. Sze, *Physics of Semiconductor Devices* (Wiley, New York, 1981).
35. M. Shayegan, V. J. Goldman, and H. D. Drew, *Phys. Rev. B* **38**, 5585 (1988).
36. B. I. Shklovskii and A. L. Efros, *Electronic Properties of Doped Semiconductors*, Chap. 7 (Springer Verlag, Berlin, Heidelberg, New York, Tokio, 1984).
37. N. Gauss, *Hall Effect and Resistance*, Dissertation Universität Konstanz (1997).
38. M. Pepper, *J. Non-cryst. Solids* **32**, 161 (1979).
39. N. F. Mott and E. A. Davis, *Electronic Processes in Non-Crystalline Materials* (Clarendon Press, Oxford, 1979).
40. Laura M. R. and Petros N. A. in *Semiconductors and Semimetals*, Physics of III-V compounds, Vol. 1, Chap. 6, R. K. Willardson and A. C. Beer, eds. (Academic Press, New York, San Francisco, and London, 1966).
41. R. A. Isaacson, *Phys. Rev.* **169**, 312 (1968).
42. O. Viehweger and K. B. Efetov, *Phys. Rev. B* **44**, 1168 (1991).
43. O. Viehweger, *J. Phys. B - Condens. Matter* **83**, 45 (1991).

A Contribution to the Tinkham Festschrift

Materials Physics and Quantum Coherence in Superconducting Qubits

M. R. Beasley¹

Received August 15, 2004; accepted September 4, 2004

Nonidealities of real superconductors in the form of residual rf losses and conductance below the superconducting energy gap in tunneling Josephson junctions are discussed as possible sources of decoherence in Josephson junction flux qubits. The purpose of the paper is pedagogical and aimed at taking a first step in a unified view of the quantum behavior of superconducting qubits and the realities of the materials out of which they are constructed. The need for a dialog between the quantum physicist and the materials physicist is stressed. Residual rf losses and localized states in junction barriers are identified as important subjects for this dialog.

KEY WORDS: superconducting qubits; decoherence; localized states; rf residual losses.

1. INTRODUCTION

Clearly one of the major developments in superconductivity in the past few decades has been the demonstration that the superconducting pair wave function must be fully quantized under appropriate circumstances [1]. In the conventional descriptions (e.g., the GL theory and the RSJ model of Josephson junctions), it is taken as a classical variable. The understanding of this quantum regime is now sufficiently advanced that applications in the form of quantum computing are center stage in the field [2]. At the same time, the superconductor/insulator transition in two-dimensional disordered superconductors is thought to be a quantum phase transition [3].

Of course, in any quantum system that consists of a macroscopic number of particles, the issue of quantum decoherence comes to the fore. Specifically, the system must be decoupled from any continuum of states that could decohere its quantum behavior. Superconductors are attractive macroscopic quantum systems in this regard because they exhibit an energy gap in their single-particle excitation spectrum that serves in principle to decouple the macroscopic

quantum degrees of freedom from the continuum of single-particle (normal electron) states above the gap. In particular, theoretically, the number of normal excitations decreases as $e^{-\Delta/kT}$ as the temperature goes to zero, where Δ is the superconducting energy gap and T is the temperature.

And now we come to the crux of this paper. In real superconductors, material non-idealities foil this complete freezing out of the normal excitations through mechanisms that are at best poorly understood. It is here that quantum physics meets materials physics, and, concomitantly, quantum and material physicists must join forces. The purpose of this paper is to foster the needed dialog.

Our specific goal at this early stage is pedagogical. We discuss a typical Josephson junction flux qubit and introduce appropriate dissipative elements as sources of decoherence. Dissipative elements are not the only conceivable sources of decoherence, nor *a priori* necessarily the most important, but they are the natural place to start. We will return to this point later in this paper. Also, see [2] for a broader discussion of possible sources of decoherence.

Two non-ideal sources of dissipation in real superconducting qubits are residual rf losses in the superconducting wires that make up the circuit and conductance below the gap in the tunneling Josephson junction. The latter has received

¹Department of Applied Physics, Stanford University, Stanford, California.

considerable attention, the former almost none. To gauge their relative importance, we consider a typical Josephson junction flux qubit and apply a simple model of decoherence suitable for order of magnitude estimates of decoherence times due to dissipation. We also review in a preliminary fashion what is known and not known about these non-ideal sources of dissipation from a materials physics point of view. We make no pretense of being either definitive or complete. Our objective is simply to take a useful first step in the dialog advocated above.

2. A JOSEPHSON JUNCTION FLUX QUBIT

Figure 1a shows the circuit of a typical Josephson junction flux qubit. It consists of a single Josephson junction, including its shunt capacitance, in parallel along with an inductance to form overall a superconducting loop. The capacitance is included explicitly at this stage because it is the source of the “mass” of the system in the quantum limit. To keep things simple, we assume a lumped parameter description is sufficient at all relevant frequencies. We also assume for definiteness that the loop is biased by an external applied flux at a value near half a flux quantum to create a two-well potential [4].

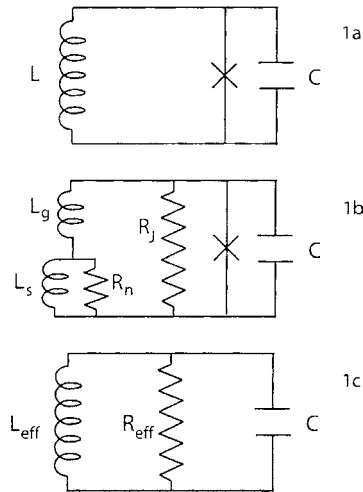


Fig. 1. Figure 1(a) shows a typical Josephson junction flux qubit. Figure 1(b) shows the same circuit including the dissipative elements that can produce decoherence in the two-fluid model of superconductivity and the RSJ model of Josephson junctions. Fig. 1(c) shows the simplified circuit actually analyzed in this paper in which the geometric inductance of the circuit is neglected. See discussion in the text.

Figure 1b, shows the same circuit with the appropriate lumped parameter dissipative elements included. Here, R_n is the resistance of the normal channel in the two-fluid model, L_s is the inductance (kinetic and magnetic) associated with the currents and fields inside the superconductor, and L_g is the purely geometric inductance associated with the fields outside the superconductor. Ideally both R_n and R_j increase as $e^{\Delta/kT}$ with decreasing temperature as the density of thermally activated normal electrons freezes out.

To greatly simplify the circuit analysis, we henceforth neglect L_g . This would be true for a strip line inductor for which $d < \lambda$, where d is the thickness of the dielectric and λ is the superconducting penetration depth. Under this (only fair) assumption, the circuit of Fig. 1b reduces to that shown in Fig. 1c, in which $R_{\text{eff}} = 1/(R_n^{-1} + R_j^{-1})$ and $L_{\text{eff}} = 1/(L_s^{-1} + L_j^{-1})$ where L_j is the Josephson inductance of the Josephson junction. Associated with R_{eff} is a noise source with spectral density $\langle \delta I \delta I \rangle_\omega$ that is the source of decoherence in this model. We also assume that all external sources of decoherence are under control and can be neglected. Our focus is on those effects that cannot be avoided without materials optimization.

3. ESTIMATION OF THE DECOHERENCE TIMES

Given this simplified circuit, it is straightforward to derive expressions for the decoherence times of the system. Here, we follow the derivation developed by Dale [5] based on the earlier formulation presented by van der Wal [6]. In these treatments, the decoherence times due to relaxation and dephasing are given in terms of the spectral density of energy fluctuations by

$$\tau_r^{-1} = \frac{1}{2} \left(\frac{\Delta}{v} \right)^2 J(\omega) \coth \left(\frac{\hbar\omega}{2kT} \right)$$

$$\tau_\phi^{-1} = \frac{1}{2\tau_r} + \frac{1}{2} \left(\frac{\varepsilon}{v} \right)^2 \alpha 2\pi \frac{kT}{\hbar}$$

where $J(\omega) \coth \left(\frac{\hbar\omega}{2kT} \right) = \frac{\langle \delta\varepsilon \delta\varepsilon \rangle_\omega}{\hbar}$, and $\alpha = \lim_{\omega \rightarrow 0} \left(\frac{J(\omega)}{2\pi\omega} \right)$ is a dimensionless parameter, determined by the slope of $J(\omega)$ at low frequencies. The factors in front of these two equations involve the quantum tunnel splitting Δ of (in our example) the degenerate states of the two-well potential formed by flux biased loop of

Fig. 1, and the energy bias ε , which is related to the level separation ν by $\nu^2 = \Delta^2 + \varepsilon^2$. For details, see [6]. From these equations, we see that it is sufficient to determine $\langle \delta\varepsilon\delta\varepsilon \rangle_\omega$ to determine the decoherence times for the circuit in Fig. 1.

Using the fluctuation–dissipation theorem and elementary circuit theory, it is straightforward to show (see [5]) that for the simplified circuit (Fig. 1c) being considered here

$$J(\omega) = \frac{4I^2}{\hbar\omega R_{\text{eff}}} |Z|^2$$

where

$$Z = \frac{1}{\frac{1}{R_{\text{eff}}} + i\omega C + \frac{1}{i\omega L_{\text{eff}}}}$$

After some straightforward algebra, one finds the decoherence rate

$$\Gamma_r = \tau_r^{-1} = \frac{1}{2} \left(\frac{\Delta}{\nu} \right)^2 \frac{4I^2}{\hbar\omega R_{\text{eff}}} |Z|^2 \coth \left(\frac{\hbar\omega}{2kT} \right)$$

where I is the circulating current in the loop due to the bias ε . Note that in the low frequency limit relevant to practical circuits, $|Z|^2 \approx \omega^2 L_{\text{eff}}^2$. Note also that as the effective resistance R_{eff} increases, the decoherence rate Γ_r decreases—a physically obvious result of general qualitative applicability for any superconducting qubit.

4. EMPIRICAL VALUES OF R_n AND R_j

Empirical values of R_n can be readily determined from measurements of the rf surface resistance of a superconductor. Note that although the surface resistance typically goes as ω^2 , the resistance of the normal channel is independent of frequency [7]. Of interest to us here is the residual value as T goes to zero. Values of R_j can be estimated directly from the I–V curve of a Josephson junction.

The materials of greatest interest currently for Josephson junction qubits are Al and Nb. To our knowledge, there are no good measurements of the residual surface resistance of Al thin films. For Nb thin films, two recent measurements yield residual values of R_n (expressed as a sheet resistance for a film 1000 Å thick) in the range of 10^2 to 10^3 ohms/square [8,9]. Assuming the thin-film strip-line inductor L is roughly 10 squares long, the actual value of R_n would be 10^3 to 10^4 ohms. Further, as shown by Dale [5] using the expressions above, for the relaxation rate, for $R_n = 10^4$ ohms and taking the circuit parameters and

operating conditions used in the very early experiments by Friedman *et al.* [4], Γ_r^{-1} is of order 100 ns.

Much more is known about the magnitude of the sub-gap resistance R_j . Early on it was recognized as a potential source of decohering dissipation in Josephson circuits and therefore concerted efforts to determine its magnitude were undertaken. Kirtley *et al.* determined the sub-gap resistance in Nb–PbAuIn edge junctions by means of measurements of the return current (switching current to the zero-resistance state) of the hysteretic I–V characteristic of under damped Josephson junctions. The theory of this process is well developed and can be used to extract R_j . They found that $R_j > 1 \text{ M}\Omega$ for junction with a normal resistance of 7.3 K Ω yielding a ratio of sub-gap to normal resistance >100 . Later, Johnson *et al.* showed that in their Sn/Sn-oxide/Sn junctions the effective sub-gap resistance saturated as temperature was reduced due to a shunting effect of the measurement leads at high frequencies. Their data put a lower limit of the ratio of sub-gap to normal resistance $>10^4$ for a junction with a normal resistance of 8.3 K Ω . As noted in [2], these are favorable values from the point of view of decoherence. Apparently, a similarly favorable situation pertains to Al/Al-oxide/Al junctions [10]. Assuming that these limits on the ratio of the sub-gap to normal resistance are typical and that the current measurements or residual rf losses are valid in the context of Josephson junction flux qubits, we conclude that for a typical junction normal resistance of 1 k Ω , residual rf losses should dominate the decoherence.

To our knowledge, this point has not previously been appreciated. But, of course, this analysis is far too simple to draw definitive conclusions. Also, it is possible to greatly reduce the problem of residual rf losses by using the Josephson inductance of a second Josephson junction to provide the needed loop inductance. Then, only the junction sub-gap resistances are relevant, and they appear to be more favorable.

5. SOME THOUGHTS ON THE RELEVANT MATERIALS PHYSICS

The residual rf losses in superconductors is a difficult, messy business. There is little specific theoretical guidance beyond the notion of avoiding trapped vortices or ugly geometries with large demagnetization factors that might permit premature vortex penetration. Much work has been done to improve

the rf performance of bulk high power Nb cavities for high-energy physics applications. But essentially no work has been carried out to minimize residual rf losses in thin-film superconductors for electronic applications.

From a materials point of view, Nb is notorious for having normally conducting suboxides near its surface. Indeed, the great utility of using a thin layer of oxidized Al to form the tunnel barrier in the Nb SIS Josephson junctions is in part due to the chemical reduction of these surface suboxides by the Al layer. Similarly in our laboratory, we found years ago that Nb–Ti alloy thin films make very much better tunnel junctions than do pure Nb films [11]. T_c is higher as well. These facts suggest that creative use of surface layers and/or chemical substitution in Nb could have a positive effect on the residual rf losses.

Another oft suggested source of problems are the grain boundaries in Nb films. Here scanning probe studies would be interesting, and again the use of chemical substitutions might have beneficial effects. We certainly know that this is true in the case of the infamous weak-link grain boundaries in 123 YBCO [12]. The use of epitaxial Nb films could also be interesting.

Returning to trapped vortices and premature vortex penetration, scanning Hall probes are now available with single-vortex resolution and wide-area scanning capabilities [13]. These new tools should be ideal for studying vortex processes at the single-vortex level. The point of this discussion is to emphasize that systematic attempts to reduce residual rf losses in superconducting thin films is a virtually unexplored field and that progress can reasonably be expected. Moreover, there are some clearly defined ways to proceed. Such studies might also prove beneficial for applications of superconductors in rf filters for telecommunications applications where residual rf nonlinearities in 123 YBCO thin films limit performance.

The possible role of non-idealities on the conductance below the gap in superconducting tunnel junctions is an equally murky subject. Speculations usually invoke some kind of alternative transport channel, ranging from simple nanoshorts to transport via localized states. At least in the latter case, a great deal is known about the transport processes, thanks to a thorough study of amorphous Si barriers as a model system [14]. The localized states in amorphous Si are known to have a positive on-site Coulomb repulsion U , and therefore the states near the Fermi energy are singly occupied and carry an un-

compensated spin. A very successful theory of these experiments has been worked out by Glazman and coworkers [15].

The upshot of this work is that coherent resonant tunneling and incoherent hopping via localized states both certainly occur, but their contribution relative to direct tunneling decreases exponentially as the barrier is made thinner. The statistical nature of the position and energy of these localized states leads to a novel dependence on temperature and applied voltage bias. At low bias, resonant tunneling and hopping can be made to dominate but only in very thick barriers of overall conductance too low to sustain Josephson coupling in the presence of thermal fluctuations. Interestingly, the junctions formed due to this resonant tunneling are π -junctions, due to peculiarities of coupling through a singly occupied state [16]. Thus, resonant tunneling via localized states is unlikely to contribute substantially to conductance through tunnel junctions in the thin barrier limit relevant to the very small tunnel junctions needed for qubits.

On the other hand, even in the case of very thin amorphous Si tunnel barriers, a substantial conductance below the gap in SIS Nb tunnel junctions was observed that is not understood [17]. Peculiar zero-bias anomalies were also observed. One thing seems clear, however. These anomalies are not due to transport through the junction via localized states. Much more likely is that they are due to an interaction of localized states near the electrode/barrier interface with the conduction electrons in the electrodes, presumably as some manifestation of the Kondo effect.

We should note here that localized states acting as two-state fluctuators are implicated in critical current fluctuations leading to $1/f$ noise in many contexts of superconducting tunnel junctions. The evidence for this is quite compelling although the exact mechanism by which the fluctuations in the position of the localized state actually affect the critical current is not completely clear [18]. Usually, it is assumed that charge fluctuations of the state are involved leading to a local modification of the barrier for direct tunneling.

Recently, Simmonds *et al.* have proposed very subtle way by which localized states can affect Josephson junction qubits [19]. They propose that some localized states in their barriers form two-state fluctuators (quantum mechanically coherent motion between sites in the barrier) that hybridize quantum mechanically with the Josephson coupling itself, thereby increasing the dimension of the relevant

Hilbert space of the qubit. They further propose that these localized states may be associated with grain boundaries in the aluminum oxide barrier.

From a materials physics point of view, several ideas stand out. Clearly the modern arsenal of scanning probes should be brought to bear on Al-oxide barriers [20]. Such work would be relevant to both superconducting Al and Nb qubits. More work on model systems might also be useful. If localized states play a role, then chemical substitutions to “passivate” these states might be brought to bear, as in the use of H to passivate the localized states in amorphous Si. Because Al-oxide is generally believed to be amorphous, it is not clear what defects or macroscopic structure they might have that could provide localized conductance paths. One source of the latter might be grain boundaries in the underlying superconducting electrode.

Clearly there is much that could and probably should be done to investigate non-idealities in the materials used to construct superconducting qubits. The preliminary analysis presented here suggests that consideration of residual rf losses and the role of localized states need more detailed study. The stakes are high for superconducting quantum computing. The necessary work will not be easy and will require knowledge of the physics of superconductors and the materials science of real materials. Collaboration will be essential. Let’s hope that the needed dialog will proceed productively.

ACKNOWLEDGMENTS

It seems fit to acknowledge here my great debt to Mike Tinkham from whom I learned phenomenology, and a similar thanks to Ted Geballe from whom I learned a respect for real materials. If nothing else, I hope this modest contribution to the field of quan-

tum computing will lead others to work seriously at the interface of pure quantum phenomena and materials physics. I also wish to acknowledge the senior thesis of Yseulte Sapphira Dale at Stanford University on which the discussion of decoherence due to dissipation and its application to residual rf losses in this paper is based. The preparation of this paper was carried out under the support of the AFOSR.

REFERENCES

1. A. J. Leggett, *Prog. Theor. Phys.* **69** (Suppl.), 80 (1980).
2. T. P. Orlando, J. E. Mooij, L. Tian, C. H. van der Wal, L. S. Levitov, S. Lloyd, and J. J. Mazo, *Phys. Rev. B* **60**, 15398 (1999).
3. N. Mason and A. Kapitulnik, *Phys. Rev. B* **64**, 060504 (2001).
4. J. R. Friedman, V. Patel, W. Chen, S. K. Tolpygo, and J. E. Lukens, *Nature* **406** (2000).
5. Y. S. Dale, Senior Thesis, Stanford University, California, 2002.
6. C. H. van der Wal, R. K. Wilhelm, C. J. P. M. Harmans, and J. E. Mooij, *Eur. Phys. J. B* **31**, 111 (2003).
7. T. Van Duzer and C. W. Turner, *Principles of Superconductive Devices* (Elsevier, 1981).
8. S. Anlage, private communication, 2002.
9. S. Sridhar, private communication, 2002.
10. See Ref. [72] in Ref. [2] above.
11. T. P. Orlando and M. R. Beasley, unpublished.
12. See H. Hilgenkamp and J. Mannhart, *Rev. Mod. Phys.* **74**, 485 (2002).
13. R. Dinner, M. R. Beasley, and K. A. Moler, unpublished.
14. Y. Xu, D. Ephron, and M. R. Beasley, *Phys. Rev. B* **52**, 2843 (1995); and previous references listed therein. Also see [17] for a particularly clear exposition of the field of transport via localized states in tunnel junctions.
15. L. I. Glazman and K. A. Matveev, *Sov. Phys. JETP* **67**, 1276 (1988).
16. L. I. Glazman and K. A. Matveev, *JETP Lett.* **49**, 659 (1989).
17. D. Efron, Ph.D. Thesis, Stanford University, California, 1996.
18. R. T. Wakai and D. J. Van Harlingen, *Phys. Rev. Lett.* **58**, 1687 (1987).
19. R. W. Simmonds, K. M. Lang, D. A. Hite, D. P. Pappas, and J. M. Matinis, cond-mat/0402470.
20. V. da Costa, C. Tisusan, T. Dimopoulos, and K. Ounadjela, *Phys. Rev. Lett.* **85**, 876 (1999).

“Pseudogap” State of Novel Superconductors: Energy Scales and Structural and Diamagnetic Transitions

Vladimir Z. Kresin,¹ Stuart A. Wolf,² and Yuri N. Ovchinnikov³

Received August 15, 2004; accepted September 4, 2004

High T_c cuprates are characterized by three characteristic energy scales: T_c , T_c^* , and T^* . The lowest scale, T_c , corresponds to the usual transition to the dissipationless state ($R = 0$) with a macroscopic phase coherence. The higher energy scale, T_c^* , describes the diamagnetic transition. The region $T_c^* > T > T_c$ is characterized by the presence of superconducting regions embedded in a normal metallic matrix. The highest energy scale (T^*) corresponds to the formation of the structure, phase separation, and to the opening of the CDW gap.

KEY WORDS: inhomogeneity; diamagnetism; characteristic temperatures.

1. INTRODUCTION

The study of the “pseudogap” state (PS) in novel superconducting systems has attracted a lot of attention. This state corresponds to temperatures $T > T_c$ (up to some characteristic temperature, T^*). Indeed, a number of unusual features have been observed for the high T_c cuprates in the region $T^* > T > T_c$, especially for the underdoped compounds. It is interesting that there are contradictory reports about the value of T^* . The aim of this paper is to demonstrate that the real picture is more complicated and we are dealing with *three* different energy scales and, correspondingly, with *three* characteristic temperatures (we denote them T_c , T_c^* , and T^*). The analysis described below is based on various experimental data and our theoretical studies [1–4].

The “pseudogap” state is characterized by the following fundamental features. First of all, one should mention the presence of an energy gap in the spectrum; the energy gap persists above T_c despite the finite resistance and the absence of macroscopic phase coherence. One should note that

the name (“pseudogap” state) is misleading, because a real energy gap structure has been observed, that is a dip in the density of states. This gap was observed with use of infrared spectroscopy: this method was pioneered by M. Tinkham and his collaborators [5], see also the book [6]. This method was used for the cuprates in [7]. In addition, the presence of the energy gap above T_c was observed by tunneling spectroscopy which is a direct probe of the density of states (see, e.g., study of Bi2212 in [8]). The presence of the gap was also detected by NMR [9] and photoemission [10] spectroscopies, heat capacity measurements [11], etc. (see also the review [12]).

One should stress that just the presence of the energy gap does not allow us to explain the nature of the PS. Indeed, in addition to the pairing, there are many reasons for an appearance of a gap structure (CDW, SDW, band gap, Coulomb disorder, etc.), and such factors can be present in such complex systems as the cuprates.

Another feature observed in the cuprates above T_c is their diamagnetism. This phenomenon has been observed in many studies. For example, for the underdoped La–Sr–Cu–O compound ($T_c \approx 20$ K) diamagnetism was observed up to $T \approx 80$ K [13]. We think that this is a fundamental property of the “pseudogap” state. As we know, the energy gap is an important parameter of the superconducting state, but diamagnetism (Meissner effect) is a more

¹Lawrence Berkeley Laboratory, University of California, Berkeley, California, 94720.

²Department of Materials Science, University of Virginia, Charlottesville, Virginia 22903.

³Landau Institute for Theoretical Physics, Moscow, Russia 117332.

fundamental feature (it is enough to recall that there is the phenomenon of gapless (!) superconductivity [14]). We think that a similar situation occurs for the PS. Therefore, an understanding of diamagnetism observed above T_c is a serious challenge. Diamagnetism above T_c was reported in [15] for YBCO and also in [16] for the T1-based cuprate. It was observed even in other complex systems, like doped bronze [17], and, recently in borocarbides [18].

There are two different transitions which occur at temperatures above T_c (“pseudogap” state). They are the structural (T^*) and diamagnetic (T_c^*) transitions. They will be discussed below.

2. ENERGY SCALES

2.1. Highest Energy Scale (T^*)

The highest energy scale ($>5 \times 10^2$ K) corresponds to the formation of the crystal structure which is characteristic for the compounds of interest. For example, for YBCO, the formation of the chain structure occurs at T^* .

An energy gap could be open in the region below T^* . Of course, this gap is not related to the pairing, but, as was mentioned above, there are many sources for the appearance of a gap. For example, the presence of chains in YBCO leads to a charge density wave and, correspondingly, to a gap on the part of the Fermi surface. Nesting of states might lead to a CDW instability in other compounds as well.

Another important property of the compound below T^* is its intrinsic inhomogeneity; this is due to statistical nature of doping and is manifested in the so-called phase separation. This concept was introduced in [19] and then studied in many papers (see, e.g., [20]). This property implies the coexistence of metallic and insulating phases. Note that the metallic phase itself appears to be inhomogeneous (see below). The periodic stripe structure [21] also appears below T^* .

2.2. Diamagnetic Transition (T_c^*)

If the compound is cooled down below T^* , then at some characteristic temperature dubbed T_c^* ($T_c^* \approx 2 \times 10^2$ K) one can observe the transition into a diamagnetic state.

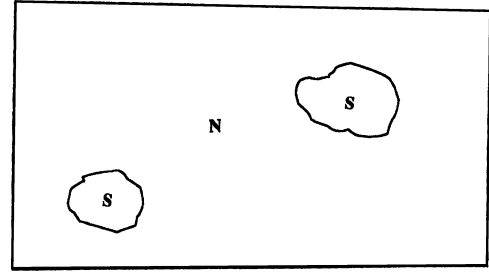


Fig. 1. Inhomogeneous metallic phase at $T_c^* > T > T_c$. “Islands” S have higher critical temperatures than the normal matrix.

We focus below on the metallic phase only. The origin of diamagnetism was discussed in our papers [1]. The metallic phase is inhomogeneous and, as a result, the superconducting critical temperature is spacially dependent: $T_c \equiv T_c(\mathbf{r})$. The characteristic temperature T_c^* corresponds to an appearance of superconducting regions embedded in the normal metallic matrix (Fig. 1). The presence of such superconducting clusters (“islands”) leads to a diamagnetic moment, whereas the resistance remains finite, because of the normal matrix. It is remarkable that the superconducting state appears at temperature T_c^* which is much higher than the resistive T_c , but it is manifested, at first, as a set of “isolated” islands.

There are various sources of inhomogeneities (see [2]). The main one is connected with pair-breaking [14]. For example, the localized magnetic moments act as pair-breakers. For D -wave symmetry even the nonmagnetic impurities are pair-breakers. Therefore, doping inevitably leads to pair-breaking and, correspondingly, to inhomogeneity. It is essential that the pair-breaking leads also to a depression in the value of T_c . Therefore, the dependence $T_c(\mathbf{r})$ is caused by a nonuniform distribution of pair-breakers. The region containing a small concentration of pair-breakers is characterized by a higher value of local critical temperature. As a result, at some value of temperature in the region $T_c^* > T > T_c$ we have a picture as illustrated in Fig. 1. Note that the minimum size of the superconducting clusters is determined by the proximity effect between the cluster and normal metallic matrix. This size should be large than ξ , where ξ is the pairing coherence length.

As was noted above, diamagnetism has been reported in many papers [13,15–17]. A remarkable study [13] which combines STM and magnetic imaging directly demonstrates the presence of the diamagnetic “islands.” This study [13] provides direct experimental support for the picture proposed by us in [1].

One should also add that the contribution to the diamagnetism may come also from fluctuations of the order parameter above T_c . However, such a large temperature range, such as, e.g., observed in [13] for the LSCO compound with $T_c \approx 20$ K (diamagnetism was observed up to $T \equiv T_c^* \approx 80$ K) can not be due to this factor. The authors of [15] analyzing the data in YBCO also come to conclusion that fluctuations make a contribution, especially near T_c , but their presence is insufficient to explain the observed phenomenon.

2.3. Resistive Transition (T_c)

As temperature is lowered below T_c^* , new superconducting clusters form (Fig. 1) and existing clusters form larger “islands.” This description is a typical percolation scenario. At some characteristic temperature (T_c), the macroscopic superconducting phase is formed (“infinite” cluster in terms of the percolation theory, see, e.g. [23]). A similar picture was described by Gor’kov and one of the authors for the transition at the Curie temperature for manganites [24]. The formation of the macroscopic phase at T_c leads to the appearance of a dissipationless state ($R = 0$).

It is important also to stress, that in the region $T_c^* > T > T_c$ each “island” has its own phase, so that there is no phase coherence for a whole sample. Macroscopic phase coherence appears below T_c .

2.4. Experimental Data. “Giant” Josephson Effect

The concept, described above (Fig. 2), has strong experimental support. First of all, one should note that the inhomogeneous structure of the compounds was directly demonstrated by STM measurements [25], inelastic neutron scattering [26], and NMR [27]. It is essential that, contrary to the optimum doping region, the underdoped samples possess an intrinsic inhomogeneity which correlates with the appearance of the pseudogap phenomenon. We mentioned above the data describing the energy gap in the normal region and observations of the diamagnetism. Paper [13] directly demonstrates the presence of “diamagnetic” clusters above T_c .

The aforementioned picture allows us to explain a recently observed phenomenon called “giant” Josephson effect [28]. The experiment was performed with an S—N—S junction formed with LaSCO superconducting electrodes with $T_c \equiv T_c^S \approx$

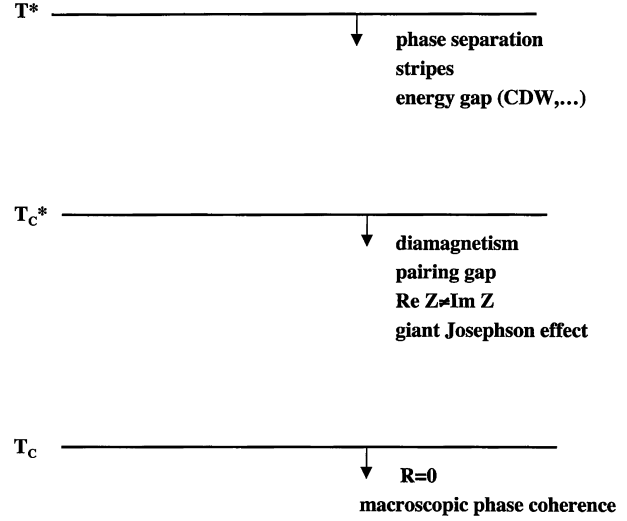


Fig. 2. Characteristic temperatures T^* , T_c^* , T_c for the structural, diamagnetic, and resistive transitions, correspondingly. The transitions lead to an appearance of the additional features listed under corresponding lines.

45 K. The barrier was made of the same, but underdoped compound with its $T_c \equiv T_c^B \approx 20$ K (such a combination avoids undesirable interface effects). The measurements were performed above T_c^B . The barrier was grown in the c direction, so that its layers were parallel to the electrodes. It is known that for an S—N—S junction the amplitude of the Josephson current $j_0^\infty \exp(-d/\xi_N)$, where d is the thickness of the barrier, and ξ_N is its coherence length. As we know, $\xi_c \approx 3$ Å, it is remarkable that a Josephson current has been observed in [28] for d up to 200 Å (!).

Such a “giant” effect is observable because the barrier is in the “pseudogap” state and contains superconducting “islands” which are present in the barrier layers in the region $T_c^* > T > T_c$, $T_c^* \approx 80$ K [13] which includes the interval $T_c^S > T > T_c^B$ corresponding to the measurements [28]. As a result, the Josephson current is transferred through the path formed by superconducting “islands.” A detailed calculation [4] is in a very good agreement with the data in [28].

3. CONCLUSION

Diamagnetism above T_c and the presence of an energy gap in this region are the most fundamental features of the “pseudogap” state. Contrary to conventional superconductors, the resistive and diamagnetic transitions are separated. The lowest

energy scale (T_c) corresponds to the transition to the dissipationless state ($R = 0$) with macroscopic phase coherence. The diamagnetic transition occurs at higher temperature (we denote it as T_c^*) and the pairing gap persists up to this second characteristic energy scale. The region $T_c^* > T > T_c$ is characterized by the presence of superconducting regions embedded in a normal metallic matrix. The depression of T_c relative to T_c^* is caused, mainly, by pair-breaking, so that T_c^* can be called an “intrinsic” critical temperature. Above T_c^* (in the region up to third characteristic energy scale, T^*), one can observe phase separation, formation of stripes, and the energy gap structure not related to the pairing, e.g. CDW. Below T_c^* , there is a coexistence of the pairing and CDW gaps.

We are pleased that this paper is a part of the Special issue honoring Michael Tinkham who has made key contributions in the field of superconductivity and other areas of the condensed matter physics.

REFERENCES

1. Yu. Ovchinnikov, S. Wolf, and V. Kresin, *Phys. Rev. B* **60**, 4329 (1999).
2. Yu. Ovchinnikov, S. Wolf, and V. Kresin, *Phys. Rev. B* **63**, 064524 (2001).
3. Yu. Ovchinnikov and V. Kresin, *Phys. Rev. B* **65**, 214507 (2002).
4. V. Kresin, Yu. Ovchinnikov, and S. Wolf, *Appl. Phys. Lett.* **83**, 722 (2003).
5. R. Glover and M. Tinkham, *Phys. Rev.* **104**, 844 (1956); D. Ginsberg and M. Tinkham, *Phys. Rev.* **118**, 844 (1960).
6. M. Tinkham, *Introduction to Superconductivity*. McGraw-Hill, New York (1996).
7. C. Homes, T. Timusk, R. Liang, D. Bohn, and W. Hardy, *Phys. Rev. Lett.* **71**, 1645 (1993).
8. a) H. Tao, F. Lu, and E. Wolf, *Physica C* **282**, 1507 (1997); b) C. Renner, B. Revaz, J. Genoud, K. Kadowaki, and O. Fischer, *Phys. Rev. Lett.* **80**, 149 (1998).
9. a) H. Alloul, T. Ohno, and P. Mendels, *Phys. Rev. Lett.* **67**, 3140 (1989); b) R. Walstedt and W. Warren, *Science* **248**, 1082 (1990).
10. a) A. Loeser, Z. Shen, D. Dessau, D. Marshall, C. Park, P. Fournie, and A. Kapitulnik, *Science* **273**, 325 (1996); b) H. Ding, T. Yokota, J. Campusano, T. Takahashi, M. Randeria, M. Norman, T. Mochiki, K. Kadowaki, and J. Giapintzakis, *Nature* **382**, 51 (1996).
11. a) J. Loram, K. Mirza, J. Wade, J. Cooper, and W. Liang, *Physica C* **235**, 134 (1994); b) N. Momono, T. Matsuzaki, T. Nagata, M. Oda, and M. Ido, *J. Low. Temp. Phys.* **117**, 353 (1999).
12. T. Timusk and B. Statt, *Rep. Progr. Phys.* **62**, 61 (1999).
13. I. Igushi, T. Yamagushi, and A. Sugimoto, *Nature* **412**, 420 (2001).
14. A. Abrikosov and L. Gor'kov, *Sov. Phys. JETP* **12**, 1243 (1961).
15. P. Caretta, A. Lascialfari, A. Rigamonti, A. Rosso, and A. Varlamov, *Phys. Rev. B* **61**, 12420 (2000); A. Lascialfari, A. Rigamonti, A. Romano, P. Tedesco, A. Varlamov, and D. Embriaco, *Phys. Rev. B* **65**, 144523 (2002).
16. C. Bergemann, A. Tyler, A. Mackenzie, J. Cooper, S. Julian, and D. Farrell, *Phys. Rev. B* **57**, 14387 (1998).
17. S. Reich and Y. Tsabba, *Eur. Phys. J. B* **12**, 13 (1999).
18. A. Lascialfari, T. Mishonov, A. Rigamonti, I. Zucca, G. Berg, W. Loser, and S. Drechsler, *Eur. Phys. J. B* **35**, 326 (2003).
19. L. Gor'kov and A. Sokol, *JETP Lett.* **46**, 429 (1987).
20. E. Sigmund and K. Mueller, *Phase Separation in Cuprate Superconductors* (Springer-Verlag, Berlin, 1994).
21. a) A. Bianconi, N. Saini, A. Lanzara, M. Missori, T. Rosetti, H. Oyanagi, H. Yamagushi, K. Oka, and T. Ito, *Phys. Rev. Lett.* **76**, 3412 (1996); b) J. Tranquada, J. Axe, N. Ichikawa, Y. Nakamura, S. Uchida, and B. Nachunu, *Phys. Rev. B* **54**, 7489 (1996).
22. L. Gor'kov and G. Tetelbaum, *JETP Lett.* **80**, 195 (2004).
23. B. Shklovskii and A. Efros, *Electronic Properties of Doped Semiconductor* (Springer, Berlin, 1984).
24. L. Gor'kov and V. Kresin, *JETP Lett.* **67**, 985 (1998); *Phys. Rep.* **400**, 149 (2004).
25. K. Lang, V. Madharan, J. Hoffman, E. Hudson, S. Pan, H. Esaki, S. Ushida, and J. Davis, *Nature*, **415**, 412 (2002).
26. T. Egami and S. Billinge, in *Physical Properties of High Temperature Superconductors*, D. Ginsberg, ed. (World, Singapore, 1996), p. 265.
27. J. Haase, C. Slichter, C. Milling, and D. Hinks, *Physica C* **341**, 1727 (2000).
28. I. Bozovic, G. Logvenor, M. Verhoener, P. Caputo, E. Goldobin, and M. Beasley, *Phys. Rev. Lett.* **93**, 157002 (2004); we are grateful to I. Bozovic for sending the preprint prior to publication.

Recollections

Michael Tinkham: The Early Years

Donald M. Ginsberg¹

I am happy to have been invited to help celebrate Michael Tinkham's 75th birthday by composing a brief memoir about his teaching and research at the University of California at Berkeley in the late 1950s. He was a major source of ideas for seminal experiments and for methods of applying theoretical principles of physics to the data to help gain a deep understanding of superconductivity. He also worked intensively on problems related to magnetic ordering and other subjects, but this memoir must concentrate on the area of physics in which I worked with him.

I was one of his first three PhD students. (The others were Robert C. Ohlmann and Paul L. Richards). Ultimately there were to be 57 PhDs earned with his guidance at Berkeley (1955–1966) or at Harvard (1966 to now). He has also had many postdoctoral people working in the group, but they are difficult to count, since they came and went at random times and frequently worked simultaneously on more than one project, affiliated with more than one group.

Mike, as we all called him, set the group's hard-working style by example; he seemed to be working all of the time except for our daily group coffee hour, which lasted about 20 min. He took a lot of work home with him for late night sessions. Occasionally he gave one further hints about hard work. For example, he once told me that the best research is done on national holidays.

We used the latest technology of the day, and the results were compared in depth with current theoretical ideas, some of which Mike helped to formulate.

His initial research efforts at Berkeley were paramagnetic resonance studies of molecules, liquids, and crystals. These provided a natural evolution

of his PhD work with M. W. P. Strandberg at MIT and his postdoctoral research at Oxford University. In his early days at Berkeley, he collaborated with A. F. Kip, who used cyclotron resonance to determine the Fermi-surface of various semiconductors and metals. The analysis of the data was backed up by theoretical help from the renowned Berkeley solid state theorist Charles Kittel. Solid state physics was thriving at Berkeley, and famous physicists were frequently seen passing through or visiting for a while. Even the legendary Wolfgang Pauli was there for one semester near the end of his life. Graduate students as well as more senior investigators gave seminars, speaking to a large roomful of impressive people who were free to ask the toughest questions they could devise. Thus did one learn to control one's nervousness.

In Michael Tinkham's first days at Berkeley, before he was on the tenure-track faculty, he met another postdoc there, Rolfe E. Glover, III, who had worked in the group of R. Hilsch at the University of Göttingen, fabricating and investigating thin-film samples. Using a cryostat designed by Rolfe, with far-infrared gratings and mirrors designed by Mike and made in the Berkeley Physics Department's machine shop, and a commercially available infrared detector called a Golay cell, Tinkham and Glover measured the transmission of far-infrared radiation by superconducting films. They obtained the first spectroscopic evidence of a superconducting energy gap before the 1957 appearance of the BCS theory of superconductivity. Mike's analysis of the spectroscopic data was a brilliant example of theoretical interpretation. He relied only on the idea of a superconducting energy gap (which had been suggested by B. B. Goodman and a few other groups, to account for thermodynamic and transport data) and general principles of physics: Maxwell's equations, causality (in the form of the Kramers-Kronig relations),

¹University of Illinois at Urbana-Champaign Department of Physics 1110 West Green Street, Urbana, Illinois 61801.

energy conservation, and Einstein's application of the Planck relation ($E = h\nu$) to photons.

With Mike's daily guidance, Paul Richards and I continued to develop the apparatus. In place of the Golay cell, we made and used low-temperature bolometer detectors of far-infrared radiation that were invented at the Bell Telephone Laboratory in the mid-1950s by W. S. Boyle and K. F. Rodgers. We made our own detectors. The new techniques improved the precision of the measurements by roughly a factor of 50. Paul measured far-infrared reflection from bulk samples, and I measured transmission through thin films. The two experiments had different limitations, and comparing the two types of data was instructive, as Mike had foreseen. The quantitative fit to the BCS theory was good. An unexpected small dip in the absorption just below the energy gap edge was observed, however. It diminished in size when Tinkham and a later student, L. H. Palmer, improved the spectral purity of the radiation incident on the film.

A few words about Michael Tinkham's early development will describe how "just a country boy, trying to do well," (to quote his own words in a message to me), climbed the first steps ascending to a life in science.

Mike was born in rural Wisconsin. He grew up on a dairy farm in that state, attended a one-room school house, and moved at age 11 with his family to the town of Ripon, Wisconsin. He attended Ripon College for his undergraduate work, majoring in Physics and Mathematics and earning the AB degree. His parents and several uncles preceded him there, studying chemistry and/or physics. Two of his uncles taught chemistry at Marietta College; they helped to stimulate Mike's early interest in science. In his senior year in high school, he was a winner of the prestigious national Westinghouse Science Talent Search, and was rewarded with a trip to Washington, DC. This experience helped to convince him that he could be a successful scientist, even with his "small-town background," as he has said.

Serving in the U.S. Navy for about the last year of World War II, Mike learned the electronics techniques of that time. He also learned electronics as an amateur radio operator both before and after his days in the Navy. This knowledge served him well in his postwar life as a physicist. In the 1950s, low-temperature physicists still designed their own cryostats, to be built in a machine shop, and they

designed and built their own lock-in amplifiers and most of their other electronics, using vacuum tubes as the active elements, of course. (Physicists no longer had to make their own vacuum tubes.) Calculations were performed by an electrically powered mechanical calculator or on a slide rule.

Mike's lecturing, both at scientific meetings and in the class room, had (and still have) an informal style, with occasional humorous parenthetical remarks to help keep the audience's attention. Like all good speakers, he made it look easy.

Michael Tinkham's progress from a one-room Wisconsin school house to Ripon College, to MIT to earn his PhD, to Oxford University and then Berkeley were followed by major achievements at Harvard. This is not the place to describe in detail his 38 years (so far) at Harvard, except to note that his recent work centers on the properties of superconducting and normal circuits made of parts so small that the flow of a single electron can be detected, and the wave nature of the electron has a major effect on the devices being investigated.

Berkeley's Charles Kittel, a "walking encyclopaedia" and guru of solid state physics, once commented that, of the many physics research groups he had visited, the most effective were those having a question in mind, for which they sought an answer by doing their research. Mike's group has always had this type of motivation. How fortunate are we, his students and postdocs, to have had him as our teacher and mentor. His unfailing good humor and constructive remarks, even when confronted with minor catastrophes in the lab, taught us how to meet the challenges of a physicist.

For his pioneering research, Michael Tinkham won the 1974 Oliver E. Buckley Condensed Matter Physics Prize of the American Physical Society. His other honors are too numerous to list here, except to say that he is both the Rumford Professor of Physics and the Gordon McKay Professor of Applied Physics at Harvard. His success encourages others to avail themselves of the intellectual cross-fertilization and mutual aid between fundamental and applied physics.

Michael Tinkham has written two widely used books, *Introduction to Superconductivity* and *Group Theory and Quantum Mechanics*. They are still available; the publisher is Dover. Those who read these books become Professor Tinkham's students, along with hundreds of other fortunate people.

My 14 years in the Tinkham Group

Chris Lobb

I started working as a beginning graduate student in Mike Tinkham's lab in the summer of 1975. Even with my limited perspective, it was clear that the Tinkham lab was an extraordinary place. The range of research projects was very broad, with each student working on something very different from the other students. There were projects on point contacts exposed to far-infrared radiation, phase-slip centers in one-dimensional superconductors, niobium nitride, intercalated layered compounds, tunnel junctions, and *in situ* composites. This could have seemed like an assortment of disconnected topics, but it was not: Mike's broad understanding and enthusiasm were contagious, making it possible, for example, to view the composites (which were being studied as a possible replacement for conventional multifilamentary composite magnet wire) as arrays of Josephson junctions. His weekly group seminars were an extraordinary opportunity to learn about a wide range of topics—they were an informal ongoing course in superconductivity.

I was very fortunate to stay at Harvard after receiving my PhD, so I witnessed the exciting things that came from his group for many years. It is hard to single out specific topics, given how many exciting things were going on, but certainly the famous work on Andreev reflection should be mentioned. At time the work was done, Mike said that it was the

last nail in the coffin, because he, Teun Klapwijk, and Greg Blonder had done so much; even Mike could not foresee how important the work would become years later when applied to the high- T_c superconductors. His group's work on ultra-small tunnel junctions, and his effort to understand their behavior as macroscopic quantum phenomena, have also taken on renewed importance because of their connection to quantum computing. And, to mention a topic of special interest to me, the work on Josephson-junction arrays provided important experiments in two-dimensional phase transitions. It still seems wonderful to me that one can study statistical mechanics by making integrated circuits which undergo phase transitions.

I worked directly with Mike for 14 years, joining his group as a graduate student in 1975, and leaving Harvard as an associate professor in 1989. The opportunity to work with Mike for so long was one of the greatest experiences of my life. As a researcher, Mike's rare combination of experimental and theoretical ability has kept him at the top of the field for decades. As a teacher, Mike worked constantly to make things understandable, and did so with enthusiasm and wit. Any success I've had since leaving his group is largely due to what I learned from him during those extraordinary 14 years.

Selected Publications

M. Tinkham and Group

BOOKS

Superconductivity: M. Tinkham, Chapter in *Low Temperature Physics*, ed. by C. deWitt, B. Dreyfus, and P.G. deGennes, Gordon and Breach, New York, 1962; also published separately.

Group Theory and Quantum Mechanics: M. Tinkham, McGraw-Hill Book Co., New York (1964); reprinted by Dover Publications.

Introduction to Superconductivity: M. Tinkham, McGraw-Hill Book Co., New York, (1975); 2nd Edition, (1996); reprinted by Dover Publications.

Physical Properties of the New Superconductors: M. Tinkham and C.J. Lobb, Chapter in *Solid State Physics* **42**, pp. 91–134, Academic Press, San Diego (1989).

JOURNAL ARTICLES

Paramagnetic resonance in liquids: M. Tinkham, R. Weinstein, and A.F. Kip, *Phys. Rev.* **84**, 848–849 (1951).

Interaction of molecular oxygen with a magnetic field: M. Tinkham and M.W.P. Strandberg, *Phys. Rev.* **97**, 951–966 (1955).

Paramagnetic resonance in dilute iron group fluorides: I. Fluorine h.f.s., M. Tinkham, *Proc. Roy. Soc. (London)* **A236**, 535–548 (1956).

Transmission of superconducting films at millimeter-microwave and far infrared frequencies: R.E. Glover IE and M. Tinkham, *Phys. Rev.* **104**, 844–845 (1956).

Energy gap interpretation of experiments on infrared transmission through superconducting films: M. Tinkham, *Phys. Rev.* **104**, 845–846 (1956).

Determination of the superconducting skin depth from the energy gap and sum rule: M. Tinkham and R.A. Ferrell, *Phys. Rev. Lett.* **2**, 331–333 (1959).

Far infrared transmission through superconducting films: D.M. Ginsberg and M. Tinkham, *Phys. Rev.* **118**, 990–1000 (1960).

Far infrared energy gap measurements in bulk superconducting in, Sn, Hg, Ta, V, Pb, and Nb: P.L. Richards and M. Tinkham, *Phys. Rev.* **119**, 575–590 (1960).

Antiferromagnetic resonance in FeF₂ at far infrared frequencies: R.C. Ohlmann and M. Tinkham, *Phys. Rev.* **123**, 425–434 (1961).

Far infrared exchange resonance in ytterbium iron garnet: A.J. Sievers, and M. Tinkham, *Phys. Rev.* **124**, 321–325 (1961).

Effect of fluxoid quantization on transitions of superconducting films: M. Tinkham, *Phys. Rev.* **129**, 2413–2422 (1963).

Tunneling into superconducting films in a magnetic field: J. Millstein and M. Tinkham, *Phys. Rev.* **158**, 325–332 (1967).

Far infrared absorption in thin superconducting lead films: L.H. Palmer and M. Tinkham, *Phys. Rev.* **165**, 588–595 (1968).

Observation of enhanced diamagnetism above t_c in indium due to thermodynamic fluctuations: J.P. Gollub, M.R. Beasley, R.S. Newbower and M. Tinkham, *Phys. Rev.* **187**, 587–594 (1969).

Excitation of multiple-magnon bound states in CoC₁₂.2H₂O: J.B. Torrance, Jr., and M. Tinkham, *Phys. Rev.* **187**, 595–606 (1969).

Fluctuation effects on the superconducting transition of tin whisker crystals: R.S. Newbower, M.R. Beasley, and M. Tinkham, *Phys. Rev.* **B5**, 864–868 (1972).

Theory of pair-quasiparticle potential difference in nonequilibrium superconductors: M. Tinkham and John Clarke, *Phys. Rev. Lett.* **28**, 1366–1369 (1972).

Magnetic suspension and propulsion systems for high-speed transportation: P.L. Richards and M. Tinkham, *J. Appl. Phys.* **43**, 2680–2691 (1972).

- Tunneling generation, relaxation, and tunneling detection of hole-electron imbalance in superconductors: M. Tinkham, *Phys. Rev. B* **6**, 1747–1756 (1972).
- Phase-slip centers and nonequilibrium processes in superconducting tin microbridges: W.J. Skocpol, M.R. Beasley, and M. Tinkham, *J. Low Temp. Phys.* **16**, 145–167 (1974).
- Heating effects in high-frequency metallic Josephson devices: Voltage limit, bolometric mixing, and noise: M. Tinkham, M. Octavio, and W.J. Skocpol, *J. Appl. Phys.* **48**, 1311–1320 (1977).
- Niobium point-contact Josephson-junction behaviour at 604 GHz: D.A. Weitz, W.J. Skocpol, and M. Tinkham, *Appl. Phys. Lett.* **31**, 227–229 (1977).
- Onequilibrium-enhanced supercurrents in short superconducting weak links: M. Octavio, W.J. Skocpol, and M. Tinkham, *Phys. Rev. B* **17**, 159–169 (1978).
- Percolation in inhomogeneous superconducting composite wires: C.J. Lobb, M. Tinkham, and W.J. Skocpol, *Solid State Communications* **27**, 1273–1275 (1978).
- A new thermoelectric effect in tunnel junctions: A.D. Smith, M. Tinkham, and W.J. Skocpol, *Phys. Rev. B* **22**, 4346–4354 (1980).
- Transition from metallic to tunneling regimes in superconducting microconstrictions: excess current, charge imbalance, and super-current conversion: G.E. Blonder, M. Tinkham, and T.M. Klapwijk, *Phys. Rev. B* **25**, 4515–4532 (1982).
- The ac Josephson effect in small-area superconducting tunnel junctions at 604 GHz: W.C. Danchi, F. Habbal, and M. Tinkham, *Appl. Phys. Lett.* **41**, 883–885 (1982).
- Spatial decay of the quasiparticle current in phase-slip centers: J. Aponte and M. Tinkham, *J. Low Temp. Phys.* **51**, 189–206 (1983).
- The transient response of superconducting indium microbridges to supercritical current pulses: D.J. Frank, M. Tinkham, A. Davidson, and S.M. Fans, *Phys. Rev. Lett.* **50**, 1611–1614 (1983).
- Noise and chaos in a fractal basin boundary regime of a Josephson junction: M. Iansiti, Qing Hu, R.M. Westervelt, and M. Tinkham, *Phys. Rev. Lett.* **55**, 746–749 (1985).
- Response of Josephson junctions to far-infrared radiation near their plasma resonance frequencies: Qing Hu, C.J. Lobb, and M. Tinkham, *Phys. Rev. B* **35**, 1687–1691 (1987).
- The resistive transition of high temperature superconductors: M. Tinkham, *Phys. Rev. Lett.* **61**, 1658–1661 (1988).
- Critical state model for harmonic generation in high-temperature superconductors: L. Ji, R.H. Sohn, G.C. Spalding, C.J. Lobb, and M. Tinkham, *Phys. Rev. B* **40**, 10937–45 (1989).
- Critical currents in frustrated two-dimensional Josephson arrays: S.P. Benz, M.S. Rzchowski, M. Tinkham, and C.J. Lobb, *Phys. Rev. B* **42**, 6165–6171 (1990).
- Effect of leads and energy gap upon the retrapping current of Josephson junctions: A.T. Johnson, C.J. Lobb, and M. Tinkham, *Phys. Rev. Lett.* **65**, 1263–1266 (1990).
- Variation of the coulomb staircase in a two junction system by fractional electron charge: A.E. Hanna and M. Tinkham, *Phys. Rev. B* **44**, 5919–5922 (1991).
- Phase transitions in Josephson junction arrays with long-range interaction: L.L. Sohn, M.S. Rzchowski, J.U. Free, and M. Tinkham, *Phys. Rev. B* **47**, 967–974 (1993).
- Experimental evidence for parity-based 2e-periodicity in a superconducting single-electron tunneling transistor: M.T. Tuominen, J.M. Hergenrother, T.S. Tighe, and M. Tinkham, *Phys. Rev. Lett.* **69**, 1997–2000 (1992).
- Measurements of charge soliton motion in two-dimensional arrays of ultrasmall Josephson junctions: T.S. Tighe, M.T. Tuominen, J.M. Hergenrother, and M. Tinkham, *Phys. Rev. B* **47** (Rapid Communication) 1145–1148 (1993).
- Charge transport by andreev reflection through a mesoscopic superconducting island: J.M. Hergenrother, M.T. Tuominen, and M. Tinkham, *Phys. Rev. Lett.* **72**, 1742–1745 (1994).
- Photon-activated switch behavior in the single-electron transistor with a superconducting island: J.M. Hergenrother, J.G. Lu, M.T. Tuominen, D.C. Ralph, and M. Tinkham, *Phys. Rev. B* **51**, (Rapid Comm.) 9407–9410 (1995).
- Spectroscopic measurements of discrete electronic states in singlemetal particles: D.C. Ralph, C.T. Black, and M. Tinkham, *Phys. Rev. Lett.* **74**, 3241–3244 (1995).
- Temperature dependence of even-odd electron number effects in the single-electron transistor with superconducting island: M. Tinkham, J.M. Hergenrother, and J.G. Lu, *Phys. Rev. B* **51**, 12649–12652 (1995).

- Spectroscopy of the superconducting gap in individual nanometer-scale aluminum particles: C.T. Black, D.C. Ralph, and M. Tinkham. *Phys. Rev. Lett.* **76**, 688–691 (1996).
- Transition temperature of Josephson junction arrays with long-range interaction: H.R. Shea and M. Tinkham, *Phys. Rev. Lett.* **79**, 2324–2327 (1997).
- Observation of andreev reflection in all-superconducting single-electron transistors, R.J. Fitzgerald, S.L. Pohlen, and M. Tinkham, *Phys. Rev. B (Rapid Comm.)* **57**, R1 1073–11076 (1998).
- Metallic quantum dots, M. Tinkham, *Phil. Mag.* **B79**, 1267–1280 (1999).
- Quantum suppression of superconductivity in ultrathin wires, A. Bezryadin, C.N. Lau and M. Tinkham, *Nature* **404**, 971–974 (2000).
- Electronic properties of mechanically-induced defects in single-walled carbon nanotubes, D. Bozovic, M. Bockrath, W. Liang, H. Park, J. Hafner, C.M. Lieber, and M. Tinkham, *Appl. Phys. Lett.*, **78**, 3693–3695 (2001).
- Quantum phase-slips in superconducting nanowires, C.N. Lau, N. Markovic, M. Bockrath, A. Bezryadin, and M. Tinkham, *Phys. Rev. Lett.* **87**, 217003 (2001).
- Hysteretic I-V curves in superconducting nanowires, J.U. Free, C.N. Lau, and N. Markovic, *Phys. Rev. B* **68**, 134515 (2003).